Department of
CLINICAL SCIENCES, INTERVENTION AND TECHNOLOGY
Division for Medical Imaging, Function and Technology
Karolinska Institutet, Stockholm, Sweden

A TINY GLIMPSE INTO THE HUMAN BRAIN USING MODEL-FREE ANALYSIS FOR RESTING-STATE FMRI DATA

Yanlu Wang

Stockholm 2015

Department of
CLINICAL SCIENCES, INTERVENTION AND TECHNOLOGY
Division for Medical Imaging, Function and Technology
Karolinska Institutet, Stockholm, Sweden

A TINY GLIMPSE INTO THE HUMAN BRAIN USING MODEL-FREE ANALYSIS FOR RESTING-STATE FMRI DATA

Yanlu Wang

Stockholm 2015

All previously published papers were reproduced with permission from the publisher.
Published by Karolinska Institutet.
Printed by E-Print AB 2015

ISBN 978-91-7676-109-0

All previously published papers were reproduced with permission from the publisher.
Published by Karolinska Institutet.
Printed by E-Print AB 2015
© Yanlu Wang, 2015
ISBN 978-91-7676-109-0

A TINY GLIMPSE INTO THE HUMAN BRAIN USING MODEL-FREE ANALYSIS FOR RESTING-STATE FMRI DATA

THESIS FOR DOCTORAL DEGREE (Ph.D.)

By

Yanlu Wang

Principal Supervisor:
Prof. Tie-Qiang Li
Karolinska Institute
Department of Clinical Sciences, Intervention and Technology
Division for Medical Imaging, Function and Technology

Co-supervisor(s):
Prof. Mussie Msghina
Karolinska Institutet
Department of Clinical Neuroscience

Prof. Svein Kleiven
Royal Institute of Technology (KTH)
School of Technology and Health
Department of Medical Engineering
Unit of Neuronics

Prof. Istvan Furo
Royal Institute of Technology (KTH)
School of Chemical Science and Engineering
Department of Chemistry
Division for Applied Physical Chemistry

Opponent:
Prof. Peter Lundberg
Linköping University
Department of Medical and Health Sciences
Division of Radiological Sciences

Examination Board:
Prof. Pia Sundgren
Lund University
Department of Clinical Sciences, Lund
Division for Diagnostic Radiology

A TINY GLIMPSE INTO THE HUMAN BRAIN USING MODEL-FREE ANALYSIS FOR RESTING-STATE FMRI DATA

THESIS FOR DOCTORAL DEGREE (Ph.D.)

By

Yanlu Wang

Principal Supervisor:
Prof. Tie-Qiang Li
Karolinska Institute
Department of Clinical Sciences, Intervention and Technology
Division for Medical Imaging, Function and Technology

Co-supervisor(s):
Prof. Mussie Msghina
Karolinska Institutet
Department of Clinical Neuroscience

Prof. Svein Kleiven
Royal Institute of Technology (KTH)
School of Technology and Health
Department of Medical Engineering
Unit of Neuronics

Prof. Istvan Furo
Royal Institute of Technology (KTH)
School of Chemical Science and Engineering
Department of Chemistry
Division for Applied Physical Chemistry

Opponent:
Prof. Peter Lundberg
Linköping University
Department of Medical and Health Sciences
Division of Radiological Sciences

Examination Board:
Prof. Pia Sundgren
Lund University
Department of Clinical Sciences, Lund
Division for Diagnostic Radiology

To my dearly beloved wife, whom gives purpose to my resting-state functional connectivity networks.

To my dearly beloved wife, whom gives purpose to my resting-state functional connectivity networks.

ABSTRACT

Resting-state functional Magnetic Resonance Imaging (fMRI) acquires four dimensional data that indirectly depicts human brain activity. Within these four dimensional datasets reside resting-state functional connectivity networks (RFNs), depicting how the human brain is organized functionally. This series of studies delve into the use of data-driven analysis methods for resting-state fMRI data. Their strengths were explored and their weaknesses tackled, both in their methodologies and applications, all in hope to gain a better understanding of the data, and thereby how the brain function.

The journey begins through the usage of one of the most common data-driven analysis methods in use today: Independent Component Analysis (ICA). ICA requires no user input parameter apart from the input dataset and the number of output Independent Components (NIC). The requirement of the NIC, *a priori*, is troubling as the inherent number of Independent Components (ICs) that exists within non-simulated datasets is unknown, due to the existence of various noise and artefact sources to differing degrees. Furthermore, comparing datasets using ICA is problematic because of the inherently different dimensionality of different datasets. To investigate the effects of NIC on the ICA output results, a classification framework based on Support Vector Machines (SVM) was implemented to automatically classify ICs as either potential RFNs, or noise/artefact signal. This feature-optimized classification of ICs with SVM, or FOCIS, framework uses features derived from verbal instructions for manual visual inspection of ICs. With only few significant features selected through iterative feature-selection and a small training set, the classification framework performed well with over 98% in overall accuracy for group ICA output results. Analysis of different resting-state fMRI datasets using FOCIS indicated that the specification of NIC can critically affect the ICA results on resting-state fMRI data. These changes are complex and are individually different from one another, irrespective whether the IC is a potential RFN or artefact/noise signals. Applying this knowledge on group comparison studies, ICA was used to study migraine patients undergo kinetic oscillation stimulation treatment. The immediate effects of the treatment allows direct correlation of a patient's pain levels with changes in their RFNs. Differences in RFNs that include areas in the midbrain and limbic system regulating the central nervous system were discovered in migraine patients compared to healthy control group. Overlapping areas were also shown to be affected by the treatment. These results provide supporting evidence for the hypothesis that the treatment affects and regulates the parasympathetic autonomic reflex, alleviating migraine symptoms.

Hierarchical clustering is another data-driven analysis method that is almost devoid of all user-input parameters. The algorithm naturally stratifies data into a hierarchical structure. It is believed that brain function is hierarchically organized, so an algorithm which reflects this aspect is a seemingly excellent choice to use for analyzing the resting-state fMRI data. A hierarchical clustering analysis framework was developed to extract RFNs from resting-state fMRI data with full brain coverage at voxel level. The RFNs identified using hierarchical clustering conforms to those identified previously using other data processing techniques, such

ABSTRACT

Resting-state functional Magnetic Resonance Imaging (fMRI) acquires four dimensional data that indirectly depicts human brain activity. Within these four dimensional datasets reside resting-state functional connectivity networks (RFNs), depicting how the human brain is organized functionally. This series of studies delve into the use of data-driven analysis methods for resting-state fMRI data. Their strengths were explored and their weaknesses tackled, both in their methodologies and applications, all in hope to gain a better understanding of the data, and thereby how the brain function.

The journey begins through the usage of one of the most common data-driven analysis methods in use today: Independent Component Analysis (ICA). ICA requires no user input parameter apart from the input dataset and the number of output Independent Components (NIC). The requirement of the NIC, *a priori*, is troubling as the inherent number of Independent Components (ICs) that exists within non-simulated datasets is unknown, due to the existence of various noise and artefact sources to differing degrees. Furthermore, comparing datasets using ICA is problematic because of the inherently different dimensionality of different datasets. To investigate the effects of NIC on the ICA output results, a classification framework based on Support Vector Machines (SVM) was implemented to automatically classify ICs as either potential RFNs, or noise/artefact signal. This feature-optimized classification of ICs with SVM, or FOCIS, framework uses features derived from verbal instructions for manual visual inspection of ICs. With only few significant features selected through iterative feature-selection and a small training set, the classification framework performed well with over 98% in overall accuracy for group ICA output results. Analysis of different resting-state fMRI datasets using FOCIS indicated that the specification of NIC can critically affect the ICA results on resting-state fMRI data. These changes are complex and are individually different from one another, irrespective whether the IC is a potential RFN or artefact/noise signals. Applying this knowledge on group comparison studies, ICA was used to study migraine patients undergo kinetic oscillation stimulation treatment. The immediate effects of the treatment allows direct correlation of a patient's pain levels with changes in their RFNs. Differences in RFNs that include areas in the midbrain and limbic system regulating the central nervous system were discovered in migraine patients compared to healthy control group. Overlapping areas were also shown to be affected by the treatment. These results provide supporting evidence for the hypothesis that the treatment affects and regulates the parasympathetic autonomic reflex, alleviating migraine symptoms.

Hierarchical clustering is another data-driven analysis method that is almost devoid of all user-input parameters. The algorithm naturally stratifies data into a hierarchical structure. It is believed that brain function is hierarchically organized, so an algorithm which reflects this aspect is a seemingly excellent choice to use for analyzing the resting-state fMRI data. A hierarchical clustering analysis framework was developed to extract RFNs from resting-state fMRI data with full brain coverage at voxel level. The RFNs identified using hierarchical clustering conforms to those identified previously using other data processing techniques, such

as ICA. An innate ability of the clustering algorithm is to naturally organize data into a hierarchical tree (dendrogram). This was fully utilized though extensions in the framework for cluster evaluation. Extending the hierarchical clustering framework with the cluster evaluation pipeline allowed extraction of functional subdivisions of known RFNs. This demonstrated that not only can hierarchical clustering be used to extract the modular organization at the scale of large systems for entire RFNs, but can also be used to derive the functional subdivision of RFNs and provide a consistent method of analysis at different levels of detail. The sub-networks extracted using hierarchical clustering reveals the intrinsic functional connectivity amongst the subnetworks within RFNs and provide clues for further exploring the potential for currently unknown functional junctions within RFNs.

as ICA. An innate ability of the clustering algorithm is to naturally organize data into a hierarchical tree (dendrogram). This was fully utilized though extensions in the framework for cluster evaluation. Extending the hierarchical clustering framework with the cluster evaluation pipeline allowed extraction of functional subdivisions of known RFNs. This demonstrated that not only can hierarchical clustering be used to extract the modular organization at the scale of large systems for entire RFNs, but can also be used to derive the functional subdivision of RFNs and provide a consistent method of analysis at different levels of detail. The sub-networks extracted using hierarchical clustering reveals the intrinsic functional connectivity amongst the subnetworks within RFNs and provide clues for further exploring the potential for currently unknown functional junctions within RFNs.

LIST OF SCIENTIFIC PAPERS

I. **Analysis of Whole-Brain Resting-State fMRI Data Using Hierarchical Clustering Approach**, **Wang Y.**; Li TQ., PLoS ONE, 2013, **8** (10)

II. **Dimensionality of ICA in resting-state fMRI investigated by featurre optimized classification of independent components with SVM**, **Wang Y.**; Li TQ.; Frontiers in Human Neuroscience, 2015, 9 (259)

III. **Studying Sub-dendrograms of Resting-state Functional Networks with Voxel-wise Hierarchical Clustering**, **Wang Y.**; Msghina M.; Li TQ., Frontiers in Human Neuroscience, *submitted 2015, 8*

IV. **Resting-state fMRI Study of Acute Migraine Treatment with Kinetic Oscillation Stimulation in Nasal Cavity**, Li TQ.; **Wang Y.**; Juto JE., *manuscript*

LIST OF SCIENTIFIC PAPERS

I. **Analysis of Whole-Brain Resting-State fMRI Data Using Hierarchical Clustering Approach**, **Wang Y.**; Li TQ., PLoS ONE, 2013, **8** (10)

II. **Dimensionality of ICA in resting-state fMRI investigated by featurre optimized classification of independent components with SVM**, **Wang Y.**; Li TQ.; Frontiers in Human Neuroscience, 2015, 9 (259)

III. **Studying Sub-dendrograms of Resting-state Functional Networks with Voxel-wise Hierarchical Clustering**, **Wang Y.**; Msghina M.; Li TQ., Frontiers in Human Neuroscience, *submitted 2015, 8*

IV. **Resting-state fMRI Study of Acute Migraine Treatment with Kinetic Oscillation Stimulation in Nasal Cavity**, Li TQ.; **Wang Y.**; Juto JE., *manuscript*

CONTENTS

CONTENTS

1 Introduction 8
1.1 What is resting-state fMRI 8
1.2 Analysis methods 9
2 Independent Component Analysis 12
2.1 Interpreting blind-source separation 13
2.2 Dimensionality of resting-state fMRI datasets 13
2.3 Application on group comparison studies 14
2.4 Treating migraine with kinetic oscillation Stimulation 14
2.5 Study outline 15
2.6 FOCIS 16
2.7 ICA analysis 16
2.8 Classification and dimensionality investigation 17
2.9 Kinetic Oscillation Stimulation treatment effects on migraine patients 19
3 Hierarchical Clustering 22
3.1 How Hierarchical Clustering Works 22
3.2 On Distance Measures 23
3.3 On Linkage 24
3.4 Data mining and visualization 24
3.5 Definition of RFNS and sub-networks 26
3.6 cluster Evaluation and Where to stop cutting 27
3.7 Study Outline 28
3.8 Implementing the hierarchical clustering framework 28
3.8.1 The necessity of optimizations 28
3.8.2 Memory allocation 29
3.8.3 Parallel Programming 29
3.8.4 Dimensionality reduction 29
3.8.5 Libraries 29
3.9 Hierarchical clustering and ICA results 30
3.10 Functional hierarchies 30
4 Summary 34
5 Future Perspectives 35
6 Acknowledgements 37
References 39

LIST OF ABBREVIATIONS (IN ORDER OF APPEARANCE)

(f)MRI	(functional) **M**agnetic **R**esonance **I**maging
BOLD	**B**lood **O**xygen **L**evel **D**ependent (contrast)
RFN	**R**esting-state **F**unctional connectivity **N**etwork
GLM	**G**eneral **L**inear **M**odel
ROI	**R**egion **O**f **I**nterest
ICA	**I**ndependent **C**omponent **A**nalysis
IC	**I**ndependent **C**omponent
NIC	**N**umber of **I**ndependent **C**omponents (parameter)
KOS	**K**inetic **O**scillation **S**timulation (treatment)
SVM	**S**upport **V**ector **M**achines
FOCIS	**F**eature **O**ptimized **C**lassification of **I**ndependent components using **S**upport vector machines (framework)
ANOVA	**AN**alysis **O**f **VA**riance
CC	(cross-) **C**orrelation **C**oefficient

LIST OF ABBREVIATIONS (IN ORDER OF APPEARANCE)

(f)MRI	(functional) **M**agnetic **R**esonance **I**maging
BOLD	**B**lood **O**xygen **L**evel **D**ependent (contrast)
RFN	**R**esting-state **F**unctional connectivity **N**etwork
GLM	**G**eneral **L**inear **M**odel
ROI	**R**egion **O**f **I**nterest
ICA	**I**ndependent **C**omponent **A**nalysis
IC	**I**ndependent **C**omponent
NIC	**N**umber of **I**ndependent **C**omponents (parameter)
KOS	**K**inetic **O**scillation **S**timulation (treatment)
SVM	**S**upport **V**ector **M**achines
FOCIS	**F**eature **O**ptimized **C**lassification of **I**ndependent components using **S**upport vector machines (framework)
ANOVA	**AN**alysis **O**f **VA**riance
CC	(cross-) **C**orrelation **C**oefficient

PREFACE

In the digital age, large amounts of data seems to be easily acquired. A system can be set up with relative ease to acquire enormous amounts of data. The difficult part remains to extract meaningful information from a seemingly overwhelming amount of gathered data. One then, can one interpret the data, and draw useful conclusions from within. Functional magnetic resonance imaging produces large quantities of data of the human brain; and within, hides the patterns depicting shadows of our consciousness. To better understand the human brain and ourselves, tools were created to extract meaningful information from data that are difficult immediately grasp with our minds.

As tradition dictates, the following sections will include a summary of the articles I have published (and yet to publish) throughout my studies. This is often done in a standard, de-facto format, for scientific articles today. Yet, this format does not lend itself for the purpose tying in different studies into a coherent whole, with a consistent pattern of thought. This is why I have attempted to, as much as possible, write this summary in prose, believing that this format will better reflect my thought processes throughout my studies. Those of you readers with an undying need to see scientific rigor in their predefined sections, the published articles (and manuscripts) can be found appended as usual. But for those who do not feel the urge to see sections called “Materials and Methods” and “Conclusion” in everything they read, you’re welcome (or at least I tried).

Aug 2015

PREFACE

In the digital age, large amounts of data seems to be easily acquired. A system can be set up with relative ease to acquire enormous amounts of data. The difficult part remains to extract meaningful information from a seemingly overwhelming amount of gathered data. One then, can one interpret the data, and draw useful conclusions from within. Functional magnetic resonance imaging produces large quantities of data of the human brain; and within, hides the patterns depicting shadows of our consciousness. To better understand the human brain and ourselves, tools were created to extract meaningful information from data that are difficult immediately grasp with our minds.

As tradition dictates, the following sections will include a summary of the articles I have published (and yet to publish) throughout my studies. This is often done in a standard, de-facto format, for scientific articles today. Yet, this format does not lend itself for the purpose tying in different studies into a coherent whole, with a consistent pattern of thought. This is why I have attempted to, as much as possible, write this summary in prose, believing that this format will better reflect my thought processes throughout my studies. Those of you readers with an undying need to see scientific rigor in their predefined sections, the published articles (and manuscripts) can be found appended as usual. But for those who do not feel the urge to see sections called “Materials and Methods” and “Conclusion” in everything they read, you’re welcome (or at least I tried).

Aug 2015

1 INTRODUCTION

The following sections provide background information for those not directly involved in the field of functional Magnetic Resonance Imaging (fMRI) to comprehend and appreciate the thought patterns throughout my studies. This section could, and should, be averted by those with an established understanding of resting-state fMRI and its processing methods.

1.1 WHAT IS RESTING-STATE FMRI

Magnetic Resonance Imaging (MRI) is a medical imaging technique that uses the differing quantum mechanical properties of different types of tissue to form an image noninvasively. MRI is completely noninvasive, unlike most other medical imaging techniques such as X-ray, Computed Tomography, and Positron Emission Tomography, all of which requires one to be subjected to ionizing radiation to form a meaningful image.

In neuroimaging, MRI scans are traditionally used to visualize the anatomical structure of the brain. fMRI is a special type of brain scanning technique, using MRI that visualizes the brain's function by using a technique called Blood Oxygen Level Dependent (BOLD) contrast [1]. The theory behind BOLD contrast is as follows: When neurons in the brain activate during task, they will absorb energy in the form of oxygen and other nutrients from the surrounding capillaries. This causes a slight drop in blood oxygen levels in the capillaries surrounding areas of brain activity. The body will sense this drop and over-compensate by flushing fresh, oxygenated, blood to that area in excess [2, 3]. This phenomenon is called the hemodynamic response, and is important due to two reasons: (1) It can be modelled through the hemodynamic response function and (2) It can be measured using MRI because oxygenated blood and deoxygenated blood have different magnetic properties [4].

The purpose of task based fMRI (or paradigm fMRI) is to visualize regions of the brain responsible for processing specific external stimuli. In a task based fMRI experiment, a subject is scanned continuously for a duration about 6-12 minutes using a special type of pulse-sequence. This sequence (typically based on an echo-planar imaging technique [5]), is strongly T2*-weighted and sensitive to BOLD contrast. The sequence is also very fast such that an image of an entire brain is acquired in the duration of between 0.5 to 3.0 seconds. It continuously scans the brain much like sequential shooting options for digital cameras. During the scan, the subject is exposed to predefined stimuli, designed to activate specific regions of the brain at timed intervals. The stimulus can be as simple as a sound or picture, to more complex tasks such as emotional or social thought processing tasks. After processing, the specific regions of the brain responsible for processing the presented stimuli can be visualized in vibrant colors as overlays on top of a structural image of the brain.

Resting-state fMRI is simply task-based fMRI without a task. In a resting-state fMRI experiment, the subject is scanned in the same fashion as task-based fMRI, but without any stimulus presented during scanning. The data acquired in this fashion would reflect thought patterns associated with the wandering mind (unless the subject falls asleep). In one respect,

1 INTRODUCTION

The following sections provide background information for those not directly involved in the field of functional Magnetic Resonance Imaging (fMRI) to comprehend and appreciate the thought patterns throughout my studies. This section could, and should, be averted by those with an established understanding of resting-state fMRI and its processing methods.

1.1 WHAT IS RESTING-STATE FMRI

Magnetic Resonance Imaging (MRI) is a medical imaging technique that uses the differing quantum mechanical properties of different types of tissue to form an image noninvasively. MRI is completely noninvasive, unlike most other medical imaging techniques such as X-ray, Computed Tomography, and Positron Emission Tomography, all of which requires one to be subjected to ionizing radiation to form a meaningful image.

In neuroimaging, MRI scans are traditionally used to visualize the anatomical structure of the brain. fMRI is a special type of brain scanning technique, using MRI that visualizes the brain's function by using a technique called Blood Oxygen Level Dependent (BOLD) contrast [1]. The theory behind BOLD contrast is as follows: When neurons in the brain activate during task, they will absorb energy in the form of oxygen and other nutrients from the surrounding capillaries. This causes a slight drop in blood oxygen levels in the capillaries surrounding areas of brain activity. The body will sense this drop and over-compensate by flushing fresh, oxygenated, blood to that area in excess [2, 3]. This phenomenon is called the hemodynamic response, and is important due to two reasons: (1) It can be modelled through the hemodynamic response function and (2) It can be measured using MRI because oxygenated blood and deoxygenated blood have different magnetic properties [4].

The purpose of task based fMRI (or paradigm fMRI) is to visualize regions of the brain responsible for processing specific external stimuli. In a task based fMRI experiment, a subject is scanned continuously for a duration about 6-12 minutes using a special type of pulse-sequence. This sequence (typically based on an echo-planar imaging technique [5]), is strongly T2*-weighted and sensitive to BOLD contrast. The sequence is also very fast such that an image of an entire brain is acquired in the duration of between 0.5 to 3.0 seconds. It continuously scans the brain much like sequential shooting options for digital cameras. During the scan, the subject is exposed to predefined stimuli, designed to activate specific regions of the brain at timed intervals. The stimulus can be as simple as a sound or picture, to more complex tasks such as emotional or social thought processing tasks. After processing, the specific regions of the brain responsible for processing the presented stimuli can be visualized in vibrant colors as overlays on top of a structural image of the brain.

Resting-state fMRI is simply task-based fMRI without a task. In a resting-state fMRI experiment, the subject is scanned in the same fashion as task-based fMRI, but without any stimulus presented during scanning. The data acquired in this fashion would reflect thought patterns associated with the wandering mind (unless the subject falls asleep). In one respect,

the name resting-state fMRI is misleading as the brain is never truly at rest. One is typically instructed to not think about anything *in particular*, instead letting thoughts flow at will. Different regions of the brain work in synchronous with each other, for any particular thought. The regions of the brain working in synchrony for any particular thought, is known as (resting-state) functional connectivity networks, or RFNs. Even without a particular cue or stimulus, the mind wanders during the scan, and this mind wandering results in different thoughts which activates different RFNs. Multiple RFNs are consistently identified, many corresponding to task activated areas from task based fMRI studies [6, 7] (some are uniquely identified in resting-state fMRI, such as the default-mode network [8, 9]). Instead of just extracting one RFN from each scanning session, one hopes to extract multiple (if not "all") RFNs residing within resting-state fMRI data, "all at once".

1.2 ANALYSIS METHODS

fMRI data as obtained from the MRI scanner does not look anything similar to the vibrant images in the "Results" section of a published scientific paper. Many stages of processing and analysis is required to produce the final image. It should be noted that, before the actual analysis is performed, the acquired fMRI data should be subjected to multiple computational steps, collectively known as the *preprocessing* pipeline. The preprocessing steps are purposed to remove confounding factors in the fMRI data. Since preprocessing is not the main focus, further explanation shall be abstained due to space constraints. Pre-processing is an essential and important step in the analysis, and at times, more complex and heavily scrutinized than the analysis method and is a subject on its own. There are many excellent review articles explaining the most common pre-processing steps in more details [10].

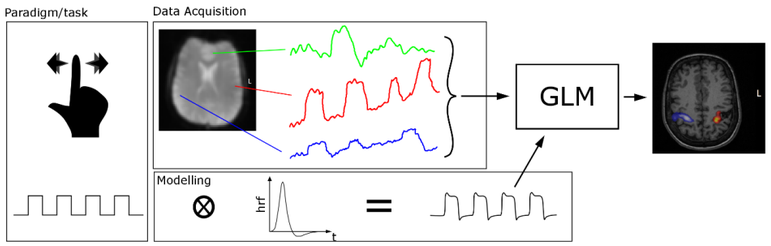

Figure 1: Illustrative overview of GLM-based analysis methods for task-based fMRI

For task-based fMRI, the conventionally used analysis method is to process each voxel (volumetric pixel) individually using the General Linear Model (GLM). This method is commonly known as the GLM-method [11, 12]. It is comparatively simple and easily comprehensible. The stimulus onset timing and duration forms basis of the model. It is then convolved with the hemodynamic response function, to create an "ideal" time-course for the

the name resting-state fMRI is misleading as the brain is never truly at rest. One is typically instructed to not think about anything *in particular*, instead letting thoughts flow at will. Different regions of the brain work in synchronous with each other, for any particular thought. The regions of the brain working in synchrony for any particular thought, is known as (resting-state) functional connectivity networks, or RFNs. Even without a particular cue or stimulus, the mind wanders during the scan, and this mind wandering results in different thoughts which activates different RFNs. Multiple RFNs are consistently identified, many corresponding to task activated areas from task based fMRI studies [6, 7] (some are uniquely identified in resting-state fMRI, such as the default-mode network [8, 9]). Instead of just extracting one RFN from each scanning session, one hopes to extract multiple (if not "all") RFNs residing within resting-state fMRI data, "all at once".

1.2 ANALYSIS METHODS

fMRI data as obtained from the MRI scanner does not look anything similar to the vibrant images in the "Results" section of a published scientific paper. Many stages of processing and analysis is required to produce the final image. It should be noted that, before the actual analysis is performed, the acquired fMRI data should be subjected to multiple computational steps, collectively known as the *preprocessing* pipeline. The preprocessing steps are purposed to remove confounding factors in the fMRI data. Since preprocessing is not the main focus, further explanation shall be abstained due to space constraints. Pre-processing is an essential and important step in the analysis, and at times, more complex and heavily scrutinized than the analysis method and is a subject on its own. There are many excellent review articles explaining the most common pre-processing steps in more details [10].

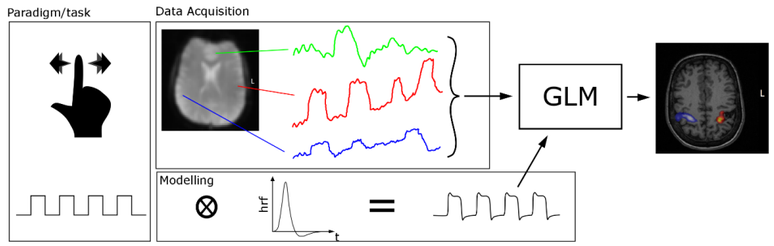

Figure 1: Illustrative overview of GLM-based analysis methods for task-based fMRI

For task-based fMRI, the conventionally used analysis method is to process each voxel (volumetric pixel) individually using the General Linear Model (GLM). This method is commonly known as the GLM-method [11, 12]. It is comparatively simple and easily comprehensible. The stimulus onset timing and duration forms basis of the model. It is then convolved with the hemodynamic response function, to create an "ideal" time-course for the

particular stimulus. The ideal time-course is then used to assess each voxel of the brain's time-course using the general linear model. Voxels with time-courses similar to the "ideal" time-course will have a high t-score and those who do not will have a low t-score. After this statistical mapping, the t-scores for all voxels are thresholded to obtain only the significant voxels. The thresholded t-map is then color mapped with bright colors and presented on top a structural image of the brain. This entire workflow can be seen illustrated in Figure 1. GLM-based statistical parametric mapping technique is conceptually transparent and relatively easy to perform, especially with ready-made software now readily available.

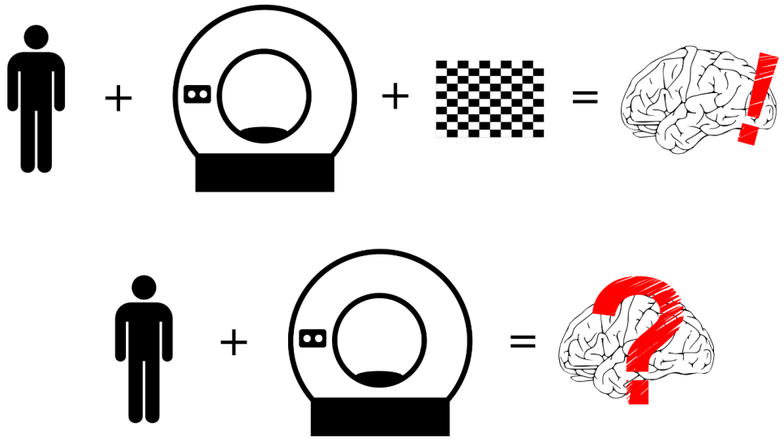

Figure 2: Task based fMRI analysis relies on the explicit timing of the stimulus presented during the scan. Without the presence of a task and its timing information in resting-state fMRI, the analysis method becomes much less intuitive

The unfortunate problem with the GLM-method is that it does not readily translate to being applied to resting-state fMRI data (Figure 2). Conventionally, the seed-voxel analysis method [13] was used on resting-state fMRI data. This method is actually a translation of the GLM-method as follows: One would draw a Region of Interest (ROI), extract the average time-course from all voxels inside the ROI, and use the averaged time-course as the "ideal" time-course to access all other voxels using GLM. This works relatively well and to this day is still frequently used, however; one fundamental problem still persists: In task based fMRI, one's interests are mostly predefined by the stimuli chosen at the time of data acquisition. For example, if an fMRI experiment is performed using an auditory stimulus, it would be the auditory network that is of interest and not the visual network. The intention of resting-state fMRI is to extract as many RFNs simultaneously without knowing what lies within the data prior to analysis. To this end, the seed-voxel analysis method is just simply lacking. Furthermore, the ROI dictates the outcome of the analysis. The ROIs are typically drawn by the hands of the individual user, which will vary from one individual to the next.

particular stimulus. The ideal time-course is then used to assess each voxel of the brain's time-course using the general linear model. Voxels with time-courses similar to the "ideal" time-course will have a high t-score and those who do not will have a low t-score. After this statistical mapping, the t-scores for all voxels are thresholded to obtain only the significant voxels. The thresholded t-map is then color mapped with bright colors and presented on top a structural image of the brain. This entire workflow can be seen illustrated in Figure 1. GLM-based statistical parametric mapping technique is conceptually transparent and relatively easy to perform, especially with ready-made software now readily available.

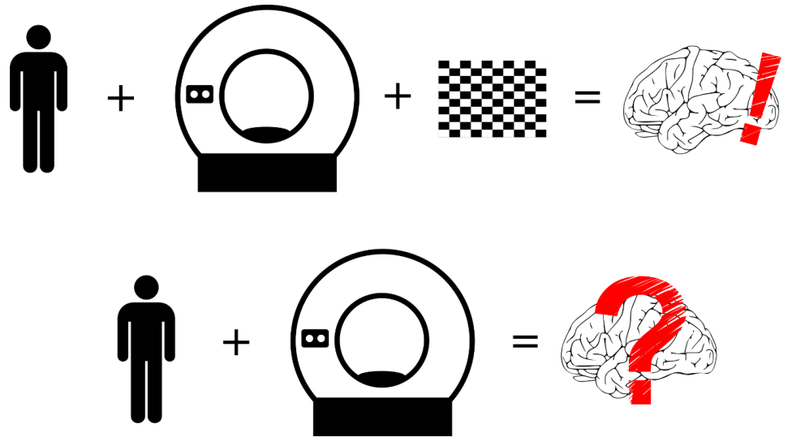

Figure 2: Task based fMRI analysis relies on the explicit timing of the stimulus presented during the scan. Without the presence of a task and its timing information in resting-state fMRI, the analysis method becomes much less intuitive

The unfortunate problem with the GLM-method is that it does not readily translate to being applied to resting-state fMRI data (Figure 2). Conventionally, the seed-voxel analysis method [13] was used on resting-state fMRI data. This method is actually a translation of the GLM-method as follows: One would draw a Region of Interest (ROI), extract the average time-course from all voxels inside the ROI, and use the averaged time-course as the "ideal" time-course to access all other voxels using GLM. This works relatively well and to this day is still frequently used, however; one fundamental problem still persists: In task based fMRI, one's interests are mostly predefined by the stimuli chosen at the time of data acquisition. For example, if an fMRI experiment is performed using an auditory stimulus, it would be the auditory network that is of interest and not the visual network. The intention of resting-state fMRI is to extract as many RFNs simultaneously without knowing what lies within the data prior to analysis. To this end, the seed-voxel analysis method is just simply lacking. Furthermore, the ROI dictates the outcome of the analysis. The ROIs are typically drawn by the hands of the individual user, which will vary from one individual to the next.

10

Researchers needed model-free analysis methods that do not require prior hypothesis or ROIs to be drawn beforehand to fully explore resting-state fMRI data. A consequence of this is that the model-free analysis methods do not often even require a solid hypothesis to be formulated prior to analysis. Hence, they are not as transparent and comprehensible due to their complexity and generality. Interpreting the results can be difficult as a drawback of their ability to function, without a solid hypothesis, is that their output may be vague in meaning.

Researchers needed model-free analysis methods that do not require prior hypothesis or ROIs to be drawn beforehand to fully explore resting-state fMRI data. A consequence of this is that the model-free analysis methods do not often even require a solid hypothesis to be formulated prior to analysis. Hence, they are not as transparent and comprehensible due to their complexity and generality. Interpreting the results can be difficult as a drawback of their ability to function, without a solid hypothesis, is that their output may be vague in meaning.

11

2 INDEPENDENT COMPONENT ANALYSIS

ICA is a popular and widely used data-driven method to analyze resting-state fMRI data [14]. How ICA works may not be very intuitive for most, but with software packages like FSL [15] (http://fsl.fmrib.ox.ac.uk/fsl/) and GIFT (http://www.nitrc.org/projects/gift) almost anyone can use ICA to analyze resting-state fMRI data.

This would normally be the place to get into the technical details of ICA, but it shall be omitted here. For those interested in the technical details behind ICA, certainly one can easily find better source of information than what can be managed on these pages. For introductory purposes, knowing how ICA functions conceptually will suffice. What is relevant, is how to interpret the output results from ICA analysis, and how to correctly apply ICA analysis on group comparison studies.

How ICA works conceptually can be intuitively explained through noise cancellation on modern mobile phones: There are usually many noise sources during a mobile phone conversation in cities. Speaking on your phone in a crowded café by a busy street is not a big problem for the modern mobile phone. Inside your phone lies a chip running a variant of ICA which decomposes the sound signal received through the microphone to its individual sources, including your voice, other people's conversations, and the traffic noise outside for example. Once the sound sources have been isolated, all noise sources can be eliminated to transmit only the sound of your voice to the recipient. How the algorithm identifies your voice amongst the noise signals is another (more difficult) question altogether. The entire process is illustrated in Figure 3.

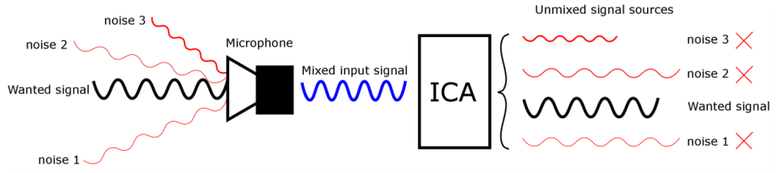

Figure 3: Illustrative example of how ICA can be used to separate signal sources from a mixture of sounds to filter out unwanted noise sources during a typical mobile phone conversation.

In the case of ICA applied to resting-state fMRI data, ICA takes the entire 4D dataset as an input and outputs a predefined number of independent components (ICs), with each component representing a potential signal source, that altogether form the original input data [16]. Each IC (time-course) is then mapped spatially using statistical mapping to form activation maps corresponding to the signal sources, in order to locate the regions of the brain where the signal source originates from.

2 INDEPENDENT COMPONENT ANALYSIS

ICA is a popular and widely used data-driven method to analyze resting-state fMRI data [14]. How ICA works may not be very intuitive for most, but with software packages like FSL [15] (http://fsl.fmrib.ox.ac.uk/fsl/) and GIFT (http://www.nitrc.org/projects/gift) almost anyone can use ICA to analyze resting-state fMRI data.

This would normally be the place to get into the technical details of ICA, but it shall be omitted here. For those interested in the technical details behind ICA, certainly one can easily find better source of information than what can be managed on these pages. For introductory purposes, knowing how ICA functions conceptually will suffice. What is relevant, is how to interpret the output results from ICA analysis, and how to correctly apply ICA analysis on group comparison studies.

How ICA works conceptually can be intuitively explained through noise cancellation on modern mobile phones: There are usually many noise sources during a mobile phone conversation in cities. Speaking on your phone in a crowded café by a busy street is not a big problem for the modern mobile phone. Inside your phone lies a chip running a variant of ICA which decomposes the sound signal received through the microphone to its individual sources, including your voice, other people's conversations, and the traffic noise outside for example. Once the sound sources have been isolated, all noise sources can be eliminated to transmit only the sound of your voice to the recipient. How the algorithm identifies your voice amongst the noise signals is another (more difficult) question altogether. The entire process is illustrated in Figure 3.

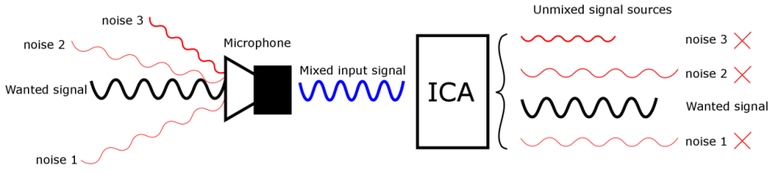

Figure 3: Illustrative example of how ICA can be used to separate signal sources from a mixture of sounds to filter out unwanted noise sources during a typical mobile phone conversation.

In the case of ICA applied to resting-state fMRI data, ICA takes the entire 4D dataset as an input and outputs a predefined number of independent components (ICs), with each component representing a potential signal source, that altogether form the original input data [16]. Each IC (time-course) is then mapped spatially using statistical mapping to form activation maps corresponding to the signal sources, in order to locate the regions of the brain where the signal source originates from.

2.1 INTERPRETING BLIND-SOURCE SEPARATION

A challenge for all data-driven methods, ICA included, are that the output results are not intuitively interpretable. ICA outputs a predefined number of separated signal sources (ICs), each with their corresponding t-map. Typically; some of these ICs will correspond to RFNs, and other ICs will represent artefacts and noise signals. Identifying an IC as either an RFN or a noise/artefact signal to be discarded, is conventionally done using manual methods, through the visual inspection of the IC time-courses and their corresponding t-maps [17]. Proficiency in visual inspection is usually obtained through years of experience and accumulated knowledge. Visual inspection is often a time-consuming process, especially when dealing with a large number of ICs. Visual inspection for large number of ICs must be done independently for each IC. This is because the output ICs are ordered randomly in a set, and one lacks prior knowledge on the number of outputs ICs corresponding to RFNs, and artefact/noise signal. The number of noise/artefact ICs obtained from ICA analysis depends heavily upon how thoroughly different sources of artefact and noise signal are removed during preprocessing. Amount of RFNs that can be identified from ICA analysis depends on a myriad of factors from group size, quality of the data, and whether the subjects in the group have any common abnormal attributes (such as disease or debilitating conditions). Furthermore, the predefined number of output ICs (NIC) influences the outcome greatly. If chosen incorrectly, it might obstruct the visual inspection process [18]. For example, when the NIC is very low (<10), some output ICs might may be RFNs merged together with one or multiple sources of noise or artefacts. This makes IC identification difficult for datasets heavily contaminated by noise and artefacts. On the other hand, for very high NICs (>100), some known RFNs might be found split into multiple output ICs. If unlucky, one might find both of the above mentioned situations simultaneously. Having a good estimate for the dimensionality of resting-state fMRI datasets, will provide valuable information from which the output NIC can be determined prior to analysis. This would in turn provide a solid foundation for future resting-state fMRI studies using ICA.

2.2 DIMENSIONALITY OF RESTING-STATE FMRI DATASETS

Estimating the dimensionality of resting-state fMRI datasets is equivalent to estimating the output NIC parameter for ICA analysis, one is mandated to provide *a priori*. The output NIC is the only user input parameter (with the exception of the input dataset itself) that is required by ICA, but it happens to be one of the greatest source of variability among researchers.

The various methods based on Akaike's information criterion, minimum description length, Bayesian estimates; and probabilistic principle component analysis have been used to model the noise signals and estimate the intrinsic dimensionality of resting-state fMRI data [19]. The aforementioned uncorrelated noise models, tend to over-estimate the intrinsic dimensionality and so several correlated noise models have been developed to improve the estimation [20, 21]. To date, no methods have been shown to dominate in terms of performance, possibly due to the difficulty in evaluating dimensionality estimation performances in non-simulated data. In

2.1 INTERPRETING BLIND-SOURCE SEPARATION

A challenge for all data-driven methods, ICA included, are that the output results are not intuitively interpretable. ICA outputs a predefined number of separated signal sources (ICs), each with their corresponding t-map. Typically; some of these ICs will correspond to RFNs, and other ICs will represent artefacts and noise signals. Identifying an IC as either an RFN or a noise/artefact signal to be discarded, is conventionally done using manual methods, through the visual inspection of the IC time-courses and their corresponding t-maps [17]. Proficiency in visual inspection is usually obtained through years of experience and accumulated knowledge. Visual inspection is often a time-consuming process, especially when dealing with a large number of ICs. Visual inspection for large number of ICs must be done independently for each IC. This is because the output ICs are ordered randomly in a set, and one lacks prior knowledge on the number of outputs ICs corresponding to RFNs, and artefact/noise signal. The number of noise/artefact ICs obtained from ICA analysis depends heavily upon how thoroughly different sources of artefact and noise signal are removed during preprocessing. Amount of RFNs that can be identified from ICA analysis depends on a myriad of factors from group size, quality of the data, and whether the subjects in the group have any common abnormal attributes (such as disease or debilitating conditions). Furthermore, the predefined number of output ICs (NIC) influences the outcome greatly. If chosen incorrectly, it might obstruct the visual inspection process [18]. For example, when the NIC is very low (<10), some output ICs might may be RFNs merged together with one or multiple sources of noise or artefacts. This makes IC identification difficult for datasets heavily contaminated by noise and artefacts. On the other hand, for very high NICs (>100), some known RFNs might be found split into multiple output ICs. If unlucky, one might find both of the above mentioned situations simultaneously. Having a good estimate for the dimensionality of resting-state fMRI datasets, will provide valuable information from which the output NIC can be determined prior to analysis. This would in turn provide a solid foundation for future resting-state fMRI studies using ICA.

2.2 DIMENSIONALITY OF RESTING-STATE FMRI DATASETS

Estimating the dimensionality of resting-state fMRI datasets is equivalent to estimating the output NIC parameter for ICA analysis, one is mandated to provide *a priori*. The output NIC is the only user input parameter (with the exception of the input dataset itself) that is required by ICA, but it happens to be one of the greatest source of variability among researchers.

The various methods based on Akaike's information criterion, minimum description length, Bayesian estimates; and probabilistic principle component analysis have been used to model the noise signals and estimate the intrinsic dimensionality of resting-state fMRI data [19]. The aforementioned uncorrelated noise models, tend to over-estimate the intrinsic dimensionality and so several correlated noise models have been developed to improve the estimation [20, 21]. To date, no methods have been shown to dominate in terms of performance, possibly due to the difficulty in evaluating dimensionality estimation performances in non-simulated data. In

practice; the NIC used in studies differ significantly, hindering direct comparison of the RFNs obtained across different studies.

Many other difficulties associated with applying ICA to resting-state fMRI data can be traced back to the dimensionality problem, including its application on group comparison studies which shall be touched upon briefly in section 2.3.

2.3 APPLICATION ON GROUP COMPARISON STUDIES

Those who originally conceived the idea of applying ICA to resting-state fMRI data probably did not have group comparison studies in mind. While the results from one group ICA analysis is difficult to interpret, it is even more difficult to compare multiple sets of varying ICA results from different datasets.

The underlying hypothesis in group comparison studies are that there are notable differences between the groups under scrutiny. It would be nonsensical to pool subjects from different groups together to perform a single ICA analysis. As comparing different sets of ICA output results is non-trivial. Not only will different dataset be of varying quality, they will invariably be contaminated by different degrees of noise and artefact sources. Multiple factors will affect the dimensionality of each dataset, which will affect the optimal NIC parameter for the different group ICA analyses. Comparing two sets of ICs with differing NIC comes with its own set of difficulties. Even if one manages to find the same RFNs in the different IC sets, how can one be sure that any differences in the RFNs' spatial maps is truly a reflection of group differences instead of an effect of setting the specified NIC? Can one feasibly justify using the same NIC for all groups in a group-comparison study? If justified, does this imply that all group differences in RFNs are devoid of influence from the specified NIC? These questions need to be thoroughly investigated before one can conduct any sort of group comparison studies using ICA with a grounded theoretical footing.

2.4 TREATING MIGRAINE WITH KINETIC OSCILLATION STIMULATION

Kinetic Oscillation Stimulation (KOS) is a completely noninvasive treatment shown to be extremely effective in the treatment of migraine [22]. Patients suffering severe onset of migraine symptoms showed a complete lack of pain, almost directly after treatment and is often cured of all symptoms for an extended period of time just after one session of treatment. The treatment is performed through vibrations administered through the nasal cavity for approximately 15-20 minutes. KOS treatment is ideal for resting-state fMRI studies, as the treatment can be safely administered during MRI scanning, and its apparent effect for migraine is almost immediate.

While the treatment has shown to be effective for various conditions including, but not limited to, migraine, the mechanism of treatment is still uncertain. One hypothesis potentially explaining its undeniable effect, is that KOS treatment stimulates the trigeminal nerve through

practice; the NIC used in studies differ significantly, hindering direct comparison of the RFNs obtained across different studies.

Many other difficulties associated with applying ICA to resting-state fMRI data can be traced back to the dimensionality problem, including its application on group comparison studies which shall be touched upon briefly in section 2.3.

2.3 APPLICATION ON GROUP COMPARISON STUDIES

Those who originally conceived the idea of applying ICA to resting-state fMRI data probably did not have group comparison studies in mind. While the results from one group ICA analysis is difficult to interpret, it is even more difficult to compare multiple sets of varying ICA results from different datasets.

The underlying hypothesis in group comparison studies are that there are notable differences between the groups under scrutiny. It would be nonsensical to pool subjects from different groups together to perform a single ICA analysis. As comparing different sets of ICA output results is non-trivial. Not only will different dataset be of varying quality, they will invariably be contaminated by different degrees of noise and artefact sources. Multiple factors will affect the dimensionality of each dataset, which will affect the optimal NIC parameter for the different group ICA analyses. Comparing two sets of ICs with differing NIC comes with its own set of difficulties. Even if one manages to find the same RFNs in the different IC sets, how can one be sure that any differences in the RFNs' spatial maps is truly a reflection of group differences instead of an effect of setting the specified NIC? Can one feasibly justify using the same NIC for all groups in a group-comparison study? If justified, does this imply that all group differences in RFNs are devoid of influence from the specified NIC? These questions need to be thoroughly investigated before one can conduct any sort of group comparison studies using ICA with a grounded theoretical footing.

2.4 TREATING MIGRAINE WITH KINETIC OSCILLATION STIMULATION

Kinetic Oscillation Stimulation (KOS) is a completely noninvasive treatment shown to be extremely effective in the treatment of migraine [22]. Patients suffering severe onset of migraine symptoms showed a complete lack of pain, almost directly after treatment and is often cured of all symptoms for an extended period of time just after one session of treatment. The treatment is performed through vibrations administered through the nasal cavity for approximately 15-20 minutes. KOS treatment is ideal for resting-state fMRI studies, as the treatment can be safely administered during MRI scanning, and its apparent effect for migraine is almost immediate.

While the treatment has shown to be effective for various conditions including, but not limited to, migraine, the mechanism of treatment is still uncertain. One hypothesis potentially explaining its undeniable effect, is that KOS treatment stimulates the trigeminal nerve through

the nasal cavity. This affects the parasympathetic autonomic reflex of the central nervous system, to regulate and correct any imbalances in the nervous system that may be involved in some types of migraine [22]. Regulation of the nervous system through stimulation through the nasal cavity may explain why KOS treatment is seemingly effective for a range of debilitating conditions. Group comparison of ICA output of resting-state fMRI data, lends itself well to provide supporting evidence for this hypothesis. Since ICA is such a popular method of analysis for resting-state fMRI data, a solid knowledge of how dimensionality selection affects ICA results is vital to using ICA to conduct this group comparison study.

2.5 STUDY OUTLINE

To confidently use ICA for group comparison studies, how the selection of dimensionality affects ICA results for resting-state fMRI data must be better understood. In order to study how the selection of NIC affects ICA results, group ICA on different resting-state fMRI datasets were performed with sequentially increasing NIC from 20 – 100. Performing group ICA analysis for multiple datasets, produces a large amount of output ICs, and visually inspecting all the output ICs is very cumbersome. To facilitate the investigation, an analysis framework to automate the time consuming process of visual inspection of output ICs was developed based on Support Vector Machines (SVM) [23]. The feature-optimized classification of ICs with SVM (FOCIS) framework was implemented in a series of *bash* and *R* (https://www.r-project.org/) scripts. FOCIS was first evaluated for its performance accuracies on both single subject and group ICA results. Classification results for FOCIS was then compared against *FSL-fix* and manual classification results obtained through visual inspection. With favorable classification performance, FOCIS was used to automatically classify all output ICs for the different resting-state fMRI datasets at the specified range of NIC. Sub-routines within FOCIS allows for tracking individual ICs in any NIC and investigate how the specified IC changes in its time-course and spatial pattern through increasing NIC. FOCIS is also capable of tracking all output ICs in a given NIC set and compare how all the ICs change with incremental NICs. These tools allowed for better understanding of how the selection of NIC affects ICA output results. This information also provides valuable insight to how ICA should be used to perform group comparison studies.

Applying the knowledge gathered from investigating the dimensionality of resting-state fMRI datasets and how the selection of NICs affect group ICA output results, a group comparison study was conducted on migraine patients before and after KOS treatment, compared to healthy control volunteers using group ICA. The aim was to provide supporting evidence for the hypothesis for a mechanism of the KOS treatment. In addition, to be able to effectively and accurately compare sets of group ICA results, to extract differences in RFNs between patient and control groups, and before and after treatment. Group ICA were performed individually for each group for migraine patients and healthy volunteers before, during; and after KOS treatment. The results were then analyzed using the 3-way analysis of variance (ANOVA) method to detect differences between the groups, and the effect of KOS treatment.

the nasal cavity. This affects the parasympathetic autonomic reflex of the central nervous system, to regulate and correct any imbalances in the nervous system that may be involved in some types of migraine [22]. Regulation of the nervous system through stimulation through the nasal cavity may explain why KOS treatment is seemingly effective for a range of debilitating conditions. Group comparison of ICA output of resting-state fMRI data, lends itself well to provide supporting evidence for this hypothesis. Since ICA is such a popular method of analysis for resting-state fMRI data, a solid knowledge of how dimensionality selection affects ICA results is vital to using ICA to conduct this group comparison study.

2.5 STUDY OUTLINE

To confidently use ICA for group comparison studies, how the selection of dimensionality affects ICA results for resting-state fMRI data must be better understood. In order to study how the selection of NIC affects ICA results, group ICA on different resting-state fMRI datasets were performed with sequentially increasing NIC from 20 – 100. Performing group ICA analysis for multiple datasets, produces a large amount of output ICs, and visually inspecting all the output ICs is very cumbersome. To facilitate the investigation, an analysis framework to automate the time consuming process of visual inspection of output ICs was developed based on Support Vector Machines (SVM) [23]. The feature-optimized classification of ICs with SVM (FOCIS) framework was implemented in a series of *bash* and *R* (https://www.r-project.org/) scripts. FOCIS was first evaluated for its performance accuracies on both single subject and group ICA results. Classification results for FOCIS was then compared against *FSL-fix* and manual classification results obtained through visual inspection. With favorable classification performance, FOCIS was used to automatically classify all output ICs for the different resting-state fMRI datasets at the specified range of NIC. Sub-routines within FOCIS allows for tracking individual ICs in any NIC and investigate how the specified IC changes in its time-course and spatial pattern through increasing NIC. FOCIS is also capable of tracking all output ICs in a given NIC set and compare how all the ICs change with incremental NICs. These tools allowed for better understanding of how the selection of NIC affects ICA output results. This information also provides valuable insight to how ICA should be used to perform group comparison studies.

Applying the knowledge gathered from investigating the dimensionality of resting-state fMRI datasets and how the selection of NICs affect group ICA output results, a group comparison study was conducted on migraine patients before and after KOS treatment, compared to healthy control volunteers using group ICA. The aim was to provide supporting evidence for the hypothesis for a mechanism of the KOS treatment. In addition, to be able to effectively and accurately compare sets of group ICA results, to extract differences in RFNs between patient and control groups, and before and after treatment. Group ICA were performed individually for each group for migraine patients and healthy volunteers before, during; and after KOS treatment. The results were then analyzed using the 3-way analysis of variance (ANOVA) method to detect differences between the groups, and the effect of KOS treatment.

2.6 FOCIS

The base of the FOCIS analysis framework is a classification routine aimed to automatically delineate noise and artefact ICs from those corresponding to functional connectivity networks. FOCIS is designed to obtain general information about the ICs in any given set of output ICs. Classification is performed using SVM, which is a supervised learning algorithm tailored towards binary classification. Classification features were derived from visual inspection guidelines. Potential functional connectivity network ICs should:

1. Have a t-map with activation voxels, that fulfills the voxel-wise threshold of $p<0.001$ and contiguous cluster size of a minimum of 20 voxels; that exhibits peak activation in cortical grey-matter; possesses little spatial overlap with known vascular, ventricular, motion, and susceptibility artefacts; and of a reasonably compact and smooth shape.
2. Have its associated time-course that reflects the expected low frequency spontaneous fluctuations with adequate dynamic range

A total of 18 features were devised based on these instructions. To avoid over-fitting, only significant classifiers were chosen from the final set of features used for the classifier. Significance tests were done iteratively using a general linear model with a logit function kernel tailored to evaluate the binary classification significance. 5 of the 18 features showed to be significant at a 99% significance level. This optimization of feature selection is crucial to avoid bias and over-fitting, while retaining computational efficiency.

The ICA framework is implemented in *R*, using the *kernlab* package based on *LIBSVM*. Since the model cannot be expected to be linear, a non-linear SVM model was constructed using a Gaussian radial basis function kernel. Technical details concerning the implementation can be found in the relevant article [23].

2.7 ICA ANALYSIS

A total of 7 datasets were investigated. One dataset was acquired locally (dataset 0) and the other 6 datasets (datasets 1-6) were downloaded from the functional connectome open access database (https://www.nitrc.org/frs/?group_id=296). Consensus from multiple studies suggests that there is a relatively stable set of 10 RFNs at the level of major brain networks [6, 7, 24]. Trial runs of ICA analysis using our existing preprocessing pipeline suggests, in the worst case, the need for twice as many NICs as approximately half of the output ICs represents artefact or noise signals. Based on this information, the range of NIC was set to 20 – 100.

Group ICA was performed using the standalone *melodic* program in the FSL package [15, 25, 26] for different resting-state fMRI datasets ranging from 20 – 100 as the output number of ICs. 6 datasets running group ICA was investigated and a 7th dataset running single subject ICA for 5 different subjects. The datasets have differing acquisition parameters, obtained from different type of scanners, and consists of different number of subjects (details on how ICA

2.6 FOCIS

The base of the FOCIS analysis framework is a classification routine aimed to automatically delineate noise and artefact ICs from those corresponding to functional connectivity networks. FOCIS is designed to obtain general information about the ICs in any given set of output ICs. Classification is performed using SVM, which is a supervised learning algorithm tailored towards binary classification. Classification features were derived from visual inspection guidelines. Potential functional connectivity network ICs should:

1. Have a t-map with activation voxels, that fulfills the voxel-wise threshold of $p<0.001$ and contiguous cluster size of a minimum of 20 voxels; that exhibits peak activation in cortical grey-matter; possesses little spatial overlap with known vascular, ventricular, motion, and susceptibility artefacts; and of a reasonably compact and smooth shape.
2. Have its associated time-course that reflects the expected low frequency spontaneous fluctuations with adequate dynamic range

A total of 18 features were devised based on these instructions. To avoid over-fitting, only significant classifiers were chosen from the final set of features used for the classifier. Significance tests were done iteratively using a general linear model with a logit function kernel tailored to evaluate the binary classification significance. 5 of the 18 features showed to be significant at a 99% significance level. This optimization of feature selection is crucial to avoid bias and over-fitting, while retaining computational efficiency.

The ICA framework is implemented in *R*, using the *kernlab* package based on *LIBSVM*. Since the model cannot be expected to be linear, a non-linear SVM model was constructed using a Gaussian radial basis function kernel. Technical details concerning the implementation can be found in the relevant article [23].

2.7 ICA ANALYSIS

A total of 7 datasets were investigated. One dataset was acquired locally (dataset 0) and the other 6 datasets (datasets 1-6) were downloaded from the functional connectome open access database (https://www.nitrc.org/frs/?group_id=296). Consensus from multiple studies suggests that there is a relatively stable set of 10 RFNs at the level of major brain networks [6, 7, 24]. Trial runs of ICA analysis using our existing preprocessing pipeline suggests, in the worst case, the need for twice as many NICs as approximately half of the output ICs represents artefact or noise signals. Based on this information, the range of NIC was set to 20 – 100.

Group ICA was performed using the standalone *melodic* program in the FSL package [15, 25, 26] for different resting-state fMRI datasets ranging from 20 – 100 as the output number of ICs. 6 datasets running group ICA was investigated and a 7th dataset running single subject ICA for 5 different subjects. The datasets have differing acquisition parameters, obtained from different type of scanners, and consists of different number of subjects (details on how ICA

analysis was performed and information on the datasets can be found in the corresponding article [23]). This process produces a great amount of ICs to investigate, more than 30000 IC time-courses with their corresponding t-maps. Without tools to partially automate the analysis process, just visually inspecting all the ICs will take a considerable amount of time.

2.8 CLASSIFICATION AND DIMENSIONALITY INVESTIGATION

Group ICA results for dataset 1 at NIC=50, was used as training input for the classification framework. For cross evaluation, the following NIC values were used for group ICA results: NIC=30 for datasets 0-5, NIC=50 and NIC=70 for dataset 0 and NIC 70 and NIC 90 for dataset 1. Overall, FOCIS achieved 0.92 in precision, 1.00 in sensitivity and 0.98 in specificity in identifying artefact/noise ICs. All misclassifications are false negatives, where the ICs have borderline characteristics of both RFN and artefact signal contamination. Visual inspection was particularly difficult for these ICs and their "ground truth" is a matter of dispute.

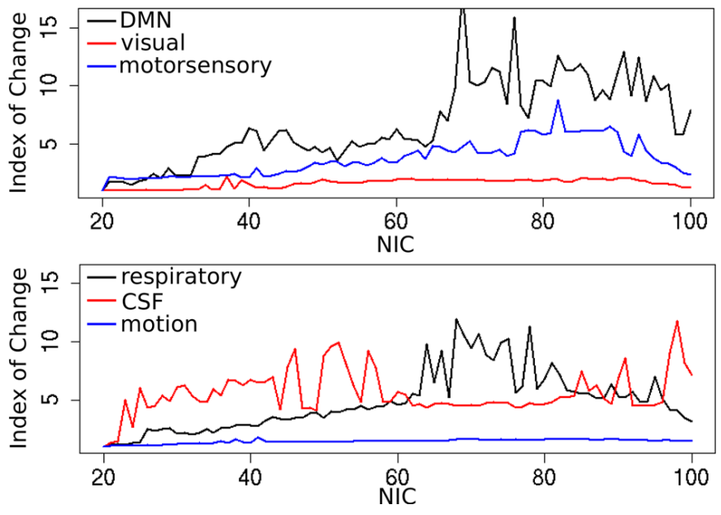

Figure 4: Index of Change for selective RFNs and artefact ICs through increasing NIC.

To quantify the changes for specific ICs, the index of change was defined based on spatial overlap and temporal association based on the ICs time course: $Index\ of\ Change = 1/(spatial\ overlap \times correlation\ coefficient\ of\ IC\ time\ course)$, where the spatial overlap for a given IC is defined as the fraction overlap area relative to the original area of the spatial pattern given as reference. Index of Change was evaluated for well-known RFNs and

analysis was performed and information on the datasets can be found in the corresponding article [23]). This process produces a great amount of ICs to investigate, more than 30000 IC time-courses with their corresponding t-maps. Without tools to partially automate the analysis process, just visually inspecting all the ICs will take a considerable amount of time.

2.8 CLASSIFICATION AND DIMENSIONALITY INVESTIGATION

Group ICA results for dataset 1 at NIC=50, was used as training input for the classification framework. For cross evaluation, the following NIC values were used for group ICA results: NIC=30 for datasets 0-5, NIC=50 and NIC=70 for dataset 0 and NIC 70 and NIC 90 for dataset 1. Overall, FOCIS achieved 0.92 in precision, 1.00 in sensitivity and 0.98 in specificity in identifying artefact/noise ICs. All misclassifications are false negatives, where the ICs have borderline characteristics of both RFN and artefact signal contamination. Visual inspection was particularly difficult for these ICs and their "ground truth" is a matter of dispute.

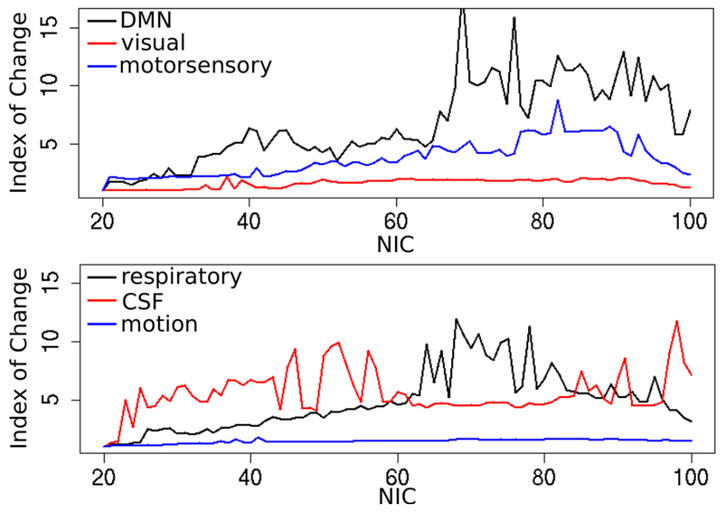

Figure 4: Index of Change for selective RFNs and artefact ICs through increasing NIC.

To quantify the changes for specific ICs, the index of change was defined based on spatial overlap and temporal association based on the ICs time course: $Index\ of\ Change = 1/(spatial\ overlap \times correlation\ coefficient\ of\ IC\ time\ course)$, where the spatial overlap for a given IC is defined as the fraction overlap area relative to the original area of the spatial pattern given as reference. Index of Change was evaluated for well-known RFNs and

artefact ICs, and irrespective of an IC being an RFN or artefact, the change of a given IC can be relatively steady or volatile (Figure 4).

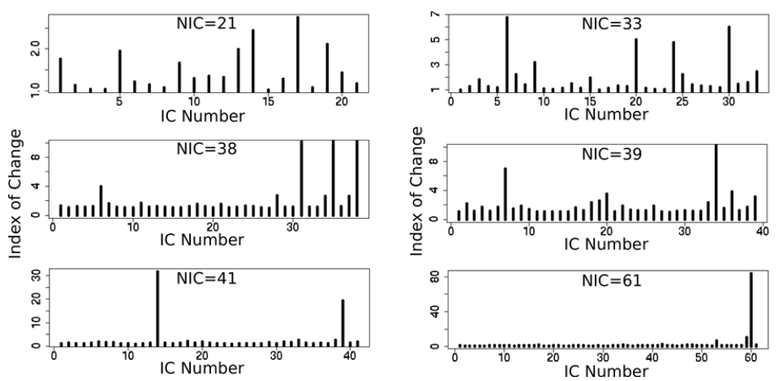

Figure 5: Cross-sectional plots of change index of spatial overlap and temporal association for all ICs at different 6 NICs. At low NICs, the majority of ICs change slightly with incremental NIC while at high NIC levels, incremental NIC leads to only a few ICs changing substantially.

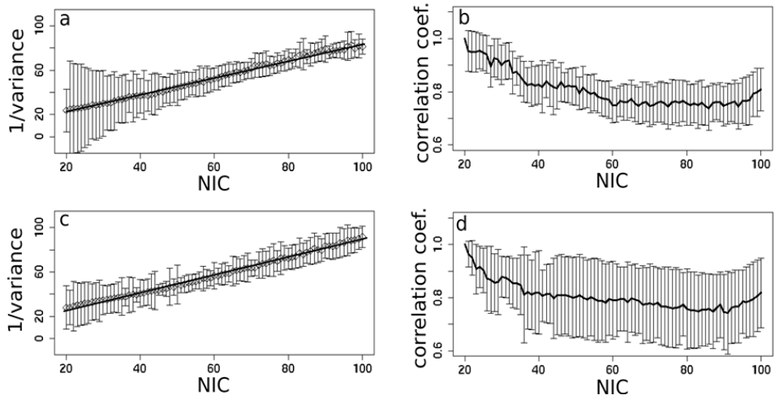

Figure 6: The effect of NIC on the variance contribution of (a) potential RFNs and (c) artefact components. The effect of NIC on the IC time-course for (b) potential RFNs and (c) artefact components.

An interesting aspect to note, is the pattern for overall change of all ICs with incremental NIC. At relatively low NICs, incrementing the NIC by 1 gives rise to changes in a large fraction of all ICs. At higher NICs, a sequential increment of NIC by 1 results in major changes to only a limited number of ICs (Figure 5). This pattern can be appreciated with the variance

artefact ICs, and irrespective of an IC being an RFN or artefact, the change of a given IC can be relatively steady or volatile (Figure 4).

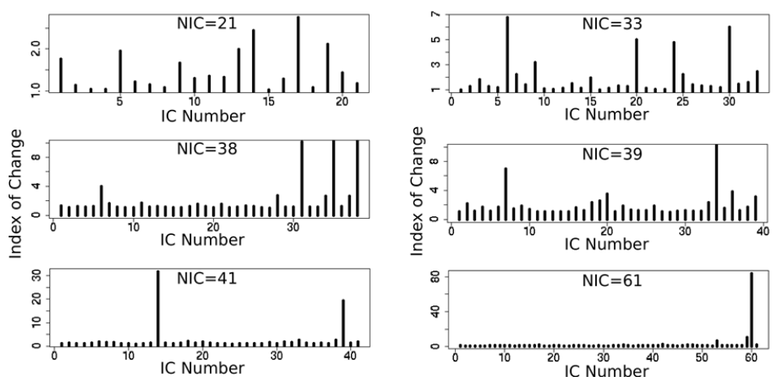

Figure 5: Cross-sectional plots of change index of spatial overlap and temporal association for all ICs at different 6 NICs. At low NICs, the majority of ICs change slightly with incremental NIC while at high NIC levels, incremental NIC leads to only a few ICs changing substantially.

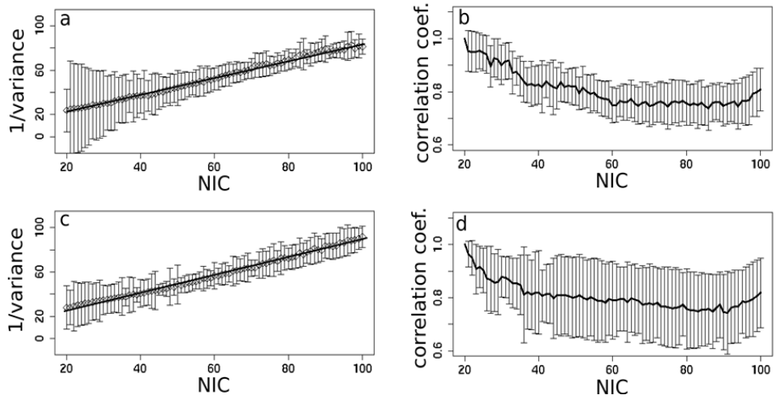

Figure 6: The effect of NIC on the variance contribution of (a) potential RFNs and (c) artefact components. The effect of NIC on the IC time-course for (b) potential RFNs and (c) artefact components.

An interesting aspect to note, is the pattern for overall change of all ICs with incremental NIC. At relatively low NICs, incrementing the NIC by 1 gives rise to changes in a large fraction of all ICs. At higher NICs, a sequential increment of NIC by 1 results in major changes to only a limited number of ICs (Figure 5). This pattern can be appreciated with the variance

contributions of various ICs (Figure 6), irrespective of RFN or artefact, being approximately inversely correlated to NIC.

Different methods have been employed by major software packages and independent analysis frameworks alike to estimate the NIC parameter. The estimates are normally dependent on the SNR of the dataset and preprocessing pipeline steps, and not directly related to the neurophysiological properties [21]. A generally proportional increase was shown for both the number of RFN, and the artefact/noise ICs with the increasing NIC, for most of the datasets with the exception of dataset 1. Neither the variation of the number of RFNs and artefact/noise ICs as a function of NIC, nor the variance contribution of ICs, showed any signs of reaching a steady state or transition point. For dataset 1, there appears to be a steady state upper limit for the number of RFN ICs at around NIC=70±10, where beyond that point, increasing the NIC parameter only results in the increase of the number of artefact/noise ICs. This is quite consistent with the previous report [18]. The question remains why the other datasets do not exhibit this behavior given similar sample size, acquisition parameters, and preprocessing with the same pipeline. It is apparent that a general conclusion cannot be drawn using the observations from a couple of datasets.

To summarize the dimensionality investigation: the problem is more complex than initially expected. For blind-source separation methods like ICA, this problem is central and impacts results greatly. While there are numerous estimators and all major ICA software packages have at least one dimensionality estimation method implemented, they are far from perfect. The SVM classification framework is designed to be as intuitive as possible, mimicking the manual visual inspection process in its choice of features. Classification performance of FOCIS is admirable overall, and its analysis pipelines were successful in their purpose of investigating the various effects NIC have on the output ICs. While the findings are certainly useful to an extent, especially for use of ICA on group comparison studies, the dimensionality problem remains as much of a problem to be solved.

2.9 KINETIC OSCILLATION STIMULATION TREATMENT EFFECTS ON MIGRAINE PATIENTS

In this study, KOS treatment for migraine patients is shown to be visible through changes in RFNs from resting-state fMRI data. While only an incomplete image of how dimensionality affects ICA output results was obtained from the previous study, some key knowledge were acquired nonetheless to facilitate the use of ICA in group studies. One such important knowledge is that preprocessing is vital. While the ICs generated from ICA results is difficult to gain control of, many artefact ICs (and the variability of having many artefact/noise ICs) can be eliminated by removing as many noise sources as possible during preprocessing.

The same NIC were chosen for all group ICA analyses. Starting form NIC=2 (lowest possible), gradually increased until one of the group ICA results showed all major RFNs typically reported in literature. This was obtained for datasets at NIC=10. Even assuming the absence of

contributions of various ICs (Figure 6), irrespective of RFN or artefact, being approximately inversely correlated to NIC.

Different methods have been employed by major software packages and independent analysis frameworks alike to estimate the NIC parameter. The estimates are normally dependent on the SNR of the dataset and preprocessing pipeline steps, and not directly related to the neurophysiological properties [21]. A generally proportional increase was shown for both the number of RFN, and the artefact/noise ICs with the increasing NIC, for most of the datasets with the exception of dataset 1. Neither the variation of the number of RFNs and artefact/noise ICs as a function of NIC, nor the variance contribution of ICs, showed any signs of reaching a steady state or transition point. For dataset 1, there appears to be a steady state upper limit for the number of RFN ICs at around NIC=70±10, where beyond that point, increasing the NIC parameter only results in the increase of the number of artefact/noise ICs. This is quite consistent with the previous report [18]. The question remains why the other datasets do not exhibit this behavior given similar sample size, acquisition parameters, and preprocessing with the same pipeline. It is apparent that a general conclusion cannot be drawn using the observations from a couple of datasets.

To summarize the dimensionality investigation: the problem is more complex than initially expected. For blind-source separation methods like ICA, this problem is central and impacts results greatly. While there are numerous estimators and all major ICA software packages have at least one dimensionality estimation method implemented, they are far from perfect. The SVM classification framework is designed to be as intuitive as possible, mimicking the manual visual inspection process in its choice of features. Classification performance of FOCIS is admirable overall, and its analysis pipelines were successful in their purpose of investigating the various effects NIC have on the output ICs. While the findings are certainly useful to an extent, especially for use of ICA on group comparison studies, the dimensionality problem remains as much of a problem to be solved.

2.9 KINETIC OSCILLATION STIMULATION TREATMENT EFFECTS ON MIGRAINE PATIENTS

In this study, KOS treatment for migraine patients is shown to be visible through changes in RFNs from resting-state fMRI data. While only an incomplete image of how dimensionality affects ICA output results was obtained from the previous study, some key knowledge were acquired nonetheless to facilitate the use of ICA in group studies. One such important knowledge is that preprocessing is vital. While the ICs generated from ICA results is difficult to gain control of, many artefact ICs (and the variability of having many artefact/noise ICs) can be eliminated by removing as many noise sources as possible during preprocessing.

The same NIC were chosen for all group ICA analyses. Starting form NIC=2 (lowest possible), gradually increased until one of the group ICA results showed all major RFNs typically reported in literature. This was obtained for datasets at NIC=10. Even assuming the absence of

noise/artefact ICs, some variability of which RFNs are extracted between the different group ICA runs is expected. Only common RFNs across all groups were chosen for further analysis. Overall, the majority of the RFNs were common and comparable.

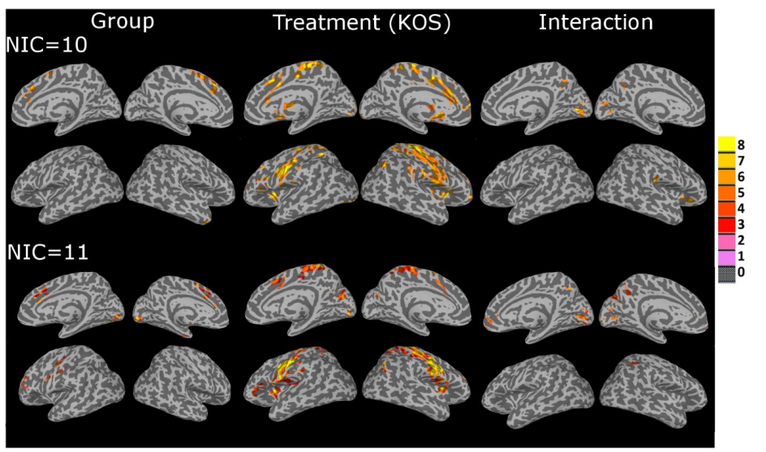

Figure 7: 3-way ANOVA results of differences in RFNS obtained from individual group ICA for NIC=10 and NIC=11.

First, the impact of dimensionality selection on ANOVA results was illustrated by systematically performing 3-way ANOVA on the ICA results ranging from NIC=2-19. No noticeable differences can be found in the ANOVA results for NIC<7. The differences between ANOVA results from NIC=10 and 11 is shown in Figure 7. The differences is solely due to the slight differences in the resulting RFNS from group ICA performed with the different NICs. This shows that dimensionality selection is a basic and crucial prerequisite for statistical analysis of ICA results.

Regarding the 3-way ANOVA difference maps across the comparable RFNs for NIC=10, differences were found in the RFNs involving the Limbic systems with significant differences in pre- and post-central gyrus, anterior cingulate gyrus, and insula when comparing migraine patients against healthy controls. Similar regions and RFNs are shown to be affected by the KOS treatment (Figure 7). The regions are known to be responsible for regulating the central nervous system and is known to have direct connections to the Trigeminal nerve. The findings support the hypothesis that KOS treatment, through stimulating the Trigeminal nerve, regulates and stabilizes the parasympathetic autonomic reflex, thereby relieving migraine patients of their symptoms.

Without resorting to pooling all the datasets together into a single group ICA session, group comparison of ICA results showed differences in some RFNs between migraine patients

noise/artefact ICs, some variability of which RFNs are extracted between the different group ICA runs is expected. Only common RFNs across all groups were chosen for further analysis. Overall, the majority of the RFNs were common and comparable.

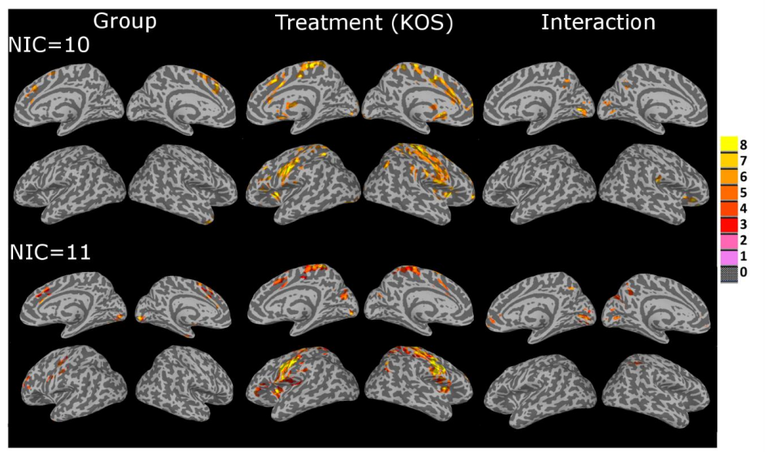

Figure 7: 3-way ANOVA results of differences in RFNS obtained from individual group ICA for NIC=10 and NIC=11.

First, the impact of dimensionality selection on ANOVA results was illustrated by systematically performing 3-way ANOVA on the ICA results ranging from NIC=2-19. No noticeable differences can be found in the ANOVA results for NIC<7. The differences between ANOVA results from NIC=10 and 11 is shown in Figure 7. The differences is solely due to the slight differences in the resulting RFNS from group ICA performed with the different NICs. This shows that dimensionality selection is a basic and crucial prerequisite for statistical analysis of ICA results.

Regarding the 3-way ANOVA difference maps across the comparable RFNs for NIC=10, differences were found in the RFNs involving the Limbic systems with significant differences in pre- and post-central gyrus, anterior cingulate gyrus, and insula when comparing migraine patients against healthy controls. Similar regions and RFNs are shown to be affected by the KOS treatment (Figure 7). The regions are known to be responsible for regulating the central nervous system and is known to have direct connections to the Trigeminal nerve. The findings support the hypothesis that KOS treatment, through stimulating the Trigeminal nerve, regulates and stabilizes the parasympathetic autonomic reflex, thereby relieving migraine patients of their symptoms.

Without resorting to pooling all the datasets together into a single group ICA session, group comparison of ICA results showed differences in some RFNs between migraine patients

compared to healthy control subjects, and the effect of KOS treatment for migraine patients. While RFNs can be reliably extracted using ICA, little information be can gained on how the various RFNs are functionally connected, both between the RFNs and within the RFNs themselves. Due to these outcomes, other methods of analysis must be considered…

compared to healthy control subjects, and the effect of KOS treatment for migraine patients. While RFNs can be reliably extracted using ICA, little information be can gained on how the various RFNs are functionally connected, both between the RFNs and within the RFNs themselves. Due to these outcomes, other methods of analysis must be considered…

21

3 HIERARCHICAL CLUSTERING

Clustering methods are another class of algorithms used to analyze resting-state fMRI data. A clustering algorithm group objects of the same type that are more similar, according to predefined measure, together compared to objects of another group (cluster). They are typically data-driven and easier to understand conceptually, than blind source separation algorithms such as ICA. Clustering algorithms have a high computational complexity, making them less widely used for processing large amounts of data without prior dimensionality reduction.

The investigation of functional connectivity networks can be split into two major parts. Not only are the appearance of RFNs of interest, but also how they are modulated internally (intra-network) and how they interact with each other (inter-network). There is a long standing theory that the brain's functional areas are modulated in a hierarchical fashion [27-33]. Hence, it seemed natural to use a processing method that naturally stratifies data into a hierarchical structure to extract and analyze functional connectivity networks.

3.1 HOW HIERARCHICAL CLUSTERING WORKS

Hierarchical clustering is a deterministic algorithm that merges two leaves or nodes that are closest together, according to some sort of distance measure at each iteration. Beginning with all *n* elements as their separate clusters, at each iteration, the algorithm finds the pair of elements (or clusters) and merges them together such that they form a new, single cluster between them. New pairwise distances are then computed for the newly formed cluster against all other elements, or clusters, that remain. After *n-1* iterations, the algorithm terminates when only a single cluster consisting of all elements remain. During the process, the algorithm will have formed a binary tree (dendrogram) with the individual elements (or voxels in this case) as leaves of the dendrogram, and the root of the dendrogram is the single cluster containing all *n* elements

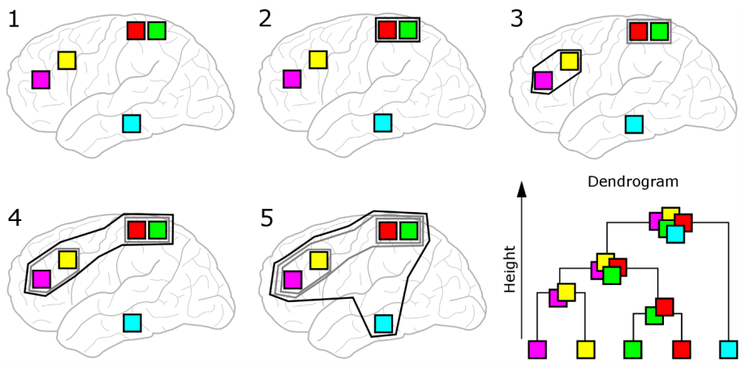

Figure 8: Illustrative example of how hierarchical clustering works.

3 HIERARCHICAL CLUSTERING

Clustering methods are another class of algorithms used to analyze resting-state fMRI data. A clustering algorithm group objects of the same type that are more similar, according to predefined measure, together compared to objects of another group (cluster). They are typically data-driven and easier to understand conceptually, than blind source separation algorithms such as ICA. Clustering algorithms have a high computational complexity, making them less widely used for processing large amounts of data without prior dimensionality reduction.

The investigation of functional connectivity networks can be split into two major parts. Not only are the appearance of RFNs of interest, but also how they are modulated internally (intra-network) and how they interact with each other (inter-network). There is a long standing theory that the brain's functional areas are modulated in a hierarchical fashion [27-33]. Hence, it seemed natural to use a processing method that naturally stratifies data into a hierarchical structure to extract and analyze functional connectivity networks.

3.1 HOW HIERARCHICAL CLUSTERING WORKS

Hierarchical clustering is a deterministic algorithm that merges two leaves or nodes that are closest together, according to some sort of distance measure at each iteration. Beginning with all *n* elements as their separate clusters, at each iteration, the algorithm finds the pair of elements (or clusters) and merges them together such that they form a new, single cluster between them. New pairwise distances are then computed for the newly formed cluster against all other elements, or clusters, that remain. After *n-1* iterations, the algorithm terminates when only a single cluster consisting of all elements remain. During the process, the algorithm will have formed a binary tree (dendrogram) with the individual elements (or voxels in this case) as leaves of the dendrogram, and the root of the dendrogram is the single cluster containing all *n* elements

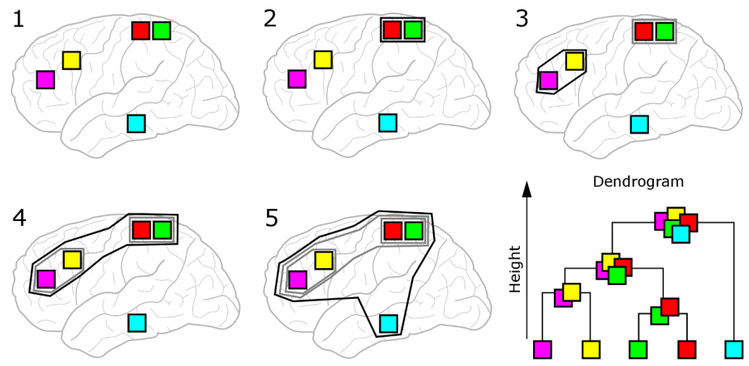

Figure 8: Illustrative example of how hierarchical clustering works.

How bottom-up (agglomerative) hierarchical clustering works, and how it can be applied to resting-state fMRI data, is illustrated as follows: Given all pair-wise distances between all voxel elements in the brain stored in a so-called distance matrix. The algorithm first assigns each element (individual voxels) as their own clusters. In the first iteration, the algorithm finds the pair with the closest distance (most similar) and merges the two together to form a single cluster. All relevant distances are then recalculated according to the specified linkage function for the newly formed cluster and the distance matrix updated accordingly. For every successive iteration, the algorithm finds the closest pair of voxels or clusters and merges them. The algorithm then recalculates the distances, for the newly formed cluster against every previously existing voxel/cluster, and updates the distance matrix. The algorithm terminates finally when a single cluster consisting of all voxels remain (Figure 8). Having a single cluster remaining does not sound particularly useful. During this process it will have generated a binary tree (dendrogram) that can be saved and (re)used in order to form the final output clusters. As illustrated in Figure 9, cutting the dendrogram at cut level *k* from the root will reveal *k* clusters.

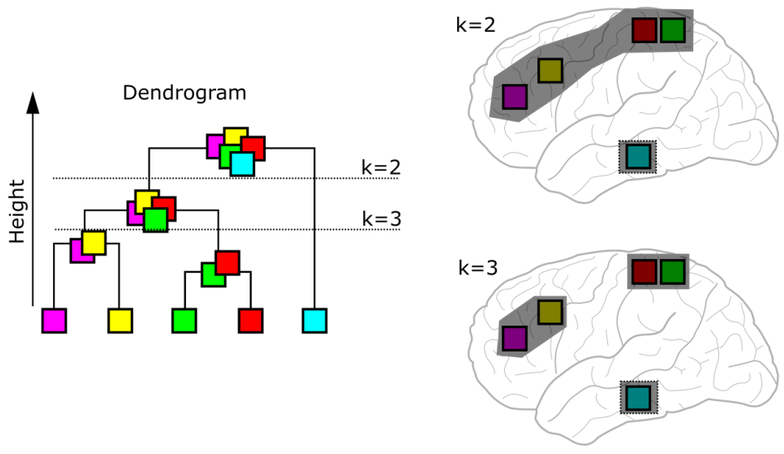

Figure 9: Illustration of how to obtain the desired number of clusters through cutting the dendrogram.

3.2 ON DISTANCE MEASURES

In Figure 8, the distance measure used is the Euclidean distance, which is very simple to understand, but not very useful for finding functional connectivity networks. A distance measure must be defined based a measure of similarity between two voxels' time-courses. The simplest and most intuitive of these measures is the Pearson's cross correlation coefficient (CC), which ranges [-1, 1]. To convert the correlation to distances, Pearson's correlation distance $d = 1 - |CC|$ is defined, which ranges [0, 1], where 0 corresponds to two time-courses being the same (or complete opposite as a CC=−1 will also result in d=0), and 1 the

How bottom-up (agglomerative) hierarchical clustering works, and how it can be applied to resting-state fMRI data, is illustrated as follows: Given all pair-wise distances between all voxel elements in the brain stored in a so-called distance matrix. The algorithm first assigns each element (individual voxels) as their own clusters. In the first iteration, the algorithm finds the pair with the closest distance (most similar) and merges the two together to form a single cluster. All relevant distances are then recalculated according to the specified linkage function for the newly formed cluster and the distance matrix updated accordingly. For every successive iteration, the algorithm finds the closest pair of voxels or clusters and merges them. The algorithm then recalculates the distances, for the newly formed cluster against every previously existing voxel/cluster, and updates the distance matrix. The algorithm terminates finally when a single cluster consisting of all voxels remain (Figure 8). Having a single cluster remaining does not sound particularly useful. During this process it will have generated a binary tree (dendrogram) that can be saved and (re)used in order to form the final output clusters. As illustrated in Figure 9, cutting the dendrogram at cut level *k* from the root will reveal *k* clusters.

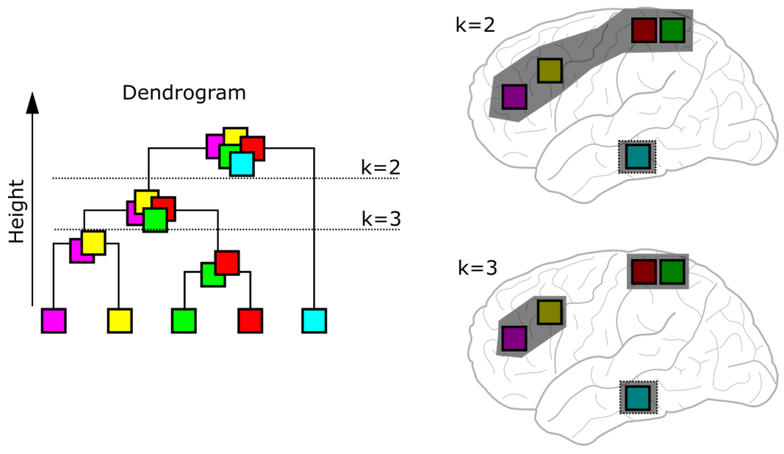

Figure 9: Illustration of how to obtain the desired number of clusters through cutting the dendrogram.

3.2 ON DISTANCE MEASURES

In Figure 8, the distance measure used is the Euclidean distance, which is very simple to understand, but not very useful for finding functional connectivity networks. A distance measure must be defined based a measure of similarity between two voxels' time-courses. The simplest and most intuitive of these measures is the Pearson's cross correlation coefficient (CC), which ranges [-1, 1]. To convert the correlation to distances, Pearson's correlation distance $d = 1 - |CC|$ is defined, which ranges [0, 1], where 0 corresponds to two time-courses being the same (or complete opposite as a CC=−1 will also result in d=0), and 1 the

maximum distance between two time-courses are statistically independent. There are of course other, potentially better [34], distance measures out there, but the standard CC was chosen because it is by far more commonly known, and more intuitive than other distance measures.

3.3 ON LINKAGE

An important aspect of the algorithm is how the distance is defined when one or both sides is a cluster rather than a voxel. This is called the linkage type. There are 4 different types of linkage methods commonly used: Single-linkage, complete-linkage, average-linkage, and centroid-linkage. Single-linkage takes the minimum distance for all voxels in a cluster and other voxel/cluster to be the distance. Complete-linkage is the complete opposite of single-linkage and takes the maximum instead of the minimum. As the name suggests, average-linkage takes the average of all voxels in a cluster to be the distance between it and another voxel/cluster. Finally, centroid-linkage takes the voxel in the (spatial) center for its calculation of new distances. The spatial location of the voxels should not affect the clustering in any way, therefore centroid-linkage was excluded from further consideration. Because both single-linkage and complete-linkage are heavily affected by outliers, and fMRI data is inherently noisy without an intuitive method to remove these outliers, average-linkage was opted as the linkage function for clustering.

3.4 DATA MINING AND VISUALIZATION

After forming the full dendrogram from top to bottom, the hierarchical clustering algorithm is complete. All the data has been sorted and ordered according to the distance measurement of choice into a dendrogram with the voxels as leaves and the root being the whole brain. Somewhere within this dendrogram lies the desired information, but the main issue when using hierarchical clustering on resting-state fMRI data at voxel-level, is the vastness of this dendrogram. It is impossible to gain any meaningful information from a plot of the full dendrogram. A “full” grey-matter dendrogram is attached and can be seen Figure 10. The complete hierarchical clustering result is simply too large to get a comprehensive overview. The full dendrogram must be decomposed (appropriately) into manageable parts, for one to have a chance at gaining some insight. This is in essence a data visualization issue.

The simplest solution is to cut the dendrogram at a certain cut level *k*, and look at the clusters that come out of the dendrogram at that cut-level. By doing that, one loses the connectivity and organizational information in the dendrogram. Having a dendrogram shows how the clusters are connected to one another and is one of the main reasons why one would choose to perform hierarchical clustering analysis instead of, say ICA-based analysis. So this is clearly not a good method. One might attempt to only investigate the sub-dendrograms by only selecting a small branch of the full dendrogram in hopes of getting better overview. However this is equivalent to investigating only a small part of the brain at a time without any overview of how the part

maximum distance between two time-courses are statistically independent. There are of course other, potentially better [34], distance measures out there, but the standard CC was chosen because it is by far more commonly known, and more intuitive than other distance measures.

3.3 ON LINKAGE

An important aspect of the algorithm is how the distance is defined when one or both sides is a cluster rather than a voxel. This is called the linkage type. There are 4 different types of linkage methods commonly used: Single-linkage, complete-linkage, average-linkage, and centroid-linkage. Single-linkage takes the minimum distance for all voxels in a cluster and other voxel/cluster to be the distance. Complete-linkage is the complete opposite of single-linkage and takes the maximum instead of the minimum. As the name suggests, average-linkage takes the average of all voxels in a cluster to be the distance between it and another voxel/cluster. Finally, centroid-linkage takes the voxel in the (spatial) center for its calculation of new distances. The spatial location of the voxels should not affect the clustering in any way, therefore centroid-linkage was excluded from further consideration. Because both single-linkage and complete-linkage are heavily affected by outliers, and fMRI data is inherently noisy without an intuitive method to remove these outliers, average-linkage was opted as the linkage function for clustering.

3.4 DATA MINING AND VISUALIZATION

After forming the full dendrogram from top to bottom, the hierarchical clustering algorithm is complete. All the data has been sorted and ordered according to the distance measurement of choice into a dendrogram with the voxels as leaves and the root being the whole brain. Somewhere within this dendrogram lies the desired information, but the main issue when using hierarchical clustering on resting-state fMRI data at voxel-level, is the vastness of this dendrogram. It is impossible to gain any meaningful information from a plot of the full dendrogram. A “full” grey-matter dendrogram is attached and can be seen Figure 10. The complete hierarchical clustering result is simply too large to get a comprehensive overview. The full dendrogram must be decomposed (appropriately) into manageable parts, for one to have a chance at gaining some insight. This is in essence a data visualization issue.

The simplest solution is to cut the dendrogram at a certain cut level *k*, and look at the clusters that come out of the dendrogram at that cut-level. By doing that, one loses the connectivity and organizational information in the dendrogram. Having a dendrogram shows how the clusters are connected to one another and is one of the main reasons why one would choose to perform hierarchical clustering analysis instead of, say ICA-based analysis. So this is clearly not a good method. One might attempt to only investigate the sub-dendrograms by only selecting a small branch of the full dendrogram in hopes of getting better overview. However this is equivalent to investigating only a small part of the brain at a time without any overview of how the part

of the brain under investigation is connected to the rest of the brain. Depending on the sub-tree, the “small” part of the brain does not necessarily mean small in terms of a dendrogram. Figure 11 illustrates the dendrogram, down to voxel elements, of the “small” part of the brain corresponding to the paracentral lobule. This cluster is only one of the sub-network hubs in the somatosensory-motor network, which is only one of the many RFNs in the brain. Figure 11 shows that it is not small and without further dimensionality reduction, still a very messy and incomprehensible data source.

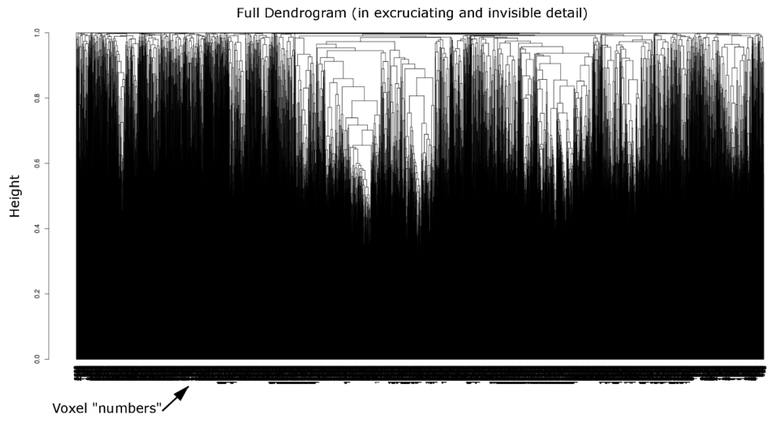

Figure 10: Output dendrogram of a full-brain, grey-matter masked, hierarchical clustering at voxel level using average-linking. Not only is there not enough pixels on the monitor to show the entire dendrogram accurately, the human brain cannot comprehend all this information at once.

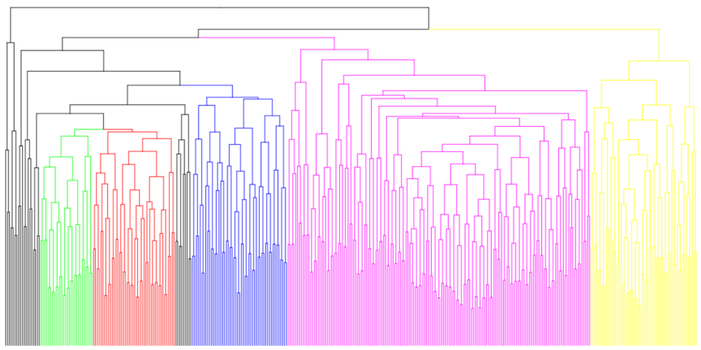

Figure 11: Dendrogram down to voxel elements for the paracentral lobule. Better than the full dendrogram, but still quite messy even with the color-coding for the different sub-networks. A better method of presenting the same sub-dendrogram is shown in Figure 14c.

of the brain under investigation is connected to the rest of the brain. Depending on the sub-tree, the “small” part of the brain does not necessarily mean small in terms of a dendrogram. Figure 11 illustrates the dendrogram, down to voxel elements, of the “small” part of the brain corresponding to the paracentral lobule. This cluster is only one of the sub-network hubs in the somatosensory-motor network, which is only one of the many RFNs in the brain. Figure 11 shows that it is not small and without further dimensionality reduction, still a very messy and incomprehensible data source.

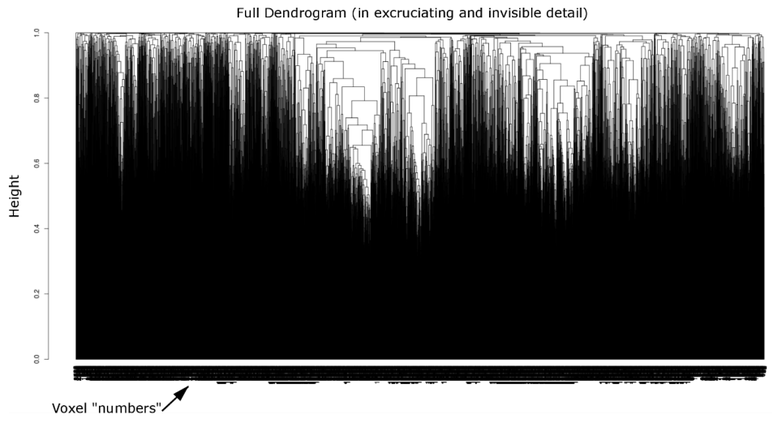

Figure 10: Output dendrogram of a full-brain, grey-matter masked, hierarchical clustering at voxel level using average-linking. Not only is there not enough pixels on the monitor to show the entire dendrogram accurately, the human brain cannot comprehend all this information at once.

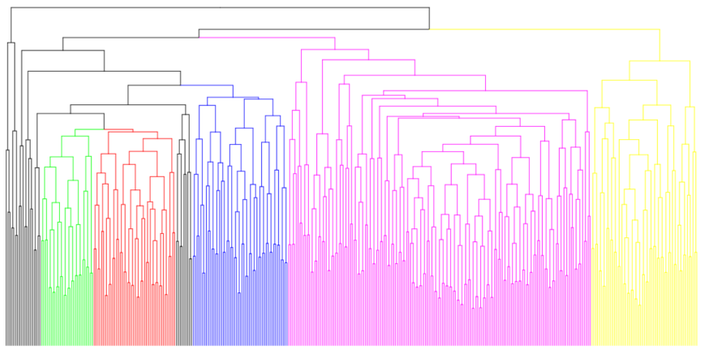

Figure 11: Dendrogram down to voxel elements for the paracentral lobule. Better than the full dendrogram, but still quite messy even with the color-coding for the different sub-networks. A better method of presenting the same sub-dendrogram is shown in Figure 14c.

The hierarchical clustering algorithm is slow to compute the full dendrogram. When complete, the dendrogram can be saved as a text file that is much smaller and manageable. A dendrogram can be loaded and cut at any other cut level almost instantaneously. After initial clustering, one can make cuts at any cut-level to the dendrogram, quickly and efficiently, and extract the clusters within. Of significance is that this allows one to systematically cut the dendrogram from top to down with increasing cut-levels to obtain all cluster information and documenting their connectivity with relative ease. This provides a powerful tool to visualize part of the full dendrogram in a meaningful way, provided one knows which parts to look at.

3.5 DEFINITION OF RFNS AND SUB-NETWORKS

It is safe to assume that only a small part of the full dendrogram can be feasibly regarded at once. The question remains as to which parts of the dendrogram to look at. This question comes with its own set of problems that the basic hierarchical clustering algorithm does not attempt to solve. At the root of the dendrogram, this question is trivial. Traversing top-down through the dendrogram, a large set of the clusters that resemble meaningful RFNs and sub-networks can be (relatively) quickly obtained.

Another issue is how to interpret the clusters. Traversing top-down through the full dendrogram, one will most likely stumble upon clusters that resemble very closely to a RFN, other clusters will be small and compact, resembling sub-networks or even hubs for some RFNs. An important question is what constitutes as a RFN and what is a sub-network? The concept of a RFN is originally derived from task-based activations with specific tasks. What might be defined commonly as the visual network, probably does not include all brain regions that are responsible for all aspects of visual processing, just those responsible for processing that particular visual stimulus. Those who are active in resting-state fMRI often find the need to emphasize that the task invoked activation patterns and resting-state synchrony patterns, and are not of the same physiological origins and cannot be regarded in the same manner. This implies that it is unreasonable to assume that the two networks are comparable. Despite this, the rough and vague definition of RFN is still commonly used today, often without an explicit definition (because any explicit definition along such lines would be incorrect). Those who actively work with resting-state fMRI find themselves using this “definition” of RFNs and this is partly due to convenience and the lack of anything better, but also because of the fact that, in practice, the task invoked activation patterns and resting-state functional connectivity patterns happen to be more alike than not (with a few exceptions). For the sake of convenience, the same pseudo-definition shall be used here and use the term RFNs to label those that are comparable to task based fMRI activations and label smaller clusters that are functionally distinct within such RFNs, as sub-networks. It must be stressed however that this is done mostly for convenience of labelling rather than a strict definition, because after-all this problem is simply a matter of definition.

One of the inherent strengths of hierarchical clustering is that the full brain dendrogram, not accounting for noise and artefacts, can be regarded as an entire network itself, connected down

The hierarchical clustering algorithm is slow to compute the full dendrogram. When complete, the dendrogram can be saved as a text file that is much smaller and manageable. A dendrogram can be loaded and cut at any other cut level almost instantaneously. After initial clustering, one can make cuts at any cut-level to the dendrogram, quickly and efficiently, and extract the clusters within. Of significance is that this allows one to systematically cut the dendrogram from top to down with increasing cut-levels to obtain all cluster information and documenting their connectivity with relative ease. This provides a powerful tool to visualize part of the full dendrogram in a meaningful way, provided one knows which parts to look at.

3.5 DEFINITION OF RFNS AND SUB-NETWORKS

It is safe to assume that only a small part of the full dendrogram can be feasibly regarded at once. The question remains as to which parts of the dendrogram to look at. This question comes with its own set of problems that the basic hierarchical clustering algorithm does not attempt to solve. At the root of the dendrogram, this question is trivial. Traversing top-down through the dendrogram, a large set of the clusters that resemble meaningful RFNs and sub-networks can be (relatively) quickly obtained.

Another issue is how to interpret the clusters. Traversing top-down through the full dendrogram, one will most likely stumble upon clusters that resemble very closely to a RFN, other clusters will be small and compact, resembling sub-networks or even hubs for some RFNs. An important question is what constitutes as a RFN and what is a sub-network? The concept of a RFN is originally derived from task-based activations with specific tasks. What might be defined commonly as the visual network, probably does not include all brain regions that are responsible for all aspects of visual processing, just those responsible for processing that particular visual stimulus. Those who are active in resting-state fMRI often find the need to emphasize that the task invoked activation patterns and resting-state synchrony patterns, and are not of the same physiological origins and cannot be regarded in the same manner. This implies that it is unreasonable to assume that the two networks are comparable. Despite this, the rough and vague definition of RFN is still commonly used today, often without an explicit definition (because any explicit definition along such lines would be incorrect). Those who actively work with resting-state fMRI find themselves using this “definition” of RFNs and this is partly due to convenience and the lack of anything better, but also because of the fact that, in practice, the task invoked activation patterns and resting-state functional connectivity patterns happen to be more alike than not (with a few exceptions). For the sake of convenience, the same pseudo-definition shall be used here and use the term RFNs to label those that are comparable to task based fMRI activations and label smaller clusters that are functionally distinct within such RFNs, as sub-networks. It must be stressed however that this is done mostly for convenience of labelling rather than a strict definition, because after-all this problem is simply a matter of definition.

One of the inherent strengths of hierarchical clustering is that the full brain dendrogram, not accounting for noise and artefacts, can be regarded as an entire network itself, connected down

to the voxel elements. As long as a cluster is not classified to be the result of outliers, noise, or some other sources of artefacts in the data, it will remain a part of the functional hierarchy to be constructed. So it can be said that the RFNs typically associated with resting-state fMRI such as the visual network, and executive function networks, are in fact not completely separate functional networks, but rather also work together in various tasks. The different RFNs together form the complete network consisting of the entire brain. In the same fashion, these networks have functional sub-divisions, for example the pre-motor, primary motor, somatosensory, and supplementary motor areas in the motor network. Each sub-network regulating a specific aspect motor control.

3.6 CLUSTER EVALUATION AND WHERE TO STOP CUTTING

It has been established that a dendrogram visualized down to its voxel elements can be visually messy, at the same time providing little meaning in terms of clarity on what the voxel elements represent. A lower limit as to where to stop cutting the dendrogram must be now established.

Hierarchical clustering does not have its own native filtering mechanisms. The algorithm is intrinsically sensitive to outliers and noise due to its deterministic nature and rigorous processing iterations. Applied to noisy resting-state fMRI data, evaluation criteria or a filtering method is required to obtain meaningful clusters.

The first attempt was to apply a minimum *CC* value threshold on the matrix with all the pair-wise voxel *CC* values, from which the distance matrix was calculated. This will guarantee only truly correlated voxels, with correlation ≥0.3, to be taken into account when forming the distances. All pair-wise correlations below the threshold is truncated to 0. In hind-sight, this probably didn't help and it is good that did not adversely affect the results.

Due to the limiting resolution and noisy nature of fMRI datasets, a minimum cluster size must be imposed where any cluster less than this threshold, cannot be regarded as significant. At low cut level, a global threshold was set to filter out noise clusters. For clusters lower down the cut level at intra-network hierarchies, a slightly different scheme for cluster size evaluation was used. At these cut levels, the cluster evaluations purpose becomes less of filtering out noise clusters, rather than evaluating the clusters significance. The evaluation threshold was set depending on each cluster's connectivity within. Generally the smaller a cluster is, the higher its intra-cluster connectivity must be, for it to be considered significant. To further evaluate the significance of a cluster, a myriad of measures were derived in order to quantify what exactly constitutes as a significant cluster. From there a natural end-point was decided where, beyond said point, further clustering will yield little to no meaningful results. One measure is to evaluate a split that is naturally derived from the hierarchical clustering algorithm, i.e: Inconsistency Coefficients. The inconsistency coefficient characterizes each node in a dendrogram by comparing its height against those of the other links' at similar heights. A node's height is simply the distance at which the node (cluster) is first joined together according to the algorithm. It is higher for nodes which are less similar to surrounding nodes. Another

to the voxel elements. As long as a cluster is not classified to be the result of outliers, noise, or some other sources of artefacts in the data, it will remain a part of the functional hierarchy to be constructed. So it can be said that the RFNs typically associated with resting-state fMRI such as the visual network, and executive function networks, are in fact not completely separate functional networks, but rather also work together in various tasks. The different RFNs together form the complete network consisting of the entire brain. In the same fashion, these networks have functional sub-divisions, for example the pre-motor, primary motor, somatosensory, and supplementary motor areas in the motor network. Each sub-network regulating a specific aspect motor control.

3.6 CLUSTER EVALUATION AND WHERE TO STOP CUTTING

It has been established that a dendrogram visualized down to its voxel elements can be visually messy, at the same time providing little meaning in terms of clarity on what the voxel elements represent. A lower limit as to where to stop cutting the dendrogram must be now established.

Hierarchical clustering does not have its own native filtering mechanisms. The algorithm is intrinsically sensitive to outliers and noise due to its deterministic nature and rigorous processing iterations. Applied to noisy resting-state fMRI data, evaluation criteria or a filtering method is required to obtain meaningful clusters.

The first attempt was to apply a minimum *CC* value threshold on the matrix with all the pair-wise voxel *CC* values, from which the distance matrix was calculated. This will guarantee only truly correlated voxels, with correlation ≥0.3, to be taken into account when forming the distances. All pair-wise correlations below the threshold is truncated to 0. In hind-sight, this probably didn't help and it is good that did not adversely affect the results.

Due to the limiting resolution and noisy nature of fMRI datasets, a minimum cluster size must be imposed where any cluster less than this threshold, cannot be regarded as significant. At low cut level, a global threshold was set to filter out noise clusters. For clusters lower down the cut level at intra-network hierarchies, a slightly different scheme for cluster size evaluation was used. At these cut levels, the cluster evaluations purpose becomes less of filtering out noise clusters, rather than evaluating the clusters significance. The evaluation threshold was set depending on each cluster's connectivity within. Generally the smaller a cluster is, the higher its intra-cluster connectivity must be, for it to be considered significant. To further evaluate the significance of a cluster, a myriad of measures were derived in order to quantify what exactly constitutes as a significant cluster. From there a natural end-point was decided where, beyond said point, further clustering will yield little to no meaningful results. One measure is to evaluate a split that is naturally derived from the hierarchical clustering algorithm, i.e: Inconsistency Coefficients. The inconsistency coefficient characterizes each node in a dendrogram by comparing its height against those of the other links' at similar heights. A node's height is simply the distance at which the node (cluster) is first joined together according to the algorithm. It is higher for nodes which are less similar to surrounding nodes. Another

possible measure is intra-cluster modularity, where the degree of connectedness within a cluster was evaluated. It makes little sense to further sub-divide clusters that possess maximum degree of intra-cluster connectivity (that is, when every voxel element in the cluster is strongly connected to each other).

3.7 STUDY OUTLINE

A model-free analysis method for resting-state fMRI data using hierarchical clustering at voxel level was implemented. The extracted RFN using hierarchical clustering was evaluated by comparing to ICA results from the same dataset. Hierarchical clustering was confirmed to be able to produce clusters that closely resemble RFNs obtained through other methods (such as ICA), hierarchical clustering analysis framework was extended to be able to efficiently study the sub-network functional organization of known RFNs. Ultimately, the hope is to use hierarchical clustering in a consistent fashion to analyze brain connectivity by starting from the whole-brain level and down to the smallest functionally distinct areas.

3.8 IMPLEMENTING THE HIERARCHICAL CLUSTERING FRAMEWORK

Before showing some of the central results from hierarchical clustering, there are a couple of implementation details worthy of mention. Being a physicist above a programmer, some choices for the implementation might seem convoluted. The main reason for these choices from Moore's Law: The processing power available at the early stages of implementing the framework is vastly overshadowed by the processing power available at the time of writing. A good example of this is the hierarchical clustering algorithm itself: Like most other clustering algorithms, hierarchical clustering operates on a high computational complexity ($O(n^3)$). This makes the algorithm scale very poorly as the computational time is cubic to the number of voxels being processed.

3.8.1 The necessity of optimizations

At the time of development, many optimization steps were needed to be taken for the framework to be feasible at all in terms of processing times (or to be able to compute at all). With computers getting steadily more memory and faster CPUs, some of the optimization steps might have ceased to be necessary and seem much less impressive today. When the framework was first developed, all the optimization steps taken were necessary for the framework to process the data within reasonable processing times. At the time of this writing, the same data can be processed using far less optimized, general purpose hierarchical clustering packages (for example that found in *MATLAB*), using a laptop rather than a workstation.

possible measure is intra-cluster modularity, where the degree of connectedness within a cluster was evaluated. It makes little sense to further sub-divide clusters that possess maximum degree of intra-cluster connectivity (that is, when every voxel element in the cluster is strongly connected to each other).

3.7 STUDY OUTLINE

A model-free analysis method for resting-state fMRI data using hierarchical clustering at voxel level was implemented. The extracted RFN using hierarchical clustering was evaluated by comparing to ICA results from the same dataset. Hierarchical clustering was confirmed to be able to produce clusters that closely resemble RFNs obtained through other methods (such as ICA), hierarchical clustering analysis framework was extended to be able to efficiently study the sub-network functional organization of known RFNs. Ultimately, the hope is to use hierarchical clustering in a consistent fashion to analyze brain connectivity by starting from the whole-brain level and down to the smallest functionally distinct areas.

3.8 IMPLEMENTING THE HIERARCHICAL CLUSTERING FRAMEWORK

Before showing some of the central results from hierarchical clustering, there are a couple of implementation details worthy of mention. Being a physicist above a programmer, some choices for the implementation might seem convoluted. The main reason for these choices from Moore's Law: The processing power available at the early stages of implementing the framework is vastly overshadowed by the processing power available at the time of writing. A good example of this is the hierarchical clustering algorithm itself: Like most other clustering algorithms, hierarchical clustering operates on a high computational complexity ($O(n^3)$). This makes the algorithm scale very poorly as the computational time is cubic to the number of voxels being processed.

3.8.1 The necessity of optimizations

At the time of development, many optimization steps were needed to be taken for the framework to be feasible at all in terms of processing times (or to be able to compute at all). With computers getting steadily more memory and faster CPUs, some of the optimization steps might have ceased to be necessary and seem much less impressive today. When the framework was first developed, all the optimization steps taken were necessary for the framework to process the data within reasonable processing times. At the time of this writing, the same data can be processed using far less optimized, general purpose hierarchical clustering packages (for example that found in *MATLAB*), using a laptop rather than a workstation.

3.8.2 Memory allocation

The base hierarchical clustering programs are written purely in *C* due to its speed and control of memory allocation. Memory allocation being very important as memory was in short(er) supply when the base processing modules were written and memory-efficiency is oftentimes the determining factor for whether the analysis pipeline will run at all, or just simply flood the computer's memory.

3.8.3 Parallel Programming

A major optimization step is the implementation of parallel processing for the program calculating CC matrices. While hierarchical clustering does not lend itself to be naturally parallelized, computing the CC matrix can be parallelized. As it happens this is also the step that is the most time consuming as in a dataset, multiple CC matrix calculations must be run (one for each subject) while hierarchical clustering only need be run once per dataset.

3.8.4 Dimensionality reduction

Another necessary optimization step is dimensionality reduction through grey-matter masking. There is the physiological reason that functional connectivity networks, and functional areas in general do not reside in white-matter and CSF (and definitely not outside the brain). The practical reason for this is that it eliminates more than half the voxels to be processed and frees up more than half the memory needed to my programs to allocate.

3.8.5 Libraries

The C-clustering library for bioinformatics (http://bonsai.hgc.jp/~mdehoon/software/cluster/) was used to implement the hierarchical clustering algorithm itself. The library also includes functions to efficiently cut a given dendrogram to store as output clusters. The library was extended to allow for saving of the tree in ASCI format (linkage file). While the clustering itself takes non-trivial amount of time, loading the tree from the linkage file and cutting the tree occurs almost instantaneously.

The analysis pipeline from this point onwards is a series of *R* and *bash* script files. The analysis traverses through the dendrogram top-down and cuts the dendrogram at every cut level. At each consecutive cut level, the children clusters at their mother cluster is identified. The children clusters at every consecutive cut is then evaluated for significance through various measures such as the IC, intra-cluster connectivity, and voxel size. These scripts also manage the construction and preparation for visualization of the filtered sub-dendrogram which contains only nodes that pass the filtering process. Would this analysis pipeline have been written at the same time the base hierarchical clustering routines were, they would have mostly likely been written in C with optimizations of their own. But since they are written more

3.8.2 Memory allocation

The base hierarchical clustering programs are written purely in *C* due to its speed and control of memory allocation. Memory allocation being very important as memory was in short(er) supply when the base processing modules were written and memory-efficiency is oftentimes the determining factor for whether the analysis pipeline will run at all, or just simply flood the computer's memory.

3.8.3 Parallel Programming

A major optimization step is the implementation of parallel processing for the program calculating CC matrices. While hierarchical clustering does not lend itself to be naturally parallelized, computing the CC matrix can be parallelized. As it happens this is also the step that is the most time consuming as in a dataset, multiple CC matrix calculations must be run (one for each subject) while hierarchical clustering only need be run once per dataset.

3.8.4 Dimensionality reduction

Another necessary optimization step is dimensionality reduction through grey-matter masking. There is the physiological reason that functional connectivity networks, and functional areas in general do not reside in white-matter and CSF (and definitely not outside the brain). The practical reason for this is that it eliminates more than half the voxels to be processed and frees up more than half the memory needed to my programs to allocate.

3.8.5 Libraries

The C-clustering library for bioinformatics (http://bonsai.hgc.jp/~mdehoon/software/cluster/) was used to implement the hierarchical clustering algorithm itself. The library also includes functions to efficiently cut a given dendrogram to store as output clusters. The library was extended to allow for saving of the tree in ASCI format (linkage file). While the clustering itself takes non-trivial amount of time, loading the tree from the linkage file and cutting the tree occurs almost instantaneously.

The analysis pipeline from this point onwards is a series of *R* and *bash* script files. The analysis traverses through the dendrogram top-down and cuts the dendrogram at every cut level. At each consecutive cut level, the children clusters at their mother cluster is identified. The children clusters at every consecutive cut is then evaluated for significance through various measures such as the IC, intra-cluster connectivity, and voxel size. These scripts also manage the construction and preparation for visualization of the filtered sub-dendrogram which contains only nodes that pass the filtering process. Would this analysis pipeline have been written at the same time the base hierarchical clustering routines were, they would have mostly likely been written in C with optimizations of their own. But since they are written more

recently on better workstations, these scripts are rough in their implementation. As necessity is the mother of invention, without the former, the one is not as motivated to the latter.

3.9 HIERARCHICAL CLUSTERING AND ICA RESULTS

RFNs extracted from hierarchical clustering were compared against typical RFNs extracted using group ICA. In general, the RFNs extracted using hierarchical clustering have relatively good match with RFNs extracted through group ICA. The RFN clusters with matching ICA t-maps can be found Figure 12.

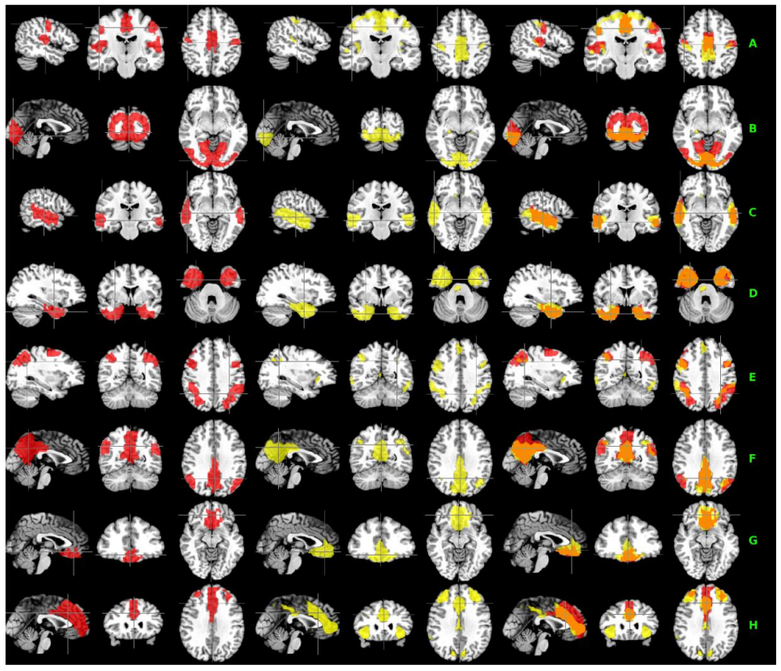

Figure 12: Comparison between the hierarchical clustering and ICA results. RFNs from hierarchical clustering (left column) and group ICA (middle column) with good matching. The right column displays their corresponding overlays with overlapping areas showing in orange. The group ICA t-maps were binarized with a threshold at p<0.001 for ease of comparison with clustering results.

3.10 FUNCTIONAL HIERARCHIES

A major advantage of using hierarchical clustering on resting-state fMRI data is the dendrogram obtained during the clustering process. Not only does the dendrogram reflect how

recently on better workstations, these scripts are rough in their implementation. As necessity is the mother of invention, without the former, the one is not as motivated to the latter.

3.9 HIERARCHICAL CLUSTERING AND ICA RESULTS

RFNs extracted from hierarchical clustering were compared against typical RFNs extracted using group ICA. In general, the RFNs extracted using hierarchical clustering have relatively good match with RFNs extracted through group ICA. The RFN clusters with matching ICA t-maps can be found Figure 12.

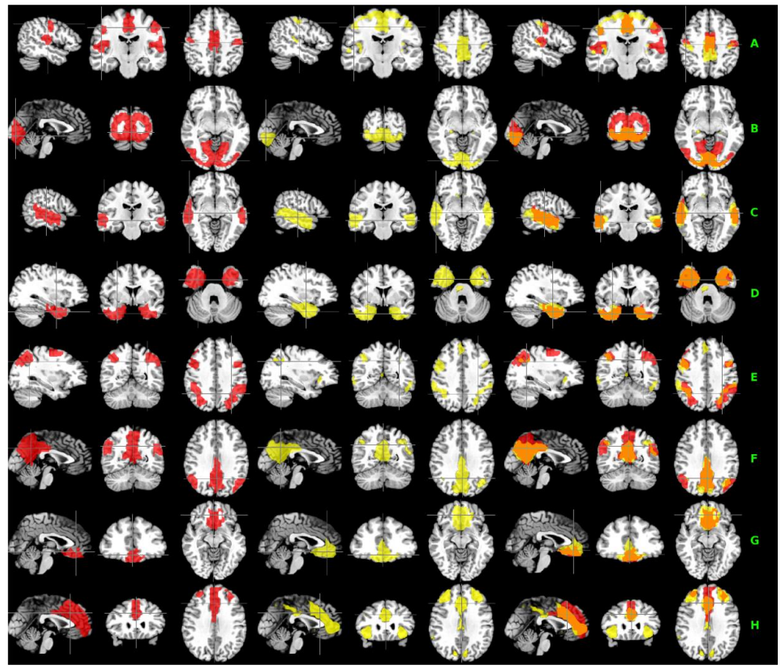

Figure 12: Comparison between the hierarchical clustering and ICA results. RFNs from hierarchical clustering (left column) and group ICA (middle column) with good matching. The right column displays their corresponding overlays with overlapping areas showing in orange. The group ICA t-maps were binarized with a threshold at p<0.001 for ease of comparison with clustering results.

3.10 FUNCTIONAL HIERARCHIES

A major advantage of using hierarchical clustering on resting-state fMRI data is the dendrogram obtained during the clustering process. Not only does the dendrogram reflect how

different RFNs are organized hierarchically in the brain, but the sub-dendrograms of the various RFNs may reveal the functional sub-division of the RFNs.

Using the definition of what constitutes as RFNs for convenience, the aim is the following: From the root of the full dendrogram, extract RFNs comparable to those from group ICA and task-based activation patterns and obtain their inter-network functional hierarchy. In a consistent manner, the framework will allow studying the RFNs' intra-network connectivity through extracting their sub-networks and their intra-network functional hierarchy.

A limit has to be set for the size of the each sub-dendrogram to be shown. While it is quite intuitive (or even through illustration) that the full dendrogram cannot be shown in a single figure, the question stands as to how large of a dendrogram can one reasonably squeeze into a single figure whilst retaining information that is comprehensible to the viewer? The answer to this question is naturally dependent on who the viewer is. Considering that the leaves represent clusters and every leaf is of major importance, a sub-dendrogram of approximately 20 leaves seems to be the maximum size for a sub-dendrogram. Anything larger and one start to lose either over-view of the dendrogram, or lose grasp of the individual leaves. This was established, like many researchers do behind the scenes, with trial and error and through many sleepless nights. As one traverses down the full dendrogram, more nodes fail the cluster evaluation process and one would need to traverse to higher cut levels to fill a figure with 20 sub-networks. Here the search was restricted to 80 cut levels as the analysis pipeline is currently poorly optimized for high cut levels. Since the dendrogram expands further down the cut levels, the full dendrogram will not be presented to its full width, but selectively presenting the full dendrogram by presenting one of the leaf clusters from the previous sub-dendrogram as root for the next sub-dendrogram.

From the entire cortical grey-matter as root to the full dendrogram, a top-down evaluation was made up to cut level k=32, at which one figure was fully occupied by 20 clusters located cortically. Of the 81 potential clusters, 23 clusters remained after cluster evaluation and 3 of them were located in the cerebellum which cannot be accurately shown through 3D cortical mapping (Figure 13). At this cut level, most of the Cortex remains a single cluster while regions near the Mid-brain start splitting apart into functionally distinct areas. The first sub-dendrogram has a natural candidate for further clustering: There is a cluster much larger than the other clusters in this hierarchy (Figure 13, left, cluster 7), so the obvious choice for presenting the next hierarchy would be to use the large cluster as root for the next. This is not to say that one cannot use another cluster in the hierarchy (some are of decent size also) and look at its sub-division, they were simply not presented here. An example of this would be in the next hierarchy, where the large cluster splits into clusters that represents known RFNs. The RFNs extracted at this level is comparable to ICA results, with the additional information about the inter-network functional hierarchy naturally obtained from hierarchical clustering (Figure 13, right).

different RFNs are organized hierarchically in the brain, but the sub-dendrograms of the various RFNs may reveal the functional sub-division of the RFNs.

Using the definition of what constitutes as RFNs for convenience, the aim is the following: From the root of the full dendrogram, extract RFNs comparable to those from group ICA and task-based activation patterns and obtain their inter-network functional hierarchy. In a consistent manner, the framework will allow studying the RFNs' intra-network connectivity through extracting their sub-networks and their intra-network functional hierarchy.

A limit has to be set for the size of the each sub-dendrogram to be shown. While it is quite intuitive (or even through illustration) that the full dendrogram cannot be shown in a single figure, the question stands as to how large of a dendrogram can one reasonably squeeze into a single figure whilst retaining information that is comprehensible to the viewer? The answer to this question is naturally dependent on who the viewer is. Considering that the leaves represent clusters and every leaf is of major importance, a sub-dendrogram of approximately 20 leaves seems to be the maximum size for a sub-dendrogram. Anything larger and one start to lose either over-view of the dendrogram, or lose grasp of the individual leaves. This was established, like many researchers do behind the scenes, with trial and error and through many sleepless nights. As one traverses down the full dendrogram, more nodes fail the cluster evaluation process and one would need to traverse to higher cut levels to fill a figure with 20 sub-networks. Here the search was restricted to 80 cut levels as the analysis pipeline is currently poorly optimized for high cut levels. Since the dendrogram expands further down the cut levels, the full dendrogram will not be presented to its full width, but selectively presenting the full dendrogram by presenting one of the leaf clusters from the previous sub-dendrogram as root for the next sub-dendrogram.

From the entire cortical grey-matter as root to the full dendrogram, a top-down evaluation was made up to cut level k=32, at which one figure was fully occupied by 20 clusters located cortically. Of the 81 potential clusters, 23 clusters remained after cluster evaluation and 3 of them were located in the cerebellum which cannot be accurately shown through 3D cortical mapping (Figure 13). At this cut level, most of the Cortex remains a single cluster while regions near the Mid-brain start splitting apart into functionally distinct areas. The first sub-dendrogram has a natural candidate for further clustering: There is a cluster much larger than the other clusters in this hierarchy (Figure 13, left, cluster 7), so the obvious choice for presenting the next hierarchy would be to use the large cluster as root for the next. This is not to say that one cannot use another cluster in the hierarchy (some are of decent size also) and look at its sub-division, they were simply not presented here. An example of this would be in the next hierarchy, where the large cluster splits into clusters that represents known RFNs. The RFNs extracted at this level is comparable to ICA results, with the additional information about the inter-network functional hierarchy naturally obtained from hierarchical clustering (Figure 13, right).

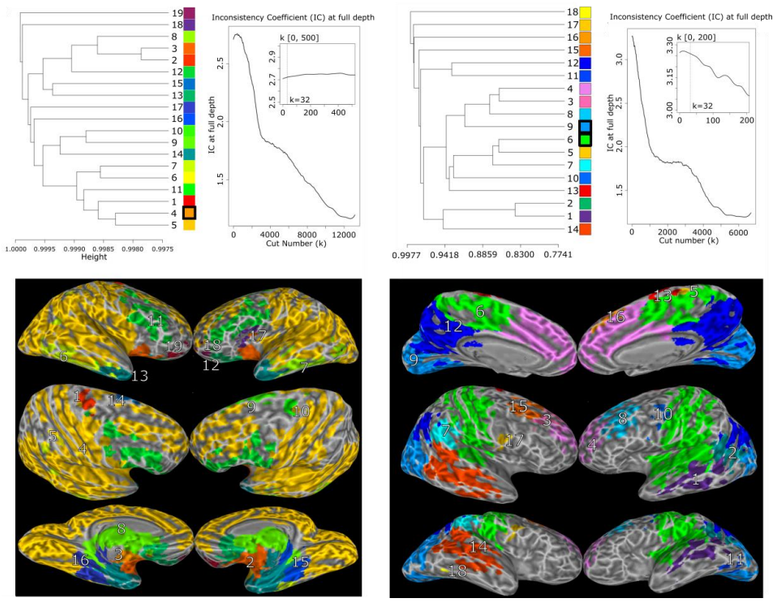

Figure 13: Inter-network hierarchies from root (left) down to cut level k=32. One large cluster (cluster 7) remain after 20 cluster limit per figure was reached. This large cluster was taken as the root and further clustered (right) down to cut level k=32. 18 clusters remain after evaluation, of which most of them resemble known RFNs such as the somatosensory-motor network (cluster 6) and visual network (cluster 9).

The intra-network functional hierarchies of the somatosensory-motor network was further investigated (Figure 14a). To illustrate the previous point of being able to select any of the leaves for a given sub-dendrogram to further study, the functional hierarchy of the visual network (Figure 14b) was also constructed. A cluster that is considerably larger in the somatosensory-motor network corresponds to the paracentral lobule. It seems that the paracentral lobule is also a highly connected hub of the network, hence the cluster was further clustered, again to cut level *k*=80 (Figure 14c). This is a natural end point, as cluster characteristics such as the Inconsistency Coefficient, cluster modularity, and cluster connectivity suggests that this would be the natural stage to terminate the hierarchical sub-division.

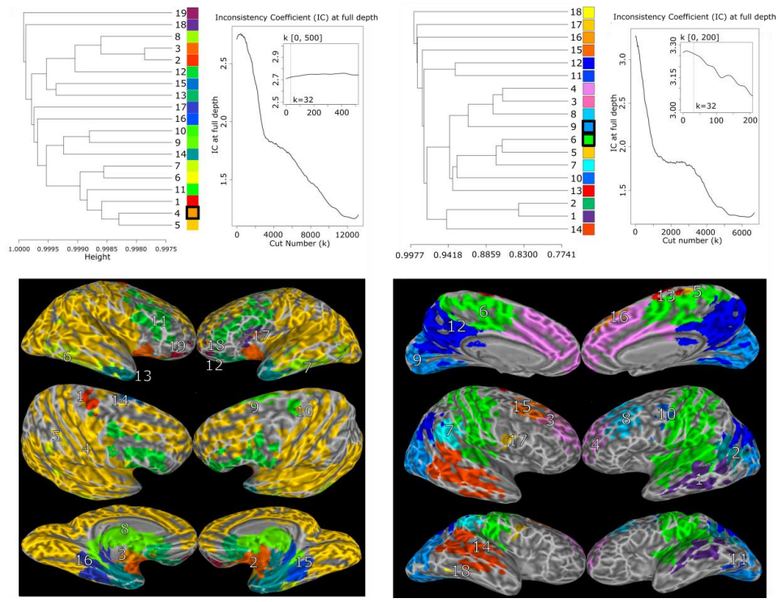

Figure 13: Inter-network hierarchies from root (left) down to cut level k=32. One large cluster (cluster 7) remain after 20 cluster limit per figure was reached. This large cluster was taken as the root and further clustered (right) down to cut level k=32. 18 clusters remain after evaluation, of which most of them resemble known RFNs such as the somatosensory-motor network (cluster 6) and visual network (cluster 9).

The intra-network functional hierarchies of the somatosensory-motor network was further investigated (Figure 14a). To illustrate the previous point of being able to select any of the leaves for a given sub-dendrogram to further study, the functional hierarchy of the visual network (Figure 14b) was also constructed. A cluster that is considerably larger in the somatosensory-motor network corresponds to the paracentral lobule. It seems that the paracentral lobule is also a highly connected hub of the network, hence the cluster was further clustered, again to cut level *k*=80 (Figure 14c). This is a natural end point, as cluster characteristics such as the Inconsistency Coefficient, cluster modularity, and cluster connectivity suggests that this would be the natural stage to terminate the hierarchical sub-division.

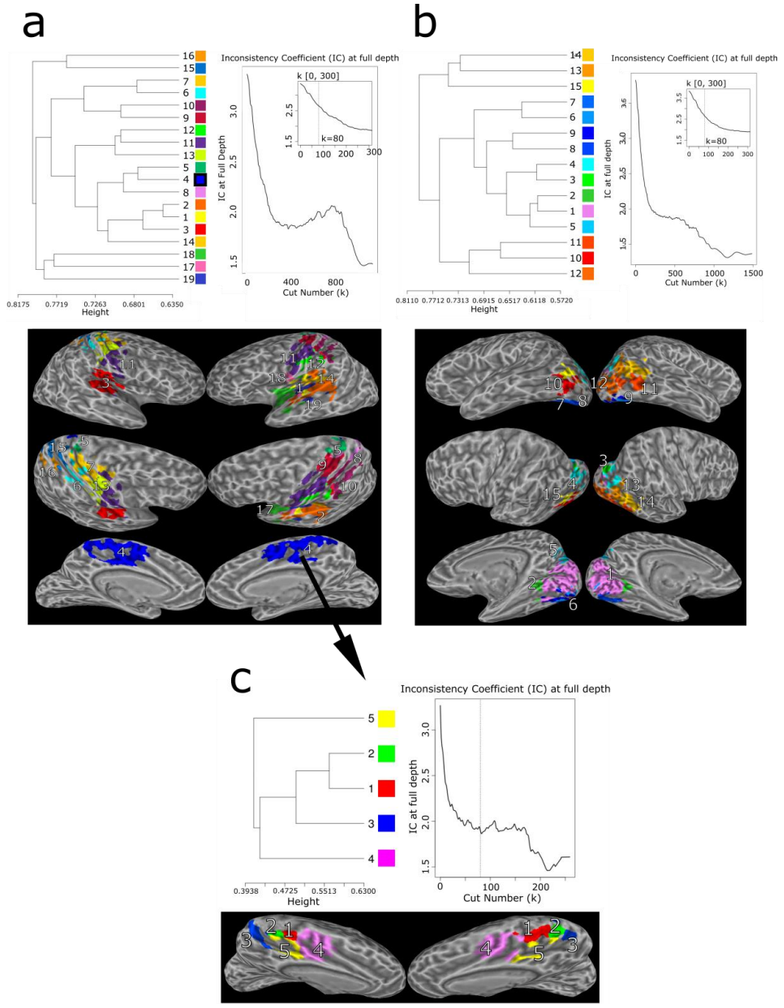

Figure 14: Intra-network functional hierarchies of the somatosensory-motor network (a) and visual network (b). The Paracentral lobule was further clustered to cut level k=80, where only 5 clusters remained. The plateau in Inconsistency Coefficient at this cut level suggests this would be a good time to terminate the analysis.

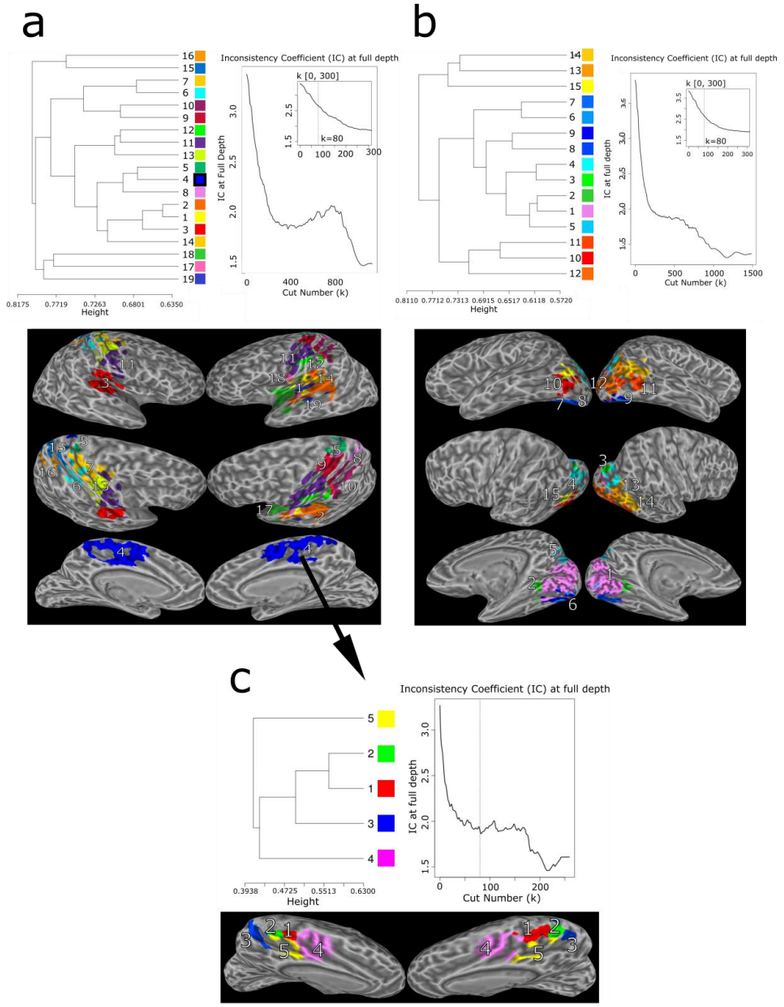

Figure 14: Intra-network functional hierarchies of the somatosensory-motor network (a) and visual network (b). The Paracentral lobule was further clustered to cut level k=80, where only 5 clusters remained. The plateau in Inconsistency Coefficient at this cut level suggests this would be a good time to terminate the analysis.

33

4 SUMMARY

Studying how the human brain functions through resting-state fMRI data is, in essence, a data mining problem. Within the vast amount of data lies information as to how the human brain is functionally organized. Model-free analysis methods lie at the center of exploratory analysis of resting-state fMRI data. These model free methods are purposed to extract meaningful information amongst noise and other artefacts that lie within the data, and reduce the high-dimensional data so that the meaningful information can be presented in a fashion that is easily comprehensible. How dimensionality estimation affects the output ICA results was investigated and how group ICA can be used for group comparison studies. To investigate brain connectivity, an analysis framework based on hierarchical clustering was developed to not only extract functional connectivity networks, but also obtain their organizational hierarchy simultaneously.

Hierarchical clustering algorithm was shown to be able to feasibly extract functional connectivity networks in resting-state fMRI data at a voxel-level. The extracted functional connectivity networks resembled those extracted using ICA. Hierarchical clustering results on resting-state fMRI data not only extracts functional connectivity networks from resting-state fMRI data, but also organizes them inherently into a hierarchical structure that mimics the brain's functional organization. Furthermore, hierarchical clustering can reveal the sub-networks and their functional organization of resting-state connectivity networks.

Through studying how the number of output ICs can affect ICA analysis results, valuable insight was gained on how ICs behave with increasing NIC, but these changes are too complex for any general patterns or conclusions to be drawn. The FOCIS analysis framework was implemented to delineate between artefacts and noise ICs and those corresponding to functional connectivity networks. While the framework performed superbly in its purposed task, the dimensionality problem proved to be more complex than initially thought for FOCIS to provide solid answer for. The insights gained from dimensionality investigations was sufficient to provide us with a solid basis to effectively utilize ICA to perform group comparison analysis. Using ICA individually on the groups with extensive preprocessing pipeline to eliminate as many noise and artefact sources as possible, group comparison can be conducted, without the need to pool all datasets into one single group ICA analysis run. Significant differences were detected in RFNs between migraine patients compared to healthy control subjects in areas in the Midbrain and Limbic system, areas which are also affected by the KOS treatment. This gives supporting evidence that KOS treatment alleviates migraine symptoms through regulating the parasympathetic autonomic reflex.

4 SUMMARY

Studying how the human brain functions through resting-state fMRI data is, in essence, a data mining problem. Within the vast amount of data lies information as to how the human brain is functionally organized. Model-free analysis methods lie at the center of exploratory analysis of resting-state fMRI data. These model free methods are purposed to extract meaningful information amongst noise and other artefacts that lie within the data, and reduce the high-dimensional data so that the meaningful information can be presented in a fashion that is easily comprehensible. How dimensionality estimation affects the output ICA results was investigated and how group ICA can be used for group comparison studies. To investigate brain connectivity, an analysis framework based on hierarchical clustering was developed to not only extract functional connectivity networks, but also obtain their organizational hierarchy simultaneously.

Hierarchical clustering algorithm was shown to be able to feasibly extract functional connectivity networks in resting-state fMRI data at a voxel-level. The extracted functional connectivity networks resembled those extracted using ICA. Hierarchical clustering results on resting-state fMRI data not only extracts functional connectivity networks from resting-state fMRI data, but also organizes them inherently into a hierarchical structure that mimics the brain's functional organization. Furthermore, hierarchical clustering can reveal the sub-networks and their functional organization of resting-state connectivity networks.

Through studying how the number of output ICs can affect ICA analysis results, valuable insight was gained on how ICs behave with increasing NIC, but these changes are too complex for any general patterns or conclusions to be drawn. The FOCIS analysis framework was implemented to delineate between artefacts and noise ICs and those corresponding to functional connectivity networks. While the framework performed superbly in its purposed task, the dimensionality problem proved to be more complex than initially thought for FOCIS to provide solid answer for. The insights gained from dimensionality investigations was sufficient to provide us with a solid basis to effectively utilize ICA to perform group comparison analysis. Using ICA individually on the groups with extensive preprocessing pipeline to eliminate as many noise and artefact sources as possible, group comparison can be conducted, without the need to pool all datasets into one single group ICA analysis run. Significant differences were detected in RFNs between migraine patients compared to healthy control subjects in areas in the Midbrain and Limbic system, areas which are also affected by the KOS treatment. This gives supporting evidence that KOS treatment alleviates migraine symptoms through regulating the parasympathetic autonomic reflex.

5 FUTURE PERSPECTIVES

1. *Programming work*. One of the reasons why fMRI has grown to be so popular among researchers is that there are software packages available that are easy to use. fMRI has become a means rather than an end for mostly this reason. Writing a complete software package for hierarchical clustering so that others might be able to use it.
2. *Incorporating a graphics user interface and visualization features*. One of the most difficult aspects about working with hierarchical clustering is on data visualization. A vast improvement of the hierarchical clustering software packages would be to implement a graphical user interface, not only benefiting the ease of use, but also incorporating visualization tools to easily navigate and manipulate the vastness that is the full dendrogram.
3. *Improving and extending the hierarchical model: Incorporate fuzziness*. One main reason why hierarchical clustering is that the algorithm organizes data in a structure that mimics the brain's functional organization. However there are downsides of the algorithm in that aspect. A property of the hierarchical clustering is that the resulting clusters are mutually exclusive, which does not seem reasonable in terms of brain's functional areas. Incorporating some sort of fuzziness into an otherwise hierarchical clustering algorithm will improve the innate modelling of the analysis method.
4. *Extending the analysis method: Incorporating time-domain analysis*. Functional connectivity networks are not stationary in time: This is why people made windowed-ICA. Further processing of resting-state fMRI data, with inclusion of time-domain aspects, similar to what windowed-ICA does for hierarchical clustering in hopes of also seeing how functional connectivity networks change and interact in time.
5. *Optimize the analysis framework for hierarchical clustering.* There seemed to be less need for optimization at the time of writing the analysis framework compared to the basis hierarchical clustering programs. Hence not much effort was dedicated to optimizing the analysis framework programs. This proved to be a mistake as it became ridiculously slow for larger cut levels, forcing us to limit the analysis to cut level 80 from any root starting point. This was not a problem for low cut levels in the full dendrogram, but was apparently becoming a limiting factor for sub-network investigations at higher cut levels. A more efficient analysis framework allows for more efficient and comprehensive analysis of hierarchical clustering results.
6. *Further investigation into the dimensionality of the resting-state fMRI datasets*. An attempt was made, but did not result in great success. All indicates to that only the surface of the problem was scratched upon. Some might say that the problem has already been solved through various dimensionality estimators, but since the inherent dimensionality of a resting-state fMRI dataset is unknown, one cannot be certain as no ground truth exist for evaluation. After all, if the noise filtering chip on your mobile phone can fail at times, why can't it fail here?

5 FUTURE PERSPECTIVES

1. *Programming work*. One of the reasons why fMRI has grown to be so popular among researchers is that there are software packages available that are easy to use. fMRI has become a means rather than an end for mostly this reason. Writing a complete software package for hierarchical clustering so that others might be able to use it.
2. *Incorporating a graphics user interface and visualization features*. One of the most difficult aspects about working with hierarchical clustering is on data visualization. A vast improvement of the hierarchical clustering software packages would be to implement a graphical user interface, not only benefiting the ease of use, but also incorporating visualization tools to easily navigate and manipulate the vastness that is the full dendrogram.
3. *Improving and extending the hierarchical model: Incorporate fuzziness*. One main reason why hierarchical clustering is that the algorithm organizes data in a structure that mimics the brain's functional organization. However there are downsides of the algorithm in that aspect. A property of the hierarchical clustering is that the resulting clusters are mutually exclusive, which does not seem reasonable in terms of brain's functional areas. Incorporating some sort of fuzziness into an otherwise hierarchical clustering algorithm will improve the innate modelling of the analysis method.
4. *Extending the analysis method: Incorporating time-domain analysis*. Functional connectivity networks are not stationary in time: This is why people made windowed-ICA. Further processing of resting-state fMRI data, with inclusion of time-domain aspects, similar to what windowed-ICA does for hierarchical clustering in hopes of also seeing how functional connectivity networks change and interact in time.
5. *Optimize the analysis framework for hierarchical clustering.* There seemed to be less need for optimization at the time of writing the analysis framework compared to the basis hierarchical clustering programs. Hence not much effort was dedicated to optimizing the analysis framework programs. This proved to be a mistake as it became ridiculously slow for larger cut levels, forcing us to limit the analysis to cut level 80 from any root starting point. This was not a problem for low cut levels in the full dendrogram, but was apparently becoming a limiting factor for sub-network investigations at higher cut levels. A more efficient analysis framework allows for more efficient and comprehensive analysis of hierarchical clustering results.
6. *Further investigation into the dimensionality of the resting-state fMRI datasets*. An attempt was made, but did not result in great success. All indicates to that only the surface of the problem was scratched upon. Some might say that the problem has already been solved through various dimensionality estimators, but since the inherent dimensionality of a resting-state fMRI dataset is unknown, one cannot be certain as no ground truth exist for evaluation. After all, if the noise filtering chip on your mobile phone can fail at times, why can't it fail here?

6 ACKNOWLEDGEMENTS

This is one of the few places where full freedom is entitled. As ever the opportunist, I shall take this opportunity to indulge myself in writing a few lines which not only do I expect nobody to read, but which I can actively recommend that nobody should read either.

I would like to thank my supervisor Tie-Qiang Li for putting up with me all these years, half of the time from across the globe and the other half with me being away working elsewhere. To my co-supervisor Mussie Msghina who always had something interesting at work. To all my former colleagues in the MR Physics department in Karolinska Hospital in Huddinge for all the coffee, especially Martin for the late nights at the scanner trying to implement Synthetic MR. To my colleagues at NordicNeuroLab for their understanding and support when I have to edit papers late at night and I am truly sorry Fredrik for scaring the living pajamas out of you one weekend evening when you thought nobody was at the office. To Shorinji Kempo Stockholm Södra, for simply existing and providing an outlet for my frustrations throughout the years. To my dear friends Mark, Vicky and Lucy, making even the dark rainy days in Scandinavia tropical and light. To my father, whom without I would never have gotten into MRI in the first place. To my mother, for everything you have done and sacrificed for me, and for everything you will do. No amount of words will suffice in expressing my gratitude and affection for you. To my grandparents who passed too soon, one of my biggest regrets in life so far includes not visiting you more often when I had the chance. Last but not least, to my wife, who never complains (much) when I am working past 3 am in the morning and who always feigns interest when I talk about my work.

Finally, you the reader have my sincerest gratitude for reading all the way up until this point, whether you feel obliged to do so or not. It is rare to have anybody read one’s thesis and even more so to have read it through. Thank you.

Aug 2015

6 ACKNOWLEDGEMENTS

This is one of the few places where full freedom is entitled. As ever the opportunist, I shall take this opportunity to indulge myself in writing a few lines which not only do I expect nobody to read, but which I can actively recommend that nobody should read either.

I would like to thank my supervisor Tie-Qiang Li for putting up with me all these years, half of the time from across the globe and the other half with me being away working elsewhere. To my co-supervisor Mussie Msghina who always had something interesting at work. To all my former colleagues in the MR Physics department in Karolinska Hospital in Huddinge for all the coffee, especially Martin for the late nights at the scanner trying to implement Synthetic MR. To my colleagues at NordicNeuroLab for their understanding and support when I have to edit papers late at night and I am truly sorry Fredrik for scaring the living pajamas out of you one weekend evening when you thought nobody was at the office. To Shorinji Kempo Stockholm Södra, for simply existing and providing an outlet for my frustrations throughout the years. To my dear friends Mark, Vicky and Lucy, making even the dark rainy days in Scandinavia tropical and light. To my father, whom without I would never have gotten into MRI in the first place. To my mother, for everything you have done and sacrificed for me, and for everything you will do. No amount of words will suffice in expressing my gratitude and affection for you. To my grandparents who passed too soon, one of my biggest regrets in life so far includes not visiting you more often when I had the chance. Last but not least, to my wife, who never complains (much) when I am working past 3 am in the morning and who always feigns interest when I talk about my work.

Finally, you the reader have my sincerest gratitude for reading all the way up until this point, whether you feel obliged to do so or not. It is rare to have anybody read one’s thesis and even more so to have read it through. Thank you.

Aug 2015

REFERENCES

1. Ogawa, S., et al., *Intrinsic signal changes accompanying sensory stimulation: functional brain mapping with magnetic resonance imaging.* Proc Natl Acad Sci U S A, 1992. **89**(13): p. 5951-5.
2. Raichle, M.E., et al., *Correlation between regional cerebral blood flow and oxidative metabolism. In vivo studies in man.* Arch Neurol, 1976. **33**(8): p. 523-6.
3. Buxton, R.B., E.C. Wong, and L.R. Frank, *Dynamics of blood flow and oxygenation changes during brain activation: the balloon model.* Magn Reson Med, 1998. **39**(6): p. 855-64.
4. Thulborn, K.R., et al., *Oxygenation dependence of the transverse relaxation time of water protons in whole blood at high field.* Biochim Biophys Acta, 1982. **714**(2): p. 265-70.
5. Mansfield, P., *Multi-planar image formation using NMR spin echoes.* Journal of Physics C: Solid State Physics, 1977. **10**(3): p. L55.
6. Damoiseaux, J.S., et al., *Consistent resting-state networks across healthy subjects.* Proc Natl Acad Sci U S A, 2006. **103**(37): p. 13848-53.
7. Smith, S.M., et al., *Correspondence of the brain's functional architecture during activation and rest.* Proc Natl Acad Sci U S A, 2009. **106**(31): p. 13040-5.
8. Buckner, R.L., J.R. Andrews-Hanna, and D.L. Schacter, *The brain's default network: anatomy, function, and relevance to disease.* Ann N Y Acad Sci, 2008. **1124**: p. 1-38.
9. Greicius, M.D., et al., *Functional connectivity in the resting brain: a network analysis of the default mode hypothesis.* Proc Natl Acad Sci U S A, 2003. **100**(1): p. 253-8.
10. Chen, J.E. and G.H. Glover, *Functional Magnetic Resonance Imaging Methods.* Neuropsychol Rev, 2015.
11. Friston, K.J., et al., *Statistical parametric maps in functional imaging: a general linear approach.* Human brain mapping, 1994. **2**(4): p. 189-210.
12. Friston, K.J., et al., *Analysis of fMRI time-series revisited.* Neuroimage, 1995. **2**(1): p. 45-53.
13. Biswal, B., et al., *Functional connectivity in the motor cortex of resting human brain using echo-planar MRI.* Magnetic resonance in medicine, 1995. **34**(4): p. 537-541.
14. Calhoun, V., et al., *A method for making group inferences from functional MRI data using independent component analysis.* Human brain mapping, 2001. **14**(3): p. 140-151.
15. Jenkinson, M., et al., *FSL.* Neuroimage, 2012. **62**(2): p. 782-90.
16. McKeown, M.J. and T.J. Sejnowski, *Independent component analysis of fMRI data: examining the assumptions.* Hum Brain Mapp, 1998. **6**(5-6): p. 368-72.
17. Bartels, A. and S. Zeki, *Brain dynamics during natural viewing conditions--a new guide for mapping connectivity in vivo.* Neuroimage, 2005. **24**(2): p. 339-49.
18. Abou-Elseoud, A., et al., *The effect of model order selection in group PICA.* Human brain mapping, 2010. **31**(8): p. 1207-1216.

REFERENCES

1. Ogawa, S., et al., *Intrinsic signal changes accompanying sensory stimulation: functional brain mapping with magnetic resonance imaging.* Proc Natl Acad Sci U S A, 1992. **89**(13): p. 5951-5.
2. Raichle, M.E., et al., *Correlation between regional cerebral blood flow and oxidative metabolism. In vivo studies in man.* Arch Neurol, 1976. **33**(8): p. 523-6.
3. Buxton, R.B., E.C. Wong, and L.R. Frank, *Dynamics of blood flow and oxygenation changes during brain activation: the balloon model.* Magn Reson Med, 1998. **39**(6): p. 855-64.
4. Thulborn, K.R., et al., *Oxygenation dependence of the transverse relaxation time of water protons in whole blood at high field.* Biochim Biophys Acta, 1982. **714**(2): p. 265-70.
5. Mansfield, P., *Multi-planar image formation using NMR spin echoes.* Journal of Physics C: Solid State Physics, 1977. **10**(3): p. L55.
6. Damoiseaux, J.S., et al., *Consistent resting-state networks across healthy subjects.* Proc Natl Acad Sci U S A, 2006. **103**(37): p. 13848-53.
7. Smith, S.M., et al., *Correspondence of the brain's functional architecture during activation and rest.* Proc Natl Acad Sci U S A, 2009. **106**(31): p. 13040-5.
8. Buckner, R.L., J.R. Andrews-Hanna, and D.L. Schacter, *The brain's default network: anatomy, function, and relevance to disease.* Ann N Y Acad Sci, 2008. **1124**: p. 1-38.
9. Greicius, M.D., et al., *Functional connectivity in the resting brain: a network analysis of the default mode hypothesis.* Proc Natl Acad Sci U S A, 2003. **100**(1): p. 253-8.
10. Chen, J.E. and G.H. Glover, *Functional Magnetic Resonance Imaging Methods.* Neuropsychol Rev, 2015.
11. Friston, K.J., et al., *Statistical parametric maps in functional imaging: a general linear approach.* Human brain mapping, 1994. **2**(4): p. 189-210.
12. Friston, K.J., et al., *Analysis of fMRI time-series revisited.* Neuroimage, 1995. **2**(1): p. 45-53.
13. Biswal, B., et al., *Functional connectivity in the motor cortex of resting human brain using echo-planar MRI.* Magnetic resonance in medicine, 1995. **34**(4): p. 537-541.
14. Calhoun, V., et al., *A method for making group inferences from functional MRI data using independent component analysis.* Human brain mapping, 2001. **14**(3): p. 140-151.
15. Jenkinson, M., et al., *FSL.* Neuroimage, 2012. **62**(2): p. 782-90.
16. McKeown, M.J. and T.J. Sejnowski, *Independent component analysis of fMRI data: examining the assumptions.* Hum Brain Mapp, 1998. **6**(5-6): p. 368-72.
17. Bartels, A. and S. Zeki, *Brain dynamics during natural viewing conditions--a new guide for mapping connectivity in vivo.* Neuroimage, 2005. **24**(2): p. 339-49.
18. Abou-Elseoud, A., et al., *The effect of model order selection in group PICA.* Human brain mapping, 2010. **31**(8): p. 1207-1216.

19. Cordes, D. and R.R. Nandy, *Estimation of the intrinsic dimensionality of fMRI data.* Neuroimage, 2006. **29**(1): p. 145-54.

20. Li, Y.O., T. Adali, and V.D. Calhoun, *Estimating the number of independent components for functional magnetic resonance imaging data.* Hum Brain Mapp, 2007. **28**(11): p. 1251-66.

21. Xie, X., et al., *Estimating intrinsic dimensionality of fMRI dataset incorporating an AR (1) noise model with cubic spline interpolation.* Neurocomputing, 2009. **72**(4): p. 1042-1055.

22. Juto, J.E. and R.G. Hallin, *Kinetic oscillation stimulation as treatment of acute migraine: a randomized, controlled pilot study.* Headache, 2015. **55**(1): p. 117-27.

23. Wang, Y. and T.Q. Li, *Dimensionality of ICA in resting-state fMRI investigated by feature optimized classification of independent components with SVM.* Front Hum Neurosci, 2015. **9**: p. 259.

24. Yeo, B.T., et al., *The organization of the human cerebral cortex estimated by intrinsic functional connectivity.* J Neurophysiol, 2011. **106**(3): p. 1125-65.

25. Woolrich, M.W., et al., *Bayesian analysis of neuroimaging data in FSL.* Neuroimage, 2009. **45**(1 Suppl): p. S173-86.

26. Smith, S.M., et al., *Advances in functional and structural MR image analysis and implementation as FSL.* Neuroimage, 2004. **23 Suppl 1**: p. S208-19.

27. Hilgetag, C.C., M.A. O'Neill, and M.P. Young, *Hierarchical organization of macaque and cat cortical sensory systems explored with a novel network processor.* Philos Trans R Soc Lond B Biol Sci, 2000. **355**(1393): p. 71-89.

28. Zhou, C., et al., *Hierarchical organization unveiled by functional connectivity in complex brain networks.* Phys Rev Lett, 2006. **97**(23): p. 238103.

29. Cohen, A.L., et al., *Defining functional areas in individual human brains using resting functional connectivity MRI.* Neuroimage, 2008. **41**(1): p. 45-57.

30. Ferrarini, L., et al., *Hierarchical functional modularity in the resting-state human brain.* Hum Brain Mapp, 2009. **30**(7): p. 2220-31.

31. Park, H.J. and K. Friston, *Structural and functional brain networks: from connections to cognition.* Science, 2013. **342**(6158): p. 1238411.

32. Zhen, Z., H. Fang, and J. Liu, *The hierarchical brain network for face recognition.* PLoS One, 2013. **8**(3): p. e59886.

33. Russo, R., H.J. Herrmann, and L. de Arcangelis, *Brain modularity controls the critical behavior of spontaneous activity.* Sci Rep, 2014. **4**: p. 4312.

34. Ryali, S., et al., *Development and validation of consensus clustering-based framework for brain segmentation using resting fMRI.* J Neurosci Methods, 2015. **240**: p. 128-40.

19. Cordes, D. and R.R. Nandy, *Estimation of the intrinsic dimensionality of fMRI data.* Neuroimage, 2006. **29**(1): p. 145-54.

20. Li, Y.O., T. Adali, and V.D. Calhoun, *Estimating the number of independent components for functional magnetic resonance imaging data.* Hum Brain Mapp, 2007. **28**(11): p. 1251-66.

21. Xie, X., et al., *Estimating intrinsic dimensionality of fMRI dataset incorporating an AR (1) noise model with cubic spline interpolation.* Neurocomputing, 2009. **72**(4): p. 1042-1055.

22. Juto, J.E. and R.G. Hallin, *Kinetic oscillation stimulation as treatment of acute migraine: a randomized, controlled pilot study.* Headache, 2015. **55**(1): p. 117-27.

23. Wang, Y. and T.Q. Li, *Dimensionality of ICA in resting-state fMRI investigated by feature optimized classification of independent components with SVM.* Front Hum Neurosci, 2015. **9**: p. 259.

24. Yeo, B.T., et al., *The organization of the human cerebral cortex estimated by intrinsic functional connectivity.* J Neurophysiol, 2011. **106**(3): p. 1125-65.

25. Woolrich, M.W., et al., *Bayesian analysis of neuroimaging data in FSL.* Neuroimage, 2009. **45**(1 Suppl): p. S173-86.

26. Smith, S.M., et al., *Advances in functional and structural MR image analysis and implementation as FSL.* Neuroimage, 2004. **23 Suppl 1**: p. S208-19.

27. Hilgetag, C.C., M.A. O'Neill, and M.P. Young, *Hierarchical organization of macaque and cat cortical sensory systems explored with a novel network processor.* Philos Trans R Soc Lond B Biol Sci, 2000. **355**(1393): p. 71-89.

28. Zhou, C., et al., *Hierarchical organization unveiled by functional connectivity in complex brain networks.* Phys Rev Lett, 2006. **97**(23): p. 238103.

29. Cohen, A.L., et al., *Defining functional areas in individual human brains using resting functional connectivity MRI.* Neuroimage, 2008. **41**(1): p. 45-57.

30. Ferrarini, L., et al., *Hierarchical functional modularity in the resting-state human brain.* Hum Brain Mapp, 2009. **30**(7): p. 2220-31.

31. Park, H.J. and K. Friston, *Structural and functional brain networks: from connections to cognition.* Science, 2013. **342**(6158): p. 1238411.

32. Zhen, Z., H. Fang, and J. Liu, *The hierarchical brain network for face recognition.* PLoS One, 2013. **8**(3): p. e59886.

33. Russo, R., H.J. Herrmann, and L. de Arcangelis, *Brain modularity controls the critical behavior of spontaneous activity.* Sci Rep, 2014. **4**: p. 4312.

34. Ryali, S., et al., *Development and validation of consensus clustering-based framework for brain segmentation using resting fMRI.* J Neurosci Methods, 2015. **240**: p. 128-40.

I

I

OPEN ACCESS Freely available online

PLOS ONE

Analysis of Whole-Brain Resting-State fMRI Data Using Hierarchical Clustering Approach

Yanlu Wang[1,2]*, **Tie-Qiang Li**[1,2]

1 Department of Clinical Sciences, Intervention, and Technology, Karolinska Institute, Stockholm, Sweden, **2** Department of Medical Physics, Karolinska University Hospital, Huddinge, Sweden

Abstract

Background: Previous studies using hierarchical clustering approach to analyze resting-state fMRI data were limited to a few slices or regions-of-interest (ROIs) after substantial data reduction.

Purpose: To develop a framework that can perform voxel-wise hierarchical clustering of whole-brain resting-state fMRI data from a group of subjects.

Materials and Methods: Resting-state fMRI measurements were conducted for 86 adult subjects using a single-shot echo-planar imaging (EPI) technique. After pre-processing and co-registration to a standard template, pair-wise cross-correlation coefficients (CC) were calculated for all voxels inside the brain and translated into absolute Pearson's distances after imposing a threshold CC≥0.3. The group averages of the Pearson's distances were then used to perform hierarchical clustering with the developed framework, which entails gray matter masking and an iterative scheme to analyze the dendrogram.

Results: With the hierarchical clustering framework, we identified most of the functional connectivity networks reported previously in the literature, such as the motor, sensory, visual, memory, and the default-mode functional networks (DMN). Furthermore, the DMN and visual system were split into their corresponding hierarchical sub-networks.

Conclusion: It is feasible to use the proposed hierarchical clustering scheme for voxel-wise analysis of whole-brain resting-state fMRI data. The hierarchical clustering result not only confirmed generally the finding in functional connectivity networks identified previously using other data processing techniques, such as ICA, but also revealed directly the hierarchical structure within the functional connectivity networks.

Citation: Wang Y, Li T-Q (2013) Analysis of Whole-Brain Resting-State fMRI Data Using Hierarchical Clustering Approach. PLoS ONE 8(10): e76315. doi:10.1371/journal.pone.0076315

Editor: Wang Zhan, University of Maryland, College Park, United States of America

Received April 16, 2013; **Accepted** August 23, 2013; **Published** October 18, 2013

Funding: The authors would like to acknowledge that this study is partly supported by a research grant from the Swedish Research Console. No additional external funding received for this study. The funders had no role in the study design, data collection and analysis, decision to publish, or preparation of the manuscript.

Competing Interests: The authors have declared that no competing interests exist.

* E-mail: yanlu.wang@ki.se

Introduction

Taking advantage of the rapidly expanding computational power in the past decade, several studies showed the feasibility to analyze whole-brain resting-state fMRI data with clustering algorithms. For example, Benjaminsson et al. used a dimensional scaling and vector quantization clustering technique to analyze resting-state fMRI data [1]. Van den Heuvel et al. used a graph-theory approach to determine several functional connectivity networks [2].

Hierarchical clustering has not been used as fluently as other clustering methods in the analysis of resting-state fMRI data due to its poor scaling, high complexity and sensitivity to outliers. On the other hand, hierarchical clustering is completely deterministic and can stratify data into a hierarchical structure [3,4,5,6]. Previous studies on hierarchical clustering of resting-state fMRI data have been limited to a few slices or region-of-interests (ROIs) after substantial data reduction. Cordes et al. used a hierarchical clustering algorithm and analyzed 4 slices of resting-state fMRI data [7]. In another hierarchical clustering study of human brain, Salvador et al. grouped the resting-state fMRI data into regions-of-interests (ROIs) according to their anatomical locations prior to the clustering [8] of the ROIs. More recently, voxel-wise hierarchical clustering was also attempted on resting-state fMRI data acquired from rodents [9].

Due to limited computational capacity, data reduction is usually needed in hierarchical clustering of resting-state fMRI data. In the earlier works this was achieved either by limiting the number of slices [7] or substantially reducing the data into anatomical ROIs [8]. In order to perform voxel-wise hierarchical clustering of whole-brain resting-state fMRI data, in this study we used a brain mask to achieve data reduction without compromising spatial resolution and coverage. This masking operation also improves the robustness of the framework by eliminating irrelevant voxels containing noise and artifact outliers which destabilize the algorithm [10]. To further improve stability of the algorithm,

OPEN ACCESS Freely available online

PLOS ONE

Analysis of Whole-Brain Resting-State fMRI Data Using Hierarchical Clustering Approach

Yanlu Wang[1,2]*, Tie-Qiang Li[1,2]

1 Department of Clinical Sciences, Intervention, and Technology, Karolinska Institute, Stockholm, Sweden, 2 Department of Medical Physics, Karolinska University Hospital, Huddinge, Sweden

Abstract

Background: Previous studies using hierarchical clustering approach to analyze resting-state fMRI data were limited to a few slices or regions-of-interest (ROIs) after substantial data reduction.

Purpose: To develop a framework that can perform voxel-wise hierarchical clustering of whole-brain resting-state fMRI data from a group of subjects.

Materials and Methods: Resting-state fMRI measurements were conducted for 86 adult subjects using a single-shot echo-planar imaging (EPI) technique. After pre-processing and co-registration to a standard template, pair-wise cross-correlation coefficients (CC) were calculated for all voxels inside the brain and translated into absolute Pearson's distances after imposing a threshold CC≥0.3. The group averages of the Pearson's distances were then used to perform hierarchical clustering with the developed framework, which entails gray matter masking and an iterative scheme to analyze the dendrogram.

Results: With the hierarchical clustering framework, we identified most of the functional connectivity networks reported previously in the literature, such as the motor, sensory, visual, memory, and the default-mode functional networks (DMN). Furthermore, the DMN and visual system were split into their corresponding hierarchical sub-networks.

Conclusion: It is feasible to use the proposed hierarchical clustering scheme for voxel-wise analysis of whole-brain resting-state fMRI data. The hierarchical clustering result not only confirmed generally the finding in functional connectivity networks identified previously using other data processing techniques, such as ICA, but also revealed directly the hierarchical structure within the functional connectivity networks.

Citation: Wang Y, Li T-Q (2013) Analysis of Whole-Brain Resting-State fMRI Data Using Hierarchical Clustering Approach. PLoS ONE 8(10): e76315. doi:10.1371/journal.pone.0076315

Editor: Wang Zhan, University of Maryland, College Park, United States of America

Received April 16, 2013; Accepted August 23, 2013; Published October 18, 2013

Copyright: © 2013 Wang, Li. This is an open-access article distributed under the terms of the Creative Commons Attribution License, which permits unrestricted use, distribution, and reproduction in any medium, provided the original author and source are credited.

Funding: The authors would like to acknowledge that this study is partly supported by a research grant from the Swedish Research Console. No additional external funding received for this study. The funders had no role in the study design, data collection and analysis, decision to publish, or preparation of the manuscript.

Competing Interests: The authors have declared that no competing interests exist.

* E-mail: yanlu.wang@ki.se

Introduction

Taking advantage of the rapidly expanding computational power in the past decade, several studies showed the feasibility to analyze whole-brain resting-state fMRI data with clustering algorithms. For example, Benjaminsson et al. used a dimensional scaling and vector quantization clustering technique to analyze resting-state fMRI data [1]. Van den Heuvel et al. used a graph-theory approach to determine several functional connectivity networks [2].

Hierarchical clustering has not been used as fluently as other clustering methods in the analysis of resting-state fMRI data due to its poor scaling, high complexity and sensitivity to outliers. On the other hand, hierarchical clustering is completely deterministic and can stratify data into a hierarchical structure [3,4,5,6]. Previous studies on hierarchical clustering of resting-state fMRI data have been limited to a few slices or region-of-interests (ROIs) after substantial data reduction. Cordes et al. used a hierarchical clustering algorithm and analyzed 4 slices of resting-state fMRI data [7]. In another hierarchical clustering study of human brain, Salvador et al. grouped the resting-state fMRI data into regions-of-interests (ROIs) according to their anatomical locations prior to the clustering [8] of the ROIs. More recently, voxel-wise hierarchical clustering was also attempted on resting-state fMRI data acquired from rodents [9].

Due to limited computational capacity, data reduction is usually needed in hierarchical clustering of resting-state fMRI data. In the earlier works this was achieved either by limiting the number of slices [7] or substantially reducing the data into anatomical ROIs [8]. In order to perform voxel-wise hierarchical clustering of whole-brain resting-state fMRI data, in this study we used a brain mask to achieve data reduction without compromising spatial resolution and coverage. This masking operation also improves the robustness of the framework by eliminating irrelevant voxels containing noise and artifact outliers which destabilize the algorithm [10]. To further improve stability of the algorithm,

PLOS ONE | www.plosone.org 1 October 2013 | Volume 8 | Issue 10 | e76315

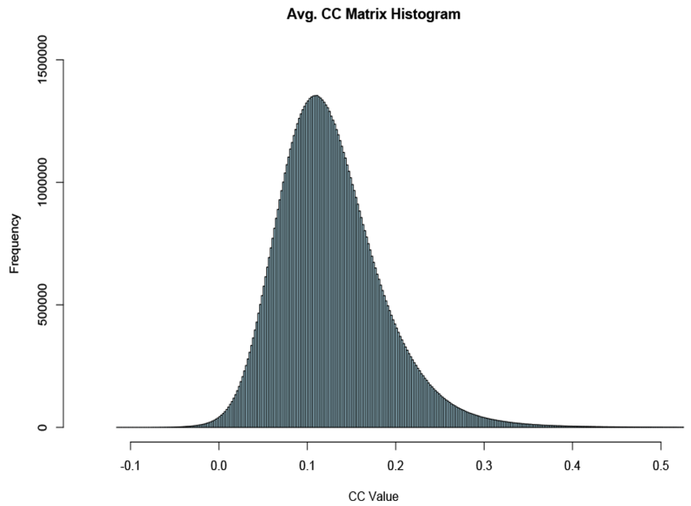

Figure 1. Average CC matrix histogram. Histogram of the average CC matrix of all datasets. The majority of CC values are below 0.2 with a relatively small number of values above 0.4. Negative values exist but are relatively few and only take on small values.
doi:10.1371/journal.pone.0076315.g001

the distance matrix for individual subject was thresholded and averaged prior to the clustering. This allows also efficient group analysis of whole-brain resting-state fMRI data.

We developed an iterative scheme with termination criteria based on cluster size to analyze the dendrogram. With the developed framework, we were able to independently identify most of the functional connectivity networks reported previously in the literature using ICA and other analysis methods. Furthermore, we illustrated that the dendrogram can directly reveal the inherent hierarchical structure within the functional connectivity networks. To the best of our knowledge, there has been no previous study succeeded in hierarchical clustering of whole-brain human resting-state fMRI data at voxel-level.

Materials and Methods

Ethical statement

This study was approved by the Central Ethical Review Board in Sweden, who also approved the consent form used to provide information and obtain consent. All participants provided informed consent by signature.

Data acquisition

Resting-state fMRI measurements were conducted for 86 normal adult subjects (male/female = 40/46, aged 21–84 years old). All resting-state fMRI measurements were performed on a Siemens whole-body 3T clinical MRI scanner (Magnetom Trio, Erlangen, Germany) using a dedicated 32-channel phased array detector. For each subject, at least one set of resting-state fMRI data was acquired using a single-shot 2D gradient-recalled echo (GRE) echo-planar imaging (EPI) technique. The essential acquisition parameters for the resting-state fMRI scan included the following: 32 transverse slices of 3.6 mm thick, TR/TE = 2000/35 ms, FOV = 220 mm, matrix size = 64×64, parallel imaging acquisition with an acceleration factor (IPAT) of 2, flip angle = 90°, and 300 dynamic timeframes.

Data preprocessing

Data preprocessing were performed using AFNI (http://afni.nimh.nih.gov/afni/) and FSL (http://www.fmrib.ox.ac.uk/fsl) programs wrapped around a bash shell script. The first 10 timeframes in each data set were removed to ensure the signal reaches steady state. Head motion correction was performed based on 6-parameter rigid body images registration. The average volume for each motion corrected time series were used to remove the skull from the images and to create whole-brain mask. Spatial normalization to the MNI template was performed using 12 parameter affine transformation and mutual information as the cost function. The data was then resampled to isotropic resolution using a Gaussian kernel with FWHM = 4 mm. Low-pass filtering at 0.1 Hz was done followed by baseline de-trending up to the third order.

Cross-correlation evaluation

To minimize processing load without promising the spatial resolution and whole-brain coverage, individual datasets were masked with a standard gray matter template derived from FSL tissue priors (http://www.fmrib.ox.ac.uk/fsl) to exclude white matter and cerebral spinal-fluid (CSF) regions. After the masking, the pair-wise Pearson's cross correlation coefficients (CC) were calculated for all datasets. The correlation coefficients were then thresholded at 0.3 [7] The correlation values below the threshold was truncated to zero while values above this threshold were not changed. After thresholding, approximately 1.1% of the correlation coefficients remained for further analysis (Fig. 1). The cross correlation matrices for all subjects were then averaged together

Analyzing fMRI Data Using Hierarchical Clustering

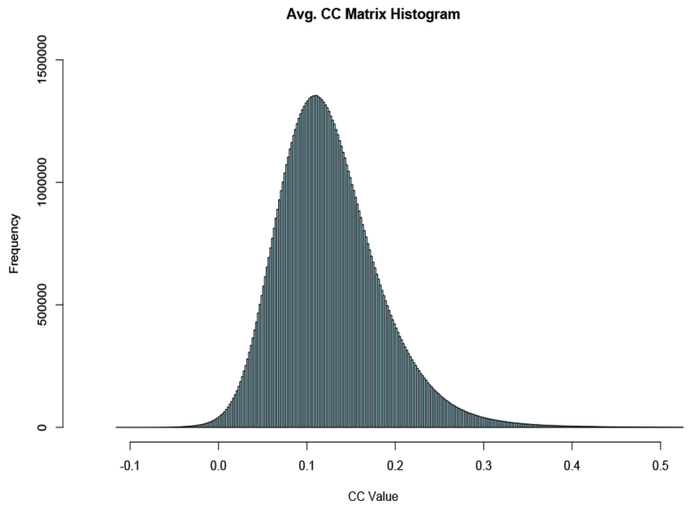

Figure 1. Average CC matrix histogram. Histogram of the average CC matrix of all datasets. The majority of CC values are below 0.2 with a relatively small number of values above 0.4. Negative values exist but are relatively few and only take on small values.
doi:10.1371/journal.pone.0076315.g001

the distance matrix for individual subject was thresholded and averaged prior to the clustering. This allows also efficient group analysis of whole-brain resting-state fMRI data.

We developed an iterative scheme with termination criteria based on cluster size to analyze the dendrogram. With the developed framework, we were able to independently identify most of the functional connectivity networks reported previously in the literature using ICA and other analysis methods. Furthermore, we illustrated that the dendrogram can directly reveal the inherent hierarchical structure within the functional connectivity networks. To the best of our knowledge, there has been no previous study succeeded in hierarchical clustering of whole-brain human resting-state fMRI data at voxel-level.

Materials and Methods

Ethical statement

This study was approved by the Central Ethical Review Board in Sweden, who also approved the consent form used to provide information and obtain consent. All participants provided informed consent by signature.

Data acquisition

Resting-state fMRI measurements were conducted for 86 normal adult subjects (male/female = 40/46, aged 21–84 years old). All resting-state fMRI measurements were performed on a Siemens whole-body 3T clinical MRI scanner (Magnetom Trio, Erlangen, Germany) using a dedicated 32-channel phased array detector. For each subject, at least one set of resting-state fMRI data was acquired using a single-shot 2D gradient-recalled echo (GRE) echo-planar imaging (EPI) technique. The essential acquisition parameters for the resting-state fMRI scan included the following: 32 transverse slices of 3.6 mm thick, TR/TE = 2000/35 ms, FOV = 220 mm, matrix size = 64×64, parallel imaging acquisition with an acceleration factor (IPAT) of 2, flip angle = 90°, and 300 dynamic timeframes.

Data preprocessing

Data preprocessing were performed using AFNI (http://afni.nimh.nih.gov/afni/) and FSL (http://www.fmrib.ox.ac.uk/fsl) programs wrapped around a bash shell script. The first 10 timeframes in each data set were removed to ensure the signal reaches steady state. Head motion correction was performed based on 6-parameter rigid body images registration. The average volume for each motion corrected time series were used to remove the skull from the images and to create whole-brain mask. Spatial normalization to the MNI template was performed using 12 parameter affine transformation and mutual information as the cost function. The data was then resampled to isotropic resolution using a Gaussian kernel with FWHM = 4 mm. Low-pass filtering at 0.1 Hz was done followed by baseline de-trending up to the third order.

Cross-correlation evaluation

To minimize processing load without promising the spatial resolution and whole-brain coverage, individual datasets were masked with a standard gray matter template derived from FSL tissue priors (http://www.fmrib.ox.ac.uk/fsl) to exclude white matter and cerebral spinal-fluid (CSF) regions. After the masking, the pair-wise Pearson's cross correlation coefficients (CC) were calculated for all datasets. The correlation coefficients were then thresholded at 0.3 [7] The correlation values below the threshold was truncated to zero while values above this threshold were not changed. After thresholding, approximately 1.1% of the correlation coefficients remained for further analysis (Fig. 1). The cross correlation matrices for all subjects were then averaged together

PLOS ONE | www.plosone.org 2 October 2013 | Volume 8 | Issue 10 | e76315

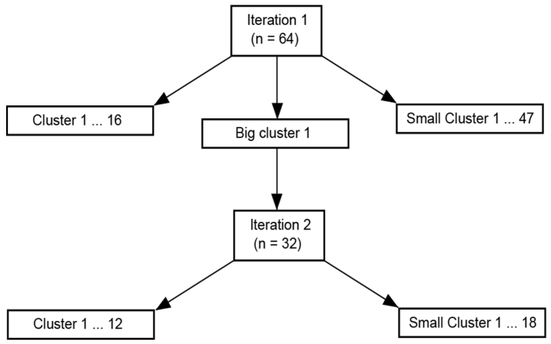

Figure 2. Schematics of the iterative clustering pipeline. Schematics for iterative hierarchical clustering framework based on resulting cluster size. Small clusters are excluded and large clusters are clustered further iteratively using a smaller cluster count.
doi:10.1371/journal.pone.0076315.g002

voxel-wise. The averaged correlation data were then converted into absolute Pearson's distances according to the definition (1-|CC|), which were used to perform hierarchical clustering.

Hierarchical clustering

An agglomerative hierarchical clustering algorithm was used as the basis for the framework. A brief description of the algorithm is summarized as follows: Given a set of N voxels to be clustered, and a corresponding $N\times N$ distance matrix:

1. Assign each voxel to a cluster, resulting in N clusters, with each cluster containing just one voxel. The distances between the clusters are the distances among the voxels.
2. Find the closest pair of clusters.
3. Merge the closest pair of clusters, resulting in one cluster less in total.
4. Repeat 2–3 until only a single cluster remains.

Step 3 can be performed in a variety of ways, referred to as linkage methods. The type of linkage in a hierarchical clustering algorithm refers to how the algorithm determines distance between newly formed clusters to all other voxels and clusters. Single-linkage takes the shortest distance between new clusters against the rest of the data, maximum-linkage takes the longest distance, and average-linkage takes the average. In our application, voxels within a cluster corresponding to a functional connectivity network should be highly correlated to each other. Hence, single-linkage is not desirable in this application. Maximum-linkage forces the algorithm to solely determine clusters with all voxels having high correlations to each other without exceptions. Average-linkage relaxes somewhat the intra-cluster connectivity requirements compared to maximum-linkage by taking the average distance. Hence, average-linkage was opted to take into account of the potential noise residues. Pseudo-code for the algorithm is shown in Appendix A in Supporting Information S1.

The algorithm produces a binary hierarchy tree (dendrogram) from which k clusters can be retrieved by cutting the k-1 longest links.

Since the number of meaningful clusters is unknown *a priori* and is affected by the noise level of the resting-state fMRI data, it is difficult to specify the number of resulting clusters directly. We tested different criterion for the selection of clusters, e.g. the inconsistency coefficient (see Appendix B in Supporting Information S1 and Figure S1 for details). It was found that the cluster size could be used as an effective approach. By referring to the group ICA result from the same dataset, a cluster larger than 5000 voxels in size ($S\geq 5000$) is considered too large to be a single functional connectivity network, whereas a cluster less than 50 voxels in size ($S\leq 50$) is considered too small to be a meaningful cluster. The selection of these parameters is determined semi-empirically and is discussed in further details below.

Testing the algorithm with different number of clusters indicates that increasing the number of clusters in the first iteration simply increases the number of spurious small clusters but does not efficiently reduce the size of the largest cluster, once the cluster count is sufficiently large. Therefore, the cluster count, for the first iteration (whole-brain clustering), was set to 64. Cluster count for the hierarchies further down was reduced by a factor of 2 than that for the previous iteration ($k_2 = 32$, $k_3 = 16$, $k_4 = 8$ *etc.*). The cluster number for subsequent iterations is decreased according to the size

Table 1. Cluster count for hierarchical clustering.

Iteration	Big cluster count	Small cluster count	Potential RSN cluster count	Total cluster count
1	1	47	16	64
2	0	18	14	32
Total	1	65	30	96

doi:10.1371/journal.pone.0076315.t001

Analyzing fMRI Data Using Hierarchical Clustering

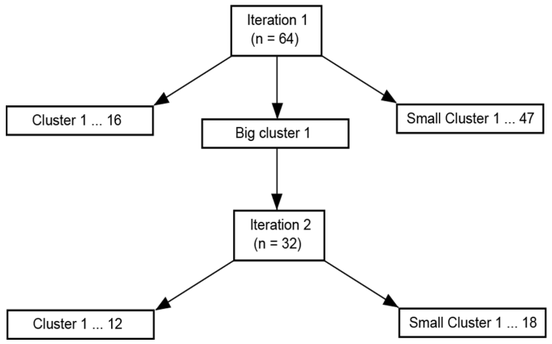

Figure 2. Schematics of the iterative clustering pipeline. Schematics for iterative hierarchical clustering framework based on resulting cluster size. Small clusters are excluded and large clusters are clustered further iteratively using a smaller cluster count.
doi:10.1371/journal.pone.0076315.g002

voxel-wise. The averaged correlation data were then converted into absolute Pearson's distances according to the definition (1-|CC|), which were used to perform hierarchical clustering.

Hierarchical clustering

An agglomerative hierarchical clustering algorithm was used as the basis for the framework. A brief description of the algorithm is summarized as follows: Given a set of N voxels to be clustered, and a corresponding $N\times N$ distance matrix:

1. Assign each voxel to a cluster, resulting in N clusters, with each cluster containing just one voxel. The distances between the clusters are the distances among the voxels.
2. Find the closest pair of clusters.
3. Merge the closest pair of clusters, resulting in one cluster less in total.
4. Repeat 2–3 until only a single cluster remains.

Step 3 can be performed in a variety of ways, referred to as linkage methods. The type of linkage in a hierarchical clustering algorithm refers to how the algorithm determines distance between newly formed clusters to all other voxels and clusters. Single-linkage takes the shortest distance between new clusters against the rest of the data, maximum-linkage takes the longest distance, and average-linkage takes the average. In our application, voxels within a cluster corresponding to a functional connectivity network should be highly correlated to each other. Hence, single-linkage is not desirable in this application. Maximum-linkage forces the algorithm to solely determine clusters with all voxels having high correlations to each other without exceptions. Average-linkage relaxes somewhat the intra-cluster connectivity requirements compared to maximum-linkage by taking the average distance. Hence, average-linkage was opted to take into account of the potential noise residues. Pseudo-code for the algorithm is shown in Appendix A in Supporting Information S1.

The algorithm produces a binary hierarchy tree (dendrogram) from which k clusters can be retrieved by cutting the k-1 longest links.

Since the number of meaningful clusters is unknown *a priori* and is affected by the noise level of the resting-state fMRI data, it is difficult to specify the number of resulting clusters directly. We tested different criterion for the selection of clusters, e.g. the inconsistency coefficient (see Appendix B in Supporting Information S1 and Figure S1 for details). It was found that the cluster size could be used as an effective approach. By referring to the group ICA result from the same dataset, a cluster larger than 5000 voxels in size ($S\geq 5000$) is considered too large to be a single functional connectivity network, whereas a cluster less than 50 voxels in size ($S\leq 50$) is considered too small to be a meaningful cluster. The selection of these parameters is determined semi-empirically and is discussed in further details below.

Testing the algorithm with different number of clusters indicates that increasing the number of clusters in the first iteration simply increases the number of spurious small clusters but does not efficiently reduce the size of the largest cluster, once the cluster count is sufficiently large. Therefore, the cluster count, for the first iteration (whole-brain clustering), was set to 64. Cluster count for the hierarchies further down was reduced by a factor of 2 than that for the previous iteration ($k_2 = 32$, $k_3 = 16$, $k_4 = 8$ *etc.*). The cluster number for subsequent iterations is decreased according to the size

Table 1. Cluster count for hierarchical clustering.

Iteration	Big cluster count	Small cluster count	Potential RSN cluster count	Total cluster count
1	1	47	16	64
2	0	18	14	32
Total	1	65	30	96

doi:10.1371/journal.pone.0076315.t001

PLOS ONE | www.plosone.org 3 October 2013 | Volume 8 | Issue 10 | e76315

Figure 3. Hierarchical clustering result. Clustering results from the selected cut levels. Bilaterally symmetric clusters are displayed in the same figures using two different colors (blue and red). The large cluster went through further iteration is marked with a green box.
doi:10.1371/journal.pone.0076315.g003

Table 2. Hierarchical clustering results.

Label	Size (Voxels)	Min CC	Max CC	Average CC
B	312	0.17	0.29	0.24
C	330	0.17	0.30	0.24
D	66	0.19	0.30	0.25
E (left/right)	168/176	0.17/0.19	0.25/0.26	0.22/0.22
F	270	0.18	0.29	0.24
G	66	0.19	0.28	0.24
H	1311	0.16	0.27	0.22
I	672	0.17	0.27	0.22
J	6828	0.15	0.29	0.22
K, blue region	240	0.20	0.31	0.27
L (left/right)	189/114	0.21/0.24	0.32/0.34	0.31/0.30
M	888	0.20	0.33	0.27
N (left/right)	67/91	0.25/0.22	0.36/0.34	0.31/0.30
O	999	0.19	0.36	0.29
P	463	0.19	0.30	0.26
Q	1540	0.19	0.35	0.27
R	1619	0.18	0.36	0.29

doi:10.1371/journal.pone.0076315.t002

of the large cluster to be further divided to avoid spurious amounts of small clusters being generated. An overview of the hierarchical clustering pipeline is schematically shown in Figure 2.

In order to identify potential resting-state functional networks (RFNs), Clusters with adequate voxel size ($50 \leq S \leq 5000$) were carefully examined by comparing their spatial distribution patterns with previously published RFNs in the literatures.

ICA analysis

In order to verify the RFN results from the hierarchical clustering, independent component analysis (ICA) of the same resting-state fMRI data sets were also performed using the GIFT toolbox, v1.3h (http://www.nitrc.org/projects/gift) implemented in MATLAB (MathWorks, Massachusetts, U.S.A). Individual data set was first concatenated and then followed by computation of the individual ICA components and corresponding time courses. Principle Component Analysis (PCA) was used prior to ICA for data reduction. The InfoMax group-ICA algorithm was then applied on the reduced data. Lastly, back-reconstruction of time series data for each individual subject was performed. The number of predefined ICA components was set to 36, as done in accordance to a previous study [11]. Independent components (ICs) that are common for the entire subject group and resemble RFNs were identified through a threshold of voxel-wise t-maps and visual examination of the spatial distribution patterns.

Analyzing fMRI Data Using Hierarchical Clustering

Figure 3. Hierarchical clustering result. Clustering results from the selected cut levels. Bilaterally symmetric clusters are displayed in the same figures using two different colors (blue and red). The large cluster went through further iteration is marked with a green box.
doi:10.1371/journal.pone.0076315.g003

Table 2. Hierarchical clustering results.

Label	Size (Voxels)	Min CC	Max CC	Average CC
B	312	0.17	0.29	0.24
C	330	0.17	0.30	0.24
D	66	0.19	0.30	0.25
E (left/right)	168/176	0.17/0.19	0.25/0.26	0.22/0.22
F	270	0.18	0.29	0.24
G	66	0.19	0.28	0.24
H	1311	0.16	0.27	0.22
I	672	0.17	0.27	0.22
J	6828	0.15	0.29	0.22
K, blue region	240	0.20	0.31	0.27
L (left/right)	189/114	0.21/0.24	0.32/0.34	0.31/0.30
M	888	0.20	0.33	0.27
N (left/right)	67/91	0.25/0.22	0.36/0.34	0.31/0.30
O	999	0.19	0.36	0.29
P	463	0.19	0.30	0.26
Q	1540	0.19	0.35	0.27
R	1619	0.18	0.36	0.29

doi:10.1371/journal.pone.0076315.t002

of the large cluster to be further divided to avoid spurious amounts of small clusters being generated. An overview of the hierarchical clustering pipeline is schematically shown in Figure 2.

In order to identify potential resting-state functional networks (RFNs), Clusters with adequate voxel size ($50 \leq S \leq 5000$) were carefully examined by comparing their spatial distribution patterns with previously published RFNs in the literatures.

ICA analysis

In order to verify the RFN results from the hierarchical clustering, independent component analysis (ICA) of the same resting-state fMRI data sets were also performed using the GIFT toolbox, v1.3h (http://www.nitrc.org/projects/gift) implemented in MATLAB (MathWorks, Massachusetts, U.S.A). Individual data set was first concatenated and then followed by computation of the individual ICA components and corresponding time courses. Principle Component Analysis (PCA) was used prior to ICA for data reduction. The InfoMax group-ICA algorithm was then applied on the reduced data. Lastly, back-reconstruction of time series data for each individual subject was performed. The number of predefined ICA components was set to 36, as done in accordance to a previous study [11]. Independent components (ICs) that are common for the entire subject group and resemble RFNs were identified through a threshold of voxel-wise t-maps and visual examination of the spatial distribution patterns.

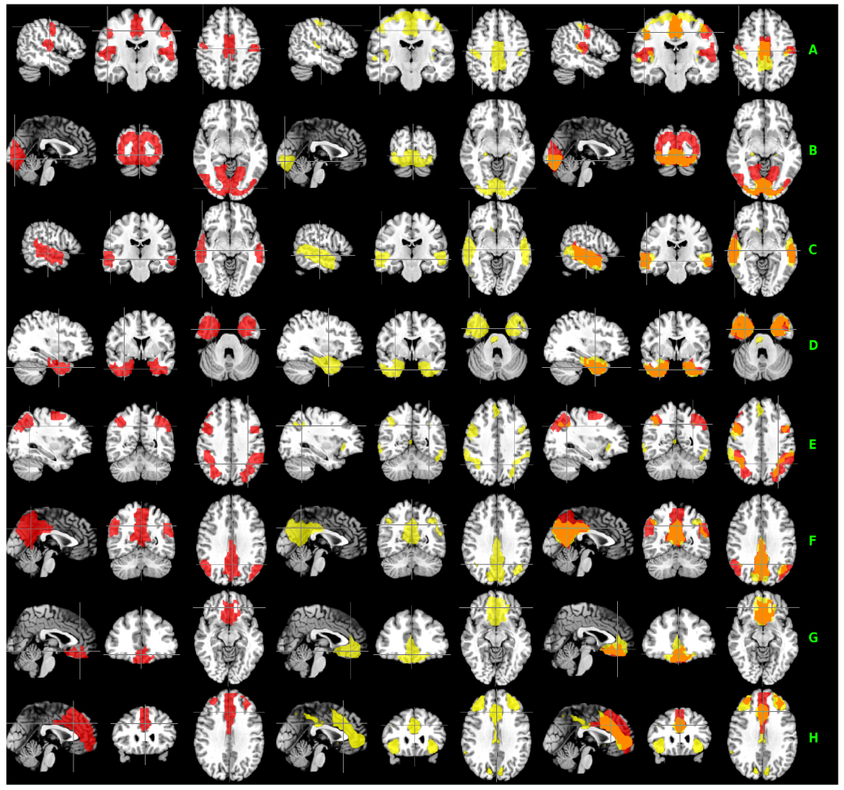

Figure 4. Comparison between the hierarchical clustering and ICA results. Set of hierarchical clusters (*left column*) and ICA components (*middle column*) with good matching. The right column displays their corresponding overlays with overlapping areas showing in orange. The group ICA t-maps were binarized with a threshold at $p<0.001$ for ease of comparison with clustering results.
doi:10.1371/journal.pone.0076315.g004

Table 3. Comparison between the ICA and clustering results.

Label	Cluster size	Component size	Intersect	Exclusive cluster	Exclusive component
A	1540	1100	636	904	464
B	1619	494	469	1125	25
C	463	841	399	64	442
D	672	843	537	135	306
E	1311	1099	558	753	541
F	999	765	517	482	248
G	270	481	247	23	234
H	888	1550	594	294	956

doi:10.1371/journal.pone.0076315.t003

Analyzing fMRI Data Using Hierarchical Clustering

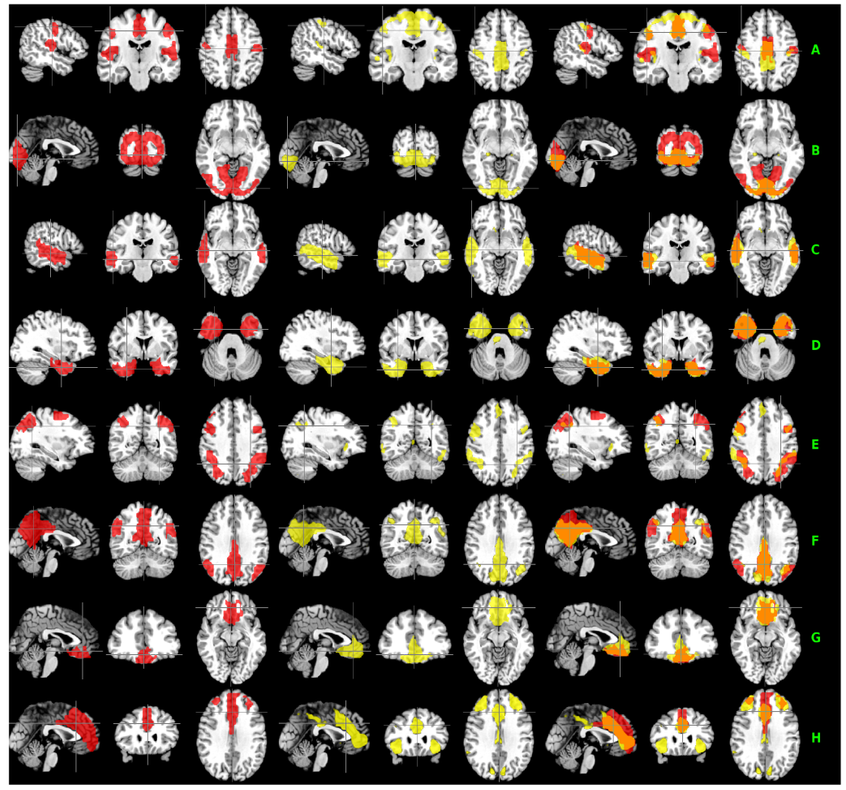

Figure 4. Comparison between the hierarchical clustering and ICA results. Set of hierarchical clusters (*left column*) and ICA components (*middle column*) with good matching. The right column displays their corresponding overlays with overlapping areas showing in orange. The group ICA t-maps were binarized with a threshold at $p<0.001$ for ease of comparison with clustering results.
doi:10.1371/journal.pone.0076315.g004

Table 3. Comparison between the ICA and clustering results.

Label	Cluster size	Component size	Intersect	Exclusive cluster	Exclusive component
A	1540	1100	636	904	464
B	1619	494	469	1125	25
C	463	841	399	64	442
D	672	843	537	135	306
E	1311	1099	558	753	541
F	999	765	517	482	248
G	270	481	247	23	234
H	888	1550	594	294	956

doi:10.1371/journal.pone.0076315.t003

PLOS ONE | www.plosone.org 5 October 2013 | Volume 8 | Issue 10 | e76315

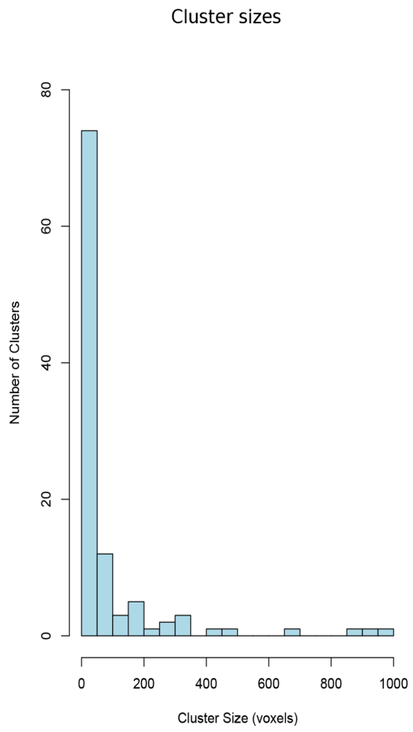

Figure 5. Histogram of cluster size. Cluster size from all clusters produced by applying the proposed framework to the acquired resting-state fMRI datasets. It is clear that many clusters have less than 50 voxels.
doi:10.1371/journal.pone.0076315.g005

Comparison between hierarchical clustering and ICA results

For quantitative comparison between the hierarchical clustering results and RFNs identified by ICA, each cluster that fulfilled the cluster size criteria ($50 \leq S \leq 5000$) was matched with a RFN identified using ICA based on its maximum overlap and the similarity of the spatial distribution. The cluster size, intersection area, and complementary non-overlapping areas were evaluated for each matched pair.

Assessment of statistical significance

Because the CC matrices were thresholded at 0.3, which corresponds to a t-score threshold of 2.88 ($df = 84$), the statistical significance at voxel-level is $p<0.001$ without correcting for multiple comparisons. For comparison the group ICA spatial t-maps were then binarized at voxel-level with the same voxel-level statistical significance.

The final statistical significance was evaluated by enforcing also a minimum voxel cluster size of 6 contiguous voxels. After specifying the original and final voxel sizes as well as the uncorrected threshold value the AFNI program, *AlphaSim*, was used to compute a list of probabilities corresponding to different cluster sizes produced by random field of noise. The final voxel size after pre-processing was $4\times4\times4$ mm^3. The used interpolation kernel along the slice direction was bicubic. The in-plane blurring kernel was Gaussian function. By enforcing a minimum cluster size of 6 contiguous voxels, probability simulations based on *AlphaSim*, using 10^5 iterations indicate that the probability of random field of noise producing a cluster of size ≥ 6 is at $p<0.05$ after the noise was thresholded at pixel level with $p<0.001$.

Results

There were 37 out of a total of 112 clusters that fulfilled the cluster size criteria (Table 1). As summarized in Figure 3, a total of 20 out of the 37 clusters were identified as potential RFNs by careful inspection of the spatial patterns. The characteristics of these identified RFNs were summarized in Table 2. The remaining 17 clusters were classified as likely artifacts after studying their spatial distribution patterns. Small clusters with less than 50 voxels usually have single or too few voxels to be considered as meaningful RFNs.

As shown in Figs. 2 and 3, the first iteration hierarchical clustering produced 8 RFNs (Figs. 3B–I) including two frontal networks (Figs. 3D and F), dorsolateral frontal network (Fig. 3C), premotor network (Fig. 3G) and 3 RFNs involving the temporal cortex. Two of the RFNs detected in the temporal lobes were split into right- and left-sided clusters along the hemisphere middle line, as indicated with two different colors (Figs. 3E, L, and N). This iteration produced also a large cluster with 6828 voxels (Fig. 3J) for further clustering in the second round.

The second iteration of the hierarchical clustering on the large cluster (Fig. 3J) produced 6 commonly observed RFNs including the default mode network (DMN) (Figs. 3M and O), visual network (Fig. 3R), sensorimotor network (Fig. 3K), and 2 temporal networks (Figs. 3N and P). The sensory motor network (Fig. 3K) includes the motor, somatic sensory, parts of the auditory cortex and parietal region. The visual network (Fig. 3R) covers the primary and secondary visual cortices and posterior hippocampus. The second iteration results in more highly intra-connected clusters. As shown in Table 2, the mean of the averaged intra-cluster CC for the second iteration is 0.29 while it is 0.23 for the first iteration.

Analysis of the same dataset with ICA, 13 independent components out of 36 were identified as relevant RFNs based on t-score threshold and visual inspection of the t-maps and corresponding time courses, whereas the remaining 23 components were classified as artifacts due to contamination from CSF, motion, and large veins.

Among the extracted 20 potential RFN clusters by using the proposed hierarchical clustering scheme, there are 8 clusters having relatively good match with RFNs identified by ICA. The details are summarized in Figure 4 and Table 3. As shown, the 8 RFN clusters cover about 58% of the total grey matter volume. For these 8 clusters, on average, there is a 61% spatial overlap between the hierarchical clustering and ICA results.

Discussion

Choices of parameters for the hierarchical clustering framework

An analysis of the resulted clusters shows that many of them are small clusters with less than 50 voxels (Fig. 5) and are spatially too

Analyzing fMRI Data Using Hierarchical Clustering

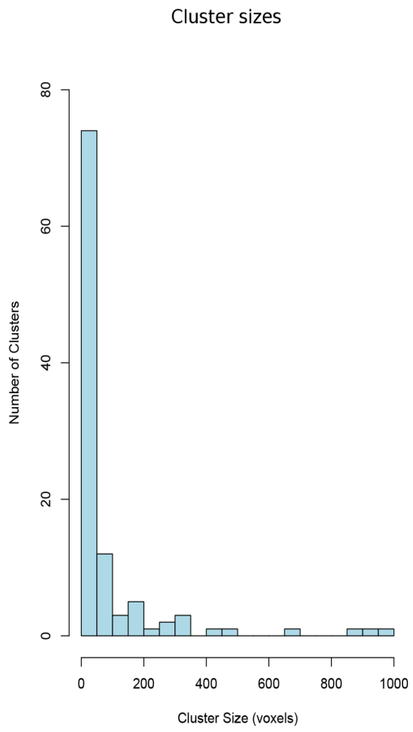

Figure 5. Histogram of cluster size. Cluster size from all clusters produced by applying the proposed framework to the acquired resting-state fMRI datasets. It is clear that many clusters have less than 50 voxels.
doi:10.1371/journal.pone.0076315.g005

Comparison between hierarchical clustering and ICA results

For quantitative comparison between the hierarchical clustering results and RFNs identified by ICA, each cluster that fulfilled the cluster size criteria ($50 \leq S \leq 5000$) was matched with a RFN identified using ICA based on its maximum overlap and the similarity of the spatial distribution. The cluster size, intersection area, and complementary non-overlapping areas were evaluated for each matched pair.

Assessment of statistical significance

Because the CC matrices were thresholded at 0.3, which corresponds to a t-score threshold of 2.88 ($df = 84$), the statistical significance at voxel-level is $p<0.001$ without correcting for multiple comparisons. For comparison the group ICA spatial t-maps were then binarized at voxel-level with the same voxel-level statistical significance.

The final statistical significance was evaluated by enforcing also a minimum voxel cluster size of 6 contiguous voxels. After specifying the original and final voxel sizes as well as the uncorrected threshold value the AFNI program, *AlphaSim*, was used to compute a list of probabilities corresponding to different cluster sizes produced by random field of noise. The final voxel size after pre-processing was $4\times4\times4$ mm^3. The used interpolation kernel along the slice direction was bicubic. The in-plane blurring kernel was Gaussian function. By enforcing a minimum cluster size of 6 contiguous voxels, probability simulations based on *AlphaSim*, using 10^5 iterations indicate that the probability of random field of noise producing a cluster of size ≥ 6 is at $p<0.05$ after the noise was thresholded at pixel level with $p<0.001$.

Results

There were 37 out of a total of 112 clusters that fulfilled the cluster size criteria (Table 1). As summarized in Figure 3, a total of 20 out of the 37 clusters were identified as potential RFNs by careful inspection of the spatial patterns. The characteristics of these identified RFNs were summarized in Table 2. The remaining 17 clusters were classified as likely artifacts after studying their spatial distribution patterns. Small clusters with less than 50 voxels usually have single or too few voxels to be considered as meaningful RFNs.

As shown in Figs. 2 and 3, the first iteration hierarchical clustering produced 8 RFNs (Figs. 3B–I) including two frontal networks (Figs. 3D and F), dorsolateral frontal network (Fig. 3C), premotor network (Fig. 3G) and 3 RFNs involving the temporal cortex. Two of the RFNs detected in the temporal lobes were split into right- and left-sided clusters along the hemisphere middle line, as indicated with two different colors (Figs. 3E, L, and N). This iteration produced also a large cluster with 6828 voxels (Fig. 3J) for further clustering in the second round.

The second iteration of the hierarchical clustering on the large cluster (Fig. 3J) produced 6 commonly observed RFNs including the default mode network (DMN) (Figs. 3M and O), visual network (Fig. 3R), sensorimotor network (Fig. 3K), and 2 temporal networks (Figs. 3N and P). The sensory motor network (Fig. 3K) includes the motor, somatic sensory, parts of the auditory cortex and parietal region. The visual network (Fig. 3R) covers the primary and secondary visual cortices and posterior hippocampus. The second iteration results in more highly intra-connected clusters. As shown in Table 2, the mean of the averaged intra-cluster CC for the second iteration is 0.29 while it is 0.23 for the first iteration.

Analysis of the same dataset with ICA, 13 independent components out of 36 were identified as relevant RFNs based on t-score threshold and visual inspection of the t-maps and corresponding time courses, whereas the remaining 23 components were classified as artifacts due to contamination from CSF, motion, and large veins.

Among the extracted 20 potential RFN clusters by using the proposed hierarchical clustering scheme, there are 8 clusters having relatively good match with RFNs identified by ICA. The details are summarized in Figure 4 and Table 3. As shown, the 8 RFN clusters cover about 58% of the total grey matter volume. For these 8 clusters, on average, there is a 61% spatial overlap between the hierarchical clustering and ICA results.

Discussion

Choices of parameters for the hierarchical clustering framework

An analysis of the resulted clusters shows that many of them are small clusters with less than 50 voxels (Fig. 5) and are spatially too

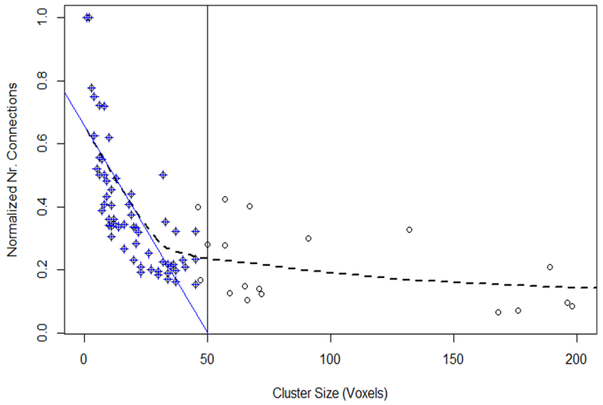

Figure 6. Intra-cluster connections of the clusters. Scatter plot of the normalized intra-cluster connections (the ratio between the number of connections with CC≥0.3 and the number of possible connections) as a function of the cluster size. Locally weighted scatterplot smoothing (LOESS) regression analysis (dashed curve) shows a distinct change in trends in the data. To emphasize this change, linear regression (shown in blue) was used to extrapolate the initial distinct trend of the LOESS curve. Linear regression occupied 63 of the smallest clusters (shown in blue crosses) and intersects the x-axis at 50.02. This observation was used to determine the minimum cluster size threshold.
doi:10.1371/journal.pone.0076315.g006

compact to portray RFNs. We investigated also the intra-cluster connectivity and measured the number of connections a voxel have with other voxels in a cluster. As shown in Fig. 6, for clusters with less than 50 voxels, the normalized number of connections decreases with the cluster size, while the larger clusters have the opposite trend. Therefore, we choose 50 as the lower limit for clusters to be considered as potential RFNs.

The whole-brain grey matter mask has 13312 voxels and analysis of the ICA results showed that clusters with more than 5000 voxels are too large to be considered as a single coherent RFN and should be refined further. Therefore, we choose 5000 as the ultimate upper limit for a cluster to be considered as an independent RFN. However, it should be pointed out that most of the extracted RFNs were much smaller (see Table 2). By lowering the upper limit, large clusters can be further analyzed with additional iterations to study the hierarchical structures within. This point is further demonstrated by Figure S2 and Appendix C in Supporting Information S1.

Cordes et al. used previously a CC threshold of 0.3 for voxel-based hierarchical clustering [7] and the same threshold was opted here for the individual dataset. Systematically changing the CC threshold showed that increasing the threshold above 0.3 resulted in the loss of robustness of the algorithm. A threshold of CC≥0.4 resulted in only about 0.1% of the values remained.

Regression removal of the global signal was deliberately omitted in the preprocessing of the data, as it is known to introduce substantial negative correlations into the data [12] and lead to controversial interpretation of the resulted RFNs [13]. Without

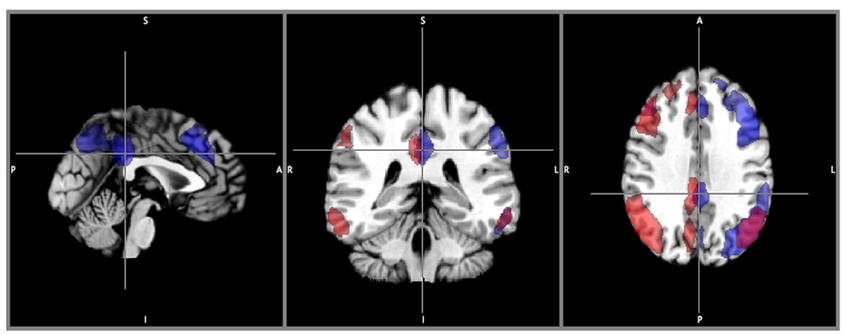

Figure 7. Unilateral networks from ICA analysis. Symmetrical one-sided networks found amongst ICA results. Both in their entirety cannot be obtained through hierarchical clustering due to the spatial overlap between them.
doi:10.1371/journal.pone.0076315.g007

Analyzing fMRI Data Using Hierarchical Clustering

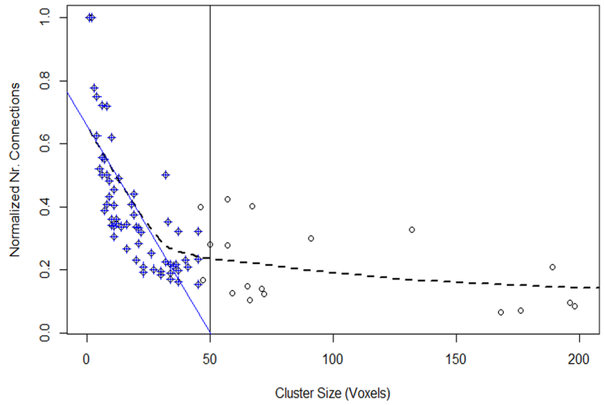

Figure 6. Intra-cluster connections of the clusters. Scatter plot of the normalized intra-cluster connections (the ratio between the number of connections with CC≥0.3 and the number of possible connections) as a function of the cluster size. Locally weighted scatterplot smoothing (LOESS) regression analysis (dashed curve) shows a distinct change in trends in the data. To emphasize this change, linear regression (shown in blue) was used to extrapolate the initial distinct trend of the LOESS curve. Linear regression occupied 63 of the smallest clusters (shown in blue crosses) and intersects the x-axis at 50.02. This observation was used to determine the minimum cluster size threshold.
doi:10.1371/journal.pone.0076315.g006

compact to portray RFNs. We investigated also the intra-cluster connectivity and measured the number of connections a voxel have with other voxels in a cluster. As shown in Fig. 6, for clusters with less than 50 voxels, the normalized number of connections decreases with the cluster size, while the larger clusters have the opposite trend. Therefore, we choose 50 as the lower limit for clusters to be considered as potential RFNs.

The whole-brain grey matter mask has 13312 voxels and analysis of the ICA results showed that clusters with more than 5000 voxels are too large to be considered as a single coherent RFN and should be refined further. Therefore, we choose 5000 as the ultimate upper limit for a cluster to be considered as an independent RFN. However, it should be pointed out that most of the extracted RFNs were much smaller (see Table 2). By lowering the upper limit, large clusters can be further analyzed with additional iterations to study the hierarchical structures within. This point is further demonstrated by Figure S2 and Appendix C in Supporting Information S1.

Cordes et al. used previously a CC threshold of 0.3 for voxel-based hierarchical clustering [7] and the same threshold was opted here for the individual dataset. Systematically changing the CC threshold showed that increasing the threshold above 0.3 resulted in the loss of robustness of the algorithm. A threshold of CC≥0.4 resulted in only about 0.1% of the values remained.

Regression removal of the global signal was deliberately omitted in the preprocessing of the data, as it is known to introduce substantial negative correlations into the data [12] and lead to controversial interpretation of the resulted RFNs [13]. Without

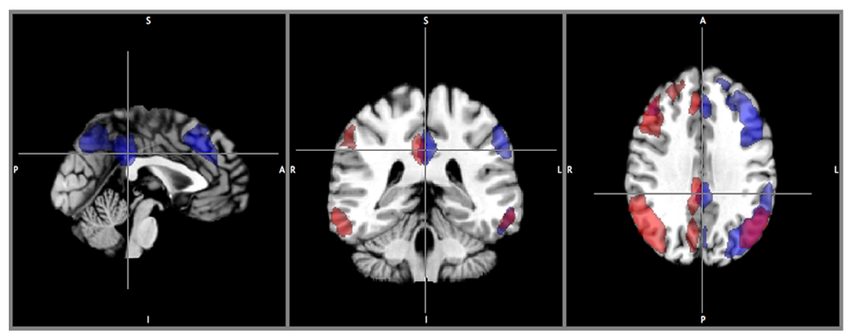

Figure 7. Unilateral networks from ICA analysis. Symmetrical one-sided networks found amongst ICA results. Both in their entirety cannot be obtained through hierarchical clustering due to the spatial overlap between them.
doi:10.1371/journal.pone.0076315.g007

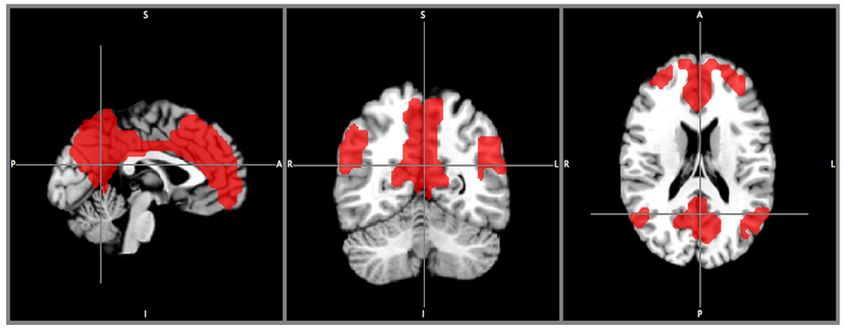

Figure 8. The default mode network. The default mode network in its entirety found at cut number k = 18 from the first iteration. This cluster was found through exhaustive search over all cut numbers.
doi:10.1371/journal.pone.0076315.g008

global signal removal, in the averaged CC matrix there are only 0.3% negative values with mean -0.03 ± 0.01. Hence, without the removal of the global signal the vast majority of the negative CC values are too small to be considered statistically significant.

Comparison between hierarchical clustering and ICA-based methods

The implemented hierarchical clustering is a deterministic algorithm and the final result is independent of the initial seed point. Its non-fuzziness implies that each voxel is exclusively assigned to a single cluster. Therefore, there is no spatial overlap among the clusters identified by the proposed framework. For example, the two unilateral frontal-parietal networks found with ICA [14] (Fig. 7) are not detectable in their entireties with the proposed hierarchical clustering method, because these two unilateral frontal-parietal networks have an overlapping component in the medial frontal cortex. With hierarchical clustering, detecting one will exclude the other from being detected in its entirety.

The computation involved in hierarchical clustering does not scale up well with the number of observations. Optimal agglomerative algorithms exist for single (SLINK [15]) and complete-linkage (CLINK [16]) scale at $O(n^2)$. Average-linkage algorithms such as the one used here scales cubically. Average-linkage tends to join clusters with small variances and is slightly biased toward producing clusters with the same variance because it considers all members in the cluster rather than just a single point. Hence, average-linkage tends to be less influenced by extreme values than other methods, despite of the fact that hierarchical clustering is overall very sensitive to outliers.

The used scheme may have not extracted all meaningful clusters from the data, because only a few numbers of cuts are applied to the dendrograms. For example, the DMN was not found in its entirety at the specified cut-levels discussed above. Through exhaustive searching, the whole DMN (Fig. 8) was found amongst clusters at the cut level from the dendrogram of the second iteration.

The DMN result illustrates once again that the hierarchical clustering approach has its inherent strength to reveal the hierarchy structure within a functional connectivity network. As shown in Fig. 3, the DMN in its entirety at cut level k = 18 (Fig. 8) was split into the frontal- (Fig. 3M) and parietal sub-networks (Fig. 3O) down in the dendrogram at cut level k = 32 from the large cluster. It is known that the DMN is composed of the prefrontal and parietal sub-units [17]. The medial prefrontal sub-network is responsible for executive functions and the parietal sub-network is responsible for sensory-related responses.

Conclusion

With the developed framework we successfully have extracted gray matter clusters with striking similarities to RFNs that are well documented in the literature using different analysis methods. The obtained results further confirm the notion that brain at resting-state is highly engaged in spontaneous synchronous activity within the various intrinsic functional networks. The present study demonstrates also that hierarchical clustering might be a very useful tool for analysis of whole-brain resting-state fMRI data at a voxel-level. This approach is model free and does not require any prior assumption about the number and location of the clusters. Furthermore, it can be used to reveal directly the hierarchical structures within the functional connectivity networks.

Supporting Information

Figure S1 Inconsistency coefficients of dendrogram. Plot of inconsistency coefficients of the full dendrogram. The nodes are sorted from lowest to highest distance in the dendrogram. The coefficients fluctuate sporadically and no general pattern can be detected for determining dendrogram cut level.
(TIF)

Figure S2 Sub-networks of visual system. Clustering results from an additional iteration with 8-cluster split of the visual network (Fig. 3R) extracted from the 2nd iteration. The results illustrate the potential for using the proposed framework to study the hierarchical structures within functional connectivity networks. As shown, the visual network was split into a sub-network containing the primary and secondary visual systems (A), the lingual gyrus (B) and inferior temporal gyrus (C). It should be possible to extract the full hierarchical structure tree of the visual system by further analysis of the larger sub-network (A).
(TIF)

Supporting Information S1 Appendices A, B, and C.
(DOC)

Analyzing fMRI Data Using Hierarchical Clustering

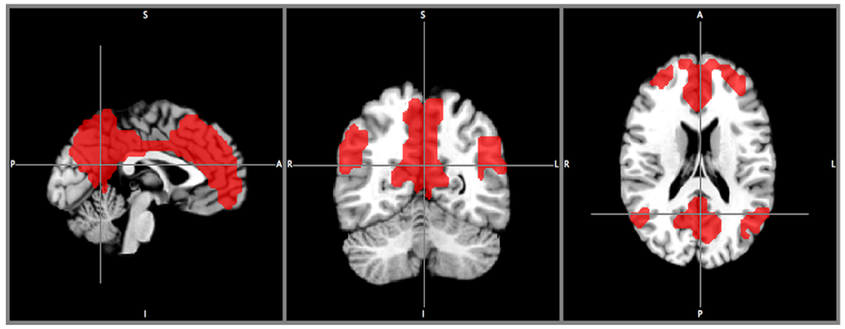

Figure 8. The default mode network. The default mode network in its entirety found at cut number k = 18 from the first iteration. This cluster was found through exhaustive search over all cut numbers.
doi:10.1371/journal.pone.0076315.g008

global signal removal, in the averaged CC matrix there are only 0.3% negative values with mean -0.03 ± 0.01. Hence, without the removal of the global signal the vast majority of the negative CC values are too small to be considered statistically significant.

Comparison between hierarchical clustering and ICA-based methods

The implemented hierarchical clustering is a deterministic algorithm and the final result is independent of the initial seed point. Its non-fuzziness implies that each voxel is exclusively assigned to a single cluster. Therefore, there is no spatial overlap among the clusters identified by the proposed framework. For example, the two unilateral frontal-parietal networks found with ICA [14] (Fig. 7) are not detectable in their entireties with the proposed hierarchical clustering method, because these two unilateral frontal-parietal networks have an overlapping component in the medial frontal cortex. With hierarchical clustering, detecting one will exclude the other from being detected in its entirety.

The computation involved in hierarchical clustering does not scale up well with the number of observations. Optimal agglomerative algorithms exist for single (SLINK [15]) and complete-linkage (CLINK [16]) scale at $O(n^2)$. Average-linkage algorithms such as the one used here scales cubically. Average-linkage tends to join clusters with small variances and is slightly biased toward producing clusters with the same variance because it considers all members in the cluster rather than just a single point. Hence, average-linkage tends to be less influenced by extreme values than other methods, despite of the fact that hierarchical clustering is overall very sensitive to outliers.

The used scheme may have not extracted all meaningful clusters from the data, because only a few numbers of cuts are applied to the dendrograms. For example, the DMN was not found in its entirety at the specified cut-levels discussed above. Through exhaustive searching, the whole DMN (Fig. 8) was found amongst clusters at the cut level from the dendrogram of the second iteration.

The DMN result illustrates once again that the hierarchical clustering approach has its inherent strength to reveal the hierarchy structure within a functional connectivity network. As shown in Fig. 3, the DMN in its entirety at cut level k = 18 (Fig. 8) was split into the frontal- (Fig. 3M) and parietal sub-networks (Fig. 3O) down in the dendrogram at cut level k = 32 from the large cluster. It is known that the DMN is composed of the prefrontal and parietal sub-units [17]. The medial prefrontal sub-network is responsible for executive functions and the parietal sub-network is responsible for sensory-related responses.

Conclusion

With the developed framework we successfully have extracted gray matter clusters with striking similarities to RFNs that are well documented in the literature using different analysis methods. The obtained results further confirm the notion that brain at resting-state is highly engaged in spontaneous synchronous activity within the various intrinsic functional networks. The present study demonstrates also that hierarchical clustering might be a very useful tool for analysis of whole-brain resting-state fMRI data at a voxel-level. This approach is model free and does not require any prior assumption about the number and location of the clusters. Furthermore, it can be used to reveal directly the hierarchical structures within the functional connectivity networks.

Supporting Information

Figure S1 Inconsistency coefficients of dendrogram. Plot of inconsistency coefficients of the full dendrogram. The nodes are sorted from lowest to highest distance in the dendrogram. The coefficients fluctuate sporadically and no general pattern can be detected for determining dendrogram cut level.
(TIF)

Figure S2 Sub-networks of visual system. Clustering results from an additional iteration with 8-cluster split of the visual network (Fig. 3R) extracted from the 2nd iteration. The results illustrate the potential for using the proposed framework to study the hierarchical structures within functional connectivity networks. As shown, the visual network was split into a sub-network containing the primary and secondary visual systems (A), the lingual gyrus (B) and inferior temporal gyrus (C). It should be possible to extract the full hierarchical structure tree of the visual system by further analysis of the larger sub-network (A).
(TIF)

Supporting Information S1 Appendices A, B, and C.
(DOC)

PLOS ONE | www.plosone.org 8 October 2013 | Volume 8 | Issue 10 | e76315

Acknowledgments

Stimulating discussion with Dr. P. Fransson has been very helpful.

Author Contributions

Conceived and designed the experiments: YL TQL. Performed the experiments: TQL. Analyzed the data: YW. Contributed reagents/materials/analysis tools: YW TQL. Wrote the paper: YW TQL.

References

1. Benjaminsson S, Fransson P, Lansner A (2010) A novel model-free data analysis technique based on clustering in a mutual information space: application to resting-state fmri. Frontiers in systems neuroscience 4.
2. Van Den Heuvel M, Mandl R, Pol HH (2008) Normalized cut group clustering of resting-state FMRI data. PLoS One 3: e2001.
3. Boly M, Perlbarg V, Marrelec G, Schabus M, Laureys S, et al. (2012) Hierarchical clustering of brain activity during human nonrapid eye movement sleep. Proceedings of the National Academy of Sciences 109: 5856–5861.
4. Gomez-Laberge C, Adler A, Cameron I, Nguyen T, Hogan M (2011) A Bayesian hierarchical correlation model for fMRI cluster analysis. Biomedical Engineering, IEEE Transactions on: 1-1.
5. Zhou C, Zemanov L, Zamora G, Hilgetag CC, Kurths J (2006) Hierarchical organization unveiled by functional connectivity in complex brain networks. Physical review letters 97: 238103.
6. Marrelec G, Bellec P, Krainik A, Duffau H, Pélégrini-Issac M, et al. (2008) Regions, systems, and the brain: hierarchical measures of functional integration in fMRI. Medical image analysis 12: 484–496.
7. Cordes D, Haughton V, Carew JD, Arfanakis K, Maravilla K (2002) Hierarchical clustering to measure connectivity in fMRI resting-state data. Magnetic resonance imaging 20: 305–317.
8. Salvador R, Suckling J, Coleman MR, Pickard JD, Menon D, et al. (2005) Neurophysiological architecture of functional magnetic resonance images of human brain. Cerebral Cortex 15: 1332.
9. Liu X, Zhu X-H, Qiu P, Chen W (2012) A correlation-matrix-based hierarchical clustering method for functional connectivity analysis. Journal of Neuroscience Methods 211(1): 94–102.
10. Narasimhan M, Jojic N, Bilmes JA (2005) Q-clustering. Available: http://melodi.ee.washington.edu/~bilmes/mypubs/narasimhan2005-q.pdf. Accessed 2013 Sep 30.
11. Johanna Ooberg TJ, Tie-Qiang Li (2011) Aging related changes in functional connectivity networks investigated by resting-state BOLD functional MRI: a study of independent component analysis and image preprocessing procedures. Stockholm.
12. Murphy K, Birn RM, Handwerker DA, Jones TB, Bandettini PA (2009) The impact of global signal regression on resting state correlations: are anti-correlated networks introduced? Neuroimage 44: 893–905.
13. Marrelec G, Fransson P (2011) Assessing the influence of different ROI selection strategies on functional connectivity analyses of fMRI data acquired during steady-state conditions. PLoS One 6: e14788.
14. Allen EA, Erhardt EB, Damaraju E, Gruner W, Segall JM, et al. (2011) A Baseline for the Multivariate Comparison of Resting-State Networks. Frontiers in systems neuroscience 5.
15. Sibson R (1973) SLINK: an optimally efficient algorithm for the single-link cluster method. The Computer Journal 16: 30–34.
16. Defays D (1977) An efficient algorithm for a complete link method. The Computer Journal 20: 364–366.
17. Pamilo S, Malinen S, Hlushchuk Y, Seppä M, Tikka P, et al. (2012) Functional Subdivision of Group-ICA Results of fMRI Data Collected during Cinema Viewing. PloS one 7: e42000.

Analyzing fMRI Data Using Hierarchical Clustering

Acknowledgments

Stimulating discussion with Dr. P. Fransson has been very helpful.

Author Contributions

Conceived and designed the experiments: YL TQL. Performed the experiments: TQL. Analyzed the data: YW. Contributed reagents/materials/analysis tools: YW TQL. Wrote the paper: YW TQL.

References

1. Benjaminsson S, Fransson P, Lansner A (2010) A novel model-free data analysis technique based on clustering in a mutual information space: application to resting-state fmri. Frontiers in systems neuroscience 4.
2. Van Den Heuvel M, Mandl R, Pol HH (2008) Normalized cut group clustering of resting-state FMRI data. PLoS One 3: e2001.
3. Boly M, Perlbarg V, Marrelec G, Schabus M, Laureys S, et al. (2012) Hierarchical clustering of brain activity during human nonrapid eye movement sleep. Proceedings of the National Academy of Sciences 109: 5856–5861.
4. Gomez-Laberge C, Adler A, Cameron I, Nguyen T, Hogan M (2011) A Bayesian hierarchical correlation model for fMRI cluster analysis. Biomedical Engineering, IEEE Transactions on: 1-1.
5. Zhou C, Zemanov L, Zamora G, Hilgetag CC, Kurths J (2006) Hierarchical organization unveiled by functional connectivity in complex brain networks. Physical review letters 97: 238103.
6. Marrelec G, Bellec P, Krainik A, Duffau H, Pélégrini-Issac M, et al. (2008) Regions, systems, and the brain: hierarchical measures of functional integration in fMRI. Medical image analysis 12: 484–496.
7. Cordes D, Haughton V, Carew JD, Arfanakis K, Maravilla K (2002) Hierarchical clustering to measure connectivity in fMRI resting-state data. Magnetic resonance imaging 20: 305–317.
8. Salvador R, Suckling J, Coleman MR, Pickard JD, Menon D, et al. (2005) Neurophysiological architecture of functional magnetic resonance images of human brain. Cerebral Cortex 15: 1332.
9. Liu X, Zhu X-H, Qiu P, Chen W (2012) A correlation-matrix-based hierarchical clustering method for functional connectivity analysis. Journal of Neuroscience Methods 211(1): 94–102.
10. Narasimhan M, Jojic N, Bilmes JA (2005) Q-clustering. Available: http://melodi.ee.washington.edu/~bilmes/mypubs/narasimhan2005-q.pdf. Accessed 2013 Sep 30.
11. Johanna Ooberg TJ, Tie-Qiang Li (2011) Aging related changes in functional connectivity networks investigated by resting-state BOLD functional MRI: a study of independent component analysis and image preprocessing procedures. Stockholm.
12. Murphy K, Birn RM, Handwerker DA, Jones TB, Bandettini PA (2009) The impact of global signal regression on resting state correlations: are anti-correlated networks introduced? Neuroimage 44: 893–905.
13. Marrelec G, Fransson P (2011) Assessing the influence of different ROI selection strategies on functional connectivity analyses of fMRI data acquired during steady-state conditions. PLoS One 6: e14788.
14. Allen EA, Erhardt EB, Damaraju E, Gruner W, Segall JM, et al. (2011) A Baseline for the Multivariate Comparison of Resting-State Networks. Frontiers in systems neuroscience 5.
15. Sibson R (1973) SLINK: an optimally efficient algorithm for the single-link cluster method. The Computer Journal 16: 30–34.
16. Defays D (1977) An efficient algorithm for a complete link method. The Computer Journal 20: 364–366.
17. Pamilo S, Malinen S, Hlushchuk Y, Seppä M, Tikka P, et al. (2012) Functional Subdivision of Group-ICA Results of fMRI Data Collected during Cinema Viewing. PloS one 7: e42000.

PLOS ONE | www.plosone.org 9 October 2013 | Volume 8 | Issue 10 | e76315

II

II

frontiers in Human Neuroscience

ORIGINAL RESEARCH
published: 08 May 2015
doi: 10.3389/fnhum.2015.00259

Dimensionality of ICA in resting-state fMRI investigated by feature optimized classification of independent components with SVM

Yanlu Wang[1]* *and Tie-Qiang Li*[1,2]

[1] *Department of Clinical Science, Intervention and Technology, Karolinska Institute, Stockholm, Sweden,* [2] *Unit of Medical Imaging, Function, and Technology, Department of Medical Physics, Karolinska University Hospital, Huddinge, Sweden*

Different machine learning algorithms have recently been used for assisting automated classification of independent component analysis (ICA) results from resting-state fMRI data. The success of this approach relies on identification of artifact components and meaningful functional networks. A limiting factor of ICA is the uncertainty of the number of independent components (NIC). We aim to develop a framework based on support vector machines (SVM) and optimized feature-selection for automated classification of independent components (ICs) and use the framework to investigate the effects of input NIC on the ICA results. Seven different resting-state fMRI datasets were studied. 18 features were devised by mimicking the empirical criteria for manual evaluation. The five most significant ($p < 0.01$) features were identified by general linear modeling and used to generate a classification model for the framework. This feature-optimized classification of ICs with SVM (FOCIS) framework was used to classify both group and single subject ICA results. The classification results obtained using FOCIS and previously published FSL-FIX were compared against manually evaluated results. On average the false negative rate in identifying artifact contaminated ICs for FOCIS and FSL-FIX were 98.27 and 92.34%, respectively. The number of artifact and functional network components increased almost linearly with the input NIC. Through tracking, we demonstrate that incrementing NIC affects most ICs when NIC < 33, whereas only a few limited ICs are affected by direct splitting when NIC is incremented beyond NIC > 40. For a given IC, its changes with increasing NIC are individually specific irrespective whether the component is a potential resting-state functional network or an artifact component. Using FOCIS, we investigated experimentally the ICA dimensionality of resting-state fMRI datasets and found that the input NIC can critically affect the ICA results of resting-state fMRI data.

Keywords: magnetic resonance imaging, functional neuroimaging, independent component analysis, pattern classification, machine learning, signal processing, image processing

OPEN ACCESS

Edited by:
Daniel S. Margulies, Max Planck Institute for Human Cognitive and Brain Sciences, Germany

Reviewed by:
Danilo Bzdok, Research Center Jülich, Germany
R. Matthew Hutchison, Harvard University, USA

***Correspondence:**
Yanlu Wang, Karolinska Institutet, Institutionen for Klinisk Vetenskap, Intervention Och Teknik (CLINTEC), H9, Enheten for Medicinsk Bild., Funktion Och Teknologi, Karolinska Universitetssjukhuset, C1:46 SE-141 86 Stockholm, Sweden
yanlu.wang@ki.se

Received: *31 January 2015*
Accepted: *21 April 2015*
Published: *08 May 2015*

Citation:
Wang Y and Li T-Q (2015) Dimensionality of ICA in resting-state fMRI investigated by feature optimized classification of independent components with SVM. Front. Hum. Neurosci. 9:259. doi: 10.3389/fnhum.2015.00259

Introduction

Independent component analysis (ICA) is a data-driven, unsupervised analysis method for extracting resting-state functional connectivity networks (RFNs) (Calhoun et al., 2001; Beckmann et al., 2005; Kiviniemi et al., 2009; Schopf et al., 2010). Although ICA has been widely used for

frontiers in Human Neuroscience

ORIGINAL RESEARCH
published: 08 May 2015
doi: 10.3389/fnhum.2015.00259

Dimensionality of ICA in resting-state fMRI investigated by feature optimized classification of independent components with SVM

Yanlu Wang[1]* *and Tie-Qiang Li*[1,2]

[1] *Department of Clinical Science, Intervention and Technology, Karolinska Institute, Stockholm, Sweden,* [2] *Unit of Medical Imaging, Function, and Technology, Department of Medical Physics, Karolinska University Hospital, Huddinge, Sweden*

Different machine learning algorithms have recently been used for assisting automated classification of independent component analysis (ICA) results from resting-state fMRI data. The success of this approach relies on identification of artifact components and meaningful functional networks. A limiting factor of ICA is the uncertainty of the number of independent components (NIC). We aim to develop a framework based on support vector machines (SVM) and optimized feature-selection for automated classification of independent components (ICs) and use the framework to investigate the effects of input NIC on the ICA results. Seven different resting-state fMRI datasets were studied. 18 features were devised by mimicking the empirical criteria for manual evaluation. The five most significant ($p < 0.01$) features were identified by general linear modeling and used to generate a classification model for the framework. This feature-optimized classification of ICs with SVM (FOCIS) framework was used to classify both group and single subject ICA results. The classification results obtained using FOCIS and previously published FSL-FIX were compared against manually evaluated results. On average the false negative rate in identifying artifact contaminated ICs for FOCIS and FSL-FIX were 98.27 and 92.34%, respectively. The number of artifact and functional network components increased almost linearly with the input NIC. Through tracking, we demonstrate that incrementing NIC affects most ICs when NIC < 33, whereas only a few limited ICs are affected by direct splitting when NIC is incremented beyond NIC > 40. For a given IC, its changes with increasing NIC are individually specific irrespective whether the component is a potential resting-state functional network or an artifact component. Using FOCIS, we investigated experimentally the ICA dimensionality of resting-state fMRI datasets and found that the input NIC can critically affect the ICA results of resting-state fMRI data.

Keywords: magnetic resonance imaging, functional neuroimaging, independent component analysis, pattern classification, machine learning, signal processing, image processing

OPEN ACCESS

Edited by:
Daniel S. Margulies, Max Planck Institute for Human Cognitive and Brain Sciences, Germany

Reviewed by:
Danilo Bzdok, Research Center Jülich, Germany
R. Matthew Hutchison, Harvard University, USA

***Correspondence:**
Yanlu Wang, Karolinska Institutet, Institutionen for Klinisk Vetenskap, Intervention Och Teknik (CLINTEC), H9, Enheten for Medicinsk Bild., Funktion Och Teknologi, Karolinska Universitetssjukhuset, C1:46 SE-141 86 Stockholm, Sweden
yanlu.wang@ki.se

Received: *31 January 2015*
Accepted: *21 April 2015*
Published: *08 May 2015*

Citation:
Wang Y and Li T-Q (2015) Dimensionality of ICA in resting-state fMRI investigated by feature optimized classification of independent components with SVM. Front. Hum. Neurosci. 9:259. doi: 10.3389/fnhum.2015.00259

Introduction

Independent component analysis (ICA) is a data-driven, unsupervised analysis method for extracting resting-state functional connectivity networks (RFNs) (Calhoun et al., 2001; Beckmann et al., 2005; Kiviniemi et al., 2009; Schopf et al., 2010). Although ICA has been widely used for

Frontiers in Human Neuroscience | www.frontiersin.org 1 May 2015 | Volume 9 | Article 259

TABLE 1 | Summary of previous studies on automated classification of ICA results.

Reference	Algorithm	Features	Applicability	Performance
Perlbarg et al., 2007	Stepwise regression	Physiological noise, movement parameters	Individual	Mean sensitivity 0.87
Sui et al., 2009	Adaptive threshold	Spatial features, templates	Group, task-based fMRI	Mean accuracy 0.91
Douglas et al., 2011	Random Forest, AdaBoost, Naïve Bayes, J48 Decision Trere, K*, SVM	Unknown	Individual, task-based fMRI	Accuracy rates 0.92, 0.91, 0.89, 0.87, 0.86, 0.84 respectively
Kundu et al., 2012	Multiple regression	TE-dependency, R2*	Group and Individual, Multi-Echo EPI	Effective at detecting motion and pulsation artifacts. Denoised datasets show higher *t*-values in their connectivity maps.
Bhaganagarapu et al., 2013	k-means clustering	4 features, spatial and temporal	Group and Individual	Accuracy 0.997; Sochat et al., 2014 reports **(Individual)** Sensitivity 0.52, Specificity 0.89, **(group)** Sensitivity 0.42, Specificity 0.91,
Xu et al., 2014	Decision Tree	4 features, Spatial	task-based and resting-state fMRI with PET	Sensitivity 0.991, Specificity 1
Salimi-Khorshidi et al., 2014	SVM	>180 features	Individual	Accuracy 0.98 (multi-band EPI), 0.95 (standard EPI)
Sochat et al., 2014	Logistic Regression	246 features, spatial and temporal	Group and Individual	**(Individual)** Sensitivity 0.91, Specificity 0.91, **(Group)** Sensitivity 0.91, Specificity 0.81
Current study	SVM	5 features, spatial and temporal	Group and Individual	**(Individual)** Accuracy 0.91; **(Group)** Accuracy 0.99

the analysis of resting-state fMRI data, there are still three inter-related issues that needs to be addressed: (1) The lack of gold standard or generally accepted RFN template; (2) the influence of the input number of independent components (NIC) or dimensionality on the ICA results; (3) the removal of artifact contaminated components. Manual classification of meaningful RFNs from the ICA results is currently a tedious but necessary step when conducting ICA of resting-state fMRI data, because only some of the independent components (ICs) represent meaningful RFNs associated with spontaneous neuronal activities, while other ICs reflect the effects of artifact contamination due to head motion, other physiological activities, and instrument imperfection. The manual evaluation of ICA results usually rely on visual inspection of the spatial patterns and their corresponding time courses of the of ICs (Bartels and Zeki, 2005). As summarized recently by Allen et al. (2011), the empirical criteria to select RFNs from ICs are based on the expectations that RFNs should exhibit peak activations in gray matter, low spatial overlap with known vascular, ventricular, motion, and susceptibility artifacts, and dominated by low frequency fluctuations below 0.08 Hz (Cordes et al., 2000). This way of manually selecting a subset of ICs as RFNs is not only biased, but also cumbersome, particularly when NIC is relatively large.

As summarized in **Table 1**, earlier studies aimed to develop automated classification of ICA results relied on relatively simple metrics from the time courses and spatial template matching. Perlbarg et al. (2007) used a step-wise regression approach and features based on the spatial and temporal patterns of the physiological noise to group ICs into noise and signal. Calhoun et al. (2005) utilized a brain atlas to sort ICs, which requires strong a priori knowledge on the spatial patterns of the activation. Sui et al. (2009) employed spatial criterion to automatically classify ICs. Their method relied on generating accurate cerebrospinal fluid (CSF) and gray matter masks. Kundu et al. (2012) conducted classification using the TE dependence of ICs, which seemed to be robust but requires the acquisition of multi-echo fMRI data.

Abbreviations: ICA, Independent Component Analysis; NIC, Number of Independent Components; SVM, Support Vector Machines; IC, Independent Component; FOCIS, Feature Optimized Classification of Independent components with SVM; (fsl) FIX, FMRIB's ICA-based X-noiseifier; RFN, Resting-state Functional Networks; CSF, Cerebral Spinal Fluid; MDL, Minimum Description Length; PPCA, Probabilistic Principle Component Analysis; AIC, Akaike Infomormation Criteria; FWHM, Full Width at Half Maximum; DMN, Default-Mode Network; Class RFN, Classification class of Potential Resting-state Functional Networks; Class ART, Classification class of artefacts and otherwise components of non-interest; RBF, Radial Basis Function (kernel); N_{RFN}, Number of members of class RFN; N_{ART}, Number of members of class ART; CISOTA, Change Index of Spatial Overlap and Temporal Association.

Wang and Li Feature optimized classification rs-fMRI ICA

TABLE 1 | Summary of previous studies on automated classification of ICA results.

Reference | Algorithm | Features | Applicability | Performance
Perlbarg et al., 2007 | Stepwise regression | Physiological noise, movement parameters | Individual | Mean sensitivity 0.87
Sui et al., 2009 | Adaptive threshold | Spatial features, templates | Group, task-based fMRI | Mean accuracy 0.91
Douglas et al., 2011 | Random Forest, AdaBoost, Naïve Bayes, J48 Decision Trere, K*, SVM | Unknown | Individual, task-based fMRI | Accuracy rates 0.92, 0.91, 0.89, 0.87, 0.86, 0.84 respectively
Kundu et al., 2012 | Multiple regression | TE-dependency, R2* | Group and Individual, Multi-Echo EPI | Effective at detecting motion and pulsation artifacts. Denoised datasets show higher t-values in their connectivity maps.
Bhaganagarapu et al., 2013 | k-means clustering | 4 features, spatial and temporal | Group and Individual | Accuracy 0.997; Sochat et al., 2014 reports (Individual) Sensitivity 0.52, Specificity 0.89, (group) Sensitivity 0.42, Specificity 0.91,
Xu et al., 2014 | Decision Tree | 4 features, Spatial | task-based and resting-state fMRI with PET | Sensitivity 0.991, Specificity 1
Salimi-Khorshidi et al., 2014 | SVM | >180 features | Individual | Accuracy 0.98 (multi-band EPI), 0.95 (standard EPI)
Sochat et al., 2014 | Logistic Regression | 246 features, spatial and temporal | Group and Individual | (Individual) Sensitivity 0.91, Specificity 0.91, (Group) Sensitivity 0.91, Specificity 0.81
Current study | SVM | 5 features, spatial and temporal | Group and Individual | (Individual) Accuracy 0.91; (Group) Accuracy 0.99

the analysis of resting-state fMRI data, there are still three inter-related issues that needs to be addressed: (1) The lack of gold standard or generally accepted RFN template; (2) the influence of the input number of independent components (NIC) or dimensionality on the ICA results; (3) the removal of artifact contaminated components. Manual classification of meaningful RFNs from the ICA results is currently a tedious but necessary step when conducting ICA of resting-state fMRI data, because only some of the independent components (ICs) represent meaningful RFNs associated with spontaneous neuronal activities, while other ICs reflect the effects of artifact contamination due to head motion, other physiological activities, and instrument imperfection. The manual evaluation of ICA results usually rely on visual inspection of the spatial patterns and their corresponding time courses of the of ICs (Bartels and Zeki, 2005). As summarized recently by Allen et al. (2011), the empirical criteria to select RFNs from ICs are based on the expectations that RFNs should exhibit peak activations in gray matter, low spatial overlap with known vascular, ventricular, motion, and susceptibility artifacts, and dominated by low frequency fluctuations below 0.08 Hz (Cordes et al., 2000). This way of manually selecting a subset of ICs as RFNs is not only biased, but also cumbersome, particularly when NIC is relatively large.

As summarized in Table 1, earlier studies aimed to develop automated classification of ICA results relied on relatively simple metrics from the time courses and spatial template matching. Perlbarg et al. (2007) used a step-wise regression approach and features based on the spatial and temporal patterns of the physiological noise to group ICs into noise and signal. Calhoun et al. (2005) utilized a brain atlas to sort ICs, which requires strong a priori knowledge on the spatial patterns of the activation. Sui et al. (2009) employed spatial criterion to automatically classify ICs. Their method relied on generating accurate cerebrospinal fluid (CSF) and gray matter masks. Kundu et al. (2012) conducted classification using the TE dependence of ICs, which seemed to be robust but requires the acquisition of multi-echo fMRI data.

Abbreviations: ICA, Independent Component Analysis; NIC, Number of Independent Components; SVM, Support Vector Machines; IC, Independent Component; FOCIS, Feature Optimized Classification of Independent components with SVM; (fsl) FIX, FMRIB's ICA-based X-noiseifier; RFN, Resting-state Functional Networks; CSF, Cerebral Spinal Fluid; MDL, Minimum Description Length; PPCA, Probabilistic Principle Component Analysis; AIC, Akaike Infomormation Criteria; FWHM, Full Width at Half Maximum; DMN, Default-Mode Network; Class RFN, Classification class of Potential Resting-state Functional Networks; Class ART, Classification class of artefacts and otherwise components of non-interest; RBF, Radial Basis Function (kernel); N_{RFN}, Number of members of class RFN; N_{ART}, Number of members of class ART; CISOTA, Change Index of Spatial Overlap and Temporal Association.

Frontiers in Human Neuroscience | www.frontiersin.org 2 May 2015 | Volume 9 | Article 259

TABLE 2 | Acquisition parameters for seven the resting-state fMRI datasets and subject demographic information.

Dataset	Source	Male/Female	Age	Time-frames	Slice thickness	Slices	TR	FOV	Matrix size
0	Our own	40/46	21–84	300	3.6	32	2	220	64 × 64
1	TRT[1]	15/11	13–29	197	3	34	2	192	64 × 64
2	1636[2]	13/15	23–44	195	4	34	2.3	192	64 × 64
3	1624[2]	16/21	20–42	195	4	47	2.3	192	64 × 64
4	1600[2]	8/15	20–40	123	3	39	2.5	256	96 × 96
5	2085[2]	10/15	22–49	197	3	36	2	192	64 × 64
6	1616[2]	12/12	20–71	115	4	32	2	220	64 × 64

[1] http://www.nitrc.org/projects/nyu_trt/
[2] https://www.nitrc.org/frs/downloadlink.php/<Datasource> (where <Datasource> is the number in the Source column where the footnote is referenced).

TABLE 3 | Results of explanatory power test for the five most significant ($p < 0.01$) features.

Coefficients	*t*-value	*p*-value
Positive *t*-value with gray-matter overlap	6.23	9.97e-07
Peak voxel location in gray matter	5.79	3.23e-06
Frequency ratio of IC time course	5.14	1.90e-05
1-lag autocorrelation of IC time course	3.60	0.12e-03
Cluster bounding box to voxel count ratio	3.38	0.21e-03

In a number of more recent studies (see **Table 1**), automatic techniques based on more sophisticated machine learning algorithms has been applied to assist in grouping ICs into artifacts and potential RFNs. Douglas et al. (2011) compared the classification performances of six different machine learning algorithms ranging from K-star to support vector machine (SVM) using time course features. Xu et al. (2014) attempted to address the mechanistic motive and generalizability of automated classification of ICA results by incorporating information from head mask, auxiliary physiological recordings and PET activation results. The FIX plug-in (Griffanti et al., 2014; Salimi-Khorshidi et al., 2014) for FSL package achieved high accuracy classification of single-subject ICA results by employing ensemble learning based on multi-level classifiers and a large number of features. Sochat et al. (2014) used even a more comprehensive pool of temporal and spatial features (up to 246) to perform automated classification of ICs but attained lower accuracy than FSL-FIX. On the other hand, Bhaganagarapu et al. (2013) accomplished robust classification of ICA results for both group and single-subject data using a method based on k-means clustering of four features associated with the smoothness, edge activity, and temporal frequencies of the ICs. Overall, the progress in improving the accuracy of the automated classification of ICs has been quite promising. It becomes feasible to test automated classification for systematic studies involving a large of ICs.

ICA results for resting-state fMRI are sensitive to the specified NIC or the dimensionality. Neither the true numbers of RFNs in the data nor the degree of artifact contamination is known *a priori* for a given resting-state fMRI dataset. The effects of input NIC on ICA results can be systematically studied by evaluating the number of RFNs as a function of the input number of components in combination with tracking the changes in the specific ICs (Abou Elseoud et al., 2010, 2011; Elseoud et al., 2011). Different methods, such as, AIC, Minimum description length (MDL), and probabilistic principle component analysis (PPCA) have been proposed to model the noise characteristics and estimate intrinsic dimensionality of resting state fMRI data (Cordes and Nandy, 2006). However, uncorrelated noise models like Akaike information criterion (AIC), MDL, and PPCA tend to over-estimate the dimensionality for fMRI data (Li et al., 2007; Xie et al., 2009). In practice, the numbers of ICs used in different studies vary widely, which makes it difficult to directly compare the RFN results from the different studies.

The purpose of this study is two-fold: (1) Develop a robust tracking and binary sorting framework based on feature optimized classification of ICs with SVM (FOCIS) techniques to reduce some of the limitations overviewed above; (2) Use the developed method to investigate how the extracted RFNs are influenced by the selection of NIC. As discussed above, optimal feature selection is not only important for improving computation efficiency, but also very critical for improving classification accuracy and general applicability through reducing model complexity which makes it less likely to over-fit. We carefully selected relatively few features based on their explanation power ($p < 0.01$) to maximize the AIC to avoid over-determination. This was done to maximize the general applicability of FOCIS in cross-dataset classification. The focus of our study was the classification of group ICA results. The manual and automated classifications of the group ICA results were carried out after t-score and cluster size filtering were conducted to the one-sampled t-score map to ensure a statistical significance $p > 0.01$.

We tested the FOCIS framework on a dataset acquired by us and 6 other datasets acquired at different sites, which are openly accessible. The study included also a formal performance evaluation through direct comparison with the published FSL-FIX package. Another important aspect of our study is to use the developed framework to investigate systematically how the selection of NIC affects the ICA results. Our results indicate that the ICA dimensionality is far from a resolved issue. Therefore, we also implemented a module in the FOCIS framework to facilitate automatic tracking of a given IC component as a function of NIC. This enabled us to study how a given IC component changes with increasing NIC.

Wang and Li Feature optimized classification rs-fMRI ICA

TABLE 2 | Acquisition parameters for seven the resting-state fMRI datasets and subject demographic information.

Dataset	Source	Male/Female	Age	Time-frames	Slice thickness	Slices	TR	FOV	Matrix size
0	Our own	40/46	21–84	300	3.6	32	2	220	64 × 64
1	TRT[1]	15/11	13–29	197	3	34	2	192	64 × 64
2	1636[2]	13/15	23–44	195	4	34	2.3	192	64 × 64
3	1624[2]	16/21	20–42	195	4	47	2.3	192	64 × 64
4	1600[2]	8/15	20–40	123	3	39	2.5	256	96 × 96
5	2085[2]	10/15	22–49	197	3	36	2	192	64 × 64
6	1616[2]	12/12	20–71	115	4	32	2	220	64 × 64

[1] http://www.nitrc.org/projects/nyu_trt/
[2] https://www.nitrc.org/frs/downloadlink.php/<Datasource> (where <Datasource> is the number in the Source column where the footnote is referenced).

TABLE 3 | Results of explanatory power test for the five most significant ($p < 0.01$) features.

Coefficients	*t*-value	*p*-value
Positive *t*-value with gray-matter overlap	6.23	9.97e-07
Peak voxel location in gray matter	5.79	3.23e-06
Frequency ratio of IC time course	5.14	1.90e-05
1-lag autocorrelation of IC time course	3.60	0.12e-03
Cluster bounding box to voxel count ratio	3.38	0.21e-03

In a number of more recent studies (see Table 1), automatic techniques based on more sophisticated machine learning algorithms has been applied to assist in grouping ICs into artifacts and potential RFNs. Douglas et al. (2011) compared the classification performances of six different machine learning algorithms ranging from K-star to support vector machine (SVM) using time course features. Xu et al. (2014) attempted to address the mechanistic motive and generalizability of automated classification of ICA results by incorporating information from head mask, auxiliary physiological recordings and PET activation results. The FIX plug-in (Griffanti et al., 2014; Salimi-Khorshidi et al., 2014) for FSL package achieved high accuracy classification of single-subject ICA results by employing ensemble learning based on multi-level classifiers and a large number of features. Sochat et al. (2014) used even a more comprehensive pool of temporal and spatial features (up to 246) to perform automated classification of ICs but attained lower accuracy than FSL-FIX. On the other hand, Bhaganagarapu et al. (2013) accomplished robust classification of ICA results for both group and single-subject data using a method based on k-means clustering of four features associated with the smoothness, edge activity, and temporal frequencies of the ICs. Overall, the progress in improving the accuracy of the automated classification of ICs has been quite promising. It becomes feasible to test automated classification for systematic studies involving a large of ICs.

ICA results for resting-state fMRI are sensitive to the specified NIC or the dimensionality. Neither the true numbers of RFNs in the data nor the degree of artifact contamination is known *a priori* for a given resting-state fMRI dataset. The effects of input NIC on ICA results can be systematically studied by evaluating the number of RFNs as a function of the input number of components in combination with tracking the changes in the specific ICs (Abou Elseoud et al., 2010, 2011; Elseoud et al., 2011). Different methods, such as, AIC, Minimum description length (MDL), and probabilistic principle component analysis (PPCA) have been proposed to model the noise characteristics and estimate intrinsic dimensionality of resting state fMRI data (Cordes and Nandy, 2006). However, uncorrelated noise models like Akaike information criterion (AIC), MDL, and PPCA tend to over-estimate the dimensionality for fMRI data (Li et al., 2007; Xie et al., 2009). In practice, the numbers of ICs used in different studies vary widely, which makes it difficult to directly compare the RFN results from the different studies.

The purpose of this study is two-fold: (1) Develop a robust tracking and binary sorting framework based on feature optimized classification of ICs with SVM (FOCIS) techniques to reduce some of the limitations overviewed above; (2) Use the developed method to investigate how the extracted RFNs are influenced by the selection of NIC. As discussed above, optimal feature selection is not only important for improving computation efficiency, but also very critical for improving classification accuracy and general applicability through reducing model complexity which makes it less likely to over-fit. We carefully selected relatively few features based on their explanation power ($p < 0.01$) to maximize the AIC to avoid over-determination. This was done to maximize the general applicability of FOCIS in cross-dataset classification. The focus of our study was the classification of group ICA results. The manual and automated classifications of the group ICA results were carried out after t-score and cluster size filtering were conducted to the one-sampled t-score map to ensure a statistical significance $p > 0.01$.

We tested the FOCIS framework on a dataset acquired by us and 6 other datasets acquired at different sites, which are openly accessible. The study included also a formal performance evaluation through direct comparison with the published FSL-FIX package. Another important aspect of our study is to use the developed framework to investigate systematically how the selection of NIC affects the ICA results. Our results indicate that the ICA dimensionality is far from a resolved issue. Therefore, we also implemented a module in the FOCIS framework to facilitate automatic tracking of a given IC component as a function of NIC. This enabled us to study how a given IC component changes with increasing NIC.

Frontiers in Human Neuroscience | www.frontiersin.org 3 May 2015 | Volume 9 | Article 259

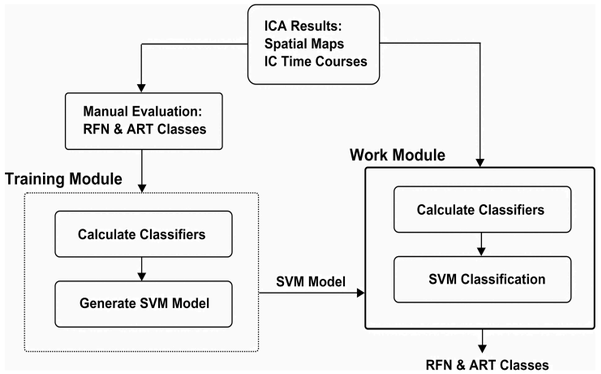

FIGURE 1 | Pipeline schematic of FOCIS framework.

Materials and Methods

Ethics Statement

The Central Ethical Review Board in Stockholm Province, Sweden approved the ethical permission application for this study. The study permission included the consent form used to provide information and obtain consent. All participants provided informed consent by voluntary signature.

Resting-State fMRI Data

Seven resting-state fMRI datasets from normal volunteers were used for the development and validation of the framework. We acquired one dataset ourselves by using a 3T whole-body clinical MRI scanner (TIM Trio, Siemens Healthcare, Erlangen, Germany) with a 2D gradient-recalled echo echo-planar imaging technique. The other 6 datasets were downloaded from an open-access database (https://www.nitrc.org/frs/?group_id=296). More details of the data acquisition parameters and the demographics of the participants are summarized in **Table 2**.

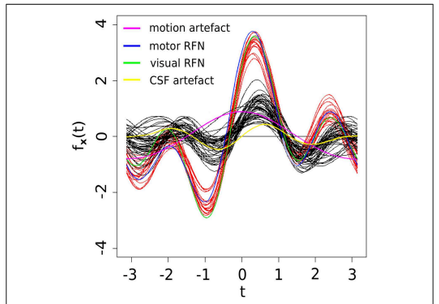

FIGURE 2 | Visually inspected ICs in feature space visualized using Andrew's curves. Selected feature space consists of only the significant ($p < 0.01$) features. Red curves represent class RFN and black curves represent class ART.

Preprocessing

The resting-state fMRI datasets underwent the same preprocessing procedure, which were performed with AFNI (http://afni.nimh.nih.gov/afni) and FSL (http://www.fmrib.ox.ac.uk/fsl) programs with a bash wrapper shell (Wang and Li, 2013). The first 10 timeframes in each data set were removed to ensure signal steady state. After temporal de-spiking, six-parameter rigid body image registration was performed for motion correction. The average volume for each motion-corrected time series was used to generate a brain mask to minimize the inclusion of the extra-cerebral tissues. Spatial normalization to the standard MNI template was performed using a 12-parameter affine transformation and mutual-information cost function. During the spatial normalization the data was also resampled to isotropic resolution using a Gaussian kernel with FWHM = 4 mm. Nuisance signal removal was achieved by voxel-wise regression using the 14 regressors based on the motion correction parameters, average signal of the ventricles and their 1st order derivatives. After baseline trend removal up to the third order polynomial, effective band-pass filtering was performed using low-pass filtering at 0.08 Hz. Local Gaussian smoothing up to FWHM = 6 mm was performed using an eroded gray matter mask (Jo et al., 2010).

Independent Component Analysis

The lowest value that we can specify for NIC is 2 in ICA of resting-state fMRI data. With adequate preprocessing, ICA at NIC = 2 produces typically two large networks: one corresponding to the motor-sensory network combined

Wang and Li Feature optimized classification rs-fMRI ICA

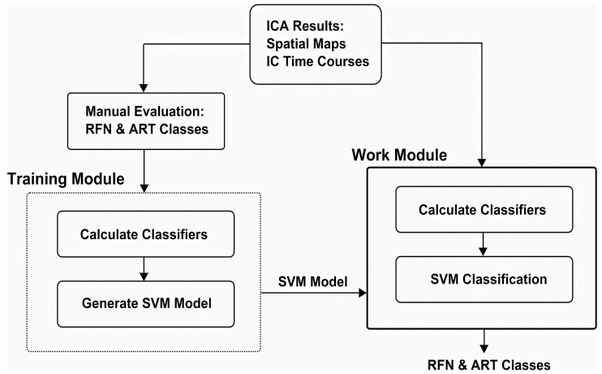

FIGURE 1 | Pipeline schematic of FOCIS framework.

Materials and Methods

Ethics Statement

The Central Ethical Review Board in Stockholm Province, Sweden approved the ethical permission application for this study. The study permission included the consent form used to provide information and obtain consent. All participants provided informed consent by voluntary signature.

Resting-State fMRI Data

Seven resting-state fMRI datasets from normal volunteers were used for the development and validation of the framework. We acquired one dataset ourselves by using a 3T whole-body clinical MRI scanner (TIM Trio, Siemens Healthcare, Erlangen, Germany) with a 2D gradient-recalled echo echo-planar imaging technique. The other 6 datasets were downloaded from an open-access database (https://www.nitrc.org/frs/?group_id=296). More details of the data acquisition parameters and the demographics of the participants are summarized in **Table 2**.

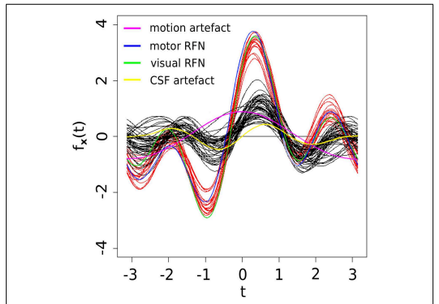

FIGURE 2 | Visually inspected ICs in feature space visualized using Andrew's curves. Selected feature space consists of only the significant ($p < 0.01$) features. Red curves represent class RFN and black curves represent class ART.

Preprocessing

The resting-state fMRI datasets underwent the same preprocessing procedure, which were performed with AFNI (http://afni.nimh.nih.gov/afni) and FSL (http://www.fmrib.ox.ac.uk/fsl) programs with a bash wrapper shell (Wang and Li, 2013). The first 10 timeframes in each data set were removed to ensure signal steady state. After temporal de-spiking, six-parameter rigid body image registration was performed for motion correction. The average volume for each motion-corrected time series was used to generate a brain mask to minimize the inclusion of the extra-cerebral tissues. Spatial normalization to the standard MNI template was performed using a 12-parameter affine transformation and mutual-information cost function. During the spatial normalization the data was also resampled to isotropic resolution using a Gaussian kernel with FWHM = 4 mm. Nuisance signal removal was achieved by voxel-wise regression using the 14 regressors based on the motion correction parameters, average signal of the ventricles and their 1st order derivatives. After baseline trend removal up to the third order polynomial, effective band-pass filtering was performed using low-pass filtering at 0.08 Hz. Local Gaussian smoothing up to FWHM = 6 mm was performed using an eroded gray matter mask (Jo et al., 2010).

Independent Component Analysis

The lowest value that we can specify for NIC is 2 in ICA of resting-state fMRI data. With adequate preprocessing, ICA at NIC = 2 produces typically two large networks: one corresponding to the motor-sensory network combined

with the visual network and the other corresponding to a cognitive functional network somewhat resembles the default mode network (DMN). The visual network usually become the next split-off at NIC = 3. With NIC > 3, the precise ICA representation of a resting-state fMRI dataset depends on the noise characteristics of the dataset. Defining a basic set of RFNs and artifacts is an extremely difficult and complex task beyond the scope of this investigation (Wig et al., 2011, 2014; Schultz et al., 2014). However, consensus from multiple studies suggests that there is a relatively stable set of RFNs that provide an appropriate description of the functional connectivity hierarchy at the level of major brain networks. For example, the 10 consistent across-subject RFNs from Damoiseaux et al. (2006), the 10 task and resting-state matched networks from Smith et al. (2009), and the 7-network parcellation from Yeo et al. (2011). Assuming a need for at least twice as many components as the 10 potential RFNs to allow for the adequate modeling of both RFNs and artifact components associated with noise and physiological sources, Schultz et al. (2014) created a 20 component ICA template and used it for template-based ICA of resting-state fMRI data. Along similar line of thinking, we assume that it is necessary to use at least a NIC = 20 to extract a complete set of RFNs with group ICA from a resting-state fMRI dataset contaminated with artifacts and focus our investigation of ICA dimensionality on NIC = 20. Since the results from previous ICA of fMRI data with NIC up to 90 indicated that performing ICA in an unnecessarily high dimensional subspace decreases the stability of the algorithm and degrades the integrity of the ICA representation of functional networks in the brain, we choose NIC = 100 as the upper limit in our investigation.

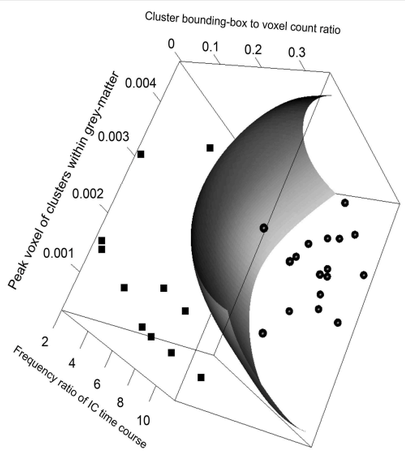

FIGURE 3 | Visualizing the FOCIS classification model as a dividing hyper-plane in 3D feature space projected onto its 3 dimensions with greatest variances.

Group ICA was performed on the resting-state fMRI datasets 0–5 using the standalone *melodic* program in FSL package (Smith et al., 2004; Woolrich et al., 2009; Jenkinson et al., 2012). The analysis option of multi-session temporal concatenation was selected to extract common spatial patterns without assuming the consistent temporal response pattern across the subjects (Beckmann and Smith, 2004). By default *melodic* can estimate the dimension of the input data by performing a Bayesian analysis and use it for ICA. The estimated dimensions for the 7 datasets varied from 21 to 38. To study how the ICA results are influenced by the specification of input NICand test the stability of the SVM-based framework, besides ICA at the estimated NIC, 80 additional group ICA runs were also carried out for the resting-state fMRI dataset 1–5 by systematically increasing NIC from 20 to 100. Single subject ICA was also performed for the first 5 subjects included in the dataset 6 with NIC = 30. When NIC was explicitly specified as an input to *melodic*, the estimated default NIC by the Bayesian analysis should not affect the ICA results.

Before automated classification of the ICs with FOCIS and FSL-FIX, the one-sampled *t*-test maps for the ICs from the group ICA were first assessed by setting an uncorrected voxel-wise threshold at $p < 0.001$ and the minimum voxel cluster size of 20 contiguous voxels. The probability of random field of noise producing a cluster of size ≥20 was estimated at $p < 0.01$. This was assessed by Monte-Carlo simulation result obtained from the AFNI program, *AlphaSim,* with the following main input parameters: FWHM = 6.2 mm estimated average by running 3dFWHM on the input data to ICA, voxel-wise threshold value $p < 0.001$, and 5×10^5 iterations.

Manual Evaluation of IC Maps

Group ICA results for the dataset 1 at NIC = 50 was chosen as the training input for both FOCIS and FSL-FIX, the ICA results for datasets 1–6 at NIC = 30, and dataset 0 at NIC = 70 were all manually classified for cross-validation. In addition, for self-verification purpose, the group ICA results for dataset 1 at NIC = 70 and 90 were also manually classified. The results of manual classification were used to test the precision, accuracy, sensitivity, and specificity of the classification model. The ICA results were

TABLE 4 | Summary of the automated (FOCIS and FLS-FIX) and manual classification results for the group ICA results.

		FOCIS		Manual Evaluation		FSL-FIX	
Dataset	**NIC**	**NART**	**NRFN**	**NART**	**NRFN**	**NART**	**NRFN**
0	70	29	41	30	40	30	40
	30	13	17	13	17	13	17
1	50	25	25	25	25	25	25
	70	39	31	39	31	37	33
	90	56	34	56	34	51	39
2	30	14	16	15	15	12	18
3	30	15	15	16	14	16	14
4	30	20	10	20	10	17	13
5	30	16	14	17	13	14	16

Wang and Li Feature optimized classification rs-fMRI ICA

with the visual network and the other corresponding to a cognitive functional network somewhat resembles the default mode network (DMN). The visual network usually become the next split-off at NIC = 3. With NIC > 3, the precise ICA representation of a resting-state fMRI dataset depends on the noise characteristics of the dataset. Defining a basic set of RFNs and artifacts is an extremely difficult and complex task beyond the scope of this investigation (Wig et al., 2011, 2014; Schultz et al., 2014). However, consensus from multiple studies suggests that there is a relatively stable set of RFNs that provide an appropriate description of the functional connectivity hierarchy at the level of major brain networks. For example, the 10 consistent across-subject RFNs from Damoiseaux et al. (2006), the 10 task and resting-state matched networks from Smith et al. (2009), and the 7-network parcellation from Yeo et al. (2011). Assuming a need for at least twice as many components as the 10 potential RFNs to allow for the adequate modeling of both RFNs and artifact components associated with noise and physiological sources, Schultz et al. (2014) created a 20 component ICA template and used it for template-based ICA of resting-state fMRI data. Along similar line of thinking, we assume that it is necessary to use at least a NIC = 20 to extract a complete set of RFNs with group ICA from a resting-state fMRI dataset contaminated with artifacts and focus our investigation of ICA dimensionality on NIC = 20. Since the results from previous ICA of fMRI data with NIC up to 90 indicated that performing ICA in an unnecessarily high dimensional subspace decreases the stability of the algorithm and degrades the integrity of the ICA representation of functional networks in the brain, we choose NIC = 100 as the upper limit in our investigation.

Group ICA was performed on the resting-state fMRI datasets 0–5 using the standalone *melodic* program in FSL package (Smith et al., 2004; Woolrich et al., 2009; Jenkinson et al., 2012). The analysis option of multi-session temporal concatenation was selected to extract common spatial patterns without assuming the consistent temporal response pattern across the subjects (Beckmann and Smith, 2004). By default *melodic* can estimate the dimension of the input data by performing a Bayesian analysis and use it for ICA. The estimated dimensions for the 7 datasets varied from 21 to 38. To study how the ICA results are influenced by the specification of input NICand test the stability of the SVM-based framework, besides ICA at the estimated NIC, 80 additional group ICA runs were also carried out for the resting-state fMRI dataset 1–5 by systematically increasing NIC from 20 to 100. Single subject ICA was also performed for the first 5 subjects included in the dataset 6 with NIC = 30. When NIC was explicitly specified as an input to *melodic*, the estimated default NIC by the Bayesian analysis should not affect the ICA results.

Before automated classification of the ICs with FOCIS and FSL-FIX, the one-sampled *t*-test maps for the ICs from the group ICA were first assessed by setting an uncorrected voxel-wise threshold at $p < 0.001$ and the minimum voxel cluster size of 20 contiguous voxels. The probability of random field of noise producing a cluster of size ≥20 was estimated at $p < 0.01$. This was assessed by Monte-Carlo simulation result obtained from the AFNI program, *AlphaSim,* with the following main input parameters: FWHM = 6.2 mm estimated average by running 3dFWHM on the input data to ICA, voxel-wise threshold value $p < 0.001$, and 5×10^5 iterations.

Manual Evaluation of IC Maps

Group ICA results for the dataset 1 at NIC = 50 was chosen as the training input for both FOCIS and FSL-FIX, the ICA results for datasets 1–6 at NIC = 30, and dataset 0 at NIC = 70 were all manually classified for cross-validation. In addition, for self-verification purpose, the group ICA results for dataset 1 at NIC = 70 and 90 were also manually classified. The results of manual classification were used to test the precision, accuracy, sensitivity, and specificity of the classification model. The ICA results were

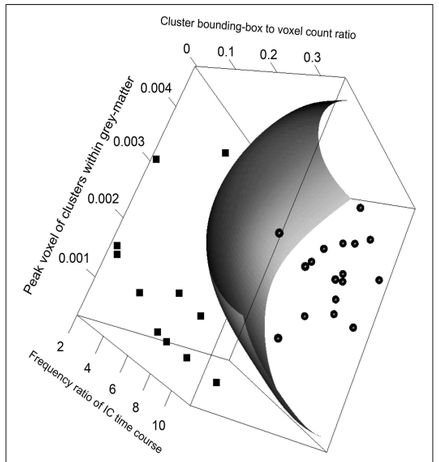

FIGURE 3 | Visualizing the FOCIS classification model as a dividing hyper-plane in 3D feature space projected onto its 3 dimensions with greatest variances.

TABLE 4 | Summary of the automated (FOCIS and FLS-FIX) and manual classification results for the group ICA results.

		FOCIS		Manual Evaluation		FSL-FIX	
Dataset	**NIC**	**NART**	**NRFN**	**NART**	**NRFN**	**NART**	**NRFN**
0	70	29	41	30	40	30	40
	30	13	17	13	17	13	17
1	50	25	25	25	25	25	25
	70	39	31	39	31	37	33
	90	56	34	56	34	51	39
2	30	14	16	15	15	12	18
3	30	15	15	16	14	16	14
4	30	20	10	20	10	17	13
5	30	16	14	17	13	14	16

Frontiers in Human Neuroscience | www.frontiersin.org 5 May 2015 | Volume 9 | Article 259

TABLE 5 | Precision, accuracy, specificity, and sensitivity of the automatic classifications based on FOCIS and FSL-fix frameworks for group ICA results.

Dataset	NIC	Precision		Sensitivity		Specificity		Accuracy	
		FOCIS	FLS-FIX	FOCIS	FLS-FIX	FOCIS	FLS-FIX	FOCIS	FLS-FIX
0	70	0.97	1.00	1.00	1.00	0.98	1.00	0.99	1.00
	30	1.00	1.00	1.00	1.00	1.00	1.00	1.00	1.00
1	50	1.00	1.00	1.00	1.00	1.00	1.00	1.00	1.00
	70	1.00	0.87	1.00	1.00	1.00	0.86	1.00	0.93
	90	1.00	0.89	1.00	1.00	1.00	0.83	1.00	0.93
2	30	0.94	0.80	1.00	1.00	0.93	0.83	0.97	0.90
3	30	1.00	1.00	1.00	1.00	1.00	1.00	1.00	1.00
4	30	1.00	0.85	1.00	1.00	1.00	0.77	1.00	0.90
5	30	0.94	0.82	1.00	1.00	0.93	0.81	0.97	0.90
Mean		0.98	0.92	1.00	1.00	0.98	0.90	0.99	0.95

TABLE 6 | Precision, accuracy, specificity and sensitivity of the automatic classification with FOCIS for single subject ICA results.

Subject	NIC	Precision	Sensitivity	Specificity	Accuracy
1	30	0.93	1.00	0.94	0.97
2	30	0.69	0.90	0.80	0.83
3	30	0.78	0.78	0.90	0.87
4	30	1.00	1.00	1.00	1.00
5	30	0.85	0.92	0.89	0.90
Mean		0.85	0.92	0.91	0.91

manually examined by at least two experienced neuroscientist raters and were classified into two broad classes: Potential RFN (class RFN) or artifacts (class ART). The classification criteria for the manual evaluation can be approximately summarized as the following:

(1) A potential RFN has to fulfill the voxel-wise threshold $p <$ 0.001 and the minimum cluster size >20.
(2) A potential RFN exhibits peak activation in cortical gray-matter.
(3) A potential RFN possesses little spatial overlap with known vascular, ventricular, motion, and susceptibility artifacts.
(4) The associated time course for a potential RFN should reflect the expected low frequency spontaneous fluctuations with adequate dynamic range.
(5) The geometry of an involved region of interests in a potential RFN is reasonably compact and smooth instead of extreme shape.

The overall classification scheme for class ART was more confined by using high cost for it to ensure that the potential RFNs are not discarded as artifacts. Whenever there exists uncertainty or inconsistency between the evaluation results from two reviewers, the involved ICs were classified into RFN class. This may increase the false negative rate in the classification results. However, this is appropriate given our goal of not discarding potential RFNs.

Feature Selection

A total of 18 initial features were devised to reflect the criteria used for visual inspection. These features include measures for spatial patterns, time-course characteristics, and spectral information. The descriptions for the initially devised features are provided in Appendix A (Supplementary Material) in more details including the relevant mathematical definitions. Calculations of the features were implemented in R in combination with AFNI programs, which are detailed in Appendix B (Supplementary Material). All features were conditioned prior to use in feature selection, training, and classification. This involves mean-centering (removal of mean) and scaling (division by standard deviation). All features were tested for explanatory power on the training dataset using a general linear model with a binomial variance function and a logit link function. We used F-score to select the features with high significant explanatory power ($p < 0.01$) out of the initial 18-item feature space. The procedure is summarized below:

(1) Calculate F-score of each feature.
(2) Manually pick a relative low F-score threshold to drop features with F-score below the threshold.
(3) Randomly split the training data into training and validation subsets.
(4) Predict the validation subset using SVM procedure based on the model built with the training subset and high F-score features.
(5) Repeat the steps 4 multiple times to achieve a steady average validation error.
(6) Repeat the steps 2–6 by incrementing F-score thresholds to drop more features with relatively low F-scores until the validation accuracy decrease significantly.

As shown in **Table 3**, with the group ICA training datasets we settled down on a model with only 5 most significant features ($p < 0.01$). A model with fewer parameters is less complex and more likely to be biased. On the other hand, a simpler classification model with limited Vapnik–Chervonenkis dimension has higher computational efficiency

Wang and Li Feature optimized classification rs-fMRI ICA

TABLE 5 | Precision, accuracy, specificity, and sensitivity of the automatic classifications based on FOCIS and FSL-fix frameworks for group ICA results.

TABLE 6 | Precision, accuracy, specificity and sensitivity of the automatic classification with FOCIS for single subject ICA results.

Feature Selection

A total of 18 initial features were devised to reflect the criteria used for visual inspection. These features include measures for spatial patterns, time-course characteristics, and spectral information. The descriptions for the initially devised features are provided in Appendix A (Supplementary Material) in more details including the relevant mathematical definitions. Calculations of the features were implemented in R in combination with AFNI programs, which are detailed in Appendix B (Supplementary Material). All features were conditioned prior to use in feature selection, training, and classification. This involves mean-centering (removal of mean) and scaling (division by standard deviation). All features were tested for explanatory power on the training dataset using a general linear model with a binomial variance function and a logit link function. We used F-score to select the features with high significant explanatory power ($p < 0.01$) out of the initial 18-item feature space. The procedure is summarized below:

(1) Calculate F-score of each feature.
(2) Manually pick a relative low F-score threshold to drop features with F-score below the threshold.
(3) Randomly split the training data into training and validation subsets.
(4) Predict the validation subset using SVM procedure based on the model built with the training subset and high F-score features.
(5) Repeat the steps 4 multiple times to achieve a steady average validation error.
(6) Repeat the steps 2–6 by incrementing F-score thresholds to drop more features with relatively low F-scores until the validation accuracy decrease significantly.

As shown in **Table 3**, with the group ICA training datasets we settled down on a model with only 5 most significant features ($p < 0.01$). A model with fewer parameters is less complex and more likely to be biased. On the other hand, a simpler classification model with limited Vapnik–Chervonenkis dimension has higher computational efficiency

and lower risk of over-fitting. Optimal feature selection is, therefore, very important for the construction of classification model.

Construction of the Classification Model

A boundary-constraint SVM C-classification model was constructed using the training datasets and the 5 most significant features with $p < 0.01$. The boundary-constraint SVM classification solves a variant of quadratic problem using modified TRON optimization software (Lin and Moré, 1999; Mangasarian and Musicant, 1999).The resulting feature space is 50 training points × 5 features. The binary classification model uses a non-linear radial basis function kernel and 100 in cost. This was chosen to penalize false positive rates more severely than false negatives to avoid misclassification of potential RFNs as artifacts.

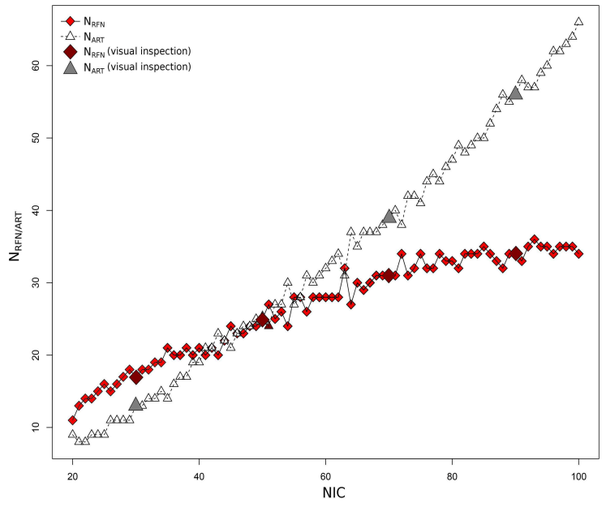

FIGURE 4 | Number of RFNs and artifact components determined from automated and manual classifications as a function of NICfor dataset 1.

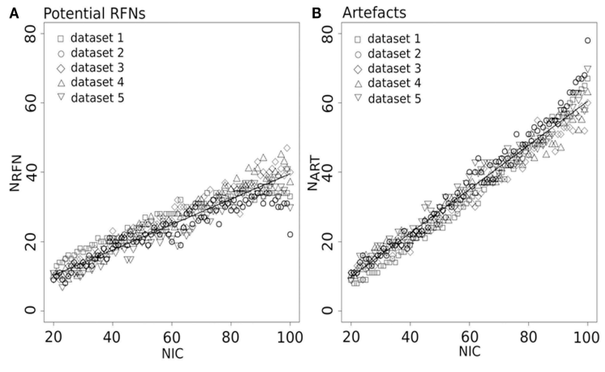

FIGURE 5 | Number of RFNs (A) and artifact components (B) determined from automated classification as a function of NIC for the datasets 1–5. The lines indicate the least-square fittings of a linear function to the average data.

Wang and Li Feature optimized classification rs-fMRI ICA

and lower risk of over-fitting. Optimal feature selection is, therefore, very important for the construction of classification model.

Construction of the Classification Model

A boundary-constraint SVM C-classification model was constructed using the training datasets and the 5 most significant features with $p < 0.01$. The boundary-constraint SVM classification solves a variant of quadratic problem using modified TRON optimization software (Lin and Moré, 1999; Mangasarian and Musicant, 1999).The resulting feature space is 50 training points × 5 features. The binary classification model uses a non-linear radial basis function kernel and 100 in cost. This was chosen to penalize false positive rates more severely than false negatives to avoid misclassification of potential RFNs as artifacts.

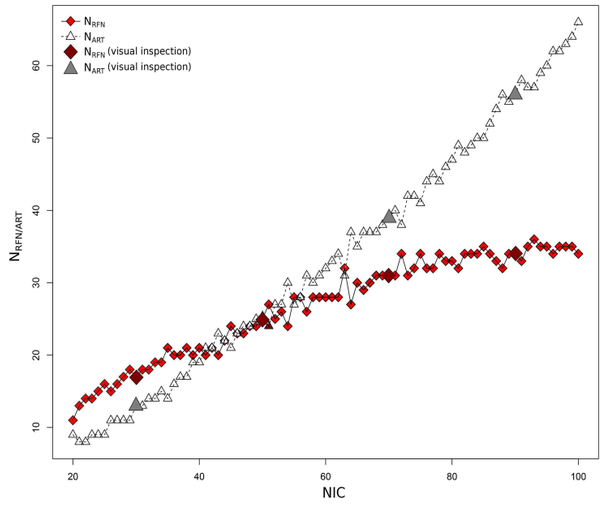

FIGURE 4 | Number of RFNs and artifact components determined from automated and manual classifications as a function of NICfor dataset 1.

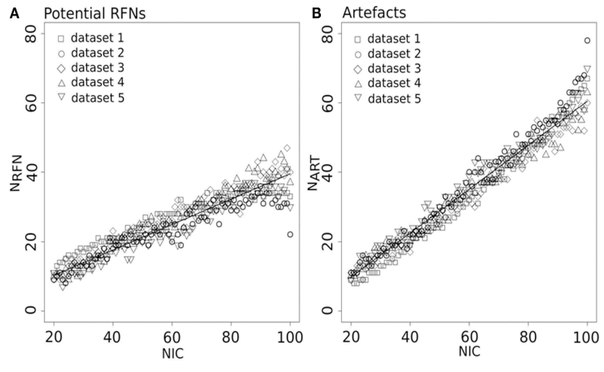

FIGURE 5 | Number of RFNs (A) and artifact components (B) determined from automated classification as a function of NIC for the datasets 1–5. The lines indicate the least-square fittings of a linear function to the average data.

The framework uses the R package *kernlab* (Karatzoglou et al., 2007) for its SVM implementations. *Kernlab's* SVM implementation is based on LIBSVM (Chang and Lin, 2011) which is a popular implementation of SVM. To solve the optimization problems encountered in the training of the kernelized SVM, LIBSVM uses a minimal optimization algorithm. Gaussian radial basis function (RBF) kernel is used as a kernel function for non-linear SVM classification (in contrast to the dot product for linear SVM). The kernel function between

TABLE 7 | The linear least-square fitting results for N_{RFN} and N_{ART} as a function of NIC.

Dataset	RFN			ART		
	Ratio	Correlation	Adjusted R^2	Ratio	Correlation	Adjusted R^2
1	0.28	0.96	0.93	0.72	0.99	0.99
2	0.29	0.93	0.87	0.71	0.99	0.98
3	0.40	0.98	0.95	0.60	0.99	0.98
4	0.41	0.98	0.96	0.59	0.99	0.98
5	0.36	0.97	0.93	0.64	0.99	0.98
Mean	0.35	0.96	0.93	0.65	0.99	0.98

TABLE 8 | The ranking and probability of the split ICs for the motor-cortex functional network as a function of NIC.

NIC	Original IC		Split IC	
	Ranking	Probability	Ranking	Probability
30	1	0.98		
40	1	0.89		
50	1	0.56	7	0.10
60	3	0.32	10	0.10
70	2	0.32	3	0.24
80	1	0.35	2	0.23
90	1	0.42	11	0.17

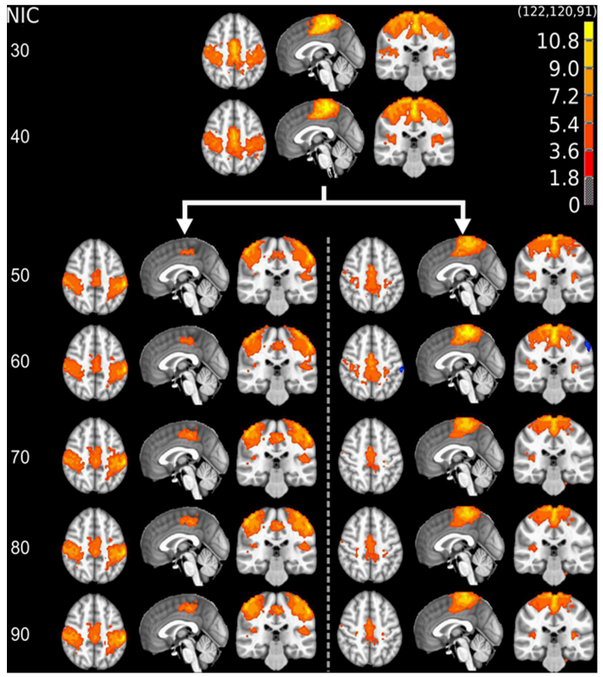

FIGURE 6 | The tracking results of dataset 1 for a typical RFN through similarity matching. The motor-sensory functional network was tracked at NIC = 20–100. The IC splits into two potential RFNs with high similarity to the original IC, when NIC = 50.

Wang and Li Feature optimized classification rs-fMRI ICA

The framework uses the R package *kernlab* (Karatzoglou et al., 2007) for its SVM implementations. *Kernlab's* SVM implementation is based on LIBSVM (Chang and Lin, 2011) which is a popular implementation of SVM. To solve the optimization problems encountered in the training of the kernelized SVM, LIBSVM uses a minimal optimization algorithm. Gaussian radial basis function (RBF) kernel is used as a kernel function for non-linear SVM classification (in contrast to the dot product for linear SVM). The kernel function between

TABLE 7 | The linear least-square fitting results for N_{RFN} and N_{ART} as a function of NIC.

TABLE 8 | The ranking and probability of the split ICs for the motor-cortex functional network as a function of NIC.

FIGURE 6 | The tracking results of dataset 1 for a typical RFN through similarity matching. The motor-sensory functional network was tracked at NIC = 20–100. The IC splits into two potential RFNs with high similarity to the original IC, when NIC = 50.

Frontiers in Human Neuroscience | www.frontiersin.org 8 May 2015 | Volume 9 | Article 259

two samples $\boldsymbol{x}$ and $\boldsymbol{y}$ is defined as:

$$k(x, y) = \exp(\sigma ||x - y||_2^2)$$

where σ is a free parameter. Optimal values of σ is shown to lie between the 0.1 and 0.9 quantiles of the ||x-y||statistic (Caputo et al., 2002) and any value is within these quantiles leads to good performance (Karatzoglou et al., 2004). Therefore, the value of σ was taken to be a random value within the 0.1 and 0.9 quantiles, which were estimated by using a random subsample of the training dataset. The choices of parameters were confirmed by hyper-parameter optimization through an exhaustive grid searching in input space of the cost (C) and free parameter (σ) within the boundary constraints C = [10, 1000] and σ = [0.1, 1.0] with a grid size of ΔC = 10 and Δσ = 0.1. Cross validation by maximizing accuracy while retaining sensitivity to 1 was carried out during self-verification with dataset 1, NIC = 30, 50, 70, and 90. It was confirmed that the performance is maximized and insensitive to the choice of σ within the predefined quantiles 0.1–0.9 and C within 100–210.

The workflow of the classification framework is illustrated in **Figure 1**. The training module takes ICA results (IC spatial map and IC time-course) as inputs to calculate the features. The calculated feature values with the manual inspection results are

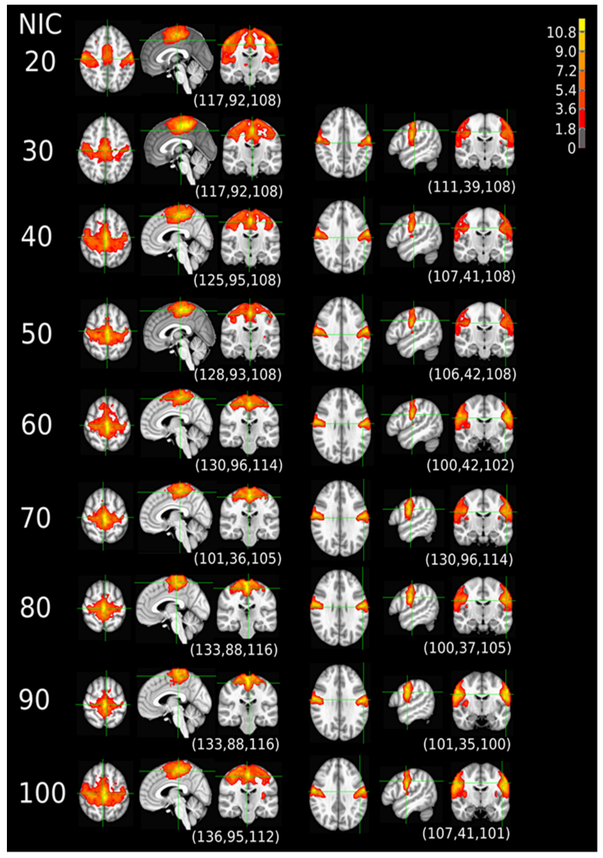

FIGURE 7 | The tracking results of dataset 4 for a typical RFN through similarity matching. The motor-sensory functional network was tracked at NIC = 20–100. The IC was split into two potential RFNs with high similarity to the original IC, when NIC = 30.

Wang and Li Feature optimized classification rs-fMRI ICA

two samples $\boldsymbol{x}$ and $\boldsymbol{y}$ is defined as:

$$k(x, y) = \exp(\sigma ||x - y||_2^2)$$

where σ is a free parameter. Optimal values of σ is shown to lie between the 0.1 and 0.9 quantiles of the ||x-y||statistic (Caputo et al., 2002) and any value is within these quantiles leads to good performance (Karatzoglou et al., 2004). Therefore, the value of σ was taken to be a random value within the 0.1 and 0.9 quantiles, which were estimated by using a random subsample of the training dataset. The choices of parameters were confirmed by hyper-parameter optimization through an exhaustive grid searching in input space of the cost (C) and free parameter (σ) within the boundary constraints C = [10, 1000] and σ = [0.1, 1.0] with a grid size of ΔC = 10 and Δσ = 0.1. Cross validation by maximizing accuracy while retaining sensitivity to 1 was carried out during self-verification with dataset 1, NIC = 30, 50, 70, and 90. It was confirmed that the performance is maximized and insensitive to the choice of σ within the predefined quantiles 0.1–0.9 and C within 100–210.

The workflow of the classification framework is illustrated in **Figure 1**. The training module takes ICA results (IC spatial map and IC time-course) as inputs to calculate the features. The calculated feature values with the manual inspection results are

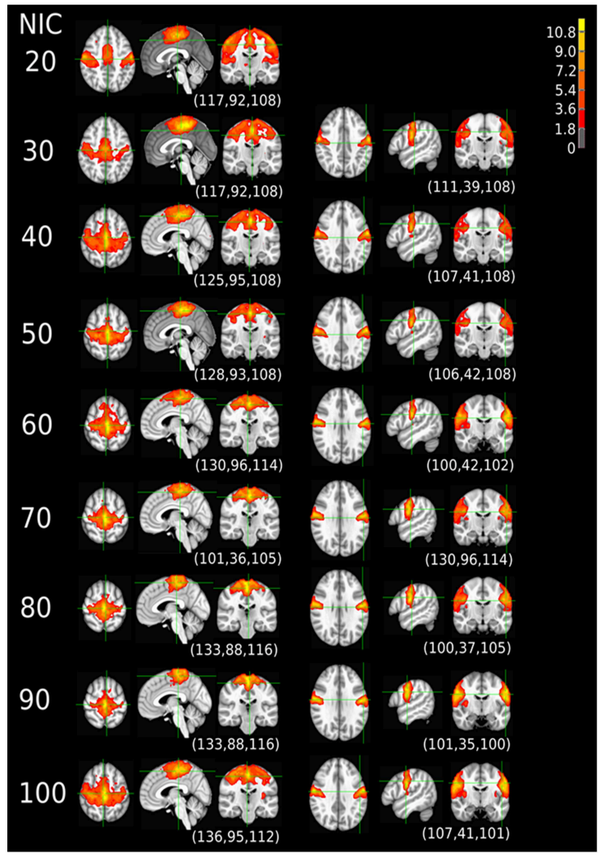

FIGURE 7 | The tracking results of dataset 4 for a typical RFN through similarity matching. The motor-sensory functional network was tracked at NIC = 20–100. The IC was split into two potential RFNs with high similarity to the original IC, when NIC = 30.

then used to generate a SVM classification model. The classifier module calculates the features from ICA results the same way as the training module. But it uses the calculated features together with the SVM classification model output from the training module to classify the ICs.

Comparison Between the Automated and Manual Classifications

We conducted direct comparison of the classification performances between FOCIS and FSL-FIX by assuming the manual evaluation result as the ground truth. For direct comparison with FSL-FIX, we adapted the output results from group ICA so that automated classification can be performed using FSL-FIX, since FSL-fix was designed for single-session ICA, some required input parameters for FSL-FIX need to be compiled manually in order to use FSL-FIX for classification of the group ICA results. These included the concatenated 4D fMRI data for individual subject, the temporal mean of the 4D fMRI data, concatenated motion parameters, and the group average of transformation matrix. It should be pointed out that the outputs of the group and single subject ICA can be directly used for automated classification with FOCIS, because it requires no additional input except for the IC time course and spatial maps. The automated classification results from both FOCIS and FSL-FIX were then compared with those from manual evaluation. For a given IC, we verified if the automated classification is consistent with the manual evaluation. We also counted and compared the numbers of ICs in the RFN (N_{RFN}) and ART (N_{ART}) classes as determined by the automated and manual classifications. The most relevant performance index for automated classification here is the accuracy or the true negative rate (the percentage of true artifact component detected), since FOCIS was trained with heavy penalty on false positive rate. When a mismatch appeared between the automated and manual classification, the misclassified IC was further investigated to identify potential causes of the misclassification.

The Effects of Input NIC on ICA Results

We analyzed the datasets 1–5 with group ICA using a wide range of input NIC from 20 to 100. To understand how the ICA results

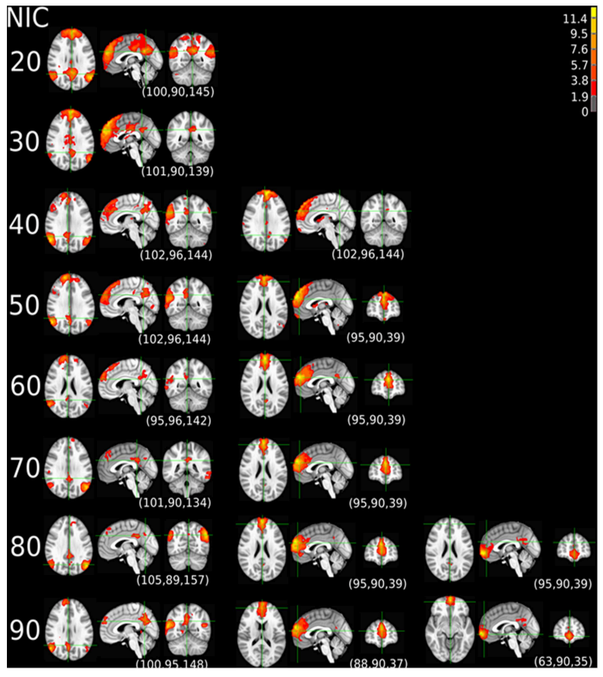

FIGURE 8 | The tracking results of dataset 4 for a typical RFN through similarity matching. The primary visual functional network was tracked at NIC = 20–90. The IC did not split in the entire investigated NIC range.

Wang and Li Feature optimized classification rs-fMRI ICA

then used to generate a SVM classification model. The classifier module calculates the features from ICA results the same way as the training module. But it uses the calculated features together with the SVM classification model output from the training module to classify the ICs.

Comparison Between the Automated and Manual Classifications

We conducted direct comparison of the classification performances between FOCIS and FSL-FIX by assuming the manual evaluation result as the ground truth. For direct comparison with FSL-FIX, we adapted the output results from group ICA so that automated classification can be performed using FSL-FIX, since FSL-fix was designed for single-session ICA, some required input parameters for FSL-FIX need to be compiled manually in order to use FSL-FIX for classification of the group ICA results. These included the concatenated 4D fMRI data for individual subject, the temporal mean of the 4D fMRI data, concatenated motion parameters, and the group average of transformation matrix. It should be pointed out that the outputs of the group and single subject ICA can be directly used for automated classification with FOCIS, because it requires no additional input except for the IC time course and spatial maps. The automated classification results from both FOCIS and FSL-FIX were then compared with those from manual evaluation. For a given IC, we verified if the automated classification is consistent with the manual evaluation. We also counted and compared the numbers of ICs in the RFN (N_{RFN}) and ART (N_{ART}) classes as determined by the automated and manual classifications. The most relevant performance index for automated classification here is the accuracy or the true negative rate (the percentage of true artifact component detected), since FOCIS was trained with heavy penalty on false positive rate. When a mismatch appeared between the automated and manual classification, the misclassified IC was further investigated to identify potential causes of the misclassification.

The Effects of Input NIC on ICA Results

We analyzed the datasets 1–5 with group ICA using a wide range of input NIC from 20 to 100. To understand how the ICA results

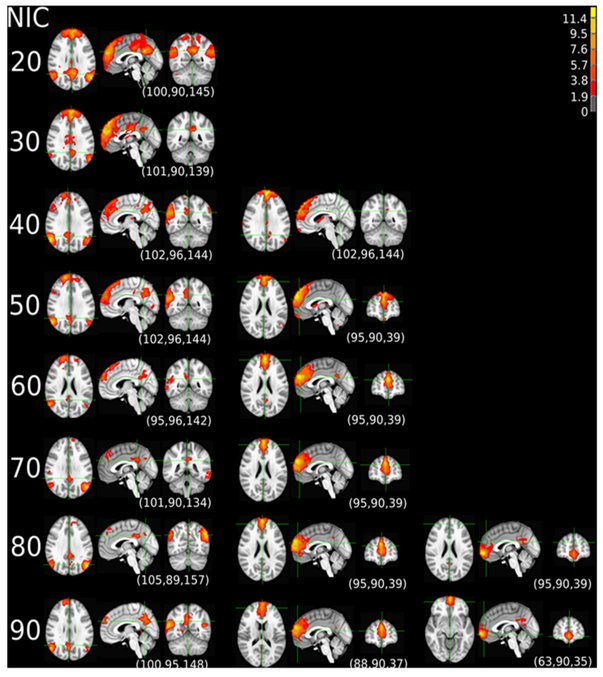

FIGURE 8 | The tracking results of dataset 4 for a typical RFN through similarity matching. The primary visual functional network was tracked at NIC = 20–90. The IC did not split in the entire investigated NIC range.

Frontiers in Human Neuroscience | www.frontiersin.org 10 May 2015 | Volume 9 | Article 259

are influenced by the selection of NIC, we investigated N_{RFN} and N_{ART} obtained from the automated and manual classifications as a function of NIC. We also investigated how the contribution of variance changed with NIC for some specific ICs. Furthermore, we constructed a regression module in FOCIS so that it can be used to track the changes of a given IC in a series of ICA results obtained from the same fMRI dataset by analyzing it with different NIC. The regression model was constructed using an epsilon (ε) support vector regression algorithm. Similar to SVM classification, the support vector regression algorithm only uses a subset of the training data (Vapnik et al., 1997). The cost function for building the model ignores any training data that is close (within a threshold ε) to the model prediction (Smola and Schölkopf, 2004). The regression model provides class probabilities as output instead of class labels. To track a specific IC in a series of ICA results, we constructed the model by labeling the specific IC as class 1 and all other ICs as class 0 using the ICA result with NIC = 30. When the SVM regression model was applied to ICA results with a larger NIC, we used the model to estimate class probabilities for all ICs. Then, we rank the ICs according to their class probabilities (the level of similarity to the specific IC). With the ranking, we can identify the corresponding IC in the ICA results of different NIC that matches closest to the given IC.

To quantify the changes in spatial patterns and the associated time courses of a given IC as a function of NIC we introduce a change index of spatial overlap and temporal association (CISOTA) which is defined in the following equation:

$$\text{CISOTA} = 1/(\text{spatial overlap} \times \text{correlation coefficient of the IC time course}).$$

where the spatial overlap for a given IC is defined as the fraction of overlap area relative to the original area of the spatial pattern. We evaluated CISOTA for three typical RFNs (motor-sensory, visual, and DMN) and three artifact components as function of NIC. Furthermore, we also evaluated the cross-sectional changes of all ICs when NIC was incremented by 1 at different NIC values.

Results

Feature Selection

Amongst the 18 initially devised features, 5 are highly significant ($p < 0.01$) as determined by the explanatory power test (see **Table 3**). The model based on the subset of 5 parameters achieved a low AIC of 3.71 compared to AIC = 17.03 for the full model including 18 parameters. The relative AIC between the two models is $AIC_{rel} = \exp\left(\frac{3.71-17.03}{2}\right) = 0.0013$, which indicate that the model based on the subset of 5 parameters is much likely to minimize the information loss than the full model (Akaike, 1974). To avoid over-fitting, therefore, we take no longer the full model into further consideration.

As shown in **Table 3**, three of the significant features are associated with the spatial patterns of IC maps, whereas the other two features are related to the characteristics of IC time courses. **Figure 2** depicts all the manually evaluated ICs used for training (dataset 1, NIC = 50) in the feature space of the five most significant features. All ICs in feature space is visualized as Andrews curves as a method to visualize high-dimensional data (Andrews, 1972). Each IC's data point in feature space $\boldsymbol{x} = [x_1,\ldots,x_5]$ defines a curve through the function $f(\boldsymbol{x}, t) = x_1 sin(t)+x_2 cos(t)+x_3 sin(2t)+x_4 cos(2t)+x_5 sin(3t)$. This function is uniquely defined and plotted between $-\pi$ and π. This formula can also be regarded as the projection of the data point onto the vector [*sin(t), cos(t), sin(2t), cos(2t), sin(3t)*].

Construction of the Classification Model

The SVM classification model constructed with the five most significant features described above was trained with the training dataset. The resulting model has 23 support vectors and the radial kernel size $\sigma = 0.38$. Self-verification of the model resulted in perfect classification with 100% in specificity and 100% in sensitivity for both the training dataset. **Figure 3** illustrates the trained SVM model as a hyper-plane in a 3D projection of the 5D feature space. As illustrated in **Figure 3**, a hyper-plane of maximum variance separates appropriately the two classes of ICs in the training dataset.

Comparison Between the Automated and Manual Classifications

The results from the automated and manual classifications are summarized in **Tables 4–6**. On average the automated classification based on FOCIS achieved zero false positive and 4/231 false negative rates in identifying artifact contaminated ICs of the group ICA results, signifying a 98.27% overlap between the FOCIS-based and human expert classifications in identifying artifact contaminated ICs (see **Table 4**). The false negative rates for FSL-FIX in identifying artifact contaminated ICs of the group ICA results is 17/231, corresponding to 92.64% overlap with the manual classification (see **Table 4**). As shown in **Table 5**, both FOCIS and FSL-FIX achieved robust classifications of the group ICA results. The performance of FOCIS in precision, accuracy and specificity is slightly higher than FSL-FIX when compared on the basis of using the identical training dataset of group ICA for dataset 1 at NIC = 50. As shown in **Table 5**, the accuracy of FOCIS in the automated classification of single subject ICA results is 91%, which is not as robust as that for the group ICA results.

The Effects of Input NIC on ICA Results

Figure 4 depicts the extracted N_{RFN} and N_{ART} for the dataset 1 as a function of NIC. The results from both the automated (with FOCIS) and manual classifications were shown. It is apparent that both N_{RFN} and N_{ART} increase with NIC, but the N_{ART} grows at faster rate than N_{RFN}, particularlyat higher NIC. This is further demonstrated by the classification results for the datasets 1–5 summarized in **Figure 5**. For the group ICA results N_{RFN} and N_{ART} are overall linearly dependent on NIC and the linear correlation coefficient is $R = 0.93$. As summarized in **Table 7**, the average ratios for N_{RFN}/NIC and N_{ART}/NICare 0.35 and 0.65, respectively. On average, the number of artifact components is about twice of that for RFNs.

The tracking results of dataset 1 as a function of NIC for the motor-sensory are shown in **Figure 6**. For this dataset the

Wang and Li Feature optimized classification rs-fMRI ICA

are influenced by the selection of NIC, we investigated N_{RFN} and N_{ART} obtained from the automated and manual classifications as a function of NIC. We also investigated how the contribution of variance changed with NIC for some specific ICs. Furthermore, we constructed a regression module in FOCIS so that it can be used to track the changes of a given IC in a series of ICA results obtained from the same fMRI dataset by analyzing it with different NIC. The regression model was constructed using an epsilon (ε) support vector regression algorithm. Similar to SVM classification, the support vector regression algorithm only uses a subset of the training data (Vapnik et al., 1997). The cost function for building the model ignores any training data that is close (within a threshold ε) to the model prediction (Smola and Schölkopf, 2004). The regression model provides class probabilities as output instead of class labels. To track a specific IC in a series of ICA results, we constructed the model by labeling the specific IC as class 1 and all other ICs as class 0 using the ICA result with NIC = 30. When the SVM regression model was applied to ICA results with a larger NIC, we used the model to estimate class probabilities for all ICs. Then, we rank the ICs according to their class probabilities (the level of similarity to the specific IC). With the ranking, we can identify the corresponding IC in the ICA results of different NIC that matches closest to the given IC.

To quantify the changes in spatial patterns and the associated time courses of a given IC as a function of NIC we introduce a change index of spatial overlap and temporal association (CISOTA) which is defined in the following equation:

$$\text{CISOTA} = 1/(\text{spatial overlap} \times \text{correlation coefficient of the IC time course}).$$

where the spatial overlap for a given IC is defined as the fraction of overlap area relative to the original area of the spatial pattern. We evaluated CISOTA for three typical RFNs (motor-sensory, visual, and DMN) and three artifact components as function of NIC. Furthermore, we also evaluated the cross-sectional changes of all ICs when NIC was incremented by 1 at different NIC values.

Results

Feature Selection

Amongst the 18 initially devised features, 5 are highly significant ($p < 0.01$) as determined by the explanatory power test (see **Table 3**). The model based on the subset of 5 parameters achieved a low AIC of 3.71 compared to AIC = 17.03 for the full model including 18 parameters. The relative AIC between the two models is $AIC_{rel} = \exp\left(\frac{3.71-17.03}{2}\right) = 0.0013$, which indicate that the model based on the subset of 5 parameters is much likely to minimize the information loss than the full model (Akaike, 1974). To avoid over-fitting, therefore, we take no longer the full model into further consideration.

As shown in **Table 3**, three of the significant features are associated with the spatial patterns of IC maps, whereas the other two features are related to the characteristics of IC time courses. **Figure 2** depicts all the manually evaluated ICs used for training (dataset 1, NIC = 50) in the feature space of the five most significant features. All ICs in feature space is visualized as Andrews curves as a method to visualize high-dimensional data (Andrews, 1972). Each IC's data point in feature space $\boldsymbol{x} = [x_1,\ldots,x_5]$ defines a curve through the function $f(\boldsymbol{x}, t) = x_1 sin(t)+x_2 cos(t)+x_3 sin(2t)+x_4 cos(2t)+x_5 sin(3t)$. This function is uniquely defined and plotted between $-\pi$ and π. This formula can also be regarded as the projection of the data point onto the vector [*sin(t), cos(t), sin(2t), cos(2t), sin(3t)*].

Construction of the Classification Model

The SVM classification model constructed with the five most significant features described above was trained with the training dataset. The resulting model has 23 support vectors and the radial kernel size $\sigma = 0.38$. Self-verification of the model resulted in perfect classification with 100% in specificity and 100% in sensitivity for both the training dataset. **Figure 3** illustrates the trained SVM model as a hyper-plane in a 3D projection of the 5D feature space. As illustrated in **Figure 3**, a hyper-plane of maximum variance separates appropriately the two classes of ICs in the training dataset.

Comparison Between the Automated and Manual Classifications

The results from the automated and manual classifications are summarized in **Tables 4–6**. On average the automated classification based on FOCIS achieved zero false positive and 4/231 false negative rates in identifying artifact contaminated ICs of the group ICA results, signifying a 98.27% overlap between the FOCIS-based and human expert classifications in identifying artifact contaminated ICs (see **Table 4**). The false negative rates for FSL-FIX in identifying artifact contaminated ICs of the group ICA results is 17/231, corresponding to 92.64% overlap with the manual classification (see **Table 4**). As shown in **Table 5**, both FOCIS and FSL-FIX achieved robust classifications of the group ICA results. The performance of FOCIS in precision, accuracy and specificity is slightly higher than FSL-FIX when compared on the basis of using the identical training dataset of group ICA for dataset 1 at NIC = 50. As shown in **Table 5**, the accuracy of FOCIS in the automated classification of single subject ICA results is 91%, which is not as robust as that for the group ICA results.

The Effects of Input NIC on ICA Results

Figure 4 depicts the extracted N_{RFN} and N_{ART} for the dataset 1 as a function of NIC. The results from both the automated (with FOCIS) and manual classifications were shown. It is apparent that both N_{RFN} and N_{ART} increase with NIC, but the N_{ART} grows at faster rate than N_{RFN}, particularlyat higher NIC. This is further demonstrated by the classification results for the datasets 1–5 summarized in **Figure 5**. For the group ICA results N_{RFN} and N_{ART} are overall linearly dependent on NIC and the linear correlation coefficient is $R = 0.93$. As summarized in **Table 7**, the average ratios for N_{RFN}/NIC and N_{ART}/NICare 0.35 and 0.65, respectively. On average, the number of artifact components is about twice of that for RFNs.

The tracking results of dataset 1 as a function of NIC for the motor-sensory are shown in **Figure 6**. For this dataset the

motor-sensory RFN splits into two ICs starting at NIC = 50. With increasing NIC, the split ICs exhibit consistently high degrees of similarity with the original IC at lower NICs as indicated by the relatively small variations in the rank of matching with the original IC (**Table 8**). The tracking results of dataset 4 as a function of NIC for the motor-sensory, visual and DMN RFNs are depicted in **Figures 7–9**, respectively. Similar to the tracking results of dataset 1, the motor-sensory RFN was only split once at NIC = 30 and the split-off ICs display little alterations over the entire investigated NIC interval 20–100. The visual RFN (medial) showed very little change over the entire range of NIC from 20 to 100, indicating that the primary visual system has very strong intra-network association. The DMN was first split into an anterior sub-network at NIC = 40. With further increase in NIC, an inferior split-off was detected at NIC = 80.

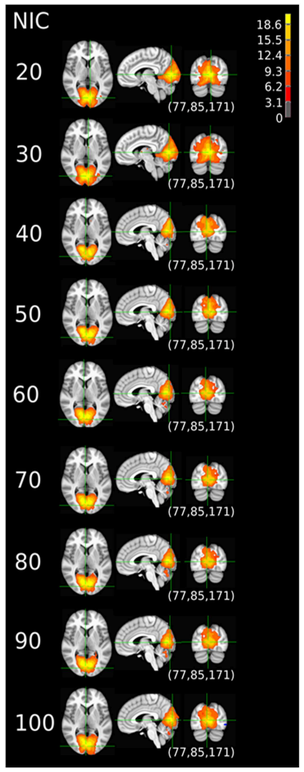

FIGURE 9 | The tracking results of dataset 4 for a typical RFN through similarity matching. The DMN was tracked at NIC = 20–100. An anterior and inferior split-offs were detected at NIC = 40 and 80, respectively.

In addition to the qualitative change associated with the split of a RFN at some specific NICs, with the increase of NIC there exist also gradual and quantitative changes in a given RFN and the trend of change can be quite specific for a given IC. This is clearly illustrated by **Figure 10** showing CISOTA as function of NIC for 3 RFNs and artifacts. Irrespective to the categories (RFN or ART), the change of a given IC can be quite steady as for motion artifact component and primary visual network or volatile as for the CSF artifact component and DMN. **Figure 11** shows another important aspect of IC change with NIC. At relatively low NIC = 33, incrementing NIC by 1 gives rise to changes in a large number of ICs. When NIC > 40, incrementing NIC by 1 results in changes in a few limited number of ICs. The NIC effect on ICA results can be further appreciated by examining the variance contribution of the ICs and the changes in the associated time courses. As shown **Figure 12**, the variance contribution from each IC is approximately an inverse function of NICirrespective to whether the IC is a potential RFN or artifact components. As indicated by the Pearson's correlation coefficient of the time courses for a given IC at different NIC (**Figures 12B,D**), the input NIC produces more significant impact on the time courses ICs when NIC is relatively small (e.g., NIC < 40).

Discussion

Classification Performance of FOCIS

When the model was trained by using a group ICA dataset and with heavy penalty on false positive rate, FOCIS tends to slightly over-estimate the number of potential RFNs and under-estimate the number of artifact ICs, as indicated by the false negative rate (4/231) in identifying artifact contaminated ICs. Compared to FSL-FIX, the performance of FOCIS in the automated classification of group ICA results is slightly improved in terms of accuracy, precisions and specificity. However, its performance in the classification of single subject data is somewhat poorer with

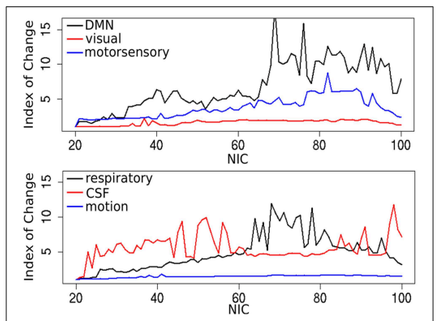

FIGURE 10 | Change index of spatial overlap and temporal association (CISOTA) as function of NIC for three typical RFNs (top) and artifact (bottom) components.

Wang and Li Feature optimized classification rs-fMRI ICA

motor-sensory RFN splits into two ICs starting at NIC = 50. With increasing NIC, the split ICs exhibit consistently high degrees of similarity with the original IC at lower NICs as indicated by the relatively small variations in the rank of matching with the original IC (**Table 8**). The tracking results of dataset 4 as a function of NIC for the motor-sensory, visual and DMN RFNs are depicted in **Figures 7–9**, respectively. Similar to the tracking results of dataset 1, the motor-sensory RFN was only split once at NIC = 30 and the split-off ICs display little alterations over the entire investigated NIC interval 20–100. The visual RFN (medial) showed very little change over the entire range of NIC from 20 to 100, indicating that the primary visual system has very strong intra-network association. The DMN was first split into an anterior sub-network at NIC = 40. With further increase in NIC, an inferior split-off was detected at NIC = 80.

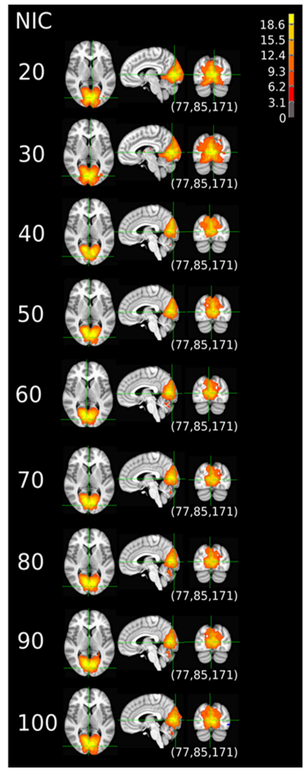

FIGURE 9 | The tracking results of dataset 4 for a typical RFN through similarity matching. The DMN was tracked at NIC = 20–100. An anterior and inferior split-offs were detected at NIC = 40 and 80, respectively.

In addition to the qualitative change associated with the split of a RFN at some specific NICs, with the increase of NIC there exist also gradual and quantitative changes in a given RFN and the trend of change can be quite specific for a given IC. This is clearly illustrated by **Figure 10** showing CISOTA as function of NIC for 3 RFNs and artifacts. Irrespective to the categories (RFN or ART), the change of a given IC can be quite steady as for motion artifact component and primary visual network or volatile as for the CSF artifact component and DMN. **Figure 11** shows another important aspect of IC change with NIC. At relatively low NIC = 33, incrementing NIC by 1 gives rise to changes in a large number of ICs. When NIC > 40, incrementing NIC by 1 results in changes in a few limited number of ICs. The NIC effect on ICA results can be further appreciated by examining the variance contribution of the ICs and the changes in the associated time courses. As shown **Figure 12**, the variance contribution from each IC is approximately an inverse function of NICirrespective to whether the IC is a potential RFN or artifact components. As indicated by the Pearson's correlation coefficient of the time courses for a given IC at different NIC (**Figures 12B,D**), the input NIC produces more significant impact on the time courses ICs when NIC is relatively small (e.g., NIC < 40).

Discussion

Classification Performance of FOCIS

When the model was trained by using a group ICA dataset and with heavy penalty on false positive rate, FOCIS tends to slightly over-estimate the number of potential RFNs and under-estimate the number of artifact ICs, as indicated by the false negative rate (4/231) in identifying artifact contaminated ICs. Compared to FSL-FIX, the performance of FOCIS in the automated classification of group ICA results is slightly improved in terms of accuracy, precisions and specificity. However, its performance in the classification of single subject data is somewhat poorer with

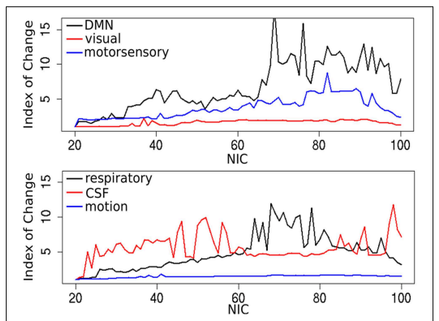

FIGURE 10 | Change index of spatial overlap and temporal association (CISOTA) as function of NIC for three typical RFNs (top) and artifact (bottom) components.

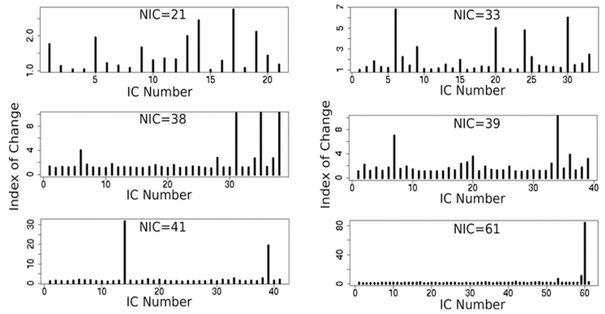

FIGURE 11 | Cross-sectional plots of change index of spatial overlap and temporal association (CISOTA) for all ICs at different 6 NICs.

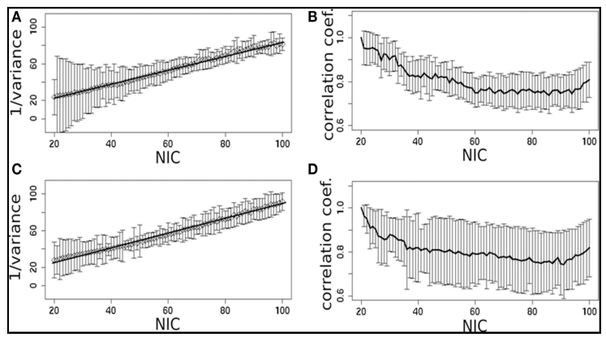

FIGURE 12 | The effect of NIC on the variance contribution of potential RFNs (A) and artifact components (C). The effect of NIC on the IC time courses for potential RFNs **(B)** and artifact components **(D)**.

an average accuracy of 91% (**Table 5**). As reported previously (Griffanti et al., 2014), the true false negative rate for FSL-FIX was 95.1% in the classification of single subject data acquired from 3T scanners with a comparable quality as that for the single subject data studied here. It is noticeable that the previously reported FSL-FIX result was based on training of multiple single-subject datasets, whereas the performance of FOCIS reported here is based on the training of a group ICA dataset (the dataset 1 at NIC = 50). It is probably reasonable to attribute the performance difference to the difference in training.

FSL-FIX employed a large number of features ranging from spatial and temporal characteristics to motion correction and image registration parameters, which is not only useful for identifying rare type of artifacts, but also favorable for situation with large within-class heterogeneity. This may partly explain the good performance of FSL-FIX in the automated classification of single subject ICA results. We cannot generalize that the more features the better performance in classification. In a recent study (Sochat et al., 2014) it was reported that as many as 246 features were employed to achieve a classification accuracy of 87%. Actually, we advocate the selection of features to optimize their classification power, because it does not only help improve the performance of the model but also enhances generalization capability, learning efficiency and model interpretability.

A closer examination of the misclassified ICs may provide some clues to account for the classification discrepancy between FOCIS and FSL-FIX. The misclassified ICs summarized in **Table 4** are depicted in in **Figure 13**. It is apparent that the main classification discrepancies between FOCIS and FSL-FIX lie in the ICs with relatively simple and regular geometries such as a single plane (e.g., most of ICs in the left column in **Figure 13**) and ICs having large portion of overlap with the cerebellum, such as most of the ICs in the middle column of **Figure 13**. As shown in **Table 2**, one of the five selected features in FOCIS is the ratio

Wang and Li Feature optimized classification rs-fMRI ICA

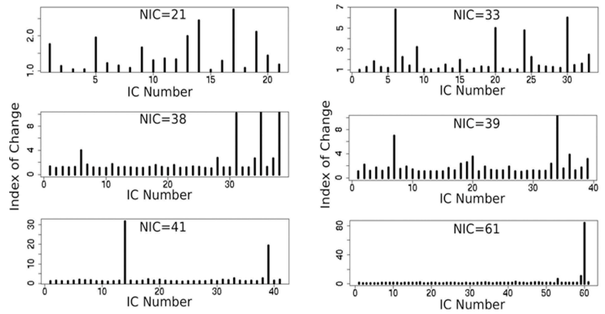

FIGURE 11 | Cross-sectional plots of change index of spatial overlap and temporal association (CISOTA) for all ICs at different 6 NICs.

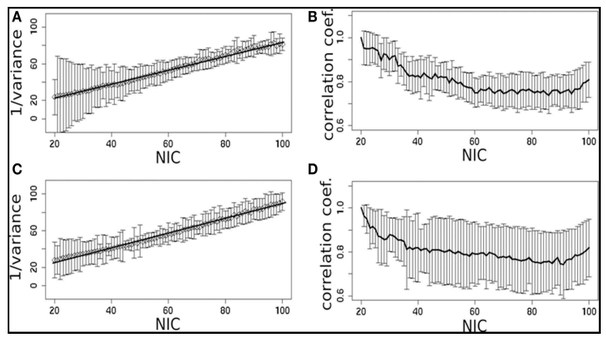

FIGURE 12 | The effect of NIC on the variance contribution of potential RFNs (A) and artifact components (C). The effect of NIC on the IC time courses for potential RFNs **(B)** and artifact components **(D)**.

an average accuracy of 91% (**Table 5**). As reported previously (Griffanti et al., 2014), the true false negative rate for FSL-FIX was 95.1% in the classification of single subject data acquired from 3T scanners with a comparable quality as that for the single subject data studied here. It is noticeable that the previously reported FSL-FIX result was based on training of multiple single-subject datasets, whereas the performance of FOCIS reported here is based on the training of a group ICA dataset (the dataset 1 at NIC = 50). It is probably reasonable to attribute the performance difference to the difference in training.

FSL-FIX employed a large number of features ranging from spatial and temporal characteristics to motion correction and image registration parameters, which is not only useful for identifying rare type of artifacts, but also favorable for situation with large within-class heterogeneity. This may partly explain the good performance of FSL-FIX in the automated classification of single subject ICA results. We cannot generalize that the more features the better performance in classification. In a recent study (Sochat et al., 2014) it was reported that as many as 246 features were employed to achieve a classification accuracy of 87%. Actually, we advocate the selection of features to optimize their classification power, because it does not only help improve the performance of the model but also enhances generalization capability, learning efficiency and model interpretability.

A closer examination of the misclassified ICs may provide some clues to account for the classification discrepancy between FOCIS and FSL-FIX. The misclassified ICs summarized in **Table 4** are depicted in in **Figure 13**. It is apparent that the main classification discrepancies between FOCIS and FSL-FIX lie in the ICs with relatively simple and regular geometries such as a single plane (e.g., most of ICs in the left column in **Figure 13**) and ICs having large portion of overlap with the cerebellum, such as most of the ICs in the middle column of **Figure 13**. As shown in **Table 2**, one of the five selected features in FOCIS is the ratio

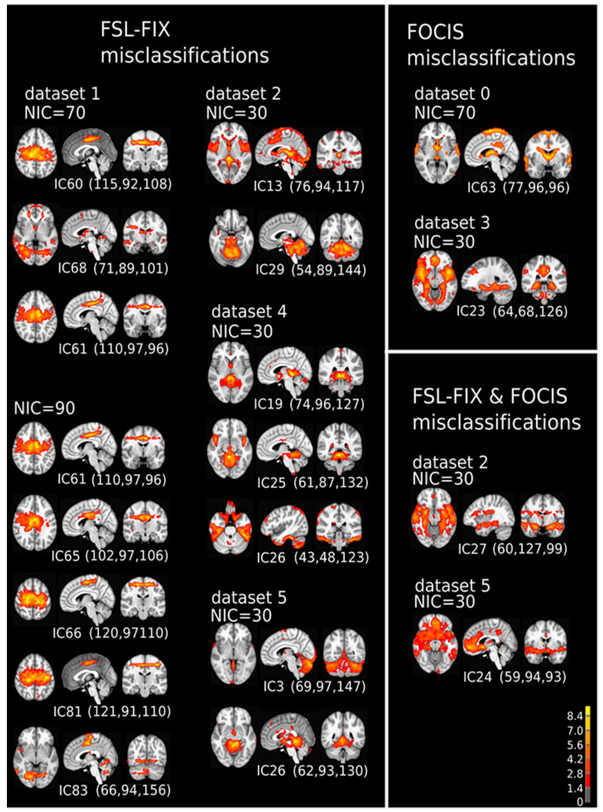

FIGURE 13 | The spatial patterns of all misclassified ICs summarized in Table 4.

of bounding box to voxel account, which is quite sensitive to IC with simple and regular geometries. For simplicity, the tissue templates used in FOCIS does not include cerebellum, it is no surprising that FOCIS reject ICs with large cerebellum overlaps.

It is noteworthy to point out that the using the manually classified ICs from two raters as the ground truth for training is certainly a limitation of the study and can be problematic. However, there is currently no good solution for it unless simulated data are used.

Classification of Borderline ICs

If the results from manual classification are considered as the ground truth, the misclassified ICs by FOCIS belong to the category of false negatives. As shown in the right column of **Figure 13**, all four ICs misclassified by FOCIS have the characteristics of borderline cases. They may represent meaningful RFN spatial patterns to some degree, but they are contaminated by one or multiple sources of artifacts such as susceptibility, motion, and vascular effects. The human raters classified these ICs as artifact components during the manual inspections due to the strong activities along the most superior location, at the bilateral edges of the temporal lobe, and smaller clusters in white matter and around the contour of the brain, which are classics of motion artifacts. However, the strong activities in the gray matter regions involving posterior cingulate, hypothalamus and thalamus are probably of RFN nature. Therefore, for the "misclassified" ICs, even the visually inspected results may be a matter of dispute.

Wang and Li Feature optimized classification rs-fMRI ICA

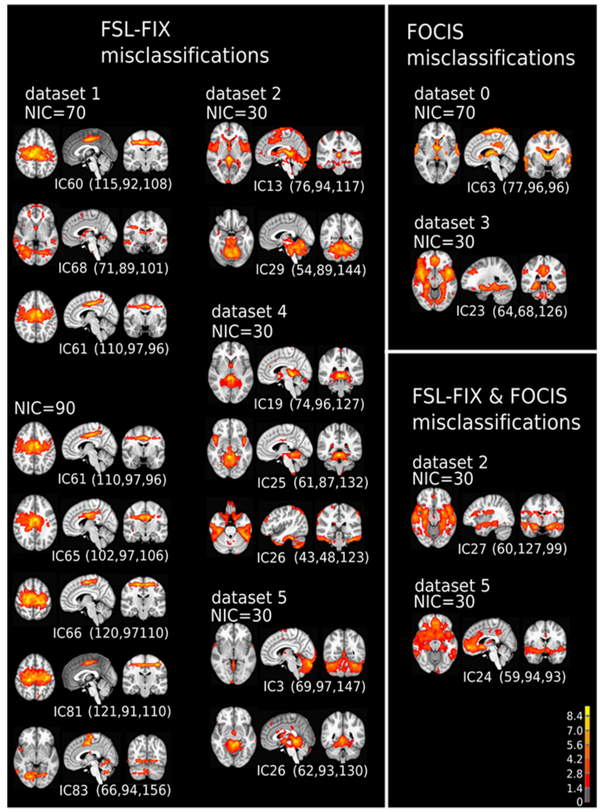

FIGURE 13 | The spatial patterns of all misclassified ICs summarized in Table 4.

of bounding box to voxel account, which is quite sensitive to IC with simple and regular geometries. For simplicity, the tissue templates used in FOCIS does not include cerebellum, it is no surprising that FOCIS reject ICs with large cerebellum overlaps.

It is noteworthy to point out that the using the manually classified ICs from two raters as the ground truth for training is certainly a limitation of the study and can be problematic. However, there is currently no good solution for it unless simulated data are used.

Classification of Borderline ICs

If the results from manual classification are considered as the ground truth, the misclassified ICs by FOCIS belong to the category of false negatives. As shown in the right column of **Figure 13**, all four ICs misclassified by FOCIS have the characteristics of borderline cases. They may represent meaningful RFN spatial patterns to some degree, but they are contaminated by one or multiple sources of artifacts such as susceptibility, motion, and vascular effects. The human raters classified these ICs as artifact components during the manual inspections due to the strong activities along the most superior location, at the bilateral edges of the temporal lobe, and smaller clusters in white matter and around the contour of the brain, which are classics of motion artifacts. However, the strong activities in the gray matter regions involving posterior cingulate, hypothalamus and thalamus are probably of RFN nature. Therefore, for the "misclassified" ICs, even the visually inspected results may be a matter of dispute.

Frontiers in Human Neuroscience | www.frontiersin.org 14 May 2015 | Volume 9 | Article 259

The Effects of NIC Input on the ICA Results

As discussed above, ICA can only extract the number of components defined a priori and the RSNs from ICA of resting-state fMRI data are very sensitive to the specified NIC input. This makes it difficult to compare ICA results of resting-state fMRI from different studies. It can even be problematic to compare group differences within the same study. Since the number of ICs are determined both by the potential RFNs and artifacts components, it less likely to find a ground truth common NIC for the different datasets. Even if the same model order parameter was used in the different studies, the obstacle could still remain, because the data acquisition and structured noise may differ substantially.

Different methods (Cordes and Nandy, 2006; Li et al., 2007; Xie et al., 2009; Chen et al., 2010; Beckmann, 2012) have been employed to improve the estimation of dimensionality. However, the rationality of the applied criterion is still questionable, because the estimates are typically dependent on SNR of the data and preprocessing pipeline steps, but not directly related to the neurophysiological properties. The use of a relatively low NIC in the range of 20–30 has the risk to discard potentially useful information, because the more complex RFNs are left aside as mixtures of real independent constituents. On the hand, the use of a large NIC can results in an excessive number of components with dissociated sources. Furthermore, algorithmic variability of ICA decomposition increases with NIC, we are left with a trade-off to choose between high modularity versus reproducibility and over-fitted ICs.

From the experimental point of view, there are nearly proportional increases in both N_{RFN} and N_{ART} with NIC for most of the datasets except for dataset 1 (see **Figure 4**). Neither the variation of N_{RFN} and N_{ART} as a function of NIC, nor the tracking the variance contribution of the ICs showed any clear sign of reaching a steady state or transition point. For dataset 1 there appears to be a clear upper limit for the number of RFNs at NIC $= 70 \pm 10$ beyond which only the number of artifact ICs increases as one increases NIC (**Figure 4**). This result is quite consistent with a previous report (Abou Elseoud et al., 2010; Elseoud et al., 2011) on the effect of NIC selection in group ICA. It was reported that NIC $= 70 \pm 10$ offered a more detailed evaluation of RSNs in spatial pattern, whereas NIC > 100 produced a decrease in ICA repeatability, but no gain in either volume or mean z-score results (Abou Elseoud et al., 2010; Elseoud et al., 2011). It is apparent that we cannot draw a general conclusion using the observations from a couple of datasets. It is unlikely that we can find a ground truth common NIC for the different datasets, because the number of ICs are determined both by the potential RFNs and artifacts components. From neuroscientific point of view, it is probably more productive to try to find a set of RFN template common for normal controls through ICA or other data-driven approaches. Therefore, tracking the spatial and temporal changes of some typical RFNs as a function of NIC can be very useful in gaining insight into how the RFNs are affected by selected NIC and deriving criterion for defining dimensionality of ICA in resting-state fMRI.

Conclusion

We have described a new tool, FOCIS, for the automated classification of artifact components in ICA results of resting-state fMRI data. Based on training of a group ICA dataset, FOCIS achieved on average 98 and 91% classification accuracy on the group and single subject ICA datasets, respectively. Therefore, FOCIS can be a very useful tool for assisting automated classification of ICA results from resting-state fMRI. The classification model employs the five most significant features to catch relevant spatial and temporal characteristics with most discriminative power to differentiate RFNs from artifacts components. Once trained a minimum account of hand-labeled data, FOCIS can be applied for automated classification of both group and single subject ICA results from resting-state fMRI datasets of different acquisition parameters without further intervention.

FOCIS is particularly useful for the studies involving a large number of ICs such as in the study of ICA dimensionality problem of resting-state fMRI datasets. With FOCIS, we were able to conduct systematically group ICA of six resting-state fMRI datasets acquired at different sites using different protocols as a function of NIC varied systematically from 20 to 100. We found that NIC can critically affect both the spatial pattern and temporal characteristics of the RFNs. The dimensionality problem deserves further investigations, because the input NIC can substantially affect group ICA results and the outcome of group comparison studies.

Acknowledgments

This study was supported by research grants from the Swedish Research Council and ALF Medicine in Stockholm. The authors also would like to acknowledge the support from Karolinska Institute and Karolinska University Hospital.

Supplementary Material

The Supplementary Material for this article can be found online at: http://journal.frontiersin.org/article/10.3389/fnhum.2015.00259/abstract

References

Abou Elseoud, A., Littow, H., Remes, J., Starck, T., Nikkinen, J., Nissila, J., et al. (2011). Group-ICA model order highlights patterns of functional brain connectivity. *Front. Syst. Neurosci.* 5:37. doi: 10.3389/fnsys.2011.00037

Abou Elseoud, A., Starck, T., Remes, J., Nikkinen, J., Tervonen, O., and Kiviniemi, V. (2010). The effect of model order selection in group PICA. *Hum. Brain Mapp.* 31, 1207–1216. doi: 10.1002/hbm.20929

Akaike, H. (1974). A new look at the statistical model identification. *Autom. Control IEEE Trans.* 19, 716–723. doi: 10.1109/TAC.1974.1100705

Wang and Li Feature optimized classification rs-fMRI ICA

The Effects of NIC Input on the ICA Results

As discussed above, ICA can only extract the number of components defined a priori and the RSNs from ICA of resting-state fMRI data are very sensitive to the specified NIC input. This makes it difficult to compare ICA results of resting-state fMRI from different studies. It can even be problematic to compare group differences within the same study. Since the number of ICs are determined both by the potential RFNs and artifacts components, it less likely to find a ground truth common NIC for the different datasets. Even if the same model order parameter was used in the different studies, the obstacle could still remain, because the data acquisition and structured noise may differ substantially.

Different methods (Cordes and Nandy, 2006; Li et al., 2007; Xie et al., 2009; Chen et al., 2010; Beckmann, 2012) have been employed to improve the estimation of dimensionality. However, the rationality of the applied criterion is still questionable, because the estimates are typically dependent on SNR of the data and preprocessing pipeline steps, but not directly related to the neurophysiological properties. The use of a relatively low NIC in the range of 20–30 has the risk to discard potentially useful information, because the more complex RFNs are left aside as mixtures of real independent constituents. On the hand, the use of a large NIC can results in an excessive number of components with dissociated sources. Furthermore, algorithmic variability of ICA decomposition increases with NIC, we are left with a trade-off to choose between high modularity versus reproducibility and over-fitted ICs.

From the experimental point of view, there are nearly proportional increases in both N_{RFN} and N_{ART} with NIC for most of the datasets except for dataset 1 (see **Figure 4**). Neither the variation of N_{RFN} and N_{ART} as a function of NIC, nor the tracking the variance contribution of the ICs showed any clear sign of reaching a steady state or transition point. For dataset 1 there appears to be a clear upper limit for the number of RFNs at NIC $= 70 \pm 10$ beyond which only the number of artifact ICs increases as one increases NIC (**Figure 4**). This result is quite consistent with a previous report (Abou Elseoud et al., 2010; Elseoud et al., 2011) on the effect of NIC selection in group ICA. It was reported that NIC $= 70 \pm 10$ offered a more detailed evaluation of RSNs in spatial pattern, whereas NIC > 100 produced a decrease in ICA repeatability, but no gain in either volume or mean z-score results (Abou Elseoud et al., 2010; Elseoud et al., 2011). It is apparent that we cannot draw a general conclusion using the observations from a couple of datasets. It is unlikely that we can find a ground truth common NIC for the different datasets, because the number of ICs are determined both by the potential RFNs and artifacts components. From neuroscientific point of view, it is probably more productive to try to find a set of RFN template common for normal controls through ICA or other data-driven approaches. Therefore, tracking the spatial and temporal changes of some typical RFNs as a function of NIC can be very useful in gaining insight into how the RFNs are affected by selected NIC and deriving criterion for defining dimensionality of ICA in resting-state fMRI.

Conclusion

We have described a new tool, FOCIS, for the automated classification of artifact components in ICA results of resting-state fMRI data. Based on training of a group ICA dataset, FOCIS achieved on average 98 and 91% classification accuracy on the group and single subject ICA datasets, respectively. Therefore, FOCIS can be a very useful tool for assisting automated classification of ICA results from resting-state fMRI. The classification model employs the five most significant features to catch relevant spatial and temporal characteristics with most discriminative power to differentiate RFNs from artifacts components. Once trained a minimum account of hand-labeled data, FOCIS can be applied for automated classification of both group and single subject ICA results from resting-state fMRI datasets of different acquisition parameters without further intervention.

FOCIS is particularly useful for the studies involving a large number of ICs such as in the study of ICA dimensionality problem of resting-state fMRI datasets. With FOCIS, we were able to conduct systematically group ICA of six resting-state fMRI datasets acquired at different sites using different protocols as a function of NIC varied systematically from 20 to 100. We found that NIC can critically affect both the spatial pattern and temporal characteristics of the RFNs. The dimensionality problem deserves further investigations, because the input NIC can substantially affect group ICA results and the outcome of group comparison studies.

Acknowledgments

This study was supported by research grants from the Swedish Research Council and ALF Medicine in Stockholm. The authors also would like to acknowledge the support from Karolinska Institute and Karolinska University Hospital.

Supplementary Material

The Supplementary Material for this article can be found online at: http://journal.frontiersin.org/article/10.3389/fnhum.2015.00259/abstract

References

Abou Elseoud, A., Littow, H., Remes, J., Starck, T., Nikkinen, J., Nissila, J., et al. (2011). Group-ICA model order highlights patterns of functional brain connectivity. *Front. Syst. Neurosci.* 5:37. doi: 10.3389/fnsys.2011.00037

Abou Elseoud, A., Starck, T., Remes, J., Nikkinen, J., Tervonen, O., and Kiviniemi, V. (2010). The effect of model order selection in group PICA. *Hum. Brain Mapp.* 31, 1207–1216. doi: 10.1002/hbm.20929

Akaike, H. (1974). A new look at the statistical model identification. *Autom. Control IEEE Trans.* 19, 716–723. doi: 10.1109/TAC.1974.1100705

Frontiers in Human Neuroscience | www.frontiersin.org 15 May 2015 | Volume 9 | Article 259

Allen, E. A., Erhardt, E. B., Damaraju, E., Gruner, W., Segall, J. M., Silva, R. F., et al. (2011). A baseline for the multivariate comparison of resting-state networks. *Front. Syst. Neurosci.* 5:2. doi: 10.3389/fnsys.2011.00002

Andrews, D. F. (1972). Plots of high-dimensional data. *Biometrics* 28, 125–136. doi: 10.2307/2528964

Bartels, A., and Zeki, S. (2005). Brain dynamics during natural viewing conditions -a new guide for mapping connectivity *in vivo*. *Neuroimage* 24, 339–349. doi: 10.1016/j.neuroimage.2004.08.044

Beckmann, C. F. (2012). Modelling with independent components. *Neuroimage* 62, 891–901. doi: 10.1016/j.neuroimage.2012.02.020

Beckmann, C. F., Deluca, M., Devlin, J. T., and Smith, S. M. (2005). Investigations into resting-state connectivity using independent component analysis. *Philos. Trans. R. Soc. B Biol. Sci.* 360, 1001–1013. doi: 10.1098/rstb.2005.1634

Beckmann, C. F., and Smith, S. M. (2004). Probabilistic independent component analysis for functional magnetic resonance imaging. *Med. Imaging IEEE Trans.* 23, 137–152. doi: 10.1109/TMI.2003.822821

Bhaganagarapu, K., Jackson, G. D., and Abbott, D. F. (2013). An automated method for identifying artifact in independent component analysis of resting-state fMRI. *Front. Hum. Neurosci.* 7:343. doi: 10.3389/fnhum.2013.00343

Calhoun, V., Adali, T., Pearlson, G., and Pekar, J. (2001). A method for making group inferences from functional MRI data using independent component analysis. *Hum. Brain Mapp.* 14, 140–151. doi: 10.1002/hbm.1048

Calhoun, V. D., Adali, T., Stevens, M. C., Kiehl, K. A., and Pekar, J. J. (2005). Semi-blind ICA of fMRI: a method for utilizing hypothesis-derived time courses in a spatial ICA analysis. *Neuroimage* 25, 527–538. doi: 10.1016/j.neuroimage.2004.12.012

Caputo, B., Sim, K., Furesjo, F., and Smola, A. (2002). "Appearance-based Object Recognition using SVMs: which Kernel Should I Use?" in *Proceedings of NIPS Workshop on Statistical Methods for Computational Experiments in Visual Processing and Computer Vision* (Vancouver, BC: Whistler).

Chang, C.-C., and Lin, C.-J. (2011). LIBSVM: a library for support vector machines. *ACM Trans. Intell. Syst. Technol.* 2, 27. doi: 10.1145/1961189.1961199

Chen, S., Ross, T. J., Chuang, K. S., Stein, E. A., Yang, Y., and Zhan, W. (2010). A new approach to estimating the signal dimension of concatenated resting-state functional MRI data sets. *Magn. Reson. Imaging* 28, 1344–1352. doi: 10.1016/j.mri.2010.04.002

Cordes, D., Haughton, V. M., Arfanakis, K., Wendt, G. J., Turski, P. A., Moritz, C. H., et al. (2000). Mapping functionally related regions of brain with functional connectivity MR imaging. *ANJR Am. J. Neuroradiol.* 21, 1636–1644.

Cordes, D., and Nandy, R. R. (2006). Estimation of the intrinsic dimensionality of fMRI data. *Neuroimage* 29, 145–154. doi: 10.1016/j.neuroimage.2005.07.054

Damoiseaux, J. S., Rombouts, S. A., Barkhof, F., Scheltens, P., Stam, C. J., Smith, S. M., et al. (2006). Consistent resting-state networks across healthy subjects. *Proc. Natl. Acad. Sci. U.S.A.* 103, 13848–13853. doi: 10.1073/pnas.0601417103

De Martino, F., Gentile, F., Esposito, F., Balsi, M., Di Salle, F., Goebel, R., et al. (2007). Classification of fMRI independent components using IC-fingerprints and support vector machine classifiers. *Neuroimage* 34, 177–194. doi: 10.1016/j.neuroimage.2006.08.041

Douglas, P. K., Harris, S., Yuille, A., and Cohen, M. S. (2011). Performance comparison of machine learning algorithms and number of independent components used in fMRI decoding of belief vs. disbelief. *Neuroimage* 56, 544–553. doi: 10.1016/j.neuroimage.2010.11.002

Elseoud, A. A., Littow, H., Remes, J., Starck, T., Nikkinen, J., Nissilä, J., et al. (2011). Group-ICA model order highlights patterns of functional brain connectivity. *Front. Syst. Neurosci.* 5:37. doi: 10.3389/fnsys.2011.00037

Formisano, E., Esposito, F., Kriegeskorte, N., Tedeschi, G., Di Salle, F., and Goebel, R. (2002). Spatial independent component analysis of functional magnetic resonance imaging time-series: characterization of the cortical components. *Neurocomputing* 49, 241–254. doi: 10.1016/S0925-2312(02)00517-9

Griffanti, L., Salimi-Khorshidi, G., Beckmann, C. F., Auerbach, E. J., Douaud, G., Sexton, C. E., et al. (2014). ICA-based artefact removal and accelerated fMRI acquisition for improved resting state network imaging. *Neuroimage* 95, 232–247. doi: 10.1016/j.neuroimage.2014.03.034

Jenkinson, M., Beckmann, C. F., Behrens, T. E., Woolrich, M. W., and Smith, S. M. (2012). FSL. *Neuroimage* 62, 782–790. doi: 10.1016/j.neuroimage.2011.09.015

Jo, H. J., Saad, Z. S., Simmons, W. K., Milbury, L. A., and Cox, R. W. (2010). Mapping sources of correlation in resting state FMRI, with artifact detection and removal. *Neuroimage* 52, 571–582. doi: 10.1016/j.neuroimage.2010.04.246

Karatzoglou, A., Smola, A., Hornik, K., Karatzoglou, M. A., Sparsem, S., and Yes, L. (2007). *The Kernlab Package.* The Comprehensive R Archive Network (CRAN). Available online at: http://cran.mirroring.de/doc/packages/kernlab.pdf

Karatzoglou, A., Smola, A., Hornik, K., and Zeileis, A. (2004). Kernlab-an S4 package for kernel methods in R. *J. Statistical Soft.* 11, 1–20. Available online at: http://www.jstatsoft.org/v11/i09/paper

Kiviniemi, V., Starck, T., Remes, J., Long, X., Nikkinen, J., Haapea, M., et al. (2009). Functional segmentation of the brain cortex using high model order group PICA. *Hum. Brain Mapp.* 30, 3865–3886. doi: 10.1002/hbm.20813

Kundu, P., Inati, S. J., Evans, J. W., Luh, W. M., and Bandettini, P. A. (2012). Differentiating BOLD and non-BOLD signals in fMRI time series using multi-echo EPI. *Neuroimage* 60, 1759–1770. doi: 10.1016/j.neuroimage.2011.12.028

Li, Y. O., Adali, T., and Calhoun, V. D. (2007). Estimating the number of independent components for functional magnetic resonance imaging data. *Hum. Brain Mapp.* 28, 1251–1266. doi: 10.1002/hbm.20359

Lin, C.-J., and Moré, J. J. (1999). Newton's method for large bound-constrained optimization problems. *SIAM J. Optimiz.* 9, 1100–1127. doi: 10.1137/S1052623498345075

Mangasarian, O. L., and Musicant, D. R. (1999). Successive overrelaxation for support vector machines. *Neural Netw. IEEE Trans.* 10, 1032–1037. doi: 10.1109/72.788643

Perlbarg, V., Bellec, P., Anton, J. L., Pelegrini-Issac, M., Doyon, J., and Benali, H. (2007). CORSICA: correction of structured noise in fMRI by automatic identification of ICA components. *Magn. Reson. Imaging* 25, 35–46. doi: 10.1016/j.mri.2006.09.042

Salimi-Khorshidi, G., Douaud, G., Beckmann, C. F., Glasser, M. F., Griffanti, L., and Smith, S. M. (2014). Automatic denoising of functional MRI data: combining independent component analysis and hierarchical fusion of classifiers. *Neuroimage* 90, 449–468. doi: 10.1016/j.neuroimage.2013.11.046

Schopf, V., Windischberger, C., Kasess, C. H., Lanzenberger, R., and Moser, E. (2010). Group ICA of resting-state data: a comparison. *Magnet. Reson. Mater. Phys. Biol. Med.* 23, 317–325. doi: 10.1007/s10334-010-0212-0

Schultz, A. P., Chhatwal, J. P., Huijbers, W., Hedden, T., Van Dijk, K. R., Mclaren, D. G., et al. (2014). Template based rotation: a method for functional connectivity analysis with a priori templates. *Neuroimage* 102(Pt 2), 620–636. doi: 10.1016/j.neuroimage.2014.08.022

Smith, S. M., Fox, P. T., Miller, K. L., Glahn, D. C., Fox, P. M., Mackay, C. E., et al. (2009). Correspondence of the brain's functional architecture during activation and rest. *Proc. Natl. Acad. Sci. U.S.A.* 106, 13040–13045. doi: 10.1073/pnas.0905267106

Smith, S. M., Jenkinson, M., Woolrich, M. W., Beckmann, C. F., Behrens, T. E., Johansen-Berg, H., et al. (2004). Advances in functional and structural MR image analysis and implementation as FSL. *Neuroimage* 23(Suppl. 1), S208–S219. doi: 10.1016/j.neuroimage.2004.07.051

Smola, A. J., and Schölkopf, B. (2004). A tutorial on support vector regression. *Stat. Comput.* 14, 199–222. doi: 10.1023/B:STCO.0000035301.49549.88

Sochat, V., Supekar, K., Bustillo, J., Calhoun, V., Turner, J. A., and Rubin, D. L. (2014). A robust classifier to distinguish noise from fMRI independent components. *PLoS ONE* 9:e95493. doi: 10.1371/journal.pone.0095493

Sui, J., Adali, T., Pearlson, G. D., and Calhoun, V. D. (2009). An ICA-based method for the identification of optimal FMRI features and components using combined group-discriminative techniques. *Neuroimage* 46, 73–86. doi: 10.1016/j.neuroimage.2009.01.026

Suzuki, K., Kiryu, T., and Nakada, T. (2002). Fast and precise independent component analysis for high field fMRI time series tailored using prior information on spatiotemporal structure. *Hum. Brain Mapp.* 15, 54–66. doi: 10.1002/hbm.1061

Vapnik, V., Golowich, S. E., and Smola, A. (1997). Support vector method for function approximation, regression estimation, and signal processing. *Adv. Neural Inform. Process. Syst.* 9, 281–287.

Wang, Y. L., and Li, T. Q. (2013). Analysis of whole-brain resting-state fMRI data using hierarchical clustering approach. *PLoS ONE* 8:e76315. doi: 10.1371/journal.pone.0076315

Wig, G. S., Laumann, T. O., and Petersen, S. E. (2014). An approach for parcellating human cortical areas using resting-state correlations. *Neuroimage* 93(Pt 2), 276–291. doi: 10.1016/j.neuroimage.2013.07.035

Wang and Li Feature optimized classification rs-fMRI ICA

Allen, E. A., Erhardt, E. B., Damaraju, E., Gruner, W., Segall, J. M., Silva, R. F., et al. (2011). A baseline for the multivariate comparison of resting-state networks. *Front. Syst. Neurosci.* 5:2. doi: 10.3389/fnsys.2011.00002

Andrews, D. F. (1972). Plots of high-dimensional data. *Biometrics* 28, 125–136. doi: 10.2307/2528964

Bartels, A., and Zeki, S. (2005). Brain dynamics during natural viewing conditions -a new guide for mapping connectivity *in vivo*. *Neuroimage* 24, 339–349. doi: 10.1016/j.neuroimage.2004.08.044

Beckmann, C. F. (2012). Modelling with independent components. *Neuroimage* 62, 891–901. doi: 10.1016/j.neuroimage.2012.02.020

Beckmann, C. F., Deluca, M., Devlin, J. T., and Smith, S. M. (2005). Investigations into resting-state connectivity using independent component analysis. *Philos. Trans. R. Soc. B Biol. Sci.* 360, 1001–1013. doi: 10.1098/rstb.2005.1634

Beckmann, C. F., and Smith, S. M. (2004). Probabilistic independent component analysis for functional magnetic resonance imaging. *Med. Imaging IEEE Trans.* 23, 137–152. doi: 10.1109/TMI.2003.822821

Bhaganagarapu, K., Jackson, G. D., and Abbott, D. F. (2013). An automated method for identifying artifact in independent component analysis of resting-state fMRI. *Front. Hum. Neurosci.* 7:343. doi: 10.3389/fnhum.2013.00343

Calhoun, V., Adali, T., Pearlson, G., and Pekar, J. (2001). A method for making group inferences from functional MRI data using independent component analysis. *Hum. Brain Mapp.* 14, 140–151. doi: 10.1002/hbm.1048

Calhoun, V. D., Adali, T., Stevens, M. C., Kiehl, K. A., and Pekar, J. J. (2005). Semi-blind ICA of fMRI: a method for utilizing hypothesis-derived time courses in a spatial ICA analysis. *Neuroimage* 25, 527–538. doi: 10.1016/j.neuroimage.2004.12.012

Caputo, B., Sim, K., Furesjo, F., and Smola, A. (2002). "Appearance-based Object Recognition using SVMs: which Kernel Should I Use?" in *Proceedings of NIPS Workshop on Statistical Methods for Computational Experiments in Visual Processing and Computer Vision* (Vancouver, BC: Whistler).

Chang, C.-C., and Lin, C.-J. (2011). LIBSVM: a library for support vector machines. *ACM Trans. Intell. Syst. Technol.* 2, 27. doi: 10.1145/1961189.1961199

Chen, S., Ross, T. J., Chuang, K. S., Stein, E. A., Yang, Y., and Zhan, W. (2010). A new approach to estimating the signal dimension of concatenated resting-state functional MRI data sets. *Magn. Reson. Imaging* 28, 1344–1352. doi: 10.1016/j.mri.2010.04.002

Cordes, D., Haughton, V. M., Arfanakis, K., Wendt, G. J., Turski, P. A., Moritz, C. H., et al. (2000). Mapping functionally related regions of brain with functional connectivity MR imaging. *ANJR Am. J. Neuroradiol.* 21, 1636–1644.

Cordes, D., and Nandy, R. R. (2006). Estimation of the intrinsic dimensionality of fMRI data. *Neuroimage* 29, 145–154. doi: 10.1016/j.neuroimage.2005.07.054

Damoiseaux, J. S., Rombouts, S. A., Barkhof, F., Scheltens, P., Stam, C. J., Smith, S. M., et al. (2006). Consistent resting-state networks across healthy subjects. *Proc. Natl. Acad. Sci. U.S.A.* 103, 13848–13853. doi: 10.1073/pnas.0601417103

De Martino, F., Gentile, F., Esposito, F., Balsi, M., Di Salle, F., Goebel, R., et al. (2007). Classification of fMRI independent components using IC-fingerprints and support vector machine classifiers. *Neuroimage* 34, 177–194. doi: 10.1016/j.neuroimage.2006.08.041

Douglas, P. K., Harris, S., Yuille, A., and Cohen, M. S. (2011). Performance comparison of machine learning algorithms and number of independent components used in fMRI decoding of belief vs. disbelief. *Neuroimage* 56, 544–553. doi: 10.1016/j.neuroimage.2010.11.002

Elseoud, A. A., Littow, H., Remes, J., Starck, T., Nikkinen, J., Nissilä, J., et al. (2011). Group-ICA model order highlights patterns of functional brain connectivity. *Front. Syst. Neurosci.* 5:37. doi: 10.3389/fnsys.2011.00037

Formisano, E., Esposito, F., Kriegeskorte, N., Tedeschi, G., Di Salle, F., and Goebel, R. (2002). Spatial independent component analysis of functional magnetic resonance imaging time-series: characterization of the cortical components. *Neurocomputing* 49, 241–254. doi: 10.1016/S0925-2312(02)00517-9

Griffanti, L., Salimi-Khorshidi, G., Beckmann, C. F., Auerbach, E. J., Douaud, G., Sexton, C. E., et al. (2014). ICA-based artefact removal and accelerated fMRI acquisition for improved resting state network imaging. *Neuroimage* 95, 232–247. doi: 10.1016/j.neuroimage.2014.03.034

Jenkinson, M., Beckmann, C. F., Behrens, T. E., Woolrich, M. W., and Smith, S. M. (2012). FSL. *Neuroimage* 62, 782–790. doi: 10.1016/j.neuroimage.2011.09.015

Jo, H. J., Saad, Z. S., Simmons, W. K., Milbury, L. A., and Cox, R. W. (2010). Mapping sources of correlation in resting state FMRI, with artifact detection and removal. *Neuroimage* 52, 571–582. doi: 10.1016/j.neuroimage.2010.04.246

Karatzoglou, A., Smola, A., Hornik, K., Karatzoglou, M. A., Sparsem, S., and Yes, L. (2007). *The Kernlab Package.* The Comprehensive R Archive Network (CRAN). Available online at: http://cran.mirroring.de/doc/packages/kernlab.pdf

Karatzoglou, A., Smola, A., Hornik, K., and Zeileis, A. (2004). Kernlab-an S4 package for kernel methods in R. *J. Statistical Soft.* 11, 1–20. Available online at: http://www.jstatsoft.org/v11/i09/paper

Kiviniemi, V., Starck, T., Remes, J., Long, X., Nikkinen, J., Haapea, M., et al. (2009). Functional segmentation of the brain cortex using high model order group PICA. *Hum. Brain Mapp.* 30, 3865–3886. doi: 10.1002/hbm.20813

Kundu, P., Inati, S. J., Evans, J. W., Luh, W. M., and Bandettini, P. A. (2012). Differentiating BOLD and non-BOLD signals in fMRI time series using multi-echo EPI. *Neuroimage* 60, 1759–1770. doi: 10.1016/j.neuroimage.2011.12.028

Li, Y. O., Adali, T., and Calhoun, V. D. (2007). Estimating the number of independent components for functional magnetic resonance imaging data. *Hum. Brain Mapp.* 28, 1251–1266. doi: 10.1002/hbm.20359

Lin, C.-J., and Moré, J. J. (1999). Newton's method for large bound-constrained optimization problems. *SIAM J. Optimiz.* 9, 1100–1127. doi: 10.1137/S1052623498345075

Mangasarian, O. L., and Musicant, D. R. (1999). Successive overrelaxation for support vector machines. *Neural Netw. IEEE Trans.* 10, 1032–1037. doi: 10.1109/72.788643

Perlbarg, V., Bellec, P., Anton, J. L., Pelegrini-Issac, M., Doyon, J., and Benali, H. (2007). CORSICA: correction of structured noise in fMRI by automatic identification of ICA components. *Magn. Reson. Imaging* 25, 35–46. doi: 10.1016/j.mri.2006.09.042

Salimi-Khorshidi, G., Douaud, G., Beckmann, C. F., Glasser, M. F., Griffanti, L., and Smith, S. M. (2014). Automatic denoising of functional MRI data: combining independent component analysis and hierarchical fusion of classifiers. *Neuroimage* 90, 449–468. doi: 10.1016/j.neuroimage.2013.11.046

Schopf, V., Windischberger, C., Kasess, C. H., Lanzenberger, R., and Moser, E. (2010). Group ICA of resting-state data: a comparison. *Magnet. Reson. Mater. Phys. Biol. Med.* 23, 317–325. doi: 10.1007/s10334-010-0212-0

Schultz, A. P., Chhatwal, J. P., Huijbers, W., Hedden, T., Van Dijk, K. R., Mclaren, D. G., et al. (2014). Template based rotation: a method for functional connectivity analysis with a priori templates. *Neuroimage* 102(Pt 2), 620–636. doi: 10.1016/j.neuroimage.2014.08.022

Smith, S. M., Fox, P. T., Miller, K. L., Glahn, D. C., Fox, P. M., Mackay, C. E., et al. (2009). Correspondence of the brain's functional architecture during activation and rest. *Proc. Natl. Acad. Sci. U.S.A.* 106, 13040–13045. doi: 10.1073/pnas.0905267106

Smith, S. M., Jenkinson, M., Woolrich, M. W., Beckmann, C. F., Behrens, T. E., Johansen-Berg, H., et al. (2004). Advances in functional and structural MR image analysis and implementation as FSL. *Neuroimage* 23(Suppl. 1), S208–S219. doi: 10.1016/j.neuroimage.2004.07.051

Smola, A. J., and Schölkopf, B. (2004). A tutorial on support vector regression. *Stat. Comput.* 14, 199–222. doi: 10.1023/B:STCO.0000035301.49549.88

Sochat, V., Supekar, K., Bustillo, J., Calhoun, V., Turner, J. A., and Rubin, D. L. (2014). A robust classifier to distinguish noise from fMRI independent components. *PLoS ONE* 9:e95493. doi: 10.1371/journal.pone.0095493

Sui, J., Adali, T., Pearlson, G. D., and Calhoun, V. D. (2009). An ICA-based method for the identification of optimal FMRI features and components using combined group-discriminative techniques. *Neuroimage* 46, 73–86. doi: 10.1016/j.neuroimage.2009.01.026

Suzuki, K., Kiryu, T., and Nakada, T. (2002). Fast and precise independent component analysis for high field fMRI time series tailored using prior information on spatiotemporal structure. *Hum. Brain Mapp.* 15, 54–66. doi: 10.1002/hbm.1061

Vapnik, V., Golowich, S. E., and Smola, A. (1997). Support vector method for function approximation, regression estimation, and signal processing. *Adv. Neural Inform. Process. Syst.* 9, 281–287.

Wang, Y. L., and Li, T. Q. (2013). Analysis of whole-brain resting-state fMRI data using hierarchical clustering approach. *PLoS ONE* 8:e76315. doi: 10.1371/journal.pone.0076315

Wig, G. S., Laumann, T. O., and Petersen, S. E. (2014). An approach for parcellating human cortical areas using resting-state correlations. *Neuroimage* 93(Pt 2), 276–291. doi: 10.1016/j.neuroimage.2013.07.035

Frontiers in Human Neuroscience | www.frontiersin.org 16 May 2015 | Volume 9 | Article 259

Wig, G. S., Schlaggar, B. L., and Petersen, S. E. (2011). Concepts and principles in the analysis of brain networks. *Ann. N. Y. Acad. Sci.* 1224, 126–146. doi: 10.1111/j.1749-6632.2010.05947.x

Woolrich, M. W., Jbabdi, S., Patenaude, B., Chappell, M., Makni, S., Behrens, T., et al. (2009). Bayesian analysis of neuroimaging data in FSL. *Neuroimage* 45, S173–S186. doi: 10.1016/j.neuroimage.2008.10.055

Xie, X., Cao, Z., Weng, X., and Jin, D. (2009). Estimating intrinsic dimensionality of fMRI dataset incorporating an AR (1) noise model with cubic spline interpolation. *Neurocomputing* 72, 1042–1055. doi: 10.1016/j.neucom.2008.04.003

Xu, Y. S., Tong, Y. X., Liu, S. Y., Chow, H., Abdulsabur, N. Y., Mattay, G. S., et al. (2014). Denoising the speaking brain: toward a robust technique for correcting artifact-contaminated fMRI data under severe motion. *Neuroimage* 103, 33–47. doi: 10.1016/j.neuroimage.2014.09.013

Yeo, B. T. T., Krienen, F. M., Sepulcre, J., Sabuncu, M. R., Lashkari, D., Hollinshead, M., et al. (2011). The organization of the human cerebral cortex estimated by intrinsic functional connectivity. *J. Neurophysiol.* 106, 1125–1165. doi: 10.1152/jn.00338.2011

Conflict of Interest Statement: The authors declare that the research was conducted in the absence of any commercial or financial relationships that could be construed as a potential conflict of interest.

Wang and Li Feature optimized classification rs-fMRI ICA

Wig, G. S., Schlaggar, B. L., and Petersen, S. E. (2011). Concepts and principles in the analysis of brain networks. *Ann. N. Y. Acad. Sci.* 1224, 126–146. doi: 10.1111/j.1749-6632.2010.05947.x

Woolrich, M. W., Jbabdi, S., Patenaude, B., Chappell, M., Makni, S., Behrens, T., et al. (2009). Bayesian analysis of neuroimaging data in FSL. *Neuroimage* 45, S173–S186. doi: 10.1016/j.neuroimage.2008.10.055

Xie, X., Cao, Z., Weng, X., and Jin, D. (2009). Estimating intrinsic dimensionality of fMRI dataset incorporating an AR (1) noise model with cubic spline interpolation. *Neurocomputing* 72, 1042–1055. doi: 10.1016/j.neucom.2008.04.003

Xu, Y. S., Tong, Y. X., Liu, S. Y., Chow, H., Abdulsabur, N. Y., Mattay, G. S., et al. (2014). Denoising the speaking brain: toward a robust technique for correcting artifact-contaminated fMRI data under severe motion. *Neuroimage* 103, 33–47. doi: 10.1016/j.neuroimage.2014.09.013

Yeo, B. T. T., Krienen, F. M., Sepulcre, J., Sabuncu, M. R., Lashkari, D., Hollinshead, M., et al. (2011). The organization of the human cerebral cortex estimated by intrinsic functional connectivity. *J. Neurophysiol.* 106, 1125–1165. doi: 10.1152/jn.00338.2011

Conflict of Interest Statement: The authors declare that the research was conducted in the absence of any commercial or financial relationships that could be construed as a potential conflict of interest.

Copyright © 2015 Wang and Li. This is an open-access article distributed under the terms of the Creative Commons Attribution License (CC BY). The use, distribution or reproduction in other forums is permitted, provided the original author(s) or licensor are credited and that the original publication in this journal is cited, in accordance with accepted academic practice. No use, distribution or reproduction is permitted which does not comply with these terms.

Frontiers in Human Neuroscience | www.frontiersin.org 17 May 2015 | Volume 9 | Article 259

III

III

Studying Sub-dendrograms of Resting-state Functional Networks with Voxel-wise Hierarchical Clustering

Yanlu Wang[1*], Mussie Msghina[2], Tie-Qiang Li[1,3]

[1]*Department of Clinical Science, Intervention, and Technology, Karolinska Institute, Stockholm, Sweden*

[2]*Department of Clinical Neuroscience, Karolinska University Hospital, Huddinge, Sweden*

[3]*Department of Medical Physics, Karolinska University Hospital, Huddinge, Sweden*

*Corresponding author:

Yanlu Wang
Department of Medical Physics,
Karolinska University Hospital Huddinge,
141 86 Stockholm
Sweden

Email: yanlu.wang@ki.se
Tel. +46 707 321 362

1

Studying Sub-dendrograms of Resting-state Functional Networks with Voxel-wise Hierarchical Clustering

Yanlu Wang[1*], Mussie Msghina[2], Tie-Qiang Li[1,3]

[1]*Department of Clinical Science, Intervention, and Technology, Karolinska Institute, Stockholm, Sweden*

[2]*Department of Clinical Neuroscience, Karolinska University Hospital, Huddinge, Sweden*

[3]*Department of Medical Physics, Karolinska University Hospital, Huddinge, Sweden*

*Corresponding author:

Yanlu Wang
Department of Medical Physics,
Karolinska University Hospital Huddinge,
141 86 Stockholm
Sweden

Email: yanlu.wang@ki.se
Tel. +46 707 321 362

Abstract

Hierarchical clustering is a useful data-driven approach to classify complex data and has been used to analyze resting-state functional magnetic resonance imaging (fMRI) data and derive functional networks of the human brain at very large scale, such as the entire visual or sensory-motor cortex. In this study, we developed a voxel-wise, whole-brain hierarchical clustering framework to perform multi-stage analysis of group-averaged resting-state fMRI data in different levels of detail. With the framework we analyzed particularly the somatosensory motor and visual systems in fine details and constructed the corresponding sub-dendrograms, which corroborate consistently with the known modular organizations from previous clinical and experimental studies. The framework provides a useful tool for data-driven analysis of resting-state fMRI data to gain insight into the hierarchical organization and degree of functional modulation among the sub-units.

2

Abstract

Hierarchical clustering is a useful data-driven approach to classify complex data and has been used to analyze resting-state functional magnetic resonance imaging (fMRI) data and derive functional networks of the human brain at very large scale, such as the entire visual or sensory-motor cortex. In this study, we developed a voxel-wise, whole-brain hierarchical clustering framework to perform multi-stage analysis of group-averaged resting-state fMRI data in different levels of detail. With the framework we analyzed particularly the somatosensory motor and visual systems in fine details and constructed the corresponding sub-dendrograms, which corroborate consistently with the known modular organizations from previous clinical and experimental studies. The framework provides a useful tool for data-driven analysis of resting-state fMRI data to gain insight into the hierarchical organization and degree of functional modulation among the sub-units.

2

2

Introduction

Different clustering techniques have been used for exploratory analysis of resting-state functional magnetic resonance imaging (fMRI) data aimed to group together functionally similar voxels or regions of interests (ROIs) and identify functionally connected brain networks. These include, among others, fuzzy C-means (Baumgartner et al., 1997;Hilgetag et al., 2000), spectral clustering (Snyder et al., 1997;Mattingley et al., 1998), K-means clustering (Fogassi et al., 2005), hierarchical clustering (Cordes et al., 2002;Foxe et al., 2002;Menon and Uddin, 2010;Wang and Li, 2013), consensus clustering (Moretti and Munoz, 2013) and constrained clustering (Snyder et al., 1997;Foxe et al., 2002). Hierarchical clustering analysis (HCA) has not been used as fluently as other clustering methods in the analysis of resting-state fMRI data probably due to its poor scalability, high complexity and sensitivity to noise outliers. However, HCA is completely deterministic and can stratify inherently the data into a hierarchical structure (Zhou et al., 2006;Marrelec et al., 2008;Gomez-Laberge et al., 2011;Boly et al., 2012). Although the structure nature of resting-state functional networks (RFNs) is still a matter of debate (Sporns, 2014), the notion that both structure and function connection networks exhibit a hierarchical organization of distinct brain modules that communicate through connector hubs is supported by a massive body of evidence ranging from cellular circuit of neuron connections to large-scale brain networks (Hilgetag et al., 2000;Zhou et al., 2006;Cohen et al., 2008;Ferrarini et al., 2009;Park and Friston, 2013;Zhen et al., 2013;Russo et al., 2014). Hence, extraction and characterization of such a hierarchical organization is an important issue in the study of brain function networks.

In spite of the successful application of HCA in extracting RFNs (Liu et al., 2012;Wang and Li, 2013;Alho et al., 2014), the results are strongly affected by the specified number of network clusters, which is not known *a priori*. Almost all of the previous clustering studies of resting-state fMRI attempt to parcel the data into a predefined number of clusters so that the clusters have high intra-cluster similarity and low inter-cluster similarity according to a chosen distance metric. Therefore, the outcome depends significantly on the choice of distance metric and the predefined number of clusters. In HCA, the cutting depth of dendrogram directly defines the number of produced clusters. Typically, over 10 RFNs are extracted from the group-averaged resting-state fMRI data (Cavanna and Trimble, 2006;Bellec et al., 2010;Wang and Li, 2013) in reference to the result form independent component analysis (ICA) studies (Damoiseaux et al., 2006;Smith et al., 2009), However, ICA result itself is also plagued with the issue of unknown number of independent components (Meunier et al., 2010;Bullmore and Sporns, 2012).

Due to lack of "ground truth" for the number of RFNs, clustering studies of resting-state fMRI data have to deal with the optimization of the number of clusters and assessment of clustering quality. Cluster validity index provides a tool to validate the performance of clustering algorithm and identify the natural structure in the input data.

3

Introduction

Different clustering techniques have been used for exploratory analysis of resting-state functional magnetic resonance imaging (fMRI) data aimed to group together functionally similar voxels or regions of interests (ROIs) and identify functionally connected brain networks. These include, among others, fuzzy C-means (Baumgartner et al., 1997;Hilgetag et al., 2000), spectral clustering (Snyder et al., 1997;Mattingley et al., 1998), K-means clustering (Fogassi et al., 2005), hierarchical clustering (Cordes et al., 2002;Foxe et al., 2002;Menon and Uddin, 2010;Wang and Li, 2013), consensus clustering (Moretti and Munoz, 2013) and constrained clustering (Snyder et al., 1997;Foxe et al., 2002). Hierarchical clustering analysis (HCA) has not been used as fluently as other clustering methods in the analysis of resting-state fMRI data probably due to its poor scalability, high complexity and sensitivity to noise outliers. However, HCA is completely deterministic and can stratify inherently the data into a hierarchical structure (Zhou et al., 2006;Marrelec et al., 2008;Gomez-Laberge et al., 2011;Boly et al., 2012). Although the structure nature of resting-state functional networks (RFNs) is still a matter of debate (Sporns, 2014), the notion that both structure and function connection networks exhibit a hierarchical organization of distinct brain modules that communicate through connector hubs is supported by a massive body of evidence ranging from cellular circuit of neuron connections to large-scale brain networks (Hilgetag et al., 2000;Zhou et al., 2006;Cohen et al., 2008;Ferrarini et al., 2009;Park and Friston, 2013;Zhen et al., 2013;Russo et al., 2014). Hence, extraction and characterization of such a hierarchical organization is an important issue in the study of brain function networks.

In spite of the successful application of HCA in extracting RFNs (Liu et al., 2012;Wang and Li, 2013;Alho et al., 2014), the results are strongly affected by the specified number of network clusters, which is not known *a priori*. Almost all of the previous clustering studies of resting-state fMRI attempt to parcel the data into a predefined number of clusters so that the clusters have high intra-cluster similarity and low inter-cluster similarity according to a chosen distance metric. Therefore, the outcome depends significantly on the choice of distance metric and the predefined number of clusters. In HCA, the cutting depth of dendrogram directly defines the number of produced clusters. Typically, over 10 RFNs are extracted from the group-averaged resting-state fMRI data (Cavanna and Trimble, 2006;Bellec et al., 2010;Wang and Li, 2013) in reference to the result form independent component analysis (ICA) studies (Damoiseaux et al., 2006;Smith et al., 2009), However, ICA result itself is also plagued with the issue of unknown number of independent components (Meunier et al., 2010;Bullmore and Sporns, 2012).

Due to lack of "ground truth" for the number of RFNs, clustering studies of resting-state fMRI data have to deal with the optimization of the number of clusters and assessment of clustering quality. Cluster validity index provides a tool to validate the performance of clustering algorithm and identify the natural structure in the input data.

3

Moreover, it can be used to determine the correct number of clusters in a dataset through comparing the results of different clustering algorithms and different number of clusters. Many different cluster validity indexes have been proposed in the literature, e.g., Milligan and Cooper (Milligan and Cooper, 1985) presented a comparison of 30 HCA validity indexes. In general, these indices can be classified as internal and external indexes, the former are usually based on information intrinsic to the data, while the latter are based on prior knowledge about the data. The optimal number of clusters can be determined by identifying the "knee point" (where the validity index exhibits a sharp change) among the validity index values as a function of different numbers of clusters. This procedure can fail in practice, because there might not exist any "knee points" or the existence of multiple. Therefore, knowing how to define a robust clustering criterion is critical and requires a good understanding of the data. In single subject-based clustering, several works have reported that spatial reproducibility is an important quality measures (Zhou et al., 2006;Chan et al., 2008;Ferrarini et al., 2009;Bellec et al., 2010;Alho et al., 2014;Russo et al., 2014;Mejia et al., 2015) for resting-state fMRI data.

HCA has been previously used to analyze resting-state fMRI data (Cordes et al., 2002;Zhou et al., 2006;Marrelec et al., 2008;Gomez-Laberge et al., 2011;Ma et al., 2011;Boly et al., 2012). Most of these studies are based on either pre-defined region-of-interests (ROIs) or independent components from ICA (Zhou et al., 2006;Marrelec et al., 2008;Gomez-Laberge et al., 2011;Ma et al., 2011;Boly et al., 2012). With distance metrics derived from the average time course of ROIS or RFNs, the higher-level interrelationship among ROIs and independent components can be studied (Ma et al., 2011), In this study, we focus on voxel-based whole-brain HCA of average resting-state fMRI data. Our approach is based on multi-stage dissection of the full connectivity dendrogram derived using the time course of individual voxel (Wang and Li, 2013), We employed an average-linking agglomerative hierarchical clustering algorithm to generate the full correlation-coefficient dendrogram for grey matter in the brain with over $13x10^3$ nodes. We developed a framework that can be used to retrieve the entire linkage tree, dissect it at any desired level and track a given mother node and its associated children clusters in any two consecutive cuts of the dendrogram. Based on stop criteria derived from internal characteristics of the produced clusters, such as cluster size, weakest linkage, and inconsistency coefficient (IC), we devised an iterative procedure to extract the potential RFNs and sub-networks within a given RFN. Particularly, we investigated the somatosensory motor (SSM) and visual systems in fine details and constructed the sub-dendrograms of the RFNs according to the tracked association and distance metrics among the sub-units.

Materials and Methods

Ethics statement

The Central Ethical Review Board in Stockholm region approved this study permission including the recruiting ad and consent form used to provide information and obtain consent. All participants provided informed consent by voluntary signature.

4

Moreover, it can be used to determine the correct number of clusters in a dataset through comparing the results of different clustering algorithms and different number of clusters. Many different cluster validity indexes have been proposed in the literature, e.g., Milligan and Cooper (Milligan and Cooper, 1985) presented a comparison of 30 HCA validity indexes. In general, these indices can be classified as internal and external indexes, the former are usually based on information intrinsic to the data, while the latter are based on prior knowledge about the data. The optimal number of clusters can be determined by identifying the "knee point" (where the validity index exhibits a sharp change) among the validity index values as a function of different numbers of clusters. This procedure can fail in practice, because there might not exist any "knee points" or the existence of multiple. Therefore, knowing how to define a robust clustering criterion is critical and requires a good understanding of the data. In single subject-based clustering, several works have reported that spatial reproducibility is an important quality measures (Zhou et al., 2006;Chan et al., 2008;Ferrarini et al., 2009;Bellec et al., 2010;Alho et al., 2014;Russo et al., 2014;Mejia et al., 2015) for resting-state fMRI data.

HCA has been previously used to analyze resting-state fMRI data (Cordes et al., 2002;Zhou et al., 2006;Marrelec et al., 2008;Gomez-Laberge et al., 2011;Ma et al., 2011;Boly et al., 2012). Most of these studies are based on either pre-defined region-of-interests (ROIs) or independent components from ICA (Zhou et al., 2006;Marrelec et al., 2008;Gomez-Laberge et al., 2011;Ma et al., 2011;Boly et al., 2012). With distance metrics derived from the average time course of ROIS or RFNs, the higher-level interrelationship among ROIs and independent components can be studied (Ma et al., 2011), In this study, we focus on voxel-based whole-brain HCA of average resting-state fMRI data. Our approach is based on multi-stage dissection of the full connectivity dendrogram derived using the time course of individual voxel (Wang and Li, 2013), We employed an average-linking agglomerative hierarchical clustering algorithm to generate the full correlation-coefficient dendrogram for grey matter in the brain with over $13x10^3$ nodes. We developed a framework that can be used to retrieve the entire linkage tree, dissect it at any desired level and track a given mother node and its associated children clusters in any two consecutive cuts of the dendrogram. Based on stop criteria derived from internal characteristics of the produced clusters, such as cluster size, weakest linkage, and inconsistency coefficient (IC), we devised an iterative procedure to extract the potential RFNs and sub-networks within a given RFN. Particularly, we investigated the somatosensory motor (SSM) and visual systems in fine details and constructed the sub-dendrograms of the RFNs according to the tracked association and distance metrics among the sub-units.

Materials and Methods

Ethics statement

The Central Ethical Review Board in Stockholm region approved this study permission including the recruiting ad and consent form used to provide information and obtain consent. All participants provided informed consent by voluntary signature.

4

Data acquisition

Resting-state fMRI measurements were conducted for a total of 84 normal adult subjects (male=40, 46, age=21-84) using a 3T whole-body clinical MRI scanner (TIM Trio, Siemens Healthcare, Erlangen, Germany). A single-shot 2D gradient-recalled echo echo-planar imaging sequence was used with the following acquisition parameters: 32 transverse slices (3.6mm thickness), TR/TE=2000/35ms, FOV=220mm, matrix size=64x64, flip angle=90°, 300 dynamic timeframes, IPAT=2. A 32-channel phased-array head coil was used for the signal reception. Foam paddings were used to for every subject reduce the head motions.

Preprocessing

The resting-state fMRI datasets underwent the same preprocessing procedure, which were performed with AFNI (http://afni.nimh.nih.gov/afni) and FSL (http://www.fmrib.ox.ac.uk/fsl) programs with a bash wrapper shell. The first 10 time frames in each data set were removed to ensure signal steady state. After temporal de-spiking, six-parameter rigid body image registration was performed for motion correction. The average volume for each motion-corrected time series was used to generate a brain mask to minimize the inclusion of the extra-cerebral tissues. Spatial normalization to the standard Talairach template was performed using a 12-parameter affine transformation and mutual-information cost function. The data was then resampled to isotropic resolution using a Gaussian kernel with FWHM=4mm. Nuisance signal removal was achieved by voxel-wise regression using the 14 regressors based on the motion correction parameters, average signal of the ventricles and their 1st order derivatives. To avoid creating excessive negative functional connectivity no regression of white matter signal was included. After baseline trend removal up to the third order polynomial, effective band-pass filtering was performed using low-pass filtering at 0.08Hz. Local Gaussian smoothing up to FWHM=6mm was performed using an eroded gray matter mask to reduce unnecessary partial volume effect from CSF and white matter. The actual FWHM of the smoothed data was 6.2±2 mm as estimated by using the AFNI program, 3dFWHM.

Hierarchical clustering to extract RFNs

Clustering was restricted to voxels inside the grey-matter using a grey-matter masked derived from FSL grey-matter tissue priors (http://www.fmrib.ox.ac.uk/fsl). For each subject, the Pearson's cross correlation (CC) distances were calculated voxel-wise for all datasets. The correlation distances were then evaluated with a threshold ≤0.7 corresponding to a correlation coefficient threshold CC≥0.3 (Cordes et al., 2002). After thresholding, approximately 1.1% of the correlation coefficients remained. Cordes et al (Cordes et al., 2002) used previously the same CC threshold of 0.3 for voxel-based hierarchical clustering and the same threshold was opted here for the individual dataset. We systematically changed the CC threshold and found that increasing the threshold above 0.3 resulted in the loss of robustness of the algorithm. A threshold of CC≥0.4 resulted in only about 0.1% of the values remained. After threshholding, all values above the threshold were set to an arbitrary large value. The cross correlation matrices for all subjects were then averaged together voxel-wise. The averaged distance matrix was then computed, which was used to perform hierarchical clustering through an average-linking agglomerative clustering algorithm as the basis for the framework (Wang and Li, 2013).

5

Data acquisition

Resting-state fMRI measurements were conducted for a total of 84 normal adult subjects (male=40, 46, age=21-84) using a 3T whole-body clinical MRI scanner (TIM Trio, Siemens Healthcare, Erlangen, Germany). A single-shot 2D gradient-recalled echo echo-planar imaging sequence was used with the following acquisition parameters: 32 transverse slices (3.6mm thickness), TR/TE=2000/35ms, FOV=220mm, matrix size=64x64, flip angle=90°, 300 dynamic timeframes, IPAT=2. A 32-channel phased-array head coil was used for the signal reception. Foam paddings were used to for every subject reduce the head motions.

Preprocessing

The resting-state fMRI datasets underwent the same preprocessing procedure, which were performed with AFNI (http://afni.nimh.nih.gov/afni) and FSL (http://www.fmrib.ox.ac.uk/fsl) programs with a bash wrapper shell. The first 10 time frames in each data set were removed to ensure signal steady state. After temporal de-spiking, six-parameter rigid body image registration was performed for motion correction. The average volume for each motion-corrected time series was used to generate a brain mask to minimize the inclusion of the extra-cerebral tissues. Spatial normalization to the standard Talairach template was performed using a 12-parameter affine transformation and mutual-information cost function. The data was then resampled to isotropic resolution using a Gaussian kernel with FWHM=4mm. Nuisance signal removal was achieved by voxel-wise regression using the 14 regressors based on the motion correction parameters, average signal of the ventricles and their 1st order derivatives. To avoid creating excessive negative functional connectivity no regression of white matter signal was included. After baseline trend removal up to the third order polynomial, effective band-pass filtering was performed using low-pass filtering at 0.08Hz. Local Gaussian smoothing up to FWHM=6mm was performed using an eroded gray matter mask to reduce unnecessary partial volume effect from CSF and white matter. The actual FWHM of the smoothed data was 6.2±2 mm as estimated by using the AFNI program, 3dFWHM.

Hierarchical clustering to extract RFNs

Clustering was restricted to voxels inside the grey-matter using a grey-matter masked derived from FSL grey-matter tissue priors (http://www.fmrib.ox.ac.uk/fsl). For each subject, the Pearson's cross correlation (CC) distances were calculated voxel-wise for all datasets. The correlation distances were then evaluated with a threshold ≤0.7 corresponding to a correlation coefficient threshold CC≥0.3 (Cordes et al., 2002). After thresholding, approximately 1.1% of the correlation coefficients remained. Cordes et al (Cordes et al., 2002) used previously the same CC threshold of 0.3 for voxel-based hierarchical clustering and the same threshold was opted here for the individual dataset. We systematically changed the CC threshold and found that increasing the threshold above 0.3 resulted in the loss of robustness of the algorithm. A threshold of CC≥0.4 resulted in only about 0.1% of the values remained. After threshholding, all values above the threshold were set to an arbitrary large value. The cross correlation matrices for all subjects were then averaged together voxel-wise. The averaged distance matrix was then computed, which was used to perform hierarchical clustering through an average-linking agglomerative clustering algorithm as the basis for the framework (Wang and Li, 2013).

5

A brief description of the algorithm is summarized as follows: Given a set of *N* voxels to be clustered, and a corresponding *N*×*N* distance matrix: 1) Assign each voxel to a cluster, resulting in *N* clusters, with each cluster containing just one voxel. The distances between the clusters are the distances among the voxels; 2) Find the closest pair of clusters; 3) Merge the closest pair of clusters, resulting in one cluster less in total; 4) Repeat 2-3 until only a single cluster remains. Step 3 can be performed in a variety of ways, referred to as linkage methods. The type of linkage in a hierarchical clustering algorithm refers to how the algorithm determines distance between newly formed clusters to all other voxels and clusters. Single-linkage takes the shortest distance between new clusters against the rest of the data, maximum-linkage takes the longest distance, and average-linkage takes the average. In our application, voxels within a cluster corresponding to a functional connectivity network should be highly correlated to each other. Hence, single-linkage is not desirable in this application. Maximum-linkage forces the algorithm to solely determine clusters with all voxels having high correlations to each other without exceptions. Average-linkage relaxes somewhat the intra-cluster connectivity requirements compared to maximum-linkage by taking the average distance. Hence, average-linkage was opted to take into account of the potential noise residues. We have previously described the algorithm in more details elsewhere (Wang and Li, 2013).

The algorithm produces a binary tree, known as a dendrogram, presenting the hierarchical organization of the individual elements as leafs according the pre-defined distance measure. *k* number of clusters can be retrieved by cutting the *k-1* longest links in the dendrogram. Since the number of meaningful clusters is unknown *a priori* and is affected by the noise level of the resting-state fMRI data, it is difficult to use the number of clusters as the termination criteria. Through tests on different cutting depths of the dendrogram, we developed an iterative scheme with termination criteria based on cluster size (*S*) to extract RFNs. A cluster larger than 5000 voxels in size ($S \geq 5000$) is considered too large to be a single RFNs, because the whole-brain grey matter mask that was used has 13312 voxels and analysis of the ICA results showed that clusters with more than 5000 voxels are usually too large to be considered as a single coherent RFN and should be refined further. Therefore, we choose 5000 as the upper limit for a cluster to be considered as an independent RFN. Analyses of the resulted clusters at different cutting levels showed that many of clusters are small clusters with less than 50 voxels (Wang and Li, 2013) and are not associated with any known RFNs. Therefore, we choose 50 as the lower limit for clusters to be considered as potential RFNs. In order to identify potential RFNs, Clusters with adequate voxel size ($50 \leq S \leq 5000$) were carefully examined by comparing their spatial distribution patterns with previously published RFNs in the literatures.

In the first iteration the cluster count for whole-brain dendrogram (k_1), was set to 64. Clusters above 5000 voxels in size (*S*) were then further dissected with a reduced cluster count by a factor of 2 than that for the previous iteration (k_2=32, k_3=16, and etc.). The cluster numbers for subsequent iterations were successively decreased accordingly to avoid spurious amounts of small clusters being generated. In order to identify potential RFNs, the empirical cluster size criteria ($50 \leq S \leq 5000$) discussed above was adopted to filter away small clusters (Wang and Li, 2013). The remaining

6

A brief description of the algorithm is summarized as follows: Given a set of *N* voxels to be clustered, and a corresponding *N*×*N* distance matrix: 1) Assign each voxel to a cluster, resulting in *N* clusters, with each cluster containing just one voxel. The distances between the clusters are the distances among the voxels; 2) Find the closest pair of clusters; 3) Merge the closest pair of clusters, resulting in one cluster less in total; 4) Repeat 2-3 until only a single cluster remains. Step 3 can be performed in a variety of ways, referred to as linkage methods. The type of linkage in a hierarchical clustering algorithm refers to how the algorithm determines distance between newly formed clusters to all other voxels and clusters. Single-linkage takes the shortest distance between new clusters against the rest of the data, maximum-linkage takes the longest distance, and average-linkage takes the average. In our application, voxels within a cluster corresponding to a functional connectivity network should be highly correlated to each other. Hence, single-linkage is not desirable in this application. Maximum-linkage forces the algorithm to solely determine clusters with all voxels having high correlations to each other without exceptions. Average-linkage relaxes somewhat the intra-cluster connectivity requirements compared to maximum-linkage by taking the average distance. Hence, average-linkage was opted to take into account of the potential noise residues. We have previously described the algorithm in more details elsewhere (Wang and Li, 2013).

The algorithm produces a binary tree, known as a dendrogram, presenting the hierarchical organization of the individual elements as leafs according the pre-defined distance measure. *k* number of clusters can be retrieved by cutting the *k-1* longest links in the dendrogram. Since the number of meaningful clusters is unknown *a priori* and is affected by the noise level of the resting-state fMRI data, it is difficult to use the number of clusters as the termination criteria. Through tests on different cutting depths of the dendrogram, we developed an iterative scheme with termination criteria based on cluster size (*S*) to extract RFNs. A cluster larger than 5000 voxels in size ($S \geq 5000$) is considered too large to be a single RFNs, because the whole-brain grey matter mask that was used has 13312 voxels and analysis of the ICA results showed that clusters with more than 5000 voxels are usually too large to be considered as a single coherent RFN and should be refined further. Therefore, we choose 5000 as the upper limit for a cluster to be considered as an independent RFN. Analyses of the resulted clusters at different cutting levels showed that many of clusters are small clusters with less than 50 voxels (Wang and Li, 2013) and are not associated with any known RFNs. Therefore, we choose 50 as the lower limit for clusters to be considered as potential RFNs. In order to identify potential RFNs, Clusters with adequate voxel size ($50 \leq S \leq 5000$) were carefully examined by comparing their spatial distribution patterns with previously published RFNs in the literatures.

In the first iteration the cluster count for whole-brain dendrogram (k_1), was set to 64. Clusters above 5000 voxels in size (*S*) were then further dissected with a reduced cluster count by a factor of 2 than that for the previous iteration (k_2=32, k_3=16, and etc.). The cluster numbers for subsequent iterations were successively decreased accordingly to avoid spurious amounts of small clusters being generated. In order to identify potential RFNs, the empirical cluster size criteria ($50 \leq S \leq 5000$) discussed above was adopted to filter away small clusters (Wang and Li, 2013). The remaining

6

prospective clusters were then carefully examined by comparing their spatial distribution patterns with ICA results and previously published RFNs in the literature (Wang and Li, 2013). Among the identified potential RFN clusters, we selected the RFNs corresponding to the SSM and visual systems for further analysis with the method described below. The basic information for the extracted SSM and visual RFNs is replicated and summarized in Table 1.

Hierarchical modular decomposition of the SSM and visual RFNs

One of the outputs from the framework is the whole dendrogram as a simple ASCII file that contains a list of nodes, their linking distance; connections to their children clusters; and the size of children clusters. With the node list and the associated information, any given node, cluster or sub-tree can be efficiently retrieved. Our framework contains a module that can be used to identify and visualize the split children clusters from any given mother node. For a given RFN (a sub-dendrogram), the module can be used to iterate through the list of nodes ordered in descending heights and systematically dissect through all nodes in the network. For a cut at node $k>0$, we compare the clusters with the results from the previous cut at node *k-1* to identify which cluster is split. Whenever a significant cluster ($p<0.01$) is split into two significant clusters, the mother node is denoted as a dissociable node and its children clusters are labeled for inspection and further analysis. The above process is repeated again for each significant child cluster. In principle, the iteration process can continue down to any desirable level of fine details. To facilitate the comparison between the results from the SSM and visual systems, we choose the cluster count corresponding to the first intersect point of the IC curves for the 2 investigated RFNs as the cutting depth. As shown in Figure 1, the IC curves intersect at IC=2.65 and the corresponding cut level is 80, which is a manageable size both for cluster characterization and visualization. For each RFN, the extracted functional connectivity sub-networks together with their node heights were then used to construct the intra-network sub-dendrogram.

Statistical assessment of the clustering results

As described above, for each resting-state fMRI dataset, we computed voxel-wise the Pearson's cross-correlation coefficients (CC) and thresholded at $CC\geq0.3$ (corresponding to a distance threshold ≤0.7). To assess the statistical significance of the inter-subject averaged CC matrix, we performed voxel-wise one-sampled t-test for the thresholded CC data (N=84 subjects) to test the null hypothesis that the inter-subject averaged CC at a given voxel is not significantly larger than 0. We computed also the voxel-wise skewness and kurtosis for the inter-subject averaged CC matrix. Examinations of the skewness and kurtosis versus the mean CC values show that the $-1.01<skewness<-1.0$ and $1.0<kurtosis<1.02$ when the averaged $CC\geq0.18$, indicating that the mean CC can be reasonably approximated as a normal distribution. Figure 2 depicts the scatter plot of the voxel-wise t-scores versus the mean CC values. Since the minimum averaged CC value for the voxels in the SSM and visual RFNs is 0.18 (Table 1), the voxel-wise t-score for any voxel in the RFNs is, therefore, at least ≥4.8 (Fig. 2), corresponding to voxel-wise $p<0.0001$ (uncorrected). A family-wise error (FEW) $p<0.01$ is guaranteed by imposing a minimum cluster size $s\geq12$, as estimated by using the AFNI program, AlphaSim with following inputs: voxel-wise $p<0.0001$, FWHM=6.2 mm, and 10^6 iterations. FWHM=6.2mm was the estimated average by

7

prospective clusters were then carefully examined by comparing their spatial distribution patterns with ICA results and previously published RFNs in the literature (Wang and Li, 2013). Among the identified potential RFN clusters, we selected the RFNs corresponding to the SSM and visual systems for further analysis with the method described below. The basic information for the extracted SSM and visual RFNs is replicated and summarized in Table 1.

Hierarchical modular decomposition of the SSM and visual RFNs

One of the outputs from the framework is the whole dendrogram as a simple ASCII file that contains a list of nodes, their linking distance; connections to their children clusters; and the size of children clusters. With the node list and the associated information, any given node, cluster or sub-tree can be efficiently retrieved. Our framework contains a module that can be used to identify and visualize the split children clusters from any given mother node. For a given RFN (a sub-dendrogram), the module can be used to iterate through the list of nodes ordered in descending heights and systematically dissect through all nodes in the network. For a cut at node $k>0$, we compare the clusters with the results from the previous cut at node *k-1* to identify which cluster is split. Whenever a significant cluster ($p<0.01$) is split into two significant clusters, the mother node is denoted as a dissociable node and its children clusters are labeled for inspection and further analysis. The above process is repeated again for each significant child cluster. In principle, the iteration process can continue down to any desirable level of fine details. To facilitate the comparison between the results from the SSM and visual systems, we choose the cluster count corresponding to the first intersect point of the IC curves for the 2 investigated RFNs as the cutting depth. As shown in Figure 1, the IC curves intersect at IC=2.65 and the corresponding cut level is 80, which is a manageable size both for cluster characterization and visualization. For each RFN, the extracted functional connectivity sub-networks together with their node heights were then used to construct the intra-network sub-dendrogram.

Statistical assessment of the clustering results

As described above, for each resting-state fMRI dataset, we computed voxel-wise the Pearson's cross-correlation coefficients (CC) and thresholded at $CC\geq0.3$ (corresponding to a distance threshold ≤0.7). To assess the statistical significance of the inter-subject averaged CC matrix, we performed voxel-wise one-sampled t-test for the thresholded CC data (N=84 subjects) to test the null hypothesis that the inter-subject averaged CC at a given voxel is not significantly larger than 0. We computed also the voxel-wise skewness and kurtosis for the inter-subject averaged CC matrix. Examinations of the skewness and kurtosis versus the mean CC values show that the $-1.01<skewness<-1.0$ and $1.0<kurtosis<1.02$ when the averaged $CC\geq0.18$, indicating that the mean CC can be reasonably approximated as a normal distribution. Figure 2 depicts the scatter plot of the voxel-wise t-scores versus the mean CC values. Since the minimum averaged CC value for the voxels in the SSM and visual RFNs is 0.18 (Table 1), the voxel-wise t-score for any voxel in the RFNs is, therefore, at least ≥4.8 (Fig. 2), corresponding to voxel-wise $p<0.0001$ (uncorrected). A family-wise error (FEW) $p<0.01$ is guaranteed by imposing a minimum cluster size $s\geq12$, as estimated by using the AFNI program, AlphaSim with following inputs: voxel-wise $p<0.0001$, FWHM=6.2 mm, and 10^6 iterations. FWHM=6.2mm was the estimated average by

7

applying the AFNI program, 3dFWHMx, to the final smoothed fMRI data, which was quite close to FWHM=6mm used in the final smoothing procedure described above.

Results

Sub-dendrogram of the SSM network

The Sub-networks for the SSM RFN were dissected down to 80 nodes (cut level *k*=79). Among the 80 nodes, 19 sub-networks amongst 20 dissociable nodes were identified (Tables 1 and 2) to be statistically significant ($p<0.01$ and $s\geq12$) and functionally distinct. The intra-network hierarchy of the extracted sub-networks and their neuroanatomical locations are depicted in Fig. 3. As shown, the extracted sub-networks for the SSM network include the following 4 groups of bilateral sub-networks: insula-auditory sub-networks (Fig. 3, clusters 1-3), paracentral lobule and cingulate motor cortex sub-networks (Fig. 3, clusters 4 and 5), sub-networks for facial expression control (Fig. 3, clusters 11-13), and sub-networks for hand movement control (Fig. 3, clusters 6, 7, 9, and 10). Furthermore, there exist also 2 groups of unilateral sub-networks: the right parietal sub-network group (Fig. 3, clusters 15 and 16) and the left insular-STG (superior temporal gyrus) sub-network group (Fig. 3, clusters 17-19). An overview of these sub-network groups in relation to the central sulcus is outlined in Fig. 4 as a 2D-projection in the Talairach coordinates. This intra-network organization of intrinsic functional connectivity derived from spontaneous activity of the brain at rest reflects consistently the functional and neural anatomic connectivity topography of the SSM network. SSM system in the human brain consists of S1, M1, and some pre/post- central gyrus areas divided into dorsal and ventral subgroups in addition to the parietal operculum and the auditory cortex (Power et al., 2011).

As shown in Figs. 3 and 4, the extracted sub-networks of SSM system are not exclusively localized to either side of the central sulcus rather its division is along the ventral-dorsal direction. This sub-division roughly separates the facial motor control from those for the rest of the body, as illustrated by the results of stimulus-evoked responses (Penfield and Boldrey, 1937;Mayka et al., 2006).

Another finding is that the cophenetic distance, defined as the threshold height at which the two sub-network groups join together, between two sub-network groups is not determined by the anatomical spatial distance rather than the level of functional conjunction between the involved brain sub-networks. E.g., the cophenetic distance between auditory (Fig 3, clusters 1-3) and paracentral lobule (Fig. 3 cluster 4) sub-network groups is 0.72, which is closer than that between auditory and facial-expression control (Fig3, clusters 11-13) sub-network groups (0.74) or between auditory and hand control (Fig. 3 clusters 6, 7, 9, and 10) sub-network groups (0.76).

The unilateral sub-network group in the right hemisphere (Fig. 3, clusters 15 and 16) involves two anterior regions of the parietal lobe: Precuneus and inferior parietal, which have closely related functions for visual-spatial abilities and motor coordination strategies (Snyder et al., 1997;Mattingley et al., 1998;Margulies et al.,

8

applying the AFNI program, 3dFWHMx, to the final smoothed fMRI data, which was quite close to FWHM=6mm used in the final smoothing procedure described above.

Results

Sub-dendrogram of the SSM network

The Sub-networks for the SSM RFN were dissected down to 80 nodes (cut level *k*=79). Among the 80 nodes, 19 sub-networks amongst 20 dissociable nodes were identified (Tables 1 and 2) to be statistically significant ($p<0.01$ and $s\geq12$) and functionally distinct. The intra-network hierarchy of the extracted sub-networks and their neuroanatomical locations are depicted in Fig. 3. As shown, the extracted sub-networks for the SSM network include the following 4 groups of bilateral sub-networks: insula-auditory sub-networks (Fig. 3, clusters 1-3), paracentral lobule and cingulate motor cortex sub-networks (Fig. 3, clusters 4 and 5), sub-networks for facial expression control (Fig. 3, clusters 11-13), and sub-networks for hand movement control (Fig. 3, clusters 6, 7, 9, and 10). Furthermore, there exist also 2 groups of unilateral sub-networks: the right parietal sub-network group (Fig. 3, clusters 15 and 16) and the left insular-STG (superior temporal gyrus) sub-network group (Fig. 3, clusters 17-19). An overview of these sub-network groups in relation to the central sulcus is outlined in Fig. 4 as a 2D-projection in the Talairach coordinates. This intra-network organization of intrinsic functional connectivity derived from spontaneous activity of the brain at rest reflects consistently the functional and neural anatomic connectivity topography of the SSM network. SSM system in the human brain consists of S1, M1, and some pre/post- central gyrus areas divided into dorsal and ventral subgroups in addition to the parietal operculum and the auditory cortex (Power et al., 2011).

As shown in Figs. 3 and 4, the extracted sub-networks of SSM system are not exclusively localized to either side of the central sulcus rather its division is along the ventral-dorsal direction. This sub-division roughly separates the facial motor control from those for the rest of the body, as illustrated by the results of stimulus-evoked responses (Penfield and Boldrey, 1937;Mayka et al., 2006).

Another finding is that the cophenetic distance, defined as the threshold height at which the two sub-network groups join together, between two sub-network groups is not determined by the anatomical spatial distance rather than the level of functional conjunction between the involved brain sub-networks. E.g., the cophenetic distance between auditory (Fig 3, clusters 1-3) and paracentral lobule (Fig. 3 cluster 4) sub-network groups is 0.72, which is closer than that between auditory and facial-expression control (Fig3, clusters 11-13) sub-network groups (0.74) or between auditory and hand control (Fig. 3 clusters 6, 7, 9, and 10) sub-network groups (0.76).

The unilateral sub-network group in the right hemisphere (Fig. 3, clusters 15 and 16) involves two anterior regions of the parietal lobe: Precuneus and inferior parietal, which have closely related functions for visual-spatial abilities and motor coordination strategies (Snyder et al., 1997;Mattingley et al., 1998;Margulies et al.,

8

2010). The unilateral sub-network group in the left hemisphere (Fig. 3 clusters 17-18) is the most loosely connected components in SSM network. It consists of lateral premotor cortex (cluster 17), anterior insula (cluster 18) and caudal auditory cortex (cluster 19). This sub-network group plays an important role in the sensorimotor integration to mediate the categorization of incoming speech sounds through reciprocal auditory-to-motor and motor-to-auditory projections (Schroeder et al., 2001;Foxe et al., 2002;Alho et al., 2014).

Sub-dendrogram of the visual RFN

Figure 5 shows the hierarchical clustering results for the visual RFN at cutting level k=79. Among the 80 nodes, 15 sub-networks amongst 14 dissociable nodes were identified (Tables 1 and 3) to be statistically significant ($p<0.01$ and $S\geq12$) and functional distinct. The intra-network hierarchical organization of the extracted sub-networks depicts 5 groups of bilateral sub-networks: primary visual cortex sub-network (Fig. 5, cluster 1), ventral medial sub-network (Fig. 5, cluster 2), dorsal sub-networks (Fig. 5 clusters 3-5), ventral inferior-occipital sub-networks (Fig. 5, clusters 6-9), and ventral posterior-temporal sub-networks (Fig. 5, clusters 10-15).

Central to the visual network is the primary visual area sub-network (Figure 5, cluster 1). The location of cluster 1 overlaps with the anatomical location of the primary visual cortex V1 and dorsal visual association area V2d. These visual areas are strongly correlated with each other, as it is known that V2 receives strong feed-forward from V1 and sends feedback to V1 (Gazzaniga et al., 2002). The sub-network with the least cophenetic distance to the primary visual cortex is the ventral medial visual sub-network (Figure 5, cluster 2). The anatomical location of this cluster (Table 3, cluster 2) is consistent with the retinotopical locations of the ventral medial visual area, located within the posterior parahippocampal cortex (PHC) extending along the collateral sulcus and flanked by the lingual gyrus (Arcaro et al., 2009;Wang et al., 2014). This sub-network is known to respond more strongly to scenes than objects or faces (Arcaro et al., 2009).

Overall, the sub-dendrogram of the visual RFN reflects the known functional sub-division of the visual system summarized as the two-stream hypothesis that the ventral stream and the dorsal stream have distinct functional sub-divisions (Ungerleider, 1982). The dorsal visual areas are specific for the detection of motion, locating objects in space, and processing visual information used to guide movements(Goodale and Milner, 1992), whereas the ventral visual association areas are associated with form recognition and object representation (Vartanian and Skov, 2014). As shown in Fig. 5, the cophenetic distance between the dorsal visual areas (Fig. 5, clusters 3-5) and V1 (Fig. 1, cluster 1) is 0.65, whereas the cophenetic distance between the ventral visual areas (Fig. 5, clusters 6-15) and V1 is 0.72. Therefore, the primary visual cortex is more closely associated with the dorsal visual stream than that with the ventral visual stream.

The bilateral clusters 3 and 4 correspond to visual association areas V3a and V3b respectively, both in terms of their anatomical locations and their lateral sub-divisions

9

2010). The unilateral sub-network group in the left hemisphere (Fig. 3 clusters 17-18) is the most loosely connected components in SSM network. It consists of lateral premotor cortex (cluster 17), anterior insula (cluster 18) and caudal auditory cortex (cluster 19). This sub-network group plays an important role in the sensorimotor integration to mediate the categorization of incoming speech sounds through reciprocal auditory-to-motor and motor-to-auditory projections (Schroeder et al., 2001;Foxe et al., 2002;Alho et al., 2014).

Sub-dendrogram of the visual RFN

Figure 5 shows the hierarchical clustering results for the visual RFN at cutting level k=79. Among the 80 nodes, 15 sub-networks amongst 14 dissociable nodes were identified (Tables 1 and 3) to be statistically significant ($p<0.01$ and $S\geq12$) and functional distinct. The intra-network hierarchical organization of the extracted sub-networks depicts 5 groups of bilateral sub-networks: primary visual cortex sub-network (Fig. 5, cluster 1), ventral medial sub-network (Fig. 5, cluster 2), dorsal sub-networks (Fig. 5 clusters 3-5), ventral inferior-occipital sub-networks (Fig. 5, clusters 6-9), and ventral posterior-temporal sub-networks (Fig. 5, clusters 10-15).

Central to the visual network is the primary visual area sub-network (Figure 5, cluster 1). The location of cluster 1 overlaps with the anatomical location of the primary visual cortex V1 and dorsal visual association area V2d. These visual areas are strongly correlated with each other, as it is known that V2 receives strong feed-forward from V1 and sends feedback to V1 (Gazzaniga et al., 2002). The sub-network with the least cophenetic distance to the primary visual cortex is the ventral medial visual sub-network (Figure 5, cluster 2). The anatomical location of this cluster (Table 3, cluster 2) is consistent with the retinotopical locations of the ventral medial visual area, located within the posterior parahippocampal cortex (PHC) extending along the collateral sulcus and flanked by the lingual gyrus (Arcaro et al., 2009;Wang et al., 2014). This sub-network is known to respond more strongly to scenes than objects or faces (Arcaro et al., 2009).

Overall, the sub-dendrogram of the visual RFN reflects the known functional sub-division of the visual system summarized as the two-stream hypothesis that the ventral stream and the dorsal stream have distinct functional sub-divisions (Ungerleider, 1982). The dorsal visual areas are specific for the detection of motion, locating objects in space, and processing visual information used to guide movements(Goodale and Milner, 1992), whereas the ventral visual association areas are associated with form recognition and object representation (Vartanian and Skov, 2014). As shown in Fig. 5, the cophenetic distance between the dorsal visual areas (Fig. 5, clusters 3-5) and V1 (Fig. 1, cluster 1) is 0.65, whereas the cophenetic distance between the ventral visual areas (Fig. 5, clusters 6-15) and V1 is 0.72. Therefore, the primary visual cortex is more closely associated with the dorsal visual stream than that with the ventral visual stream.

The bilateral clusters 3 and 4 correspond to visual association areas V3a and V3b respectively, both in terms of their anatomical locations and their lateral sub-divisions

9

(Wang et al., 2014). V3a and V3b border the inferior parietal sulcus visual area (IPS0/1) (Tootell et al., 1998;Press et al., 2001). This is consistent with our observation that clusters 3 and 4 are adjacent to the bilateral cluster 5, which corresponds to parietal visual areas IPS0. The cophenetic distance between the primary visual sub-network (Fig. 5, cluster 1) and visual areas IPS0/1 (Fig. 5, cluster 5) is 0.65, whereas the cophenetic distance between IPS0/1 and the visual association areas V3a and V3b (Fig. 5, clusters 3 and 4) is 0.69. This implies that IPS0/1 is more closely associated to the primary visual cortex than visual association areas V3a and V3b. This conforms the view that the parietal visual areas responsible for detection of motion, is comparatively faster relative to the ventral-temporal areas responsible for recognition and identification (Norman, 2002).

The ventral-stream visual association areas can be sub-divided into 2 sub-network groups according to the hierarchical functional sub-dendrogram: Inferior-occipital visual areas (Fig. 5, clusters 6-9) and posterior-temporal visual areas (Fig. 5, clusters 10-15). As shown in figure 5, the inferior-occipital ventral visual areas are more closely associated to V1 with a mean cophenetic distance of 0.68, compared to the posterior-temporal ventral visual areas (Fig. 5, clusters 10-15) with a mean cophenetic distance of 0.75. The anatomical location of cluster 6 overlaps with ventral visual area V2v and ventral visual area V3v (Wang et al., 2014). The cluster 7-9 forms bilateral clusters corresponding to ventral-temporal areas of human visual area V4 (hV4) and ventral- occipital visual area (VO1). Comparing with previously determined probabilistic maps of visual topography, we found that the boundaries of cluster 6 with clusters 7-9 are consistent with the known boundaries between hV4/VO1 and V3v (Sereno et al., 1995;DeYoe et al., 1996;Engel et al., 1997;Wade et al., 2002;Brewer et al., 2005). The clusters 10 and 11 correspond to the left and right middle-temporal visual area (MT)/V5 (Kolster et al., 2010), respectively. The bilateral cluster 12 corresponds well to the lateral occipital area 1 (LO1) (Wang et al., 2014). The clusters 13-15 have the largest cophenetic distances to V1 in the visual network and correspond to the medial superior temporal area (MST) (Wang et al., 2014).

Discussion

Voxel-wise Hierarchical Clustering of Resting-state fMRI Data

The agglomerative hierarchical clustering algorithm used in this study works by grouping the data one-by-one on the basis of the nearest distance measure of all the pairwise distance between voxel data points. It can inherently stratify the image data into hierarchical structures of different scales, such as RFNs and sub-networks within a given RFN. We have previously used HCA to analyze whole-brain resting-state fMRI data voxel-by-voxel and obtained large-scale RFN results that are comparable with what were obtained from ICA studies (Wang and Li, 2013). One of the main issues in using HCA of resting-state fMRI data to extract large-scale RFNs is the prerequisite to specify the number of clusters produced by the algorithm. Neither the number of RFNs present in the data nor the noise characteristics are known *a priori* when applying the algorithm to a given resting-state fMRI dataset. In other words, we need to establish the cutting depth of the dendrogram. After testing the framework with the group-averaged resting-state fMRI data using different number of clusters

10

(Wang et al., 2014). V3a and V3b border the inferior parietal sulcus visual area (IPS0/1) (Tootell et al., 1998;Press et al., 2001). This is consistent with our observation that clusters 3 and 4 are adjacent to the bilateral cluster 5, which corresponds to parietal visual areas IPS0. The cophenetic distance between the primary visual sub-network (Fig. 5, cluster 1) and visual areas IPS0/1 (Fig. 5, cluster 5) is 0.65, whereas the cophenetic distance between IPS0/1 and the visual association areas V3a and V3b (Fig. 5, clusters 3 and 4) is 0.69. This implies that IPS0/1 is more closely associated to the primary visual cortex than visual association areas V3a and V3b. This conforms the view that the parietal visual areas responsible for detection of motion, is comparatively faster relative to the ventral-temporal areas responsible for recognition and identification (Norman, 2002).

The ventral-stream visual association areas can be sub-divided into 2 sub-network groups according to the hierarchical functional sub-dendrogram: Inferior-occipital visual areas (Fig. 5, clusters 6-9) and posterior-temporal visual areas (Fig. 5, clusters 10-15). As shown in figure 5, the inferior-occipital ventral visual areas are more closely associated to V1 with a mean cophenetic distance of 0.68, compared to the posterior-temporal ventral visual areas (Fig. 5, clusters 10-15) with a mean cophenetic distance of 0.75. The anatomical location of cluster 6 overlaps with ventral visual area V2v and ventral visual area V3v (Wang et al., 2014). The cluster 7-9 forms bilateral clusters corresponding to ventral-temporal areas of human visual area V4 (hV4) and ventral- occipital visual area (VO1). Comparing with previously determined probabilistic maps of visual topography, we found that the boundaries of cluster 6 with clusters 7-9 are consistent with the known boundaries between hV4/VO1 and V3v (Sereno et al., 1995;DeYoe et al., 1996;Engel et al., 1997;Wade et al., 2002;Brewer et al., 2005). The clusters 10 and 11 correspond to the left and right middle-temporal visual area (MT)/V5 (Kolster et al., 2010), respectively. The bilateral cluster 12 corresponds well to the lateral occipital area 1 (LO1) (Wang et al., 2014). The clusters 13-15 have the largest cophenetic distances to V1 in the visual network and correspond to the medial superior temporal area (MST) (Wang et al., 2014).

Discussion

Voxel-wise Hierarchical Clustering of Resting-state fMRI Data

The agglomerative hierarchical clustering algorithm used in this study works by grouping the data one-by-one on the basis of the nearest distance measure of all the pairwise distance between voxel data points. It can inherently stratify the image data into hierarchical structures of different scales, such as RFNs and sub-networks within a given RFN. We have previously used HCA to analyze whole-brain resting-state fMRI data voxel-by-voxel and obtained large-scale RFN results that are comparable with what were obtained from ICA studies (Wang and Li, 2013). One of the main issues in using HCA of resting-state fMRI data to extract large-scale RFNs is the prerequisite to specify the number of clusters produced by the algorithm. Neither the number of RFNs present in the data nor the noise characteristics are known *a priori* when applying the algorithm to a given resting-state fMRI dataset. In other words, we need to establish the cutting depth of the dendrogram. After testing the framework with the group-averaged resting-state fMRI data using different number of clusters

10

and iterations to investigate how the choice of clustering parameters affect the outcomes, we proposed a multiple-iteration clustering scheme in combination with a cluster-size based criterion as the decision rules to extract potential RFNs (Wang and Li, 2013).

In this study, we further explored the potential of voxel-based hierarchical clustering of resting-state fMRI data and extended the previously developed framework to extract sub-networks within SSM and visual RFNs. As discussed above, the intra-network hierarchical organizations of the intrinsic functional connectivity derived from spontaneous activity of the brain at rest reflect consistently the known functional modular organizations of the corresponding neural networks. It is apparent that the level of details that can be achieved using the voxel-wise HCA framework spans from the large-scale RFNs down to a single voxel defined the fMRI spatial resolution. For simplicity of comparison in this study, we chose the 1st crossing point of their IC curves as the clustering stop condition. With this choice we have also taken into consideration of that the number of clusters should be within a manageable magnitude.

There are limitations in the implementation suggested here. Firstly, a threshold of 2.65 for the IC curves corresponding to the first crossing point is arguably somewhat arbitrary. As shown in Figure 1, the IC curves do not reach a plateau until IC<2.0, which corresponds to a cluster count over 200. This indicates that we can obtain substantially more clusters with considerable differences in correlation distance by lowering the threshold to IC>2.0. However, further lowering the threshold gives rise mostly smaller clusters, which are split-offs from the small clusters. It is difficult to give putative functional assignments to these split-offs. As shown in Tables 2 and 3, most clusters extracted at the threshold of 2.65 have already become relatively small except for the core clusters (cluster 4 in SSM and cluster 1 in visual RFN). It is more productive to dissect selectively the largest cluster with an additional iteration. Secondly, the criterion for cluster size and weakest linkage (minimum mean CC) were not automatically combined with the IC threshold instead they were manually implemented in a stepwise fashion.

The implemented hierarchical clustering scheme is, nevertheless, a principled means in which certain internal characteristics of the data, such as cluster size, IC, and weakest linkage, functioned as a validity metric for selecting the clustering results. The obtained sub-dendrograms for the SSM and visual system corroborate remarkably well with the known modular organizations from previous clinical and experimental studies. On the other hand, not only the core sub-networks (cluster 4 for SSM and cluster 1 for the visual RFN) are sufficiently large to warrant further iterations, it is also very interesting to investigate further their functional and structural subdivisions. Result from preliminary testing (not shown) indicates indeed that an additional HCA iteration applied directly to these clusters can produce interesting subdivisions that can lead better understanding of the functional organizations within these sub-networks.

11

and iterations to investigate how the choice of clustering parameters affect the outcomes, we proposed a multiple-iteration clustering scheme in combination with a cluster-size based criterion as the decision rules to extract potential RFNs (Wang and Li, 2013).

In this study, we further explored the potential of voxel-based hierarchical clustering of resting-state fMRI data and extended the previously developed framework to extract sub-networks within SSM and visual RFNs. As discussed above, the intra-network hierarchical organizations of the intrinsic functional connectivity derived from spontaneous activity of the brain at rest reflect consistently the known functional modular organizations of the corresponding neural networks. It is apparent that the level of details that can be achieved using the voxel-wise HCA framework spans from the large-scale RFNs down to a single voxel defined the fMRI spatial resolution. For simplicity of comparison in this study, we chose the 1st crossing point of their IC curves as the clustering stop condition. With this choice we have also taken into consideration of that the number of clusters should be within a manageable magnitude.

There are limitations in the implementation suggested here. Firstly, a threshold of 2.65 for the IC curves corresponding to the first crossing point is arguably somewhat arbitrary. As shown in Figure 1, the IC curves do not reach a plateau until IC<2.0, which corresponds to a cluster count over 200. This indicates that we can obtain substantially more clusters with considerable differences in correlation distance by lowering the threshold to IC>2.0. However, further lowering the threshold gives rise mostly smaller clusters, which are split-offs from the small clusters. It is difficult to give putative functional assignments to these split-offs. As shown in Tables 2 and 3, most clusters extracted at the threshold of 2.65 have already become relatively small except for the core clusters (cluster 4 in SSM and cluster 1 in visual RFN). It is more productive to dissect selectively the largest cluster with an additional iteration. Secondly, the criterion for cluster size and weakest linkage (minimum mean CC) were not automatically combined with the IC threshold instead they were manually implemented in a stepwise fashion.

The implemented hierarchical clustering scheme is, nevertheless, a principled means in which certain internal characteristics of the data, such as cluster size, IC, and weakest linkage, functioned as a validity metric for selecting the clustering results. The obtained sub-dendrograms for the SSM and visual system corroborate remarkably well with the known modular organizations from previous clinical and experimental studies. On the other hand, not only the core sub-networks (cluster 4 for SSM and cluster 1 for the visual RFN) are sufficiently large to warrant further iterations, it is also very interesting to investigate further their functional and structural subdivisions. Result from preliminary testing (not shown) indicates indeed that an additional HCA iteration applied directly to these clusters can produce interesting subdivisions that can lead better understanding of the functional organizations within these sub-networks.

11

Hierarchical modular organization of functional connectivity

Although the exact nature of the organization of brain function networks derived from resting-state fMRI is still a matter of debate, from cellular circuit of neuron connections to large-scale networks, there exists a massive body of evidence indicating that brain networks demonstrate the property of hierarchical modularity (Hilgetag et al., 2000;Zhou et al., 2006;Cohen et al., 2008;Ferrarini et al., 2009;Park and Friston, 2013;Zhen et al., 2013;Russo et al., 2014). This hierarchical modularity exists on multiple topological scales: Within each module there are a set of sub-modules, and within each sub-module a set of sub-sub-modules, etc. At a given topological scale, a module is often made up of densely inter-connected, anatomically and/or functionally related cortical regions, while inter-modular connections tend to be relatively long-distance and sparse. Although the detailed organization of brain networks across all scales is currently not yet fully experimentally accessible, there is a rapidly growing arsenal of data analytic tools, including the voxel-based hierarchical clustering developed in this study, that have been tested to analyze complex dendrograms of brain structural and functional networks.

At the large-scale and global levels, our understanding of brain connectivity topology relies mainly on the analysis of anatomical and functional connections measured by non-invasive brain imaging (Hilgetag et al., 2000;Zhou et al., 2006;Cohen et al., 2008;Ferrarini et al., 2009;Park and Friston, 2013;Zhen et al., 2013;Russo et al., 2014). Both clustering (Golland et al., 2008;Wang and Li, 2013) and ICA of brain imaging data (Wang and Li, 2015) are particularly important data-driven approaches to study brain network organization. Accumulating results from clustering and ICA studies demonstrate that the cerebral cortex can be divided into the extrinsic and intrinsic systems at the global scale (Golland et al., 2008). The former comprises the sensory–motor cortex and is associated with the external environment. The later overlaps substantially with the default mode network and is likely associated with inner-oriented processing. The development of voxel-based hierarchical clustering of brain imaging data provides not only a complementary approach to ICA for the analysis of brain networks at large-scale level, it allows also the study of sub-dendrograms of a given network or even sub-network as demonstrated by the results from this study. It can be used to explore the sub-units of a brain network down to the level of voxel of a few millimeters limited ultimately by the spatial resolution of the *in vivo* brain imaging data acquisition techniques.

Not only empirical data confirm the hierarchical modular organization at different scales (Hilgetag et al., 2000;Park and Friston, 2013), but also theoretical considerations favor the assumed hierarchical modular topology of brain networks (Meunier et al., 2010;Bullmore and Sporns, 2012;Moretti and Munoz, 2013;Park and Friston, 2013). It has been hypothesized that hierarchical modular organization of the brain is evolutionary advantageous, contributing to adaptive aspects of anatomical and functional brain connectivity. It enables the efficient processing of information, supports complex brain functions, and fits particularly for diverse dynamics and divergent functionalities within a fixed structure.

12

Hierarchical modular organization of functional connectivity

Although the exact nature of the organization of brain function networks derived from resting-state fMRI is still a matter of debate, from cellular circuit of neuron connections to large-scale networks, there exists a massive body of evidence indicating that brain networks demonstrate the property of hierarchical modularity (Hilgetag et al., 2000;Zhou et al., 2006;Cohen et al., 2008;Ferrarini et al., 2009;Park and Friston, 2013;Zhen et al., 2013;Russo et al., 2014). This hierarchical modularity exists on multiple topological scales: Within each module there are a set of sub-modules, and within each sub-module a set of sub-sub-modules, etc. At a given topological scale, a module is often made up of densely inter-connected, anatomically and/or functionally related cortical regions, while inter-modular connections tend to be relatively long-distance and sparse. Although the detailed organization of brain networks across all scales is currently not yet fully experimentally accessible, there is a rapidly growing arsenal of data analytic tools, including the voxel-based hierarchical clustering developed in this study, that have been tested to analyze complex dendrograms of brain structural and functional networks.

At the large-scale and global levels, our understanding of brain connectivity topology relies mainly on the analysis of anatomical and functional connections measured by non-invasive brain imaging (Hilgetag et al., 2000;Zhou et al., 2006;Cohen et al., 2008;Ferrarini et al., 2009;Park and Friston, 2013;Zhen et al., 2013;Russo et al., 2014). Both clustering (Golland et al., 2008;Wang and Li, 2013) and ICA of brain imaging data (Wang and Li, 2015) are particularly important data-driven approaches to study brain network organization. Accumulating results from clustering and ICA studies demonstrate that the cerebral cortex can be divided into the extrinsic and intrinsic systems at the global scale (Golland et al., 2008). The former comprises the sensory–motor cortex and is associated with the external environment. The later overlaps substantially with the default mode network and is likely associated with inner-oriented processing. The development of voxel-based hierarchical clustering of brain imaging data provides not only a complementary approach to ICA for the analysis of brain networks at large-scale level, it allows also the study of sub-dendrograms of a given network or even sub-network as demonstrated by the results from this study. It can be used to explore the sub-units of a brain network down to the level of voxel of a few millimeters limited ultimately by the spatial resolution of the *in vivo* brain imaging data acquisition techniques.

Not only empirical data confirm the hierarchical modular organization at different scales (Hilgetag et al., 2000;Park and Friston, 2013), but also theoretical considerations favor the assumed hierarchical modular topology of brain networks (Meunier et al., 2010;Bullmore and Sporns, 2012;Moretti and Munoz, 2013;Park and Friston, 2013). It has been hypothesized that hierarchical modular organization of the brain is evolutionary advantageous, contributing to adaptive aspects of anatomical and functional brain connectivity. It enables the efficient processing of information, supports complex brain functions, and fits particularly for diverse dynamics and divergent functionalities within a fixed structure.

12

In this report we limited our exploration within the intra-network sub-dendrograms of the SSM and visual RFNs at rather crude scale. In the future we will explore for using the developed HCA framework to study the following topics: 1) extract sub-dendrograms for other RFNs such as the default-mode network; 2) refine sub-dendrograms of the large clusters of the SSM and visual RNFs based on resting-state fMRI data at higher spatial resolution. We believe it is feasible to use voxel-based hierarchical clustering of resting-state fMRI data for detailed retinotopical and somatosensory mappings; 3) study the variations in sub-dendrograms, particularly in subjects with neurological and neuropsychiatric diseases.

Conclusion

Using the SSM and visual RFNs as examples, we have demonstrated that the developed HCA framework is a useful tool for analyzing resting-state fMRI data voxel-by-voxel. Not only can it be used to extract the modular organizations of brain functional networks at the scale of large systems (Wang and Li, 2013), such as the entire SSM and visual systems, but also can be used to derive the sub-dendrogram of a given RFN and dissect it at different level of details. The constructed sub-dendrogram for each RFN reveals the intrinsic functional connectivity among all sub-units within a RFN. For the two investigated RFNs (SSM and visual systems), the derived sub-dendrograms reflect consistently the known functional topographic mapping results. It should be possible to use the HCA framework for constructing sub-dendrograms of other RFNs and explore for potential but currently unknown functional junctions among the sub-units.

Acknowledgements

The authors also would like to acknowledge the support from Karolinska Institute and Karolinska University Hospital. This study was supported by research grants from the Swedish Research Council and ALF Medicine in Stockholm.

References

Alho, J., Lin, F.H., Sato, M., Tiitinen, H., Sams, M., and Jaaskelainen, I.P. (2014). Enhanced neural synchrony between left auditory and premotor cortex is associated with successful phonetic categorization. *Front Psychol* 5**,** 394.

Arcaro, M.J., Mcmains, S.A., Singer, B.D., and Kastner, S. (2009). Retinotopic organization of human ventral visual cortex. *J Neurosci* 29**,** 10638-10652. doi: 10.1523/jneurosci.2807-09.2009.

Baumgartner, R., Scarth, G., Teichtmeister, C., Somorjai, R., and Moser, E. (1997). Fuzzy clustering of gradient-echo functional MRI in the human visual cortex. Part I: reproducibility. *J Magn Reson Imaging* 7**,** 1094-1101.

Bellec, P., Rosa-Neto, P., Lyttelton, O.C., Benali, H., and Evans, A.C. (2010). Multi-level bootstrap analysis of stable clusters in resting-state fMRI. *Neuroimage* 51**,** 1126-1139.

Boly, M., Perlbarg, V., Marrelec, G., Schabus, M., Laureys, S., Doyon, J., Pélégrini-Issac, M., Maquet, P., and Benali, H. (2012). Hierarchical clustering of brain activity during human nonrapid eye movement sleep. *Proceedings of the National Academy of Sciences* 109**,** 5856-5861.

Brewer, A.A., Liu, J., Wade, A.R., and Wandell, B.A. (2005). Visual field maps and stimulus selectivity in human ventral occipital cortex. *Nat Neurosci* 8**,** 1102-1109. doi: 10.1038/nn1507.

13

In this report we limited our exploration within the intra-network sub-dendrograms of the SSM and visual RFNs at rather crude scale. In the future we will explore for using the developed HCA framework to study the following topics: 1) extract sub-dendrograms for other RFNs such as the default-mode network; 2) refine sub-dendrograms of the large clusters of the SSM and visual RNFs based on resting-state fMRI data at higher spatial resolution. We believe it is feasible to use voxel-based hierarchical clustering of resting-state fMRI data for detailed retinotopical and somatosensory mappings; 3) study the variations in sub-dendrograms, particularly in subjects with neurological and neuropsychiatric diseases.

Conclusion

Using the SSM and visual RFNs as examples, we have demonstrated that the developed HCA framework is a useful tool for analyzing resting-state fMRI data voxel-by-voxel. Not only can it be used to extract the modular organizations of brain functional networks at the scale of large systems (Wang and Li, 2013), such as the entire SSM and visual systems, but also can be used to derive the sub-dendrogram of a given RFN and dissect it at different level of details. The constructed sub-dendrogram for each RFN reveals the intrinsic functional connectivity among all sub-units within a RFN. For the two investigated RFNs (SSM and visual systems), the derived sub-dendrograms reflect consistently the known functional topographic mapping results. It should be possible to use the HCA framework for constructing sub-dendrograms of other RFNs and explore for potential but currently unknown functional junctions among the sub-units.

Acknowledgements

The authors also would like to acknowledge the support from Karolinska Institute and Karolinska University Hospital. This study was supported by research grants from the Swedish Research Council and ALF Medicine in Stockholm.

References

Alho, J., Lin, F.H., Sato, M., Tiitinen, H., Sams, M., and Jaaskelainen, I.P. (2014). Enhanced neural synchrony between left auditory and premotor cortex is associated with successful phonetic categorization. *Front Psychol* 5**,** 394.

Arcaro, M.J., Mcmains, S.A., Singer, B.D., and Kastner, S. (2009). Retinotopic organization of human ventral visual cortex. *J Neurosci* 29**,** 10638-10652. doi: 10.1523/jneurosci.2807-09.2009.

Baumgartner, R., Scarth, G., Teichtmeister, C., Somorjai, R., and Moser, E. (1997). Fuzzy clustering of gradient-echo functional MRI in the human visual cortex. Part I: reproducibility. *J Magn Reson Imaging* 7**,** 1094-1101.

Bellec, P., Rosa-Neto, P., Lyttelton, O.C., Benali, H., and Evans, A.C. (2010). Multi-level bootstrap analysis of stable clusters in resting-state fMRI. *Neuroimage* 51**,** 1126-1139.

Boly, M., Perlbarg, V., Marrelec, G., Schabus, M., Laureys, S., Doyon, J., Pélégrini-Issac, M., Maquet, P., and Benali, H. (2012). Hierarchical clustering of brain activity during human nonrapid eye movement sleep. *Proceedings of the National Academy of Sciences* 109**,** 5856-5861.

Brewer, A.A., Liu, J., Wade, A.R., and Wandell, B.A. (2005). Visual field maps and stimulus selectivity in human ventral occipital cortex. *Nat Neurosci* 8**,** 1102-1109. doi: 10.1038/nn1507.

Bullmore, E., and Sporns, O. (2012). The economy of brain network organization. *Nature Reviews Neuroscience* 13**,** 336-349.

Cavanna, A.E., and Trimble, M.R. (2006). The precuneus: a review of its functional anatomy and behavioural correlates. *Brain* 129**,** 564-583.

Chan, R.C., Shum, D., Toulopoulou, T., and Chen, E.Y. (2008). Assessment of executive functions: Review of instruments and identification of critical issues. *Archives of Clinical Neuropsychology* 23**,** 201-216.

Cohen, A.L., Fair, D.A., Dosenbach, N.U.F., Miezin, F.M., Dierker, D., Van Essen, D.C., Schlaggar, B.L., and Petersen, S.E. (2008). Defining functional areas in individual human brains using resting functional connectivity MRI. *Neuroimage* 41**,** 45-57. doi: 10.1016/j.neuroimage.2008.01.066.

Cordes, D., Haughton, V., Carew, J.D., Arfanakis, K., and Maravilla, K. (2002). Hierarchical clustering to measure connectivity in fMRI resting-state data. *Magnetic resonance imaging* 20**,** 305-317.

Damoiseaux, J., Rombouts, S., Barkhof, F., Scheltens, P., Stam, C., Smith, S., and Beckmann, C. (2006). Consistent resting-state networks across healthy subjects. *Proceedings of the National Academy of Sciences* 103**,** 13848.

Deyoe, E.A., Carman, G.J., Bandettini, P., Glickman, S., Wieser, J., Cox, R., Miller, D., and Neitz, J. (1996). Mapping striate and extrastriate visual areas in human cerebral cortex. *Proc Natl Acad Sci U S A* 93**,** 2382-2386.

Engel, S.A., Glover, G.H., and Wandell, B.A. (1997). Retinotopic organization in human visual cortex and the spatial precision of functional MRI. *Cereb Cortex* 7**,** 181-192.

Ferrarini, L., Veer, I.M., Baerends, E., Van Tol, M.J., Renken, R.J., Van Der Wee, N.J., Veltman, D.J., Aleman, A., Zitman, F.G., Penninx, B.W., Van Buchem, M.A., Reiber, J.H., Rombouts, S.A., and Milles, J. (2009). Hierarchical functional modularity in the resting-state human brain. *Hum Brain Mapp* 30**,** 2220-2231. doi: 10.1002/hbm.20663.

Fogassi, L., Ferrari, P.F., Gesierich, B., Rozzi, S., Chersi, F., and Rizzolatti, G. (2005). Parietal lobe: from action organization to intention understanding. *Science* 308**,** 662-667. doi: 10.1126/science.1106138.

Foxe, J.J., Wylie, G.R., Martinez, A., Schroeder, C.E., Javitt, D.C., Guilfoyle, D., Ritter, W., and Murray, M.M. (2002). Auditory-somatosensory multisensory processing in auditory association cortex: an fMRI study. *J Neurophysiol* 88**,** 540-543.

Gazzaniga, M., Ivry, R., and Mangun, G. (2002). The methods of cognitive Neuroscience. *Cognitive Neuroscience: The biology of mind* 2**,** 96-147.

Golland, Y., Golland, P., Bentin, S., and Malach, R. (2008). Data-driven clustering reveals a fundamental subdivision of the human cortex into two global systems. *Neuropsychologia* 46**,** 540-553.

Gomez-Laberge, C., Adler, A., Cameron, I., Nguyen, T., and Hogan, M. (2011). A Bayesian hierarchical correlation model for fMRI cluster analysis. *Biomedical Engineering, IEEE Transactions on***,** 1-1.

Goodale, M.A., and Milner, A.D. (1992). Separate visual pathways for perception and action. *Trends in neurosciences* 15**,** 20-25.

Hilgetag, C.C., O'neill, M.A., and Young, M.P. (2000). Hierarchical organization of macaque and cat cortical sensory systems explored with a novel network processor. *Philos Trans R Soc Lond B Biol Sci* 355**,** 71-89. doi: 10.1098/rstb.2000.0550.

Kolster, H., Peeters, R., and Orban, G.A. (2010). The retinotopic organization of the human middle temporal area MT/V5 and its cortical neighbors. *J Neurosci* 30**,** 9801-9820. doi: 10.1523/jneurosci.2069-10.2010.

Liu, X., Zhu, X.-H., Qiu, P., and Chen, W. (2012). A correlation-matrix-based hierarchical clustering method for functional connectivity analysis. *Journal of Neuroscience Methods*.

Ma, S., Eichele, T., Correa, N.M., Calhoun, V.D., and Adali, T. (Year). "Hierarchical and graphical analysis of fMRI network connectivity in healthy and schizophrenic groups", in: *Biomedical Imaging: From Nano to Macro, 2011 IEEE International Symposium on*: IEEE), 1031-1034.

Margulies, D.S., Böttger, J., Long, X., Lv, Y., Kelly, C., Schäfer, A., Goldhahn, D., Abbushi, A., Milham, M.P., and Lohmann, G. (2010). Resting developments: a review of fMRI post-processing methodologies for spontaneous brain activity. *Magnetic Resonance Materials in Physics, Biology and Medicine***,** 1-19.

Marrelec, G., Bellec, P., Krainik, A., Duffau, H., Pélégrini-Issac, M., Lehericy, S., Benali, H., and Doyon, J. (2008). Regions, systems, and the brain: hierarchical measures of functional integration in fMRI. *Medical image analysis* 12**,** 484-496.

14

Bullmore, E., and Sporns, O. (2012). The economy of brain network organization. *Nature Reviews Neuroscience* 13**,** 336-349.

Cavanna, A.E., and Trimble, M.R. (2006). The precuneus: a review of its functional anatomy and behavioural correlates. *Brain* 129**,** 564-583.

Chan, R.C., Shum, D., Toulopoulou, T., and Chen, E.Y. (2008). Assessment of executive functions: Review of instruments and identification of critical issues. *Archives of Clinical Neuropsychology* 23**,** 201-216.

Cohen, A.L., Fair, D.A., Dosenbach, N.U.F., Miezin, F.M., Dierker, D., Van Essen, D.C., Schlaggar, B.L., and Petersen, S.E. (2008). Defining functional areas in individual human brains using resting functional connectivity MRI. *Neuroimage* 41**,** 45-57. doi: 10.1016/j.neuroimage.2008.01.066.

Cordes, D., Haughton, V., Carew, J.D., Arfanakis, K., and Maravilla, K. (2002). Hierarchical clustering to measure connectivity in fMRI resting-state data. *Magnetic resonance imaging* 20**,** 305-317.

Damoiseaux, J., Rombouts, S., Barkhof, F., Scheltens, P., Stam, C., Smith, S., and Beckmann, C. (2006). Consistent resting-state networks across healthy subjects. *Proceedings of the National Academy of Sciences* 103**,** 13848.

Deyoe, E.A., Carman, G.J., Bandettini, P., Glickman, S., Wieser, J., Cox, R., Miller, D., and Neitz, J. (1996). Mapping striate and extrastriate visual areas in human cerebral cortex. *Proc Natl Acad Sci U S A* 93**,** 2382-2386.

Engel, S.A., Glover, G.H., and Wandell, B.A. (1997). Retinotopic organization in human visual cortex and the spatial precision of functional MRI. *Cereb Cortex* 7**,** 181-192.

Ferrarini, L., Veer, I.M., Baerends, E., Van Tol, M.J., Renken, R.J., Van Der Wee, N.J., Veltman, D.J., Aleman, A., Zitman, F.G., Penninx, B.W., Van Buchem, M.A., Reiber, J.H., Rombouts, S.A., and Milles, J. (2009). Hierarchical functional modularity in the resting-state human brain. *Hum Brain Mapp* 30**,** 2220-2231. doi: 10.1002/hbm.20663.

Fogassi, L., Ferrari, P.F., Gesierich, B., Rozzi, S., Chersi, F., and Rizzolatti, G. (2005). Parietal lobe: from action organization to intention understanding. *Science* 308**,** 662-667. doi: 10.1126/science.1106138.

Foxe, J.J., Wylie, G.R., Martinez, A., Schroeder, C.E., Javitt, D.C., Guilfoyle, D., Ritter, W., and Murray, M.M. (2002). Auditory-somatosensory multisensory processing in auditory association cortex: an fMRI study. *J Neurophysiol* 88**,** 540-543.

Gazzaniga, M., Ivry, R., and Mangun, G. (2002). The methods of cognitive Neuroscience. *Cognitive Neuroscience: The biology of mind* 2**,** 96-147.

Golland, Y., Golland, P., Bentin, S., and Malach, R. (2008). Data-driven clustering reveals a fundamental subdivision of the human cortex into two global systems. *Neuropsychologia* 46**,** 540-553.

Gomez-Laberge, C., Adler, A., Cameron, I., Nguyen, T., and Hogan, M. (2011). A Bayesian hierarchical correlation model for fMRI cluster analysis. *Biomedical Engineering, IEEE Transactions on***,** 1-1.

Goodale, M.A., and Milner, A.D. (1992). Separate visual pathways for perception and action. *Trends in neurosciences* 15**,** 20-25.

Hilgetag, C.C., O'neill, M.A., and Young, M.P. (2000). Hierarchical organization of macaque and cat cortical sensory systems explored with a novel network processor. *Philos Trans R Soc Lond B Biol Sci* 355**,** 71-89. doi: 10.1098/rstb.2000.0550.

Kolster, H., Peeters, R., and Orban, G.A. (2010). The retinotopic organization of the human middle temporal area MT/V5 and its cortical neighbors. *J Neurosci* 30**,** 9801-9820. doi: 10.1523/jneurosci.2069-10.2010.

Liu, X., Zhu, X.-H., Qiu, P., and Chen, W. (2012). A correlation-matrix-based hierarchical clustering method for functional connectivity analysis. *Journal of Neuroscience Methods*.

Ma, S., Eichele, T., Correa, N.M., Calhoun, V.D., and Adali, T. (Year). "Hierarchical and graphical analysis of fMRI network connectivity in healthy and schizophrenic groups", in: *Biomedical Imaging: From Nano to Macro, 2011 IEEE International Symposium on*: IEEE), 1031-1034.

Margulies, D.S., Böttger, J., Long, X., Lv, Y., Kelly, C., Schäfer, A., Goldhahn, D., Abbushi, A., Milham, M.P., and Lohmann, G. (2010). Resting developments: a review of fMRI post-processing methodologies for spontaneous brain activity. *Magnetic Resonance Materials in Physics, Biology and Medicine***,** 1-19.

Marrelec, G., Bellec, P., Krainik, A., Duffau, H., Pélégrini-Issac, M., Lehericy, S., Benali, H., and Doyon, J. (2008). Regions, systems, and the brain: hierarchical measures of functional integration in fMRI. *Medical image analysis* 12**,** 484-496.

14

Mattingley, J.B., Husain, M., Rorden, C., Kennard, C., and Driver, J. (1998). Motor role of human inferior parietal lobe revealed in unilateral neglect patients. *Nature* 392**,** 179-182. doi: 10.1038/32413.

Mayka, M.A., Corcos, D.M., Leurgans, S.E., and Vaillancourt, D.E. (2006). Three-dimensional locations and boundaries of motor and premotor cortices as defined by functional brain imaging: a meta-analysis. *Neuroimage* 31**,** 1453-1474. doi: 10.1016/j.neuroimage.2006.02.004.

Mejia, A.F., Nebel, M.B., Shou, H., Crainiceanu, C.M., Pekar, J.J., Mostofsky, S., Caffo, B., and Lindquist, M.A. (2015). Improving reliability of subject-level resting-state fMRI parcellation with shrinkage estimators. *Neuroimage* 112**,** 14-29. doi: 10.1016/j.neuroimage.2015.02.042.

Menon, V., and Uddin, L.Q. (2010). Saliency, switching, attention and control: a network model of insula function. *Brain Struct Funct* 214**,** 655-667. doi: 10.1007/s00429-010-0262-0.

Meunier, D., Lambiotte, R., and Bullmore, E.T. (2010). Modular and hierarchically modular organization of brain networks. *Frontiers in neuroscience* 4**,** 200. doi: 10.3389/fnins.2010.0020.

Milligan, G., and Cooper, M. (1985). An examination of procedures for determining the number of clusters in a data set. *Psychometrika* 50**,** 159-179.

Moretti, P., and Munoz, M.A. (2013). Griffiths phases and the stretching of criticality in brain networks. *Nature Communications* 4**,** 10. doi: 10.1038/ncomms3521.

Norman, J. (2002). Two visual systems and two theories of perception: An attempt to reconcile the constructivist and ecological approaches. *Behav Brain Sci* 25**,** 73-96; discussion 96-144.

Park, H.J., and Friston, K.J. (2013). Structural and Functional Brain Networks: From Connections to Cognition. *Science* 342**,** 579. doi: 10.1126/science.1238411.

Penfield, W., and Boldrey, E. (1937). Somatic motor and sensory representation in the cerebral cortex of man as studied by electrical stimulation. *Brain: A journal of neurology* 60**,** 389-443.

Power, J.D., Cohen, A.L., Nelson, S.M., Wig, G.S., Barnes, K.A., Church, J.A., Vogel, A.C., Laumann, T.O., Miezin, F.M., Schlaggar, B.L., and Petersen, S.E. (2011). Functional network organization of the human brain. *Neuron* 72**,** 665-678. doi: 10.1016/j.neuron.2011.09.006.

Press, W.A., Brewer, A.A., Dougherty, R.F., Wade, A.R., and Wandell, B.A. (2001). Visual areas and spatial summation in human visual cortex. *Vision Res* 41**,** 1321-1332.

Russo, R., Herrmann, H.J., and De Arcangelis, L. (2014). Brain modularity controls the critical behavior of spontaneous activity. *Sci Rep* 4**,** 4312. doi: 10.1038/srep04312.

Schroeder, C.E., Lindsley, R.W., Specht, C., Marcovici, A., Smiley, J.F., and Javitt, D.C. (2001). Somatosensory input to auditory association cortex in the macaque monkey. *J Neurophysiol* 85**,** 1322-1327.

Sereno, M.I., Dale, A.M., Reppas, J.B., Kwong, K.K., Belliveau, J.W., Brady, T.J., Rosen, B.R., and Tootell, R.B. (1995). Borders of multiple visual areas in humans revealed by functional magnetic resonance imaging. *Science* 268**,** 889-893.

Smith, S.M., Fox, P.T., Miller, K.L., Glahn, D.C., Fox, P.M., Mackay, C.E., Filippini, N., Watkins, K.E., Toro, R., and Laird, A.R. (2009). Correspondence of the brain's functional architecture during activation and rest. *Proceedings of the National Academy of Sciences* 106**,** 13040-13045.

Snyder, L.H., Batista, A.P., and Andersen, R.A. (1997). Coding of intention in the posterior parietal cortex. *Nature* 386**,** 167-170. doi: 10.1038/386167a0.

Sporns, O. (2014). Contributions and challenges for network models in cognitive neuroscience. *Nat Neurosci* 17**,** 652-660. doi: 10.1038/nn.3690.

Tootell, R.B., Hadjikhani, N., Hall, E.K., Marrett, S., Vanduffel, W., Vaughan, J.T., and Dale, A.M. (1998). The retinotopy of visual spatial attention. *Neuron* 21**,** 1409-1422.

Ungerleider, L.G. (1982). Two cortical visual systems. *Analysis of visual behavior***,** 549-586.

Vartanian, O., and Skov, M. (2014). Neural correlates of viewing paintings: Evidence from a quantitative meta-analysis of functional magnetic resonance imaging data. *Brain Cogn* 87**,** 52-56. doi: 10.1016/j.bandc.2014.03.004.

Wade, A.R., Brewer, A.A., Rieger, J.W., and Wandell, B.A. (2002). Functional measurements of human ventral occipital cortex: retinotopy and colour. *Philos Trans R Soc Lond B Biol Sci* 357**,** 963-973. doi: 10.1098/rstb.2002.1108.

Wang, L., Mruczek, R.E., Arcaro, M.J., and Kastner, S. (2014). Probabilistic Maps of Visual Topography in Human Cortex. *Cereb Cortex* 35. doi: 10.1093/cercor/bhu277.

15

Mattingley, J.B., Husain, M., Rorden, C., Kennard, C., and Driver, J. (1998). Motor role of human inferior parietal lobe revealed in unilateral neglect patients. *Nature* 392**,** 179-182. doi: 10.1038/32413.

Mayka, M.A., Corcos, D.M., Leurgans, S.E., and Vaillancourt, D.E. (2006). Three-dimensional locations and boundaries of motor and premotor cortices as defined by functional brain imaging: a meta-analysis. *Neuroimage* 31**,** 1453-1474. doi: 10.1016/j.neuroimage.2006.02.004.

Mejia, A.F., Nebel, M.B., Shou, H., Crainiceanu, C.M., Pekar, J.J., Mostofsky, S., Caffo, B., and Lindquist, M.A. (2015). Improving reliability of subject-level resting-state fMRI parcellation with shrinkage estimators. *Neuroimage* 112**,** 14-29. doi: 10.1016/j.neuroimage.2015.02.042.

Menon, V., and Uddin, L.Q. (2010). Saliency, switching, attention and control: a network model of insula function. *Brain Struct Funct* 214**,** 655-667. doi: 10.1007/s00429-010-0262-0.

Meunier, D., Lambiotte, R., and Bullmore, E.T. (2010). Modular and hierarchically modular organization of brain networks. *Frontiers in neuroscience* 4**,** 200. doi: 10.3389/fnins.2010.0020.

Milligan, G., and Cooper, M. (1985). An examination of procedures for determining the number of clusters in a data set. *Psychometrika* 50**,** 159-179.

Moretti, P., and Munoz, M.A. (2013). Griffiths phases and the stretching of criticality in brain networks. *Nature Communications* 4**,** 10. doi: 10.1038/ncomms3521.

Norman, J. (2002). Two visual systems and two theories of perception: An attempt to reconcile the constructivist and ecological approaches. *Behav Brain Sci* 25**,** 73-96; discussion 96-144.

Park, H.J., and Friston, K.J. (2013). Structural and Functional Brain Networks: From Connections to Cognition. *Science* 342**,** 579. doi: 10.1126/science.1238411.

Penfield, W., and Boldrey, E. (1937). Somatic motor and sensory representation in the cerebral cortex of man as studied by electrical stimulation. *Brain: A journal of neurology* 60**,** 389-443.

Power, J.D., Cohen, A.L., Nelson, S.M., Wig, G.S., Barnes, K.A., Church, J.A., Vogel, A.C., Laumann, T.O., Miezin, F.M., Schlaggar, B.L., and Petersen, S.E. (2011). Functional network organization of the human brain. *Neuron* 72**,** 665-678. doi: 10.1016/j.neuron.2011.09.006.

Press, W.A., Brewer, A.A., Dougherty, R.F., Wade, A.R., and Wandell, B.A. (2001). Visual areas and spatial summation in human visual cortex. *Vision Res* 41**,** 1321-1332.

Russo, R., Herrmann, H.J., and De Arcangelis, L. (2014). Brain modularity controls the critical behavior of spontaneous activity. *Sci Rep* 4**,** 4312. doi: 10.1038/srep04312.

Schroeder, C.E., Lindsley, R.W., Specht, C., Marcovici, A., Smiley, J.F., and Javitt, D.C. (2001). Somatosensory input to auditory association cortex in the macaque monkey. *J Neurophysiol* 85**,** 1322-1327.

Sereno, M.I., Dale, A.M., Reppas, J.B., Kwong, K.K., Belliveau, J.W., Brady, T.J., Rosen, B.R., and Tootell, R.B. (1995). Borders of multiple visual areas in humans revealed by functional magnetic resonance imaging. *Science* 268**,** 889-893.

Smith, S.M., Fox, P.T., Miller, K.L., Glahn, D.C., Fox, P.M., Mackay, C.E., Filippini, N., Watkins, K.E., Toro, R., and Laird, A.R. (2009). Correspondence of the brain's functional architecture during activation and rest. *Proceedings of the National Academy of Sciences* 106**,** 13040-13045.

Snyder, L.H., Batista, A.P., and Andersen, R.A. (1997). Coding of intention in the posterior parietal cortex. *Nature* 386**,** 167-170. doi: 10.1038/386167a0.

Sporns, O. (2014). Contributions and challenges for network models in cognitive neuroscience. *Nat Neurosci* 17**,** 652-660. doi: 10.1038/nn.3690.

Tootell, R.B., Hadjikhani, N., Hall, E.K., Marrett, S., Vanduffel, W., Vaughan, J.T., and Dale, A.M. (1998). The retinotopy of visual spatial attention. *Neuron* 21**,** 1409-1422.

Ungerleider, L.G. (1982). Two cortical visual systems. *Analysis of visual behavior***,** 549-586.

Vartanian, O., and Skov, M. (2014). Neural correlates of viewing paintings: Evidence from a quantitative meta-analysis of functional magnetic resonance imaging data. *Brain Cogn* 87**,** 52-56. doi: 10.1016/j.bandc.2014.03.004.

Wade, A.R., Brewer, A.A., Rieger, J.W., and Wandell, B.A. (2002). Functional measurements of human ventral occipital cortex: retinotopy and colour. *Philos Trans R Soc Lond B Biol Sci* 357**,** 963-973. doi: 10.1098/rstb.2002.1108.

Wang, L., Mruczek, R.E., Arcaro, M.J., and Kastner, S. (2014). Probabilistic Maps of Visual Topography in Human Cortex. *Cereb Cortex* 35. doi: 10.1093/cercor/bhu277.

15

Wang, Y., and Li, T.Q. (2015). Dimensionality of ICA in Resting-State fMRI Investigated by Feature Optimized Classification of Independent Components with SVM. *Front Hum Neurosci* 9**,** 259. doi: 10.3389/fnhum.2015.00259.
Wang, Y.L., and Li, T.Q. (2013). Analysis of Whole-Brain Resting-State fMRI Data Using Hierarchical Clustering Approach. *Plos One* 8. doi: 10.1371/journal.pone.0076315.
Zhen, Z., Fang, H., and Liu, J. (2013). The hierarchical brain network for face recognition. *PLoS One* 8**,** e59886. doi: 10.1371/journal.pone.0059886.
Zhou, C., Zemanova, L., Zamora, G., Hilgetag, C.C., and Kurths, J. (2006). Hierarchical organization unveiled by functional connectivity in complex brain networks. *Phys Rev Lett* 97**,** 238103.

16

Wang, Y., and Li, T.Q. (2015). Dimensionality of ICA in Resting-State fMRI Investigated by Feature Optimized Classification of Independent Components with SVM. *Front Hum Neurosci* 9**,** 259. doi: 10.3389/fnhum.2015.00259.
Wang, Y.L., and Li, T.Q. (2013). Analysis of Whole-Brain Resting-State fMRI Data Using Hierarchical Clustering Approach. *Plos One* 8. doi: 10.1371/journal.pone.0076315.
Zhen, Z., Fang, H., and Liu, J. (2013). The hierarchical brain network for face recognition. *PLoS One* 8**,** e59886. doi: 10.1371/journal.pone.0059886.
Zhou, C., Zemanova, L., Zamora, G., Hilgetag, C.C., and Kurths, J. (2006). Hierarchical organization unveiled by functional connectivity in complex brain networks. *Phys Rev Lett* 97**,** 238103.

16

Tables

Table 1: Summary of the SSM and visual RFNs as extracted by voxel-wise hierarchical clustering of the mean cross-correlation confident matrix derived from the resting-state fMRI data of 86 normal adult subjects. The dissection was terminated at the inconsistency coefficient of 2.65, which corresponds to the first crossing point of the inconsistency coefficient curves for the SSM and visual RFNs.

RFN	SSM	VISUAL
SIZE (VOXELS)	1540	1619
CC_{MIN}	0.19	0.18
CC_{AVG}	0.27	0.29
CC_{MAX}	0.35	0.36
IC_{MEAN}	3.10±0.17	3.25±0.34
DIVISIBLE NODES	20	19
SUB-NETWORKS	14	15

17

Tables

Table 1: Summary of the SSM and visual RFNs as extracted by voxel-wise hierarchical clustering of the mean cross-correlation confident matrix derived from the resting-state fMRI data of 86 normal adult subjects. The dissection was terminated at the inconsistency coefficient of 2.65, which corresponds to the first crossing point of the inconsistency coefficient curves for the SSM and visual RFNs.

RFN	SSM	VISUAL
SIZE (VOXELS)	1540	1619
CC_{MIN}	0.19	0.18
CC_{AVG}	0.27	0.29
CC_{MAX}	0.35	0.36
IC_{MEAN}	3.10±0.17	3.25±0.34
DIVISIBLE NODES	20	19
SUB-NETWORKS	14	15

17

17

Table 2: Summary of the significant sub-networks extracted from the SSM RFN. The sub-networks are labeled in ascending order according to their heights in the hierarchical sub-dendrogram. The closest matching Brodmann area (BA) for reach cluster is also included in the cortical location labeling.

Cluster	Size	Height	Cortical Location	Focal Point
1	25	0.66	Left insula; BA13	(-47, -14, 12)
2	99	0.66	Left Superior Temporal Gyrus (STG); BA41	(-53, -24, 8)
3	99	0.69	Right STG; BA42	(46, -20, 12)
4	370	0.69	Paracentral lobule; BA31; Cingulate-motor	(0, -20, 51)
5	34	0.69	Left postcentral gyrus; BA3	(-20, -32, 60)
			Right postcentral gyrus; BA3	(22, -28, 60)
6	40	0.69	Right Inferior parietal lobule; BA40	(38, -33, 46)
7	55	0.69	Right pre- postostcentral Gyrus; BA3-4	(37, -23, 50)
8	36	0.71	Left Superior Parietal Lobule; BA7	(-22, -44, 57)
9	67	0.71	Left pre- postcentral Gyrus; BA3-4	(-38, -28, 49)
10	63	0.71	Left Inferior parietal lobule; BA40	(-41, -37, 45)
11	150	0.71	Left precentral gyrus; BA4	(-48, -12, 36)
			Right precentral gyrus; BA4	(53, -9, 27)
12	36	0.71	Left postcentral Gyrus; BA2	(-52, -19, 31)
13	32	0.72	Right postcentral Gyrus; BA2	(47, -18, 36)
14	37	0.72	Left STG; BA41	(-39, -30, 16)
15	55	0.77	Right Inferior parietal lobule; BA40	(21, -49, 56)
16	33	0.77	Right Precuneus; BA7	(29, -51, 49)
17	22	0.78	Left STG BA22, Precentral gyrus; BA6	(-50, -6, 6)
18	54	0.78	Left Insula; BA13	(-40, -6, -2)
19	29	0.79	Left STG;BA22; Insula; BA13	(-43, -21, 5)

18

Table 2: Summary of the significant sub-networks extracted from the SSM RFN. The sub-networks are labeled in ascending order according to their heights in the hierarchical sub-dendrogram. The closest matching Brodmann area (BA) for reach cluster is also included in the cortical location labeling.

Cluster	Size	Height	Cortical Location	Focal Point
1	25	0.66	Left insula; BA13	(-47, -14, 12)
2	99	0.66	Left Superior Temporal Gyrus (STG); BA41	(-53, -24, 8)
3	99	0.69	Right STG; BA42	(46, -20, 12)
4	370	0.69	Paracentral lobule; BA31; Cingulate-motor	(0, -20, 51)
5	34	0.69	Left postcentral gyrus; BA3	(-20, -32, 60)
			Right postcentral gyrus; BA3	(22, -28, 60)
6	40	0.69	Right Inferior parietal lobule; BA40	(38, -33, 46)
7	55	0.69	Right pre- postostcentral Gyrus; BA3-4	(37, -23, 50)
8	36	0.71	Left Superior Parietal Lobule; BA7	(-22, -44, 57)
9	67	0.71	Left pre- postcentral Gyrus; BA3-4	(-38, -28, 49)
10	63	0.71	Left Inferior parietal lobule; BA40	(-41, -37, 45)
11	150	0.71	Left precentral gyrus; BA4	(-48, -12, 36)
			Right precentral gyrus; BA4	(53, -9, 27)
12	36	0.71	Left postcentral Gyrus; BA2	(-52, -19, 31)
13	32	0.72	Right postcentral Gyrus; BA2	(47, -18, 36)
14	37	0.72	Left STG; BA41	(-39, -30, 16)
15	55	0.77	Right Inferior parietal lobule; BA40	(21, -49, 56)
16	33	0.77	Right Precuneus; BA7	(29, -51, 49)
17	22	0.78	Left STG BA22, Precentral gyrus; BA6	(-50, -6, 6)
18	54	0.78	Left Insula; BA13	(-40, -6, -2)
19	29	0.79	Left STG;BA22; Insula; BA13	(-43, -21, 5)

18

Table 3: Summary of the significant sub-networks extracted from the visual network. The sub-networks are labeled in ascending order according to their heights in the hierarchical sub-dendrogram. The closest matching Brodmann area (BA) for each cluster is also included in the cortical location labeling.

Cluster	Size	Height	Cortical Location	Focal Point
1	546	0.64	Cuneus; Lingual Gyrus; Striate & extrastriate Cortex; BA18, 30	(3, -74, 1)
2	62	0.64	Left Lingual/Parahippocampal Gyrus; Right Lingual/Parahippocampal Gyrus; BA19	(16, -49, -4) (-15, -53, -4)
3	37	0.65	Left Superior Cuneus/Precuneus; Right Superior Cuneus/Precuneus; BA18	(18 -81, 25) (-18 -82, 24)
4	87	0.65	Left Middle Occipital Gyrus; Right Middle Occipital Gyrus; BA19	(-27, -83, 16) (30, -77, 22)
5	86	0.66	Left Cuneus; Right Cuneus; BA18, 7, & 31	(14, -74, 29) (-11, -78, 29)
6	150	0.67	Right Declive; Fusiform Gyrus; BA19	(4, -74, -20)
7	36	0.67	Left Declive: Fusiform Gyrus; BA19	(-32, -66, -22)
8	48	0.69	Left Fusiform Gyrus; BA19	(-23, -75, -14)
9	47	0.69	Right Fusiform Gyrus; BA19	(26, -74, -12)
10	33	0.71	Left Inferior Temporal Gyrus; BA19	(-41, -72, -1)
11	41	0.71	Right Inferior Temporal Gyrus; BA37	(45, -67, -2)
12	64	0.76	Left Middle Occipital Gyrus; Right Middle Occipital Gyrus; BA18	(32, -83, -1) (-34, -82, 0)
13	45	0.77	Right Middle Temporal Gyrus; BA39	(40, -73, 19)
14	59	0.77	Right Middle Temporal Gyrus; BA37	(48, -61, 7)
15	33	0.80	Left Middle Temporal Gyrus; BA37	(-40, -73, 12)

19

Table 3: Summary of the significant sub-networks extracted from the visual network. The sub-networks are labeled in ascending order according to their heights in the hierarchical sub-dendrogram. The closest matching Brodmann area (BA) for each cluster is also included in the cortical location labeling.

Cluster	Size	Height	Cortical Location	Focal Point
1	546	0.64	Cuneus; Lingual Gyrus; Striate & extrastriate Cortex; BA18, 30	(3, -74, 1)
2	62	0.64	Left Lingual/Parahippocampal Gyrus; Right Lingual/Parahippocampal Gyrus; BA19	(16, -49, -4) (-15, -53, -4)
3	37	0.65	Left Superior Cuneus/Precuneus; Right Superior Cuneus/Precuneus; BA18	(18 -81, 25) (-18 -82, 24)
4	87	0.65	Left Middle Occipital Gyrus; Right Middle Occipital Gyrus; BA19	(-27, -83, 16) (30, -77, 22)
5	86	0.66	Left Cuneus; Right Cuneus; BA18, 7, & 31	(14, -74, 29) (-11, -78, 29)
6	150	0.67	Right Declive; Fusiform Gyrus; BA19	(4, -74, -20)
7	36	0.67	Left Declive: Fusiform Gyrus; BA19	(-32, -66, -22)
8	48	0.69	Left Fusiform Gyrus; BA19	(-23, -75, -14)
9	47	0.69	Right Fusiform Gyrus; BA19	(26, -74, -12)
10	33	0.71	Left Inferior Temporal Gyrus; BA19	(-41, -72, -1)
11	41	0.71	Right Inferior Temporal Gyrus; BA37	(45, -67, -2)
12	64	0.76	Left Middle Occipital Gyrus; Right Middle Occipital Gyrus; BA18	(32, -83, -1) (-34, -82, 0)
13	45	0.77	Right Middle Temporal Gyrus; BA39	(40, -73, 19)
14	59	0.77	Right Middle Temporal Gyrus; BA37	(48, -61, 7)
15	33	0.80	Left Middle Temporal Gyrus; BA37	(-40, -73, 12)

19

19

Figure Legends

Figure 1: Inconsistency coefficients at full depth for all nodes in the SSM and visual RFNs.

Figure 2: One-sampled t-test score as a function of the cross-correlation coefficients of the resting-state fMRI time courses between voxels inside the brain. The average results for 84 normal adult volunteers are displayed.

Figure 3: The intra-network hierarchical organization of the sub-networks extracted from the SSM RFN. The lines in the sub-dendrogram are drawn in proportion to the distance measure of the nodes (left). The sub-networks are labeled in ascending order according to their distances in the sub-dendrogram. Each sub-network is color coded to depict the neuroanatomical location in the Talairach template. The top panel shows the color-coded sub-networks imposed on the smoothed white matter surface. The middle and bottom panels show the medial and lateral views of the inflated hemispheres, respectively.

Figure 4: An overview of SSM sub-network groups in relation to the fontal edge of the central sulcus as a 2D-projection in the Talairach coordinate system. The colors indicate the different sub-network groups and the lines were drawn to guide the eyes.

Figure 5: Intra-network hierarchical organization of the sub-networks extracted from the visual system. The lines in the dendrogram are drawn in proportion to the distance measure of the nodes (left). The sub-networks are labeled in ascending order according to their distances in the sub-dendrogram. Each sub-network is color coded to depict the neuroanatomical location in the Talairach template. The top panel shows the color-coded sub-networks imposed on the smoothed white matter surface. The middle and bottom panels show the medial and lateral views of the inflated hemispheres, respectively.

20

Figure Legends

Figure 1: Inconsistency coefficients at full depth for all nodes in the SSM and visual RFNs.

Figure 2: One-sampled t-test score as a function of the cross-correlation coefficients of the resting-state fMRI time courses between voxels inside the brain. The average results for 84 normal adult volunteers are displayed.

Figure 3: The intra-network hierarchical organization of the sub-networks extracted from the SSM RFN. The lines in the sub-dendrogram are drawn in proportion to the distance measure of the nodes (left). The sub-networks are labeled in ascending order according to their distances in the sub-dendrogram. Each sub-network is color coded to depict the neuroanatomical location in the Talairach template. The top panel shows the color-coded sub-networks imposed on the smoothed white matter surface. The middle and bottom panels show the medial and lateral views of the inflated hemispheres, respectively.

Figure 4: An overview of SSM sub-network groups in relation to the fontal edge of the central sulcus as a 2D-projection in the Talairach coordinate system. The colors indicate the different sub-network groups and the lines were drawn to guide the eyes.

Figure 5: Intra-network hierarchical organization of the sub-networks extracted from the visual system. The lines in the dendrogram are drawn in proportion to the distance measure of the nodes (left). The sub-networks are labeled in ascending order according to their distances in the sub-dendrogram. Each sub-network is color coded to depict the neuroanatomical location in the Talairach template. The top panel shows the color-coded sub-networks imposed on the smoothed white matter surface. The middle and bottom panels show the medial and lateral views of the inflated hemispheres, respectively.

20

Figures

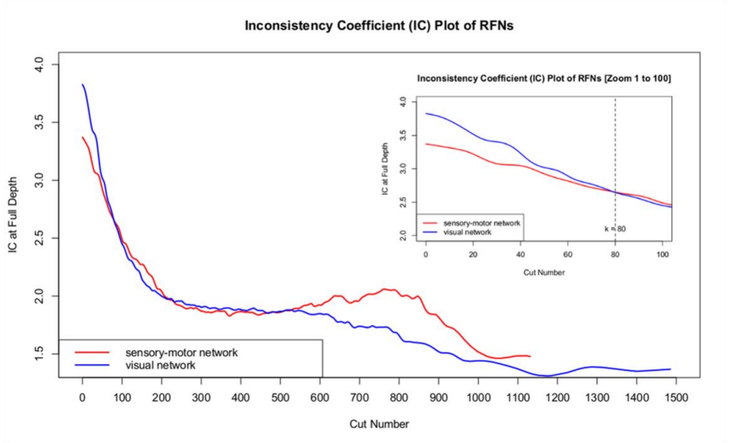

Figure 1

21

Figures

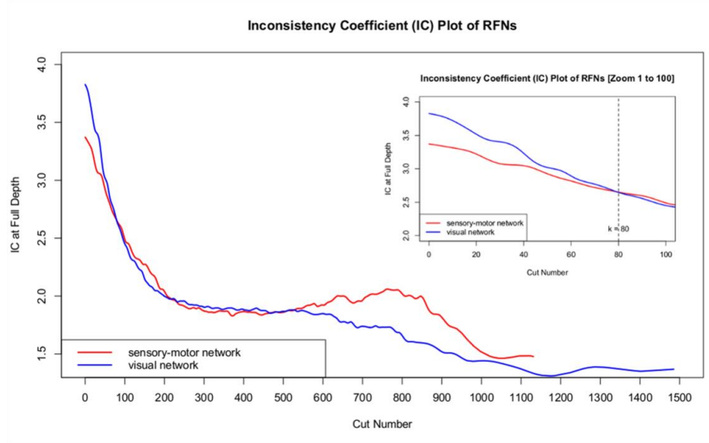

Figure 1

21

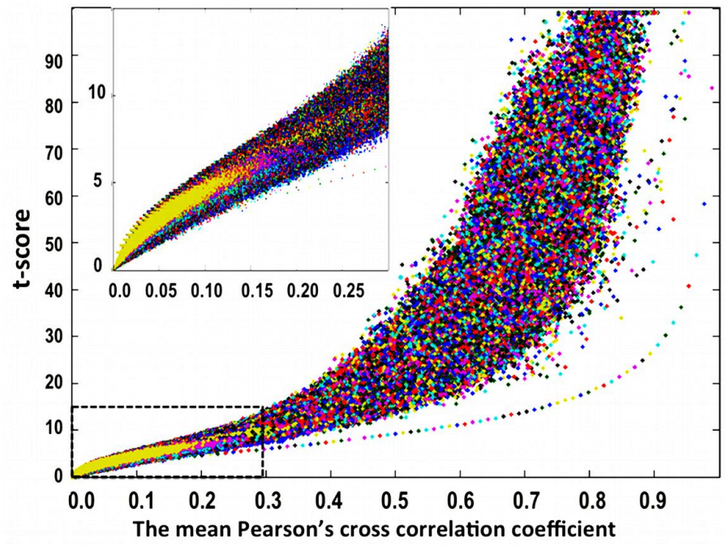

Figure 2

22

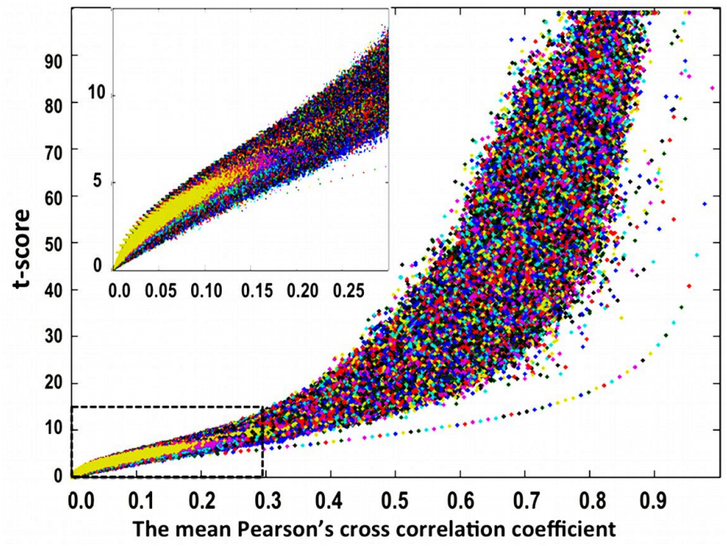

Figure 2

22

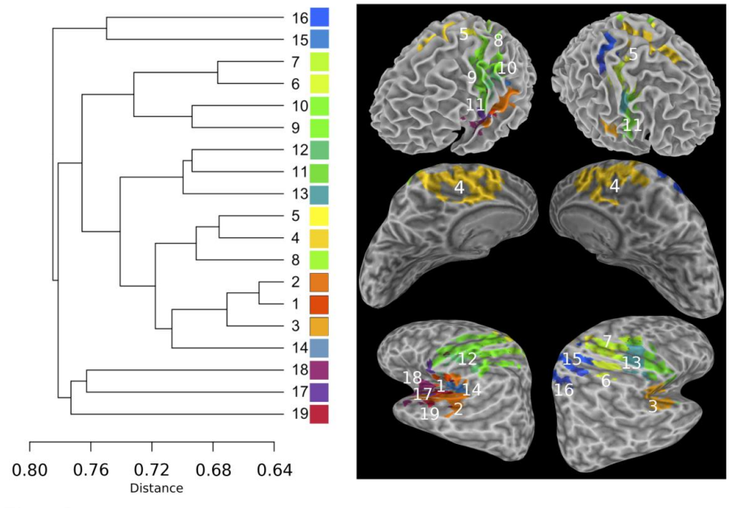

Figure 3

23

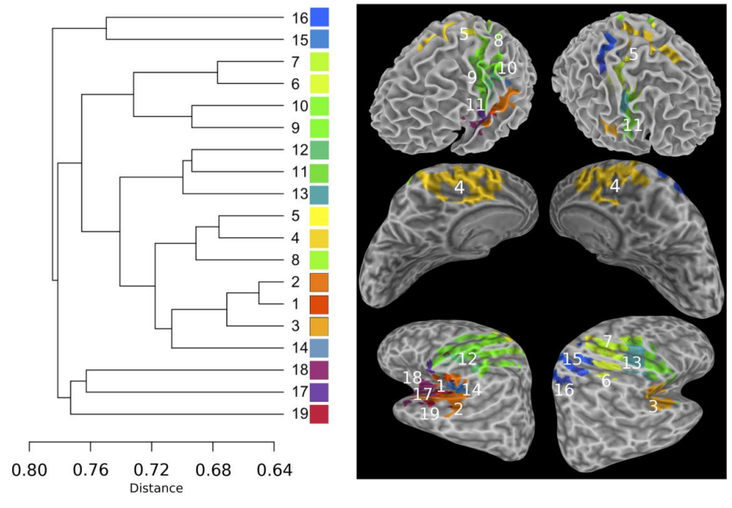

Figure 3

23

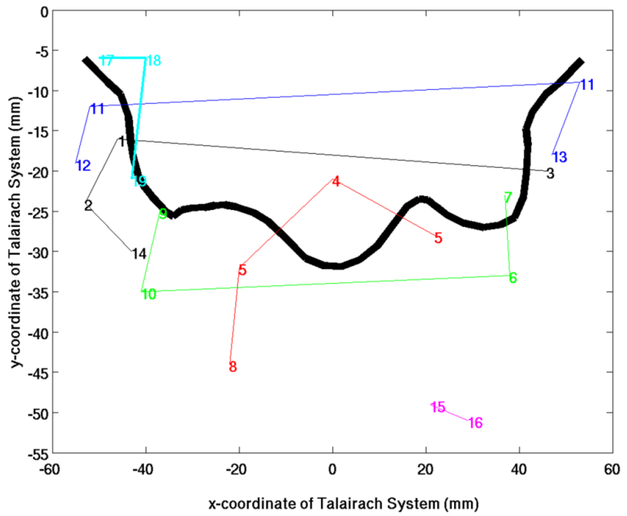

Figure 4

24

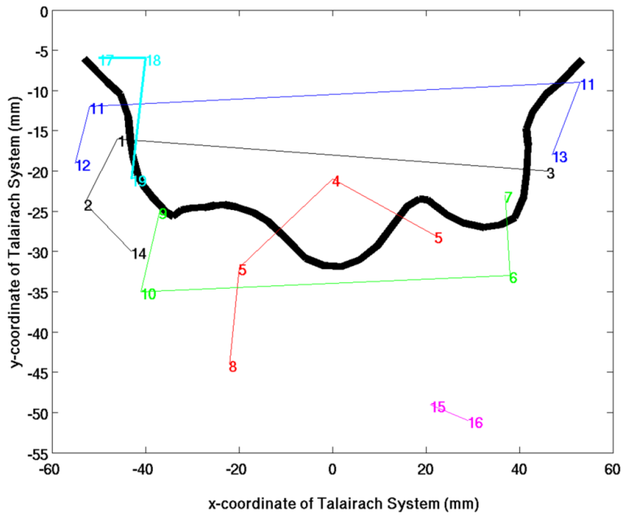

Figure 4

24

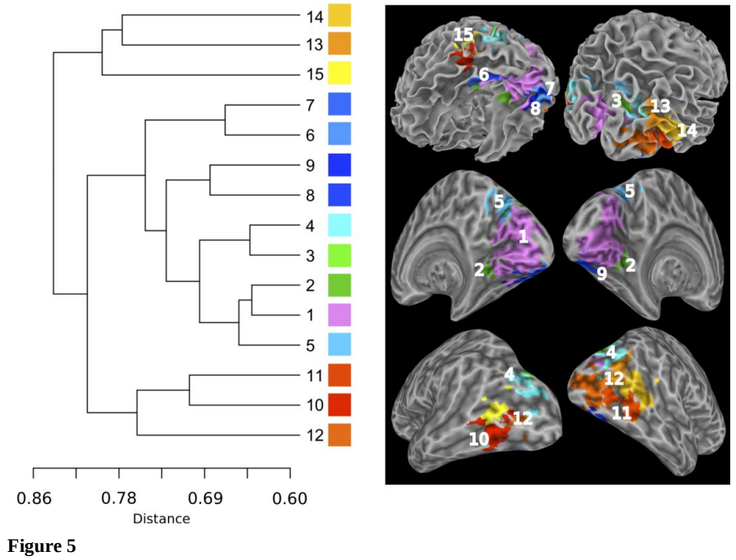

Figure 5

25

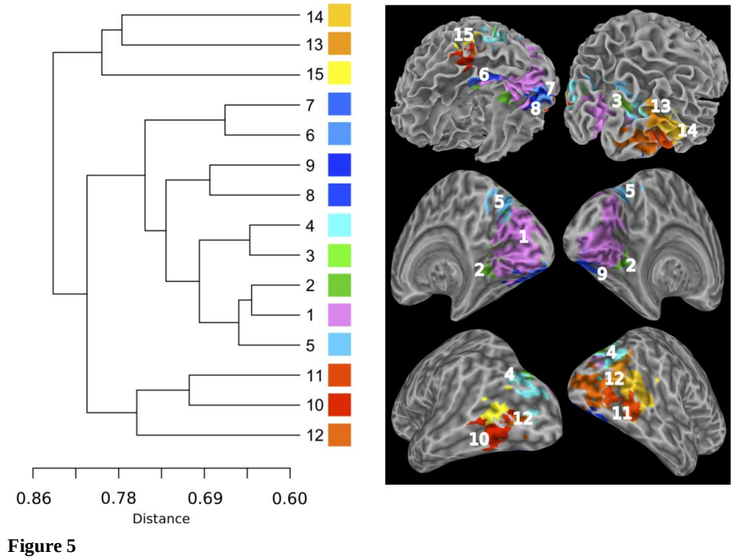

Figure 5

IV

IV

Resting-state fMRI Study of Acute Migraine Treatment with Kinetic Oscillation Stimulation in Nasal Cavity

Tie-Qiang Li1,2, Yanlu Wang2, Jan-Erik Juto3*

[1]Department of Medical Physics, Karolinska University Hospital,

Huddinge, Sweden,

[2]Department of Clinical Science, Intervention and Technology, Karolinska Institute, Stockholm, Sweden

**Corresponding author:*

Tie-Qiang Li, Ph.D.
Professor of MRI Physics
Department of Medical Physics,
Karolinska University Hospital Huddinge,
141 86 Stockholm
Sweden

Email: tie-qiang-li@karolinska.se
Tel. +46858580888

Resting-state fMRI Study of Acute Migraine Treatment with Kinetic Oscillation Stimulation in Nasal Cavity

Tie-Qiang Li1,2, Yanlu Wang2, Jan-Erik Juto3*

[1]Department of Medical Physics, Karolinska University Hospital,

Huddinge, Sweden,

[2]Department of Clinical Science, Intervention and Technology, Karolinska Institute, Stockholm, Sweden

**Corresponding author:*

Tie-Qiang Li, Ph.D.
Professor of MRI Physics
Department of Medical Physics,
Karolinska University Hospital Huddinge,
141 86 Stockholm
Sweden

Email: tie-qiang-li@karolinska.se
Tel. +46858580888

Abstract

Kinetic oscillatory stimulation (KOS) in nasal cavity is a non-invasive cranial nerve stimulation method with promising efficacy for acute migraine and other inflammatory disorders. To better understand the underlying neurophysiological mechanisms of KOS treatment, we conducted a resting-state functional magnetic resonance imaging (fMRI) study of 10 acute migraine patients and 10 normal control subjects during KOS treatment in a 3T clinical MRI scanner. The fMRI data were first processed using a group independent component analysis (ICA) method and then further modeled with a voxel-wise 3-way ANOVA approach.

All migraine participants were relieved from their acute migraine symptoms after 10-20 minutes of KOS treatment and remained migraine free for 3-6 months. The analysis of the resting-state fMRI data indicates that migraine patients have altered intrinsic activity in their anterior cingulate, inferior frontal gyrus, and middle/superior temporal gyrus. KOS treatment up-regulated intrinsic functional activity in a number of broad brain regions involving the limbic and primary sensory systems, while down-regulating the activity in few more specific brain areas, such as the right dorsal posterior insula and inferior frontal gyrus.

The result of this study confirms the efficacy of KOS treatment for relieving acute migraine symptom and reducing attack frequency. Resting-state fMRI measurements demonstrate that migraine is associated with aberrant intrinsic functional activity in the limbic and primary sensory systems. Furthermore, KOS in the nasal cavity gives rise to the adjustment of the intrinsic functional connectivity in the limbic and primary sensory networks and restores the physiological homeostasis in the autonomic nervous system.

KEY WORDS: Kinetic oscillatory stimulation (KOS), migraine, autonomic nervous system (ANS), resting-state fMRI, intrinsic functional activity, independent component analysis (ICA), 3-way ANOVA.

RUNNING TITLE: fMRI study of KOS treatment for migraine

Abstract

Kinetic oscillatory stimulation (KOS) in nasal cavity is a non-invasive cranial nerve stimulation method with promising efficacy for acute migraine and other inflammatory disorders. To better understand the underlying neurophysiological mechanisms of KOS treatment, we conducted a resting-state functional magnetic resonance imaging (fMRI) study of 10 acute migraine patients and 10 normal control subjects during KOS treatment in a 3T clinical MRI scanner. The fMRI data were first processed using a group independent component analysis (ICA) method and then further modeled with a voxel-wise 3-way ANOVA approach.

All migraine participants were relieved from their acute migraine symptoms after 10-20 minutes of KOS treatment and remained migraine free for 3-6 months. The analysis of the resting-state fMRI data indicates that migraine patients have altered intrinsic activity in their anterior cingulate, inferior frontal gyrus, and middle/superior temporal gyrus. KOS treatment up-regulated intrinsic functional activity in a number of broad brain regions involving the limbic and primary sensory systems, while down-regulating the activity in few more specific brain areas, such as the right dorsal posterior insula and inferior frontal gyrus.

The result of this study confirms the efficacy of KOS treatment for relieving acute migraine symptom and reducing attack frequency. Resting-state fMRI measurements demonstrate that migraine is associated with aberrant intrinsic functional activity in the limbic and primary sensory systems. Furthermore, KOS in the nasal cavity gives rise to the adjustment of the intrinsic functional connectivity in the limbic and primary sensory networks and restores the physiological homeostasis in the autonomic nervous system.

KEY WORDS: Kinetic oscillatory stimulation (KOS), migraine, autonomic nervous system (ANS), resting-state fMRI, intrinsic functional activity, independent component analysis (ICA), 3-way ANOVA.

RUNNING TITLE: fMRI study of KOS treatment for migraine

Introduction

Migraine is a common neurological disorder characterized by severe headache and affecting approximately 18 percent of women and 6 percent of men[1-3]. Triptans such as *Sumatriptan* are widely used for acute symptom relief of migraine headaches. About 2% of the population suffers from refractory chronic migraine and the trigeminal autonomic cephalalgias (TACs), which is often associated with drug-resistance, disability, and low quality of life.

There exist a number of theories trying to account for the ethnology of migraine. For example, inadequate regulation of the autonomic nervous system (ANS)[4-6], derangement of serotonin metabolism[7-9], insensitive reaction to reduced oxygen in the vasculature and tissue[10-12], disruption of the normal pain pathways[13], peculiar platelet metabolism[14-16], neurogenic inflammation[17] and etc[18]. Researchers have yet to disseminate a unified theory to account for the different aspects of the complex pathophysiology involved in migraine. Despite extensive neuroimaging studies of headache disorders in the last decade[3,19-32], functional imaging acquired during transient attack of migraine has been rare. Such studies can provide important insight into the pathogenesis of migraine headaches. Earlier PET studies have shown persisting activation in the brain stem and hypothalamus during migraine attacks[33,34]. MRI studies based on arterial spin labeling have also reported hemodynamic abnormality in the hypothalamus during treatment of migraine with triptan[31,35,36]. These findings have led to the hypothesis that the hypothalamic pathway might play a critical role in the pathogenesis of migraine attacks[3,21,26]. Results from neuroimaging and spectroscopy studies of TACs provided further evidence for this view[37-39]. For TACs and refractory migraine, hypothalamic deep brain stimulation has been tested as an alternative treatment and symptom reduction has been observed in some patients[40,41].

Taking advantages of the rich innervations and inter-nerve connections in the nasal mucous membrane, we have recently developed a non-invasive approach based on kinetic oscillatory stimulation (KOS) in the nasal cavity for the treatment of migraine[42] and other chronic inflammatory disorders[43]. We have completed a randomized control trial (RCT) study (**ClinicalTrials.gov Identifier:** NCT01488110) based on 36 migraine patients and showed that KOS in the nasal cavity is an effective and safe method to relieve both acute pain and reduce the attack frequency in patients with migraine[42]. Multi-site clinical RCT studies for further testing its efficacy on acute migraine (**ClinicalTrials.gov Identifier:** NCT02185703) and prophylactic effects **(ClinicalTrials.gov Identifier:** NCT02243865**)** are currently under way.

The purpose of this study is to improve our understanding of the neurological underpinnings for KOS treatment of acute migraine. Such understanding may provide guidance for further optimization of the procedure, and extension of KOS method for other clinical applications in addition to the treatment of migraine. We used blood oxygen-level dependent (BOLD) functional magnetic resonance imaging (fMRI) technique to study the alterations in the functional connectivity in the brain in response to the KOS treatment. We compare the resting-state functional connectivity differences between patients with acute migraine and normal volunteers before, during, and after KOS treatment. We demonstrate that migraine headache is associated with abnormal functional connectivity in the limbic system, which is the central brain network for ANS control, and KOS treatment can regulate the functional connectivity of the limbic system back to normal status.

Introduction

Migraine is a common neurological disorder characterized by severe headache and affecting approximately 18 percent of women and 6 percent of men[1-3]. Triptans such as *Sumatriptan* are widely used for acute symptom relief of migraine headaches. About 2% of the population suffers from refractory chronic migraine and the trigeminal autonomic cephalalgias (TACs), which is often associated with drug-resistance, disability, and low quality of life.

There exist a number of theories trying to account for the ethnology of migraine. For example, inadequate regulation of the autonomic nervous system (ANS)[4-6], derangement of serotonin metabolism[7-9], insensitive reaction to reduced oxygen in the vasculature and tissue[10-12], disruption of the normal pain pathways[13], peculiar platelet metabolism[14-16], neurogenic inflammation[17] and etc[18]. Researchers have yet to disseminate a unified theory to account for the different aspects of the complex pathophysiology involved in migraine. Despite extensive neuroimaging studies of headache disorders in the last decade[3,19-32], functional imaging acquired during transient attack of migraine has been rare. Such studies can provide important insight into the pathogenesis of migraine headaches. Earlier PET studies have shown persisting activation in the brain stem and hypothalamus during migraine attacks[33,34]. MRI studies based on arterial spin labeling have also reported hemodynamic abnormality in the hypothalamus during treatment of migraine with triptan[31,35,36]. These findings have led to the hypothesis that the hypothalamic pathway might play a critical role in the pathogenesis of migraine attacks[3,21,26]. Results from neuroimaging and spectroscopy studies of TACs provided further evidence for this view[37-39]. For TACs and refractory migraine, hypothalamic deep brain stimulation has been tested as an alternative treatment and symptom reduction has been observed in some patients[40,41].

Taking advantages of the rich innervations and inter-nerve connections in the nasal mucous membrane, we have recently developed a non-invasive approach based on kinetic oscillatory stimulation (KOS) in the nasal cavity for the treatment of migraine[42] and other chronic inflammatory disorders[43]. We have completed a randomized control trial (RCT) study (**ClinicalTrials.gov Identifier:** NCT01488110) based on 36 migraine patients and showed that KOS in the nasal cavity is an effective and safe method to relieve both acute pain and reduce the attack frequency in patients with migraine[42]. Multi-site clinical RCT studies for further testing its efficacy on acute migraine (**ClinicalTrials.gov Identifier:** NCT02185703) and prophylactic effects **(ClinicalTrials.gov Identifier:** NCT02243865**)** are currently under way.

The purpose of this study is to improve our understanding of the neurological underpinnings for KOS treatment of acute migraine. Such understanding may provide guidance for further optimization of the procedure, and extension of KOS method for other clinical applications in addition to the treatment of migraine. We used blood oxygen-level dependent (BOLD) functional magnetic resonance imaging (fMRI) technique to study the alterations in the functional connectivity in the brain in response to the KOS treatment. We compare the resting-state functional connectivity differences between patients with acute migraine and normal volunteers before, during, and after KOS treatment. We demonstrate that migraine headache is associated with abnormal functional connectivity in the limbic system, which is the central brain network for ANS control, and KOS treatment can regulate the functional connectivity of the limbic system back to normal status.

Materials and Methods

Recruitment and clinical evaluation of the migraine patients

We recruited 10 adult patients (male/female=5/5, age=44±10) and 10 normal controls (male/female=5/5, age=43±11) into the study. The patients were previously diagnosed with migraine and experienced at least one migraine attack per month before participating in the study. The patients contacted the investigators by phone at typical signs of an attack development. Their headache has to fulfill the ICHD-2 criteria and reach at least 4.0 on the pain visual analog scale (VAS) 0-10. VAS 0 represents no pain and VAS 10 the highest level of unbearable pain. We administered the actual KOS treatment inside a clinical MRI scanner within 30 minutes of arrival on site. Patients were asked not to take any medication before the KOS treatment[44,45].

The VAS assessment of pain was conducted immediate before the KOS treatment, every 10 minute during treatment, at the end of the treatment, and 15 minutes after treatment. All patients were also asked to assess their general well-being immediately before and following the treatment. The pain level was also assessed 24 hours after by telephone interview. After the KOS treatment the patients were requested to continue with their VAS assessment of pain and report to the investigators. In case of migraine reoccurrence, we provided the patients with the option of repeated KOS treatments.

KOS treatment

KOS in the nasal cavity was administered using the same equipment described in our previous studies[42-45]. It consists of a controller and a single-use catheter. The catheter, coated with lubricating liquid (medical grade paraffin or water), was inserted into the nasal cavity on the side with the predominant pain. For active treatment of migraine, the tip was inflated and oscillated for 10 minutes at the pressure of 95mbar and frequency of 68Hz. After 10 minutes, the oscillations were terminated and the patients were asked to assess their pain level. If necessary, the catheter was deflated and moved to the other side, re-inflated, and the treatment continued for another 10 minutes.

It should be noted that the device can deliver KOS inside the entire nasal cavity, extending deep in the proximity of the pterygopalatina ganglion (PPG). The settings (pressure and frequency) and treatment duration are based on previous clinical experience[42,43], and optimized for each specific disorder and patient sub-group. For example, the optimal settings for the treatment of non-allergic rhinitis are 50mbar and 50Hz[43], whereas 95mbar and 68Hz are more effective for migraine[42,44,45].

fMRI data acquisition

The fMRI measurements were conducted using a 3T whole-body clinical MRI scanner (TIM Trio, Siemens Healthcare, Erlangen, Germany). A single-shot 2D gradient-recalled echo echo-planar imaging pulse sequence was used for the data acquisition with the following main acquisition parameters: 32 transverse slices, slice thickness=3.6 mm, TR/TE=2000/35ms, FOV=220mm, matrix size=64x64, flip angle=90°, 300 dynamic timeframes, and IPAT=2. A 32-channel phased-array head coil was used for the signal reception. Foam padding was used to for

Materials and Methods

Recruitment and clinical evaluation of the migraine patients

We recruited 10 adult patients (male/female=5/5, age=44±10) and 10 normal controls (male/female=5/5, age=43±11) into the study. The patients were previously diagnosed with migraine and experienced at least one migraine attack per month before participating in the study. The patients contacted the investigators by phone at typical signs of an attack development. Their headache has to fulfill the ICHD-2 criteria and reach at least 4.0 on the pain visual analog scale (VAS) 0-10. VAS 0 represents no pain and VAS 10 the highest level of unbearable pain. We administered the actual KOS treatment inside a clinical MRI scanner within 30 minutes of arrival on site. Patients were asked not to take any medication before the KOS treatment[44,45].

The VAS assessment of pain was conducted immediate before the KOS treatment, every 10 minute during treatment, at the end of the treatment, and 15 minutes after treatment. All patients were also asked to assess their general well-being immediately before and following the treatment. The pain level was also assessed 24 hours after by telephone interview. After the KOS treatment the patients were requested to continue with their VAS assessment of pain and report to the investigators. In case of migraine reoccurrence, we provided the patients with the option of repeated KOS treatments.

KOS treatment

KOS in the nasal cavity was administered using the same equipment described in our previous studies[42-45]. It consists of a controller and a single-use catheter. The catheter, coated with lubricating liquid (medical grade paraffin or water), was inserted into the nasal cavity on the side with the predominant pain. For active treatment of migraine, the tip was inflated and oscillated for 10 minutes at the pressure of 95mbar and frequency of 68Hz. After 10 minutes, the oscillations were terminated and the patients were asked to assess their pain level. If necessary, the catheter was deflated and moved to the other side, re-inflated, and the treatment continued for another 10 minutes.

It should be noted that the device can deliver KOS inside the entire nasal cavity, extending deep in the proximity of the pterygopalatina ganglion (PPG). The settings (pressure and frequency) and treatment duration are based on previous clinical experience[42,43], and optimized for each specific disorder and patient sub-group. For example, the optimal settings for the treatment of non-allergic rhinitis are 50mbar and 50Hz[43], whereas 95mbar and 68Hz are more effective for migraine[42,44,45].

fMRI data acquisition

The fMRI measurements were conducted using a 3T whole-body clinical MRI scanner (TIM Trio, Siemens Healthcare, Erlangen, Germany). A single-shot 2D gradient-recalled echo echo-planar imaging pulse sequence was used for the data acquisition with the following main acquisition parameters: 32 transverse slices, slice thickness=3.6 mm, TR/TE=2000/35ms, FOV=220mm, matrix size=64x64, flip angle=90°, 300 dynamic timeframes, and IPAT=2. A 32-channel phased-array head coil was used for the signal reception. Foam padding was used to for

each subject to reduce the involuntary head motions.

For each migraine subject, we conducted 4-5 sessions of BOLD fMRI scans lasting 10 minutes per session. The migraine headache was on going at the time of arrival for fMRI. Prior to the active KOS treatment, we performed two of control resting-state fMRI scans for each patient: A baseline measurement session without inserted probe (denoted as Base1), and another session with inserted catheter but no active oscillatory stimulations (denoted as Probe). Depending on the symptom assessment, we administrated one or two sessions of active KOS treatment for each patient inside the MRI scanner while continuous BOLD fMRI recording was also carried out (denoted as KOS). Only the data acquired during KOS treatment of the right nasal cavity entered into the analysis. A post-treatment control session was performed consisting of a resting-state fMRI scan after removing the KOS catheter (Base2).

Since KOS in nasal cavity is a non-invasive treatment, for comparison, we applied the same treatment procedure and fMRI protocol described above to the normal controls.

fMRI data pre-processing

The resting-state fMRI datasets underwent a pipeline of preprocessing procedure, which were performed with AFNI (http://afni.nimh.nih.gov/afni) and FSL (http://www.fmrib.ox.ac.uk/fsl) programs with a bash wrapper shell[46,47]. The first 10 timeframes in each data set were removed to ensure signal steady state. After temporal de-spiking, six-parameter rigid body image registration was performed for motion correction. The average volume for each motion-corrected time series was used to generate a brain mask to minimize the inclusion of the extra-cerebral tissues. Spatial normalization to the standard MNI template was performed using a 12-parameter affine transformation and mutual-information cost function. During the affine transformation the imaging data were also re-sampled to isotropic resolution using a Gaussian kernel with Full width at half maximum (FWHM) of 4mm. Nuisance signal removal was achieved by voxel-wise regression using 16 regressors based on the motion correction parameters, average signal of the ventricles, average signal of the core white matter and their 1st order derivatives. After baseline trend removal up to the third order polynomial, effective band-pass filtering was performed using low-pass filtering at 0.08Hz. Local Gaussian smoothing up to FWHM=6mm was performed using an eroded gray matter mask.

Group ICA and statistical assessment

To create group level functional connectivity network parcellation we performed ICA on the pre-processed resting-state fMRI data using the GIFT toolbox (mialab.mrn.org/software) implemented in MATLAB (*MathWorks*, Massachusetts, USA). It included a series of analytical steps similar to the standard group ICA procedure[46,47]. Individual datasets were first concatenated and then followed by computation of the individual ICA components and corresponding time courses. Data reduction based on principle component analysis was performed at the subject and group levels prior to ICA. The Infomax algorithm was then applied to estimate the aggregate independent components (ICs). Lastly, subject specific spatial maps and time courses were estimated using the direct group ICA back-reconstruction approach. To prepare the subject specific ICA results for higher-level statistical assessment, the subject specific ICA results were rescaled with z-transformation.

each subject to reduce the involuntary head motions.

For each migraine subject, we conducted 4-5 sessions of BOLD fMRI scans lasting 10 minutes per session. The migraine headache was on going at the time of arrival for fMRI. Prior to the active KOS treatment, we performed two of control resting-state fMRI scans for each patient: A baseline measurement session without inserted probe (denoted as Base1), and another session with inserted catheter but no active oscillatory stimulations (denoted as Probe). Depending on the symptom assessment, we administrated one or two sessions of active KOS treatment for each patient inside the MRI scanner while continuous BOLD fMRI recording was also carried out (denoted as KOS). Only the data acquired during KOS treatment of the right nasal cavity entered into the analysis. A post-treatment control session was performed consisting of a resting-state fMRI scan after removing the KOS catheter (Base2).

Since KOS in nasal cavity is a non-invasive treatment, for comparison, we applied the same treatment procedure and fMRI protocol described above to the normal controls.

fMRI data pre-processing

The resting-state fMRI datasets underwent a pipeline of preprocessing procedure, which were performed with AFNI (http://afni.nimh.nih.gov/afni) and FSL (http://www.fmrib.ox.ac.uk/fsl) programs with a bash wrapper shell[46,47]. The first 10 timeframes in each data set were removed to ensure signal steady state. After temporal de-spiking, six-parameter rigid body image registration was performed for motion correction. The average volume for each motion-corrected time series was used to generate a brain mask to minimize the inclusion of the extra-cerebral tissues. Spatial normalization to the standard MNI template was performed using a 12-parameter affine transformation and mutual-information cost function. During the affine transformation the imaging data were also re-sampled to isotropic resolution using a Gaussian kernel with Full width at half maximum (FWHM) of 4mm. Nuisance signal removal was achieved by voxel-wise regression using 16 regressors based on the motion correction parameters, average signal of the ventricles, average signal of the core white matter and their 1st order derivatives. After baseline trend removal up to the third order polynomial, effective band-pass filtering was performed using low-pass filtering at 0.08Hz. Local Gaussian smoothing up to FWHM=6mm was performed using an eroded gray matter mask.

Group ICA and statistical assessment

To create group level functional connectivity network parcellation we performed ICA on the pre-processed resting-state fMRI data using the GIFT toolbox (mialab.mrn.org/software) implemented in MATLAB (*MathWorks*, Massachusetts, USA). It included a series of analytical steps similar to the standard group ICA procedure[46,47]. Individual datasets were first concatenated and then followed by computation of the individual ICA components and corresponding time courses. Data reduction based on principle component analysis was performed at the subject and group levels prior to ICA. The Infomax algorithm was then applied to estimate the aggregate independent components (ICs). Lastly, subject specific spatial maps and time courses were estimated using the direct group ICA back-reconstruction approach. To prepare the subject specific ICA results for higher-level statistical assessment, the subject specific ICA results were rescaled with z-transformation.

To investigate how the specified number of independent component (NIC) influences ICA results, we performed group ICA of the pooled resting-state fMRI data with NIC systematically incremented from 2 to 19. We manually inspected the spatial distributions of the one-sampled t-test results of all ICs and the corresponding time courses to exclude possible artifacts. All non-artifacts ICs are considered as potential resting-state functional networks (RFNs). A mask was created for each potential RFN by imposing a voxel-wise t-score threshold of $t \geq 4.0$ ($p \geq 0.0008$ uncorrected) and a minimum cluster size $S \geq 8$. This guarantees a family-wise error rate (FWER) $p \leq 0.01$, as estimated by using the AFNI program, *AlphaSim+* with following inputs: voxel-wise $p < 0.0008$, FWHM=6.2 mm, and 10^6 iterations. FWHM=6.2mm was the estimated average by applying the AFNI program, *3dFWHMx*, to the final smoothed fMRI data, which was quite close to FWHM=6mm used in the final smoothing procedure described above.

Statistics

We performed voxel-wise 3-way analysis of variance (ANOVA) of the ICA results to assess the functional connectivity differences between migraine patients and normal controls measured before, during and after the KOS treatment. We used the AFNI program *3dANOVA3* with the model option of type=5. The model has two fixed factors. One is the group difference between migraine patients and normal controls (DF=1) and the other is the KOS treatment effect occurred in the four scanning sessions: Base1, Probe, KOS, and Base2 (DF=3). The participants in each group were modeled as a random factor (denominator DF=36). With the 3-way ANOVA, we can also assess the interaction between the two fixed factors, and interrogate how the KOS treatment affected differently the functional connectivity in migraine patients and healthy volunteers. We performed voxel-wise 3-way ANOVA for each RFN and only voxels within the RFN mask are considered.

The statistical significance of the 3-way ANOVA result for a given RFN was assessed first by setting an uncorrected voxel-wise threshold at $p \leq 0.01$, and then by imposing a minimum voxel cluster size of at least 20 contiguous voxels. The probability of random field of noise producing a cluster of size ≥ 20 was estimated at $p \leq 0.05$. This was concluded from the Monte-Carlo simulation result obtained by using the AFNI program, *AlphaSim+*. For the simulations we used following input parameters: voxel-wise threshold value $p \leq 0.01$, 10^6 iterations, the brain mask and FWHM=6.2mm. The final result for a given NIC is summarized as the non-zero mean of the ANOVA results for all potential RFNs.

To investigate how the specified number of independent component (NIC) influences ICA results, we performed group ICA of the pooled resting-state fMRI data with NIC systematically incremented from 2 to 19. We manually inspected the spatial distributions of the one-sampled t-test results of all ICs and the corresponding time courses to exclude possible artifacts. All non-artifacts ICs are considered as potential resting-state functional networks (RFNs). A mask was created for each potential RFN by imposing a voxel-wise t-score threshold of $t \geq 4.0$ ($p \geq 0.0008$ uncorrected) and a minimum cluster size $S \geq 8$. This guarantees a family-wise error rate (FWER) $p \leq 0.01$, as estimated by using the AFNI program, *AlphaSim+* with following inputs: voxel-wise $p < 0.0008$, FWHM=6.2 mm, and 10^6 iterations. FWHM=6.2mm was the estimated average by applying the AFNI program, *3dFWHMx*, to the final smoothed fMRI data, which was quite close to FWHM=6mm used in the final smoothing procedure described above.

Statistics

We performed voxel-wise 3-way analysis of variance (ANOVA) of the ICA results to assess the functional connectivity differences between migraine patients and normal controls measured before, during and after the KOS treatment. We used the AFNI program *3dANOVA3* with the model option of type=5. The model has two fixed factors. One is the group difference between migraine patients and normal controls (DF=1) and the other is the KOS treatment effect occurred in the four scanning sessions: Base1, Probe, KOS, and Base2 (DF=3). The participants in each group were modeled as a random factor (denominator DF=36). With the 3-way ANOVA, we can also assess the interaction between the two fixed factors, and interrogate how the KOS treatment affected differently the functional connectivity in migraine patients and healthy volunteers. We performed voxel-wise 3-way ANOVA for each RFN and only voxels within the RFN mask are considered.

The statistical significance of the 3-way ANOVA result for a given RFN was assessed first by setting an uncorrected voxel-wise threshold at $p \leq 0.01$, and then by imposing a minimum voxel cluster size of at least 20 contiguous voxels. The probability of random field of noise producing a cluster of size ≥ 20 was estimated at $p \leq 0.05$. This was concluded from the Monte-Carlo simulation result obtained by using the AFNI program, *AlphaSim+*. For the simulations we used following input parameters: voxel-wise threshold value $p \leq 0.01$, 10^6 iterations, the brain mask and FWHM=6.2mm. The final result for a given NIC is summarized as the non-zero mean of the ANOVA results for all potential RFNs.

RESULTS

Table 1: Summary of the clinical information for the 10 migraine patients.

Patient	Sex	Age	Pain	Treatment	Date	Outcome
1	f	40	7	Right side	2011-01-07	migraine free 6 month
2	m	37	6	Right side	2013-05-20	migraine free 3 months
3	m	43	7	Right side	2013-05-27	migraine free 3 months
4	f	35	8	Right side	2013-08-15	migraine free 6 months
5	f	41	5	Right side	2013-08-29	migraine free 5 months
6	f	53	6	Both side	2013-10-11	migraine free 6 months
7	m	61	8	Both side	2013-10-11	migraine free 5 months
8	m	61	4	Right side	2014-11-27	migraine free 3 months
9	m	42	5	Both side	2014-04-29	migraine free 3 months
10	f	31	4	Both side	2015-03-19	migraine free 3 months

As summarized in Table 1, all migraine patients were fully relieved from their acute headache symptoms after 10-20min KOS treatment inside the MRI scanner, which confirms the result from previous RCT study conducted outside the MRI scanner[42]. Furthermore, the patients experienced a prolonged period up to 3-6 months without migraine attacks, as assessed by telephone interviews after the fMRI study.

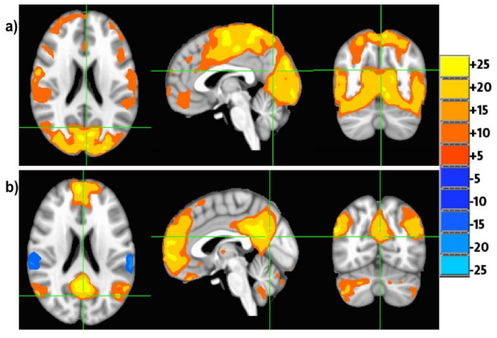

Figure 1: The cross-sectional displays of the one-sampled t-score maps (t≥4.0 and minimum cluster size of 20) for group ICA result at NIC=2. (a) The somatosensory motor network together with the auditory and visual systems. (b) The extended default mode network. The color bar indicates the t-score level.

Figures 1-3 depict the one-sampled t-score maps of the group ICA results (FWER p≤0.01) for NIC=2-4, respectively. ICA parcellation with low NIC produced over-determined and functionally less specific networks. With increasing NIC, the detected RFNs become more functional specific. E.g. at the minimum NIC=2, we observed the primary sensory network consisting of the somatosensory motor, auditory and visual systems (Fig. 1a) and the extended default mode network (Fig. 1b). With NIC=3, we observed an additional network (Fig. 2c) consisting of several left-right mirrored frontoparietal areas and corresponding to the combination of the left and right control networks[48,49]. Further increasing NIC=4, we observe

RESULTS

Table 1: Summary of the clinical information for the 10 migraine patients.

Patient	Sex	Age	Pain	Treatment	Date	Outcome
1	f	40	7	Right side	2011-01-07	migraine free 6 month
2	m	37	6	Right side	2013-05-20	migraine free 3 months
3	m	43	7	Right side	2013-05-27	migraine free 3 months
4	f	35	8	Right side	2013-08-15	migraine free 6 months
5	f	41	5	Right side	2013-08-29	migraine free 5 months
6	f	53	6	Both side	2013-10-11	migraine free 6 months
7	m	61	8	Both side	2013-10-11	migraine free 5 months
8	m	61	4	Right side	2014-11-27	migraine free 3 months
9	m	42	5	Both side	2014-04-29	migraine free 3 months
10	f	31	4	Both side	2015-03-19	migraine free 3 months

As summarized in Table 1, all migraine patients were fully relieved from their acute headache symptoms after 10-20min KOS treatment inside the MRI scanner, which confirms the result from previous RCT study conducted outside the MRI scanner[42]. Furthermore, the patients experienced a prolonged period up to 3-6 months without migraine attacks, as assessed by telephone interviews after the fMRI study.

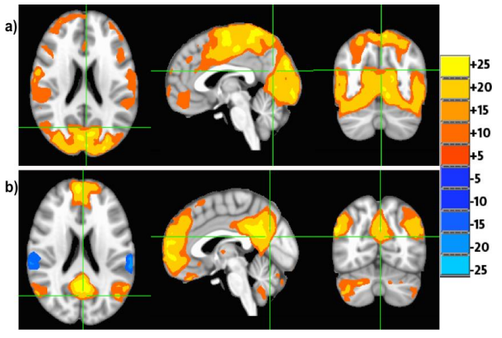

Figure 1: The cross-sectional displays of the one-sampled t-score maps (t≥4.0 and minimum cluster size of 20) for group ICA result at NIC=2. (a) The somatosensory motor network together with the auditory and visual systems. (b) The extended default mode network. The color bar indicates the t-score level.

Figures 1-3 depict the one-sampled t-score maps of the group ICA results (FWER p≤0.01) for NIC=2-4, respectively. ICA parcellation with low NIC produced over-determined and functionally less specific networks. With increasing NIC, the detected RFNs become more functional specific. E.g. at the minimum NIC=2, we observed the primary sensory network consisting of the somatosensory motor, auditory and visual systems (Fig. 1a) and the extended default mode network (Fig. 1b). With NIC=3, we observed an additional network (Fig. 2c) consisting of several left-right mirrored frontoparietal areas and corresponding to the combination of the left and right control networks[48,49]. Further increasing NIC=4, we observe

that the primary visual network (Fig. 3d) is split off from the primary sensory network (Fig. 1a or Fig. 2a).

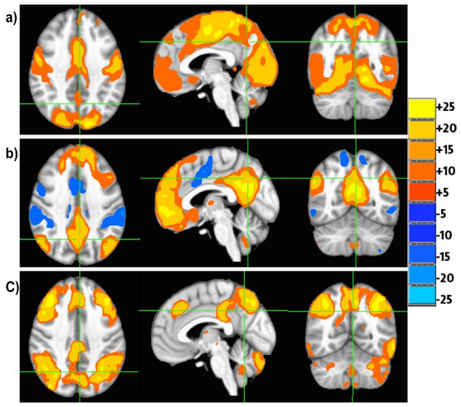

Figure 2: The cross-sectional displays of the one-sampled t-score maps (t≥4.0 and minimum cluster size of 20) for group ICA result at NIC=3. Besides the primary sensory network consisting of the somatosensory motor, auditory, and visual systems (a) and the extended default mode network (b) observed at NIC=2, the symmetrically mirrored left- and right-control RFN (c) is also seen. The color bar indicates the t-score level.

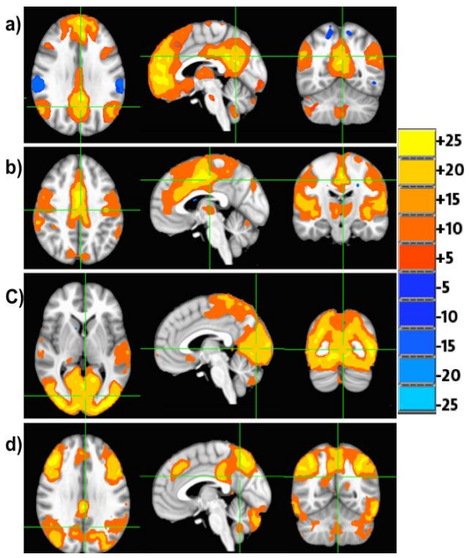

Figure 3: The cross-sectional displays of the one-sampled t-score maps (t≥4.0 and minimum cluster size of 20) for group ICA result at NIC=4. Compared with the over determined ICs observed at NIC=3, the primary sensory network is split into two separate ICs. (a) The default mode network. (b) The somatosensory motor network. (c) The visual system. (d) The symmetrically mirrored left- and right-control RFN. The color bar indicates the t-score level.

that the primary visual network (Fig. 3d) is split off from the primary sensory network (Fig. 1a or Fig. 2a).

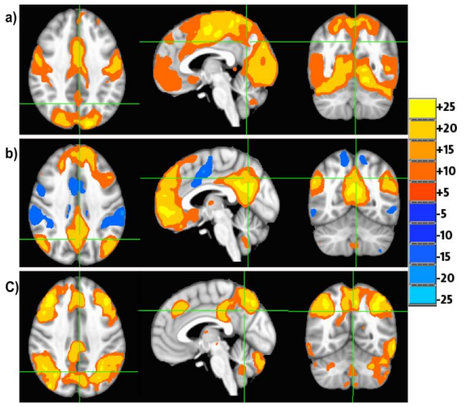

Figure 2: The cross-sectional displays of the one-sampled t-score maps (t≥4.0 and minimum cluster size of 20) for group ICA result at NIC=3. Besides the primary sensory network consisting of the somatosensory motor, auditory, and visual systems (a) and the extended default mode network (b) observed at NIC=2, the symmetrically mirrored left- and right-control RFN (c) is also seen. The color bar indicates the t-score level.

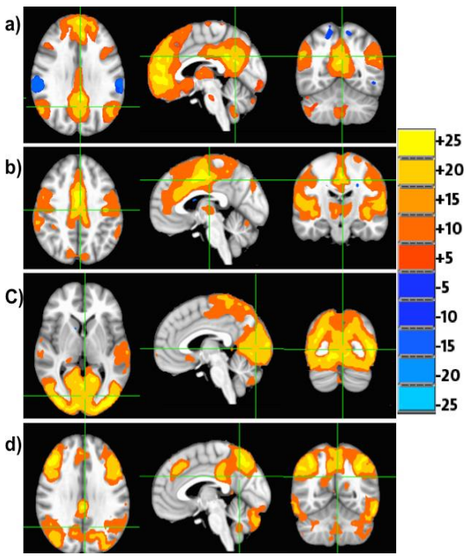

Figure 3: The cross-sectional displays of the one-sampled t-score maps (t≥4.0 and minimum cluster size of 20) for group ICA result at NIC=4. Compared with the over determined ICs observed at NIC=3, the primary sensory network is split into two separate ICs. (a) The default mode network. (b) The somatosensory motor network. (c) The visual system. (d) The symmetrically mirrored left- and right-control RFN. The color bar indicates the t-score level.

The 3-way ANOVA modeling of the ICA results at low NIC produced very little statistical contrast. When NIC≥7, the ICA parcellation becomes sufficiently specific and renders significant statistical contrast in the 3-way ANOVA. Figures 4-6 depict the 3-way ANOVA results of the ICA results at NIC=10. As shown in Fig. 4 and Table 2, the brain regions with significant group difference in functional connectivity include mainly anterior cingulate, left inferior frontal gyrus, and middle/superior temporal gyri. The boxplots of the averages for the regions of interest (ROIs) with significant group difference (see Fig. 4) indicate that migraines patients have reduced intrinsic activity in involved functional networks (Figs. 7a and b).

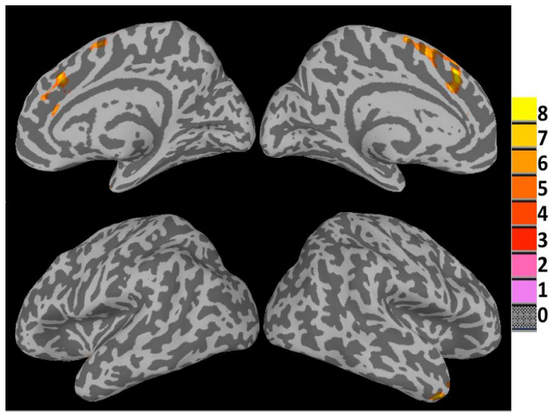

Figure 4: Brain regions with significant group differences (migraine patients versus healthy controls) in functional connectivity at NIC=10. The statistical significance was assessed with the 3-way ANOVA (model type=5) at voxel-wise F-score threshold F≥7.385 (numerator DF=1, denominator DF=36, uncorrected p≤0.01) and a minimum cluster size of 20 contiguous voxels. The color bar indicates the F-score level.

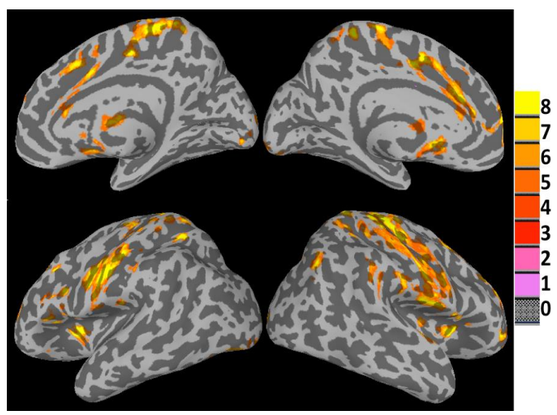

Figure 5: Brain regions with significant KOS treatment effect on functional connectivity at NIC=10. The statistical significance was assessed with the 3-way ANOVA (model type=5) at voxel-wise F-score threshold F≥4.373 (numerator DF=3, denominator DF=36, uncorrected p≤0.01) and a minimum cluster size of 20 contiguous voxels. The color bar indicates the F-score level.

The 3-way ANOVA modeling of the ICA results at low NIC produced very little statistical contrast. When NIC≥7, the ICA parcellation becomes sufficiently specific and renders significant statistical contrast in the 3-way ANOVA. Figures 4-6 depict the 3-way ANOVA results of the ICA results at NIC=10. As shown in Fig. 4 and Table 2, the brain regions with significant group difference in functional connectivity include mainly anterior cingulate, left inferior frontal gyrus, and middle/superior temporal gyri. The boxplots of the averages for the regions of interest (ROIs) with significant group difference (see Fig. 4) indicate that migraines patients have reduced intrinsic activity in involved functional networks (Figs. 7a and b).

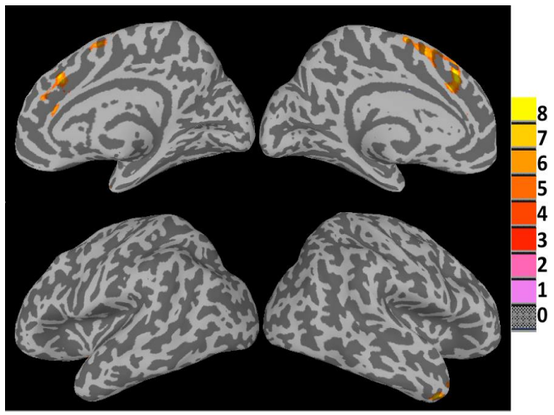

Figure 4: Brain regions with significant group differences (migraine patients versus healthy controls) in functional connectivity at NIC=10. The statistical significance was assessed with the 3-way ANOVA (model type=5) at voxel-wise F-score threshold F≥7.385 (numerator DF=1, denominator DF=36, uncorrected p≤0.01) and a minimum cluster size of 20 contiguous voxels. The color bar indicates the F-score level.

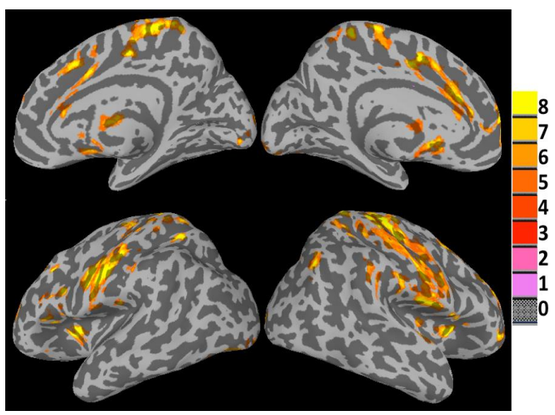

Figure 5: Brain regions with significant KOS treatment effect on functional connectivity at NIC=10. The statistical significance was assessed with the 3-way ANOVA (model type=5) at voxel-wise F-score threshold F≥4.373 (numerator DF=3, denominator DF=36, uncorrected p≤0.01) and a minimum cluster size of 20 contiguous voxels. The color bar indicates the F-score level.

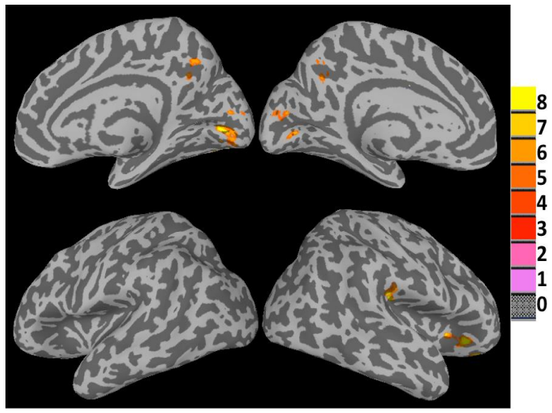

Figure 6: Brain regions with significant interaction between the two main fixed factors. That is the brain regions where the KOS treatment resulted in significantly difference in functional connectivity (at NIC=10) between migraine patients and normal controls. The statistical significance was assessed with the 3-way ANOVA (model type=5) at voxel-wise F-score threshold F≥4.373 (numerator DF=3, denominator DF=36, p≤0.01 uncorrected) and a minimum cluster size of 20 contiguous voxels. The color bar indicates the F-score level.

Table 2: List of brain regions with significant statistical contrast (FWER p≤0.05) as identified by voxel-wise 3-way ANOVA modeling of the ICA results with NIC=10. X, Y, and Z represent the focal locations of ROIs in the standard MNI coordinates. The referred voxel size is 4 mm isotropic.

Statistical Contrast	ROI	**Volume (voxel)**	**X (mm)**	**Y (mm)**	**Z (mm)**	**L/R**	**Location label**
Group	1	110	0.0	-28.0	+34.0	B	Anterior cingulate
	2	49	+16.0	-9.0	-17.0	L	Inferior frontal gyrus
	3	31	-49.0	-1.0	-33.0	R	Middle/superior temporal gyri
Treatment	4	508	+52.0	+12.0	+32.0	L	Pre- postcentral gyrus
	5	411	-60.0	+14.0	+35.0	R	Pre- postcentral gyrus
	6	126	0.0	-13.0	+37.0	B	Anterior cingulate
	7	93	+37.0	-12.0	+5.0	L	insula, inferior frontal gyrus
	8	81	-38.0	-14.0	+2.0	R	insula, inferior frontal gyrus
	9	68	-52.0	-8.0	-16.0	R	Superior temporal gyrus
	10	48	-33.0	-48.0	+26.0	R	middle prefrontal gyrus
	11	31	-31.0	-22.0	+50.0	R	middle prefrontal gyrus
	12	48	+32.0	-45.0	+16.0	L	middle prefrontal gyrus
	13	20	+41.0	-28.0	+41.0	L	middle prefrontal gyrus
	14	32	0.0	+5.0	+9.0	B	Thalamus
	15	23	0.0	-1.0	-14.0	B	Hypothalamus
	16	34	-19.0	+96.0	+7.0	R	Cuneus
	17	51	32.0	+80.0	-11.0	L	Lingual gyrus
	18	22	-38.0	+75.0	+43.0	R	Superior parietal gyrus
Interaction	19	55	-15.0	+79.0	-4.0	R	Lingual gyrus
	20	24	-11.0	+56.0	+31.0	R	Insula
	21	21	-40.0	-31.0	-9.0	R	precuneus
	22	20	-44.0	+28.0	+19.0	R	Inferior frontal gyrus

As shown Fig. 5 and Table 2, KOS treatment resulted in substantial functional connectivity changes in the limbic and primary sensory systems. The involved brain regions in the limbic system include anterior cingulate, anterior insula cortex, inferior frontal gyrus, thalamus, and

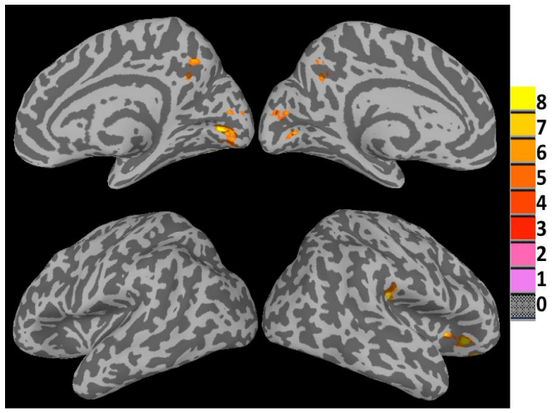

Figure 6: Brain regions with significant interaction between the two main fixed factors. That is the brain regions where the KOS treatment resulted in significantly difference in functional connectivity (at NIC=10) between migraine patients and normal controls. The statistical significance was assessed with the 3-way ANOVA (model type=5) at voxel-wise F-score threshold F≥4.373 (numerator DF=3, denominator DF=36, p≤0.01 uncorrected) and a minimum cluster size of 20 contiguous voxels. The color bar indicates the F-score level.

Table 2: List of brain regions with significant statistical contrast (FWER p≤0.05) as identified by voxel-wise 3-way ANOVA modeling of the ICA results with NIC=10. X, Y, and Z represent the focal locations of ROIs in the standard MNI coordinates. The referred voxel size is 4 mm isotropic.

Statistical Contrast	ROI	**Volume (voxel)**	**X (mm)**	**Y (mm)**	**Z (mm)**	**L/R**	**Location label**
Group	1	110	0.0	-28.0	+34.0	B	Anterior cingulate
	2	49	+16.0	-9.0	-17.0	L	Inferior frontal gyrus
	3	31	-49.0	-1.0	-33.0	R	Middle/superior temporal gyri
Treatment	4	508	+52.0	+12.0	+32.0	L	Pre- postcentral gyrus
	5	411	-60.0	+14.0	+35.0	R	Pre- postcentral gyrus
	6	126	0.0	-13.0	+37.0	B	Anterior cingulate
	7	93	+37.0	-12.0	+5.0	L	insula, inferior frontal gyrus
	8	81	-38.0	-14.0	+2.0	R	insula, inferior frontal gyrus
	9	68	-52.0	-8.0	-16.0	R	Superior temporal gyrus
	10	48	-33.0	-48.0	+26.0	R	middle prefrontal gyrus
	11	31	-31.0	-22.0	+50.0	R	middle prefrontal gyrus
	12	48	+32.0	-45.0	+16.0	L	middle prefrontal gyrus
	13	20	+41.0	-28.0	+41.0	L	middle prefrontal gyrus
	14	32	0.0	+5.0	+9.0	B	Thalamus
	15	23	0.0	-1.0	-14.0	B	Hypothalamus
	16	34	-19.0	+96.0	+7.0	R	Cuneus
	17	51	32.0	+80.0	-11.0	L	Lingual gyrus
	18	22	-38.0	+75.0	+43.0	R	Superior parietal gyrus
Interaction	19	55	-15.0	+79.0	-4.0	R	Lingual gyrus
	20	24	-11.0	+56.0	+31.0	R	Insula
	21	21	-40.0	-31.0	-9.0	R	precuneus
	22	20	-44.0	+28.0	+19.0	R	Inferior frontal gyrus

As shown Fig. 5 and Table 2, KOS treatment resulted in substantial functional connectivity changes in the limbic and primary sensory systems. The involved brain regions in the limbic system include anterior cingulate, anterior insula cortex, inferior frontal gyrus, thalamus, and

hypothalamus. These brain areas are important components of the cerebral central control network for the autonomic nervous system. Boxplots of the average IC coefficients for the relevant ROIs shown in Figs. 7c and d. It is clear that KOS treatment up-regulated the intrinsic functional activity during and after the treatment in a number of broad brain regions, such as the limbic and primary sensory systems. The trend of change with KOS procedure is quite similar for both groups of participants. However, there are a few smaller regions shown in Figs. 6, 7e and 7f that exhibited the opposite trend. The involved brain regions include lingual gyrus, dosal posterior insula, precuneus, and inferior frontal gyrus. The KOS treatment down-regulated the relatively high intrinsic activity in migraine patients (Figs. 7e and f).

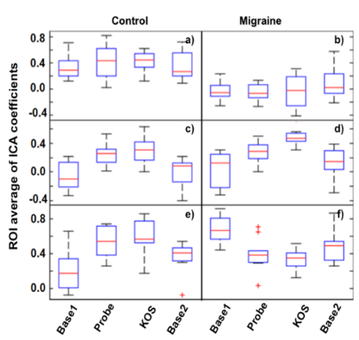

Figure 7: Boxplots of the ROI averages of IC coefficients for brain regions with significant statistical contrasts (FWER p≤0.05) as detected by 3-way ANOVA modeling of the group ICA results at NIC=10. The group difference between normal controls (a) and migraine patients (b), KOS treatment effect (c and d), and interaction between the two main fixed factors (e and f) are displayed.

NIC affects the ICA outputs and, therefore, the ANOVA results derived from it as illustrated by the supplementary materials for NIC=11 shown in Figs. S1-3. A series of ANOVA modeling of the ICA results for NIC=2-19 demonstrate that most of the relevant regions displayed stable ANOVA statistical contrast irrespective of the input NIC parameter, once NIC≥7.

DISCUSSION

Important findings of the study

Major novel findings of the study are the following: 1) ICA result is directly influenced by the input parameter NIC, and NIC has to be sufficiently high to extract functionally specific connectivity networks for interrogation of clinically relevant questions; 2) Migraines patients have altered intrinsic activity in anterior cingulate, inferior frontal gyrus, and middle/superior temporal gyrus. 3) KOS treatment in the nasal cavity can effectively relieve acute migraine symptoms and reduce attack frequency. 4) KOS treatment results in up-regulated intrinsic functional activity in a number of broad brain regions of the limbic and somatosensory systems, while down-regulating a few smaller brain areas such as the inferior frontal gyrus and dorsal posterior insula. These areas have recently been identified as a specific brain regions associated with painful experience and potential therapeutic targets[50].

hypothalamus. These brain areas are important components of the cerebral central control network for the autonomic nervous system. Boxplots of the average IC coefficients for the relevant ROIs shown in Figs. 7c and d. It is clear that KOS treatment up-regulated the intrinsic functional activity during and after the treatment in a number of broad brain regions, such as the limbic and primary sensory systems. The trend of change with KOS procedure is quite similar for both groups of participants. However, there are a few smaller regions shown in Figs. 6, 7e and 7f that exhibited the opposite trend. The involved brain regions include lingual gyrus, dosal posterior insula, precuneus, and inferior frontal gyrus. The KOS treatment down-regulated the relatively high intrinsic activity in migraine patients (Figs. 7e and f).

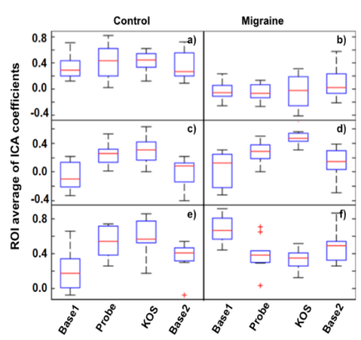

Figure 7: Boxplots of the ROI averages of IC coefficients for brain regions with significant statistical contrasts (FWER p≤0.05) as detected by 3-way ANOVA modeling of the group ICA results at NIC=10. The group difference between normal controls (a) and migraine patients (b), KOS treatment effect (c and d), and interaction between the two main fixed factors (e and f) are displayed.

NIC affects the ICA outputs and, therefore, the ANOVA results derived from it as illustrated by the supplementary materials for NIC=11 shown in Figs. S1-3. A series of ANOVA modeling of the ICA results for NIC=2-19 demonstrate that most of the relevant regions displayed stable ANOVA statistical contrast irrespective of the input NIC parameter, once NIC≥7.

DISCUSSION

Important findings of the study

Major novel findings of the study are the following: 1) ICA result is directly influenced by the input parameter NIC, and NIC has to be sufficiently high to extract functionally specific connectivity networks for interrogation of clinically relevant questions; 2) Migraines patients have altered intrinsic activity in anterior cingulate, inferior frontal gyrus, and middle/superior temporal gyrus. 3) KOS treatment in the nasal cavity can effectively relieve acute migraine symptoms and reduce attack frequency. 4) KOS treatment results in up-regulated intrinsic functional activity in a number of broad brain regions of the limbic and somatosensory systems, while down-regulating a few smaller brain areas such as the inferior frontal gyrus and dorsal posterior insula. These areas have recently been identified as a specific brain regions associated with painful experience and potential therapeutic targets[50].

KOS of the nasal mucosa with low frequency mechanical vibrations was initially developed to provide an alternative therapy for non-allergic rhinitis[43]. Completed single- and multi-site RCT studies (**ClinicalTrials.gov Identifier**: NCT01844336) have demonstrated that a single KOS treatment has significant impact on reducing the nasal symptoms of persistent rhinitis[43]. The effect was most pronounced on the days immediately following treatment, but was still present two weeks post-treatment. More recently, an exploratory trials study to test the efficacy of KOS treatment on acute migraine patients demonstrated that this treatment has a surprisingly fast-acting remedy for acute migraine pain[42]. Result from the present study confirms that KOS is indeed an effective and safe treatment for acute migraine[42,44,45]. Comparing with existing treatments for migraine, KOS therapy has the following benefits: 1) Easy to administer; 2) Well tolerated by the patients. 3) No involvement of pharmaceuticals. 4) Very few and mild side effects. KOS in the nasal cavity has the potential to offer a viable alternative, both for acute symptom relief and long-term prevention.

Underlying neurophysiological mechanisms for KOS treatment of migraine

The mechanisms of KOS treatment have not been fully understood. Besides the altered intrinsic functional activities observed in the present study, the measurements of heart rate variability (HRV) during the KOS treatments of migraine patients (not shown) also indicate active responses in the parasympathetic tone. It is evident that the intervention has very positive impact on the normal functioning of ANS, possibly by restoring homeostasis in the basal parts of the brain and the hypothalamic area, which are responsible for short-term ANS response.

It has been previously demonstrated that electrical stimulation of the PPG can mitigate severe symptoms in primary headaches[40,41], implying that the stimulation of PPG by the KOS treatment in the nasal cavity is at least partly responsible for the migraine pain relief through the trigeminal parasympathetic reflex. Recent studies provided new anatomic insight into the PPG innervation of the posterolateral nasal mucosa[51-53]. Neurons project from the PPG, via multiple individual postganglionic rami, to supply the nasal mucosa[51] and is directly connected to hypothalamus through the parasympathetic fibers from the superior salivatory nucleus[52,53]. Growing evidence from functional imaging studies indicates that hypothalamus plays a very important role in the pathogenesis of migraine attacks[3,19-32,35,54]. Migraine patients seem to have a normally regulated ANS when symptom free between attacks. However, during headache attacks they suffer typically the symptoms of an unbalanced ANS.

Preliminary studies of patients with chronic inflammatory disorders, such as Wegener's granulomatosis and dialysis patients with kidney failure (not shown), indicate that KOS in the nasal cavity may have promising anti-inflammatory efficacy. This suggests that KOS treatment may has similar impact as the electric stimulation of the vagus nerve[55-57] and might also involve the activation of the cholinergic anti-inflammatory pathway (CAP)[58,59] through the inter-connections between cranial nerves in the naval cavity. This aspect will be vigorously investigated in the near future.

The main strength and weakness of the study

The strengths of this study include the following: 1) KOS treatment of on-going acute migraine was investigated inside MRI scanner with simultaneous BOLD fMRI recordings. 2) Non-invasive KOS treatment was also conducted in normal volunteers with identical procedure,

KOS of the nasal mucosa with low frequency mechanical vibrations was initially developed to provide an alternative therapy for non-allergic rhinitis[43]. Completed single- and multi-site RCT studies (**ClinicalTrials.gov Identifier**: NCT01844336) have demonstrated that a single KOS treatment has significant impact on reducing the nasal symptoms of persistent rhinitis[43]. The effect was most pronounced on the days immediately following treatment, but was still present two weeks post-treatment. More recently, an exploratory trials study to test the efficacy of KOS treatment on acute migraine patients demonstrated that this treatment has a surprisingly fast-acting remedy for acute migraine pain[42]. Result from the present study confirms that KOS is indeed an effective and safe treatment for acute migraine[42,44,45]. Comparing with existing treatments for migraine, KOS therapy has the following benefits: 1) Easy to administer; 2) Well tolerated by the patients. 3) No involvement of pharmaceuticals. 4) Very few and mild side effects. KOS in the nasal cavity has the potential to offer a viable alternative, both for acute symptom relief and long-term prevention.

Underlying neurophysiological mechanisms for KOS treatment of migraine

The mechanisms of KOS treatment have not been fully understood. Besides the altered intrinsic functional activities observed in the present study, the measurements of heart rate variability (HRV) during the KOS treatments of migraine patients (not shown) also indicate active responses in the parasympathetic tone. It is evident that the intervention has very positive impact on the normal functioning of ANS, possibly by restoring homeostasis in the basal parts of the brain and the hypothalamic area, which are responsible for short-term ANS response.

It has been previously demonstrated that electrical stimulation of the PPG can mitigate severe symptoms in primary headaches[40,41], implying that the stimulation of PPG by the KOS treatment in the nasal cavity is at least partly responsible for the migraine pain relief through the trigeminal parasympathetic reflex. Recent studies provided new anatomic insight into the PPG innervation of the posterolateral nasal mucosa[51-53]. Neurons project from the PPG, via multiple individual postganglionic rami, to supply the nasal mucosa[51] and is directly connected to hypothalamus through the parasympathetic fibers from the superior salivatory nucleus[52,53]. Growing evidence from functional imaging studies indicates that hypothalamus plays a very important role in the pathogenesis of migraine attacks[3,19-32,35,54]. Migraine patients seem to have a normally regulated ANS when symptom free between attacks. However, during headache attacks they suffer typically the symptoms of an unbalanced ANS.

Preliminary studies of patients with chronic inflammatory disorders, such as Wegener's granulomatosis and dialysis patients with kidney failure (not shown), indicate that KOS in the nasal cavity may have promising anti-inflammatory efficacy. This suggests that KOS treatment may has similar impact as the electric stimulation of the vagus nerve[55-57] and might also involve the activation of the cholinergic anti-inflammatory pathway (CAP)[58,59] through the inter-connections between cranial nerves in the naval cavity. This aspect will be vigorously investigated in the near future.

The main strength and weakness of the study

The strengths of this study include the following: 1) KOS treatment of on-going acute migraine was investigated inside MRI scanner with simultaneous BOLD fMRI recordings. 2) Non-invasive KOS treatment was also conducted in normal volunteers with identical procedure,

allowing for direct comparison between migraine patients and normal controls. 3) Voxel-wise data-driven analysis based on 3-way ANOVA modeling of the ICA results was conducted systematically for a wide range of NIC=2-19.

The main weaknesses of the study is the following: 1) Data analysis based on ICA does not provide quantitative metrics for neurophysiology activity, which renders the results difficult to interpret and dependent on the input value for NIC. 2) There was no data available for migraine patients under migraine-free period. A crossover study design with the patients as their own controls has definitely its advantage for identifying possible prophylactic effect of KOS treatment. 3) Simultaneous monitoring of HRV during fMRI measurements would be very useful for more detailed interpretation of the neurophysiological mechanisms underlying KOS treatment of acute migraine. However, electrocardiography recording during fMRI is currently hampered by the interfering artifacts caused by the pulsing magnetic field gradients.

Conclusion

The result of this study confirms that KOS treatment is effective, both in relieving acute migraine headache and reducing attack frequency. Migraine is associated with aberrant intrinsic functional activity in the limbic and primary sensory systems. KOS in the nasal cavity can regulate the intrinsic functional connectivity in the limbic system and restore favorably the neurophysiological homeostasis in the ANS.

Acknowledgements

Experimental assistance and stimulating discussion with Dr. R. Hallin are gratefully acknowledged. This study was supported by research grants from the Swedish Research Council and ALF Medicine in Stockholm Province. The authors also want to acknowledge the support from Karolinska Institute and Karolinska University Hospital.

allowing for direct comparison between migraine patients and normal controls. 3) Voxel-wise data-driven analysis based on 3-way ANOVA modeling of the ICA results was conducted systematically for a wide range of NIC=2-19.

The main weaknesses of the study is the following: 1) Data analysis based on ICA does not provide quantitative metrics for neurophysiology activity, which renders the results difficult to interpret and dependent on the input value for NIC. 2) There was no data available for migraine patients under migraine-free period. A crossover study design with the patients as their own controls has definitely its advantage for identifying possible prophylactic effect of KOS treatment. 3) Simultaneous monitoring of HRV during fMRI measurements would be very useful for more detailed interpretation of the neurophysiological mechanisms underlying KOS treatment of acute migraine. However, electrocardiography recording during fMRI is currently hampered by the interfering artifacts caused by the pulsing magnetic field gradients.

Conclusion

The result of this study confirms that KOS treatment is effective, both in relieving acute migraine headache and reducing attack frequency. Migraine is associated with aberrant intrinsic functional activity in the limbic and primary sensory systems. KOS in the nasal cavity can regulate the intrinsic functional connectivity in the limbic system and restore favorably the neurophysiological homeostasis in the ANS.

Acknowledgements

Experimental assistance and stimulating discussion with Dr. R. Hallin are gratefully acknowledged. This study was supported by research grants from the Swedish Research Council and ALF Medicine in Stockholm Province. The authors also want to acknowledge the support from Karolinska Institute and Karolinska University Hospital.

References

1. Tfelt-Hansen PC, History of migraine with aura and cortical spreading depression from 1941 and onwards, *Cephalalgia* **30**:780 (2009).
2. Goadsby PJ, Neuroimaging in Headache, Microscopy Res Tech **53**:179 (2001).
3. Constance MM, Megan W, Blaise F, et al, Topiramate raises anterior cingulate cortex glutamine levels in healthy men; a 4.0 T magnetic resonance spectroscopy study, *Psychopharmacology* **188**:236 (2006).
4. Wilkins AJ. Reading through colour. Chichester: Wiley, 2003.
5. Welch KM et al, The concept of migraine as a state of central neuronal hyperexcitability. *Neurol Clin* **8**:817 (1990).
6. Siniatchkin M, et al, Abnormal Changes of Synaptic Excitability in Migraine with Aura, *Cerebral Cortex*, November 11, (2011).
7. Kato Y Araki N, Matsuda H, et al, Arterial spin-labeled MRI study of migraine attacks treated with rizatriptan, *J Headache Pain* **11**:255(2010)

8 Lance JW, Classification, Headache: mechanism and principles of therapy, with particular reference to migraine, *Recent Prog Med* **80**:673 (1989)

9. Prog Med 80:673–680Cohen AS, Matharu, MS, Goadsby PJ, Trigeminal Autonomic Cephalalgias: Current and Future Treatments, *Headache,* 969 (2007).
10. Luh W, Talagala LS, Li TQ, Pseudo-continuous Arterial Spin Labeling at 7T for Human Brain: Estimation and Correction for Off-resonance Effects Using a Prescan*, Magn Reson. Med*, revised (2012).
11. Li TQ et al, Inter- And Intra-Subject Variability of CBF Measurements Using PCASL Method, *Proc. Int. Soc. Magn. Reson. Med*. Stockholm, 2010
12. Luh WM, Li TQ, Wong EC, Bandettini PA. Pseudo-continuous Arterial Spin Labeling at 7T. Proc. Int. Soc. Magn. Reson. Med. Toronto, P.3339 (2008).
13. Nordin LE, Li TQ et al. Detection of exposure related cortical responses by amphetamine using pCASL and pharmacokinetik/pharmacodynamic dose modeling, Proc. Int. Soc. Magn. Reson. Med. Salt Lake City (2011).
1. Scher AI, Bigal ME, Lipton RB. Comorbidity of migraine. Curr Opin Neurol 2005;18:305-10.
2. Friedman DI, De ver Dye T. Migraine and the environment. Headache 2009;49:941-52.
3. Schwedt TJ, Chiang CC, Chong CD, Dodick DW. Functional MRI of migraine. Lancet Neurol 2015;14:81-91.
4. Geraud G, Donnet A. [Migraine and hypothalamus]. Rev Neurol (Paris) 2013;169:372-9.
5. Melek IM, Seyfeli E, Duru M, Duman T, Akgul F, Yalcin F. Autonomic dysfunction and cardiac repolarization abnormalities in patients with migraine attacks. Med Sci Monit 2007;13:RA47-9.
6. Ebinger F, Kruse M, Just U, Rating D. Cardiorespiratory regulation in migraine. Results in children and adolescents and review of the literature. Cephalalgia 2006;26:295-309.
7. Vollbracht S, Rapoport AM. New treatments for headache. Neurol Sci 2014;35 Suppl 1:89-97.
8. Dussor G. Serotonin, 5HT1 agonists, and migraine: new data, but old questions still not answered. Curr Opin Support Palliat Care 2014;8:137-42.
9. Hoffmann J, Goadsby PJ. Emerging targets in migraine. CNS Drugs 2014;28:11-7.
10. Raddant AC, Russo AF. Reactive oxygen species induce procalcitonin expression in trigeminal ganglia glia. Headache 2014;54:472-84.
11. Friberg L, Olesen J, Lassen NA, Olsen TS, Karle A. Cerebral oxygen extraction, oxygen consumption, and regional cerebral blood flow during the aura phase of migraine. Stroke; a journal of cerebral circulation 1994;25:974-9.
12. Lacombe P, Sercombe R, Correze JL, Springhetti V, Seylaz J. Spreading depression induces prolonged reduction of cortical blood flow reactivity in the rat. Exp Neurol 1992;117:278-86.
13. Kroger IL, May A. Triptan-induced disruption of trigemino-cortical connectivity. Neurology 2015;84:2124-31.
14. Danese E, Montagnana M, Lippi G. Platelets and migraine. Thromb Res 2014;134:17-22.
15. Hanington E. Migraine: the platelet hypothesis after 10 years. Biomed Pharmacother 1989;43:719-26.
16. Gawel MJ, Rose FC. Platelet function in migraineurs. Adv Neurol 1982;33:237-42.

References

1. Tfelt-Hansen PC, History of migraine with aura and cortical spreading depression from 1941 and onwards, *Cephalalgia* **30**:780 (2009).
2. Goadsby PJ, Neuroimaging in Headache, Microscopy Res Tech **53**:179 (2001).
3. Constance MM, Megan W, Blaise F, et al, Topiramate raises anterior cingulate cortex glutamine levels in healthy men; a 4.0 T magnetic resonance spectroscopy study, *Psychopharmacology* **188**:236 (2006).
4. Wilkins AJ. Reading through colour. Chichester: Wiley, 2003.
5. Welch KM et al, The concept of migraine as a state of central neuronal hyperexcitability. *Neurol Clin* **8**:817 (1990).
6. Siniatchkin M, et al, Abnormal Changes of Synaptic Excitability in Migraine with Aura, *Cerebral Cortex*, November 11, (2011).
7. Kato Y Araki N, Matsuda H, et al, Arterial spin-labeled MRI study of migraine attacks treated with rizatriptan, *J Headache Pain* **11**:255(2010)

8 Lance JW, Classification, Headache: mechanism and principles of therapy, with particular reference to migraine, *Recent Prog Med* **80**:673 (1989)

9. Prog Med 80:673–680Cohen AS, Matharu, MS, Goadsby PJ, Trigeminal Autonomic Cephalalgias: Current and Future Treatments, *Headache,* 969 (2007).
10. Luh W, Talagala LS, Li TQ, Pseudo-continuous Arterial Spin Labeling at 7T for Human Brain: Estimation and Correction for Off-resonance Effects Using a Prescan*, Magn Reson. Med*, revised (2012).
11. Li TQ et al, Inter- And Intra-Subject Variability of CBF Measurements Using PCASL Method, *Proc. Int. Soc. Magn. Reson. Med*. Stockholm, 2010
12. Luh WM, Li TQ, Wong EC, Bandettini PA. Pseudo-continuous Arterial Spin Labeling at 7T. Proc. Int. Soc. Magn. Reson. Med. Toronto, P.3339 (2008).
13. Nordin LE, Li TQ et al. Detection of exposure related cortical responses by amphetamine using pCASL and pharmacokinetik/pharmacodynamic dose modeling, Proc. Int. Soc. Magn. Reson. Med. Salt Lake City (2011).
1. Scher AI, Bigal ME, Lipton RB. Comorbidity of migraine. Curr Opin Neurol 2005;18:305-10.
2. Friedman DI, De ver Dye T. Migraine and the environment. Headache 2009;49:941-52.
3. Schwedt TJ, Chiang CC, Chong CD, Dodick DW. Functional MRI of migraine. Lancet Neurol 2015;14:81-91.
4. Geraud G, Donnet A. [Migraine and hypothalamus]. Rev Neurol (Paris) 2013;169:372-9.
5. Melek IM, Seyfeli E, Duru M, Duman T, Akgul F, Yalcin F. Autonomic dysfunction and cardiac repolarization abnormalities in patients with migraine attacks. Med Sci Monit 2007;13:RA47-9.
6. Ebinger F, Kruse M, Just U, Rating D. Cardiorespiratory regulation in migraine. Results in children and adolescents and review of the literature. Cephalalgia 2006;26:295-309.
7. Vollbracht S, Rapoport AM. New treatments for headache. Neurol Sci 2014;35 Suppl 1:89-97.
8. Dussor G. Serotonin, 5HT1 agonists, and migraine: new data, but old questions still not answered. Curr Opin Support Palliat Care 2014;8:137-42.
9. Hoffmann J, Goadsby PJ. Emerging targets in migraine. CNS Drugs 2014;28:11-7.
10. Raddant AC, Russo AF. Reactive oxygen species induce procalcitonin expression in trigeminal ganglia glia. Headache 2014;54:472-84.
11. Friberg L, Olesen J, Lassen NA, Olsen TS, Karle A. Cerebral oxygen extraction, oxygen consumption, and regional cerebral blood flow during the aura phase of migraine. Stroke; a journal of cerebral circulation 1994;25:974-9.
12. Lacombe P, Sercombe R, Correze JL, Springhetti V, Seylaz J. Spreading depression induces prolonged reduction of cortical blood flow reactivity in the rat. Exp Neurol 1992;117:278-86.
13. Kroger IL, May A. Triptan-induced disruption of trigemino-cortical connectivity. Neurology 2015;84:2124-31.
14. Danese E, Montagnana M, Lippi G. Platelets and migraine. Thromb Res 2014;134:17-22.
15. Hanington E. Migraine: the platelet hypothesis after 10 years. Biomed Pharmacother 1989;43:719-26.
16. Gawel MJ, Rose FC. Platelet function in migraineurs. Adv Neurol 1982;33:237-42.

17. Tajti J, Szok D, Majlath Z, Tuka B, Csati A, Vecsei L. Migraine and neuropeptides. Neuropeptides 2015;52:19-30.
18. Alstadhaug KB. Histamine in migraine and brain. Headache 2014;54:246-59.
19. Maniyar FH, Sprenger T, Monteith T, Schankin CJ, Goadsby PJ. The premonitory phase of migraine--what can we learn from it? Headache 2015;55:609-20.
20. Zielman R, Teeuwisse WM, Bakels F, et al. Biochemical changes in the brain of hemiplegic migraine patients measured with 7 tesla 1H-MRS. Cephalalgia 2014;34:959-67.
21. Moulton EA, Becerra L, Johnson A, Burstein R, Borsook D. Altered hypothalamic functional connectivity with autonomic circuits and the locus coeruleus in migraine. PloS one 2014;9:e95508.
22. Maniyar FH, Sprenger T, Monteith T, Schankin C, Goadsby PJ. Brain activations in the premonitory phase of nitroglycerin-triggered migraine attacks. Brain 2014;137:232-41.
23. Lipton RB, Buse DC, Hall CB, et al. Reduction in perceived stress as a migraine trigger: testing the "let-down headache" hypothesis. Neurology 2014;82:1395-401.
24. Kroger IL, May A. Central effects of acetylsalicylic acid on trigeminal-nociceptive stimuli. The journal of headache and pain 2014;15:59.
25. Sahler K. Hemicrania continua: functional imaging and clinical features with diagnostic implications. Headache 2013;53:871-2.
26. Robert C, Bourgeais L, Arreto CD, et al. Paraventricular hypothalamic regulation of trigeminovascular mechanisms involved in headaches. J Neurosci 2013;33:8827-40.
27. Morelli N, Rota E, Gori S, et al. Brainstem activation in cluster headache: an adaptive behavioural response? Cephalalgia 2013;33:416-20.
28. May A. Pearls and pitfalls: neuroimaging in headache. Cephalalgia 2013;33:554-65.
29. Charles A. The evolution of a migraine attack- a review of recent evidence. Headache 2013;53:413-9.
30. Seifert CL, Magon S, Staehle K, et al. A case-control study on cortical thickness in episodic cluster headache. Headache 2012;52:1362-8.
31. Arkink EB, Bleeker EJ, Schmitz N, et al. Cerebral perfusion changes in migraineurs: a voxelwise comparison of interictal dynamic susceptibility contrast MRI measurements. Cephalalgia 2012;32:279-88.
32. Montagna P, Pierangeli G, Cortelli P. The primary headaches as a reflection of genetic darwinian adaptive behavioral responses. Headache 2010;50:273-89.
33. Geraud G, Denuelle M, Fabre N, Payoux P, Chollet F. [Positron emission tomographic studies of migraine]. Revue neurologique 2005;161:666-70.
34. Bahra A, Matharu MS, Buchel C, Frackowiak RS, Goadsby PJ. Brainstem activation specific to migraine headache. Lancet 2001;357:1016-7.
35. Kato Y, Araki N, Matsuda H, Ito Y, Suzuki C. Arterial spin-labeled MRI study of migraine attacks treated with rizatriptan. The journal of headache and pain 2010;11:255-8.
36. Pollock JM, Deibler AR, Burdette JH, et al. Migraine associated cerebral hyperperfusion with arterial spin-labeled MR imaging. Ajnr 2008;29:1494-7.
37. Lodi R, Pierangeli G, Tonon C, et al. Study of hypothalamic metabolism in cluster headache by proton MR spectroscopy. Neurology 2006;66:1264-6.
38. Wang SJ, Lirng JF, Fuh JL, Chen JJ. Reduction in hypothalamic 1H-MRS metabolite ratios in patients with cluster headache. J Neurol Neurosurg Psychiatry 2006;77:622-5.
39. Iacovelli E, Coppola G, Tinelli E, Pierelli F, Bianco F. Neuroimaging in cluster headache and other trigeminal autonomic cephalalgias. The journal of headache and pain 2012;13:11-20.
40. Altinay M, Estemalik E, Malone DA, Jr. A comprehensive review of the use of deep brain stimulation (DBS) in treatment of psychiatric and headache disorders. Headache 2015;55:345-50.
41. Palmisani S, Al-Kaisy A, Arcioni R, et al. A six year retrospective review of occipital nerve stimulation practice--controversies and challenges of an emerging technique for treating refractory headache syndromes. The journal of headache and pain 2013;14:67.
42. Juto JE, Hallin R. Kinetic oscillation stimulation as treatment of acute migraine. A randomized, controlled pilot study. Headache 2015;55:11.

17. Tajti J, Szok D, Majlath Z, Tuka B, Csati A, Vecsei L. Migraine and neuropeptides. Neuropeptides 2015;52:19-30.
18. Alstadhaug KB. Histamine in migraine and brain. Headache 2014;54:246-59.
19. Maniyar FH, Sprenger T, Monteith T, Schankin CJ, Goadsby PJ. The premonitory phase of migraine--what can we learn from it? Headache 2015;55:609-20.
20. Zielman R, Teeuwisse WM, Bakels F, et al. Biochemical changes in the brain of hemiplegic migraine patients measured with 7 tesla 1H-MRS. Cephalalgia 2014;34:959-67.
21. Moulton EA, Becerra L, Johnson A, Burstein R, Borsook D. Altered hypothalamic functional connectivity with autonomic circuits and the locus coeruleus in migraine. PloS one 2014;9:e95508.
22. Maniyar FH, Sprenger T, Monteith T, Schankin C, Goadsby PJ. Brain activations in the premonitory phase of nitroglycerin-triggered migraine attacks. Brain 2014;137:232-41.
23. Lipton RB, Buse DC, Hall CB, et al. Reduction in perceived stress as a migraine trigger: testing the "let-down headache" hypothesis. Neurology 2014;82:1395-401.
24. Kroger IL, May A. Central effects of acetylsalicylic acid on trigeminal-nociceptive stimuli. The journal of headache and pain 2014;15:59.
25. Sahler K. Hemicrania continua: functional imaging and clinical features with diagnostic implications. Headache 2013;53:871-2.
26. Robert C, Bourgeais L, Arreto CD, et al. Paraventricular hypothalamic regulation of trigeminovascular mechanisms involved in headaches. J Neurosci 2013;33:8827-40.
27. Morelli N, Rota E, Gori S, et al. Brainstem activation in cluster headache: an adaptive behavioural response? Cephalalgia 2013;33:416-20.
28. May A. Pearls and pitfalls: neuroimaging in headache. Cephalalgia 2013;33:554-65.
29. Charles A. The evolution of a migraine attack- a review of recent evidence. Headache 2013;53:413-9.
30. Seifert CL, Magon S, Staehle K, et al. A case-control study on cortical thickness in episodic cluster headache. Headache 2012;52:1362-8.
31. Arkink EB, Bleeker EJ, Schmitz N, et al. Cerebral perfusion changes in migraineurs: a voxelwise comparison of interictal dynamic susceptibility contrast MRI measurements. Cephalalgia 2012;32:279-88.
32. Montagna P, Pierangeli G, Cortelli P. The primary headaches as a reflection of genetic darwinian adaptive behavioral responses. Headache 2010;50:273-89.
33. Geraud G, Denuelle M, Fabre N, Payoux P, Chollet F. [Positron emission tomographic studies of migraine]. Revue neurologique 2005;161:666-70.
34. Bahra A, Matharu MS, Buchel C, Frackowiak RS, Goadsby PJ. Brainstem activation specific to migraine headache. Lancet 2001;357:1016-7.
35. Kato Y, Araki N, Matsuda H, Ito Y, Suzuki C. Arterial spin-labeled MRI study of migraine attacks treated with rizatriptan. The journal of headache and pain 2010;11:255-8.
36. Pollock JM, Deibler AR, Burdette JH, et al. Migraine associated cerebral hyperperfusion with arterial spin-labeled MR imaging. Ajnr 2008;29:1494-7.
37. Lodi R, Pierangeli G, Tonon C, et al. Study of hypothalamic metabolism in cluster headache by proton MR spectroscopy. Neurology 2006;66:1264-6.
38. Wang SJ, Lirng JF, Fuh JL, Chen JJ. Reduction in hypothalamic 1H-MRS metabolite ratios in patients with cluster headache. J Neurol Neurosurg Psychiatry 2006;77:622-5.
39. Iacovelli E, Coppola G, Tinelli E, Pierelli F, Bianco F. Neuroimaging in cluster headache and other trigeminal autonomic cephalalgias. The journal of headache and pain 2012;13:11-20.
40. Altinay M, Estemalik E, Malone DA, Jr. A comprehensive review of the use of deep brain stimulation (DBS) in treatment of psychiatric and headache disorders. Headache 2015;55:345-50.
41. Palmisani S, Al-Kaisy A, Arcioni R, et al. A six year retrospective review of occipital nerve stimulation practice--controversies and challenges of an emerging technique for treating refractory headache syndromes. The journal of headache and pain 2013;14:67.
42. Juto JE, Hallin R. Kinetic oscillation stimulation as treatment of acute migraine. A randomized, controlled pilot study. Headache 2015;55:11.

15

43. Juto JE, Axelsson M. Kinetic oscillation stimulation as treatment of non-allergic rhinitis: an RCT study. Acta oto-laryngologica 2014;134:506-12.
44. Li TQ, Yang Y, Hallin R, Juto JE. Novel intervention for acute migraine headache investigated by BOLD fMRI. Proc ISMRM 2014;2014:2016.
45. Li TQ, Yang Y, Hallin R, Juto JE. Kinetic oscillatory stimulation (KOS) in the nasal cavity studied by resting-state fMRI. Proc ISMRM 2015;2015:6193.
46. Wang Y, Li TQ. Analysis of whole-brain resting-state FMRI data using hierarchical clustering approach. PloS one 2013;8:e76315.
47. Wang Y, Li TQ. Dimensionality of ICA in resting-state fMRI investigated by feature optimized classification of independent components with SVM. Front Hum Neurosci 2015;9:259.
48. Smith SM, Fox PT, Miller KL, et al. Correspondence of the brain's functional architecture during activation and rest. Proceedings of the National Academy of Sciences of the United States of America 2009;106:13040-5.
49. Schultz AP, Chhatwal JP, Huijbers W, et al. Template based rotation: a method for functional connectivity analysis with a priori templates. NeuroImage 2014;102 Pt 2:620-36.
50. Segerdahl AR, Mezue M, Okell TW, Farrar JT, Tracey I. The dorsal posterior insula subserves a fundamental role in human pain. Nat Neurosci 2015;18:499-500.
51. Bleier BS, Schlosser RJ. Endoscopic anatomy of the postganglionic pterygopalatine innervation of the posterolateral nasal mucosa. Int Forum Allergy Rhinol 2011;1:113-7.
52. Li C, Fitzgerald ME, Del Mar N, et al. The identification and neurochemical characterization of central neurons that target parasympathetic preganglionic neurons involved in the regulation of choroidal blood flow in the rat eye using pseudorabies virus, immunolabeling and conventional pathway tracing methods. Front Neuroanat 2015;9:65.
53. Li C, Fitzgerald ME, Ledoux MS, et al. Projections from the hypothalamic paraventricular nucleus and the nucleus of the solitary tract to prechoroidal neurons in the superior salivatory nucleus: Pathways controlling rodent choroidal blood flow. Brain research 2010;1358:123-39.
54. May A. [The window into headache research : what have we learned from functional and structural neuroimaging]. Schmerz 2010;24:130-6.
55. Bonaz B, Picq C, Sinniger V, Mayol JF, Clarencon D. Vagus nerve stimulation: from epilepsy to the cholinergic anti-inflammatory pathway. Neurogastroenterology 2013;25:208-21.
56. Huston JM. The vagus nerve and the inflammatory reflex: wandering on a new treatment paradigm for systemic inflammation and sepsis. Surgical infections 2012;13:187-93.
57. Andersson U, Tracey KJ. A new approach to rheumatoid arthritis: treating inflammation with computerized nerve stimulation. Cerebrum 2012;2012:3.
58. Tracey KJ. Reflex control of immunity. Nature reviews 2009;9:418-28.
59. Tracey KJ. The inflammatory reflex. Nature 2002;420:853-9.

43. Juto JE, Axelsson M. Kinetic oscillation stimulation as treatment of non-allergic rhinitis: an RCT study. Acta oto-laryngologica 2014;134:506-12.
44. Li TQ, Yang Y, Hallin R, Juto JE. Novel intervention for acute migraine headache investigated by BOLD fMRI. Proc ISMRM 2014;2014:2016.
45. Li TQ, Yang Y, Hallin R, Juto JE. Kinetic oscillatory stimulation (KOS) in the nasal cavity studied by resting-state fMRI. Proc ISMRM 2015;2015:6193.
46. Wang Y, Li TQ. Analysis of whole-brain resting-state FMRI data using hierarchical clustering approach. PloS one 2013;8:e76315.
47. Wang Y, Li TQ. Dimensionality of ICA in resting-state fMRI investigated by feature optimized classification of independent components with SVM. Front Hum Neurosci 2015;9:259.
48. Smith SM, Fox PT, Miller KL, et al. Correspondence of the brain's functional architecture during activation and rest. Proceedings of the National Academy of Sciences of the United States of America 2009;106:13040-5.
49. Schultz AP, Chhatwal JP, Huijbers W, et al. Template based rotation: a method for functional connectivity analysis with a priori templates. NeuroImage 2014;102 Pt 2:620-36.
50. Segerdahl AR, Mezue M, Okell TW, Farrar JT, Tracey I. The dorsal posterior insula subserves a fundamental role in human pain. Nat Neurosci 2015;18:499-500.
51. Bleier BS, Schlosser RJ. Endoscopic anatomy of the postganglionic pterygopalatine innervation of the posterolateral nasal mucosa. Int Forum Allergy Rhinol 2011;1:113-7.
52. Li C, Fitzgerald ME, Del Mar N, et al. The identification and neurochemical characterization of central neurons that target parasympathetic preganglionic neurons involved in the regulation of choroidal blood flow in the rat eye using pseudorabies virus, immunolabeling and conventional pathway tracing methods. Front Neuroanat 2015;9:65.
53. Li C, Fitzgerald ME, Ledoux MS, et al. Projections from the hypothalamic paraventricular nucleus and the nucleus of the solitary tract to prechoroidal neurons in the superior salivatory nucleus: Pathways controlling rodent choroidal blood flow. Brain research 2010;1358:123-39.
54. May A. [The window into headache research : what have we learned from functional and structural neuroimaging]. Schmerz 2010;24:130-6.
55. Bonaz B, Picq C, Sinniger V, Mayol JF, Clarencon D. Vagus nerve stimulation: from epilepsy to the cholinergic anti-inflammatory pathway. Neurogastroenterology 2013;25:208-21.
56. Huston JM. The vagus nerve and the inflammatory reflex: wandering on a new treatment paradigm for systemic inflammation and sepsis. Surgical infections 2012;13:187-93.
57. Andersson U, Tracey KJ. A new approach to rheumatoid arthritis: treating inflammation with computerized nerve stimulation. Cerebrum 2012;2012:3.
58. Tracey KJ. Reflex control of immunity. Nature reviews 2009;9:418-28.
59. Tracey KJ. The inflammatory reflex. Nature 2002;420:853-9.

16

Supplementary materials

Group ICA result is directly influenced by the input NIC value. Therefore, statistical analysis of the ICA result is also affected by the specified NIC. To study the impact of NIC on the statistical contrasts derived from 3-way ANOVA modelling of the group ICA result, we systematically analyzed the ICA results corresponding to NIC=2-19. Figs. S1-3 depict the 3-way ANOVA results for NIC=11. It is apparent that there are substantial differences between the results shown in Figs. 4-6 and Figs S1-3, although the corresponding NIC values differ only by 1. For comparison, ROIs with significant statistical contrast (FWER p≤0.05) are also detailed in Table S1.

Table S1: List of brain regions with significant statistical contrast (p<0.05, corrected) as identified by voxel-wise 3-way ANOVA modeling of the ICA results with NIC=11. X, Y, and Z represent the peak locations of ROIs in the standard MNI coordinates. The referred voxel size is 4 mm isotropic.

Statistical Contrast	ROI	**Volume (voxel)**	**X (mm)**	**Y (mm)**	**Z (mm)**	**L/R**	**Location label**
Group	1	118	-18.0	+90.0	-21.0	R	fusiform gyrus
	2	96	0.0	-28.0	+25.0	B	anterior cingulate
	4	57	+15.0	+2.0	-20.0	L	parahippocampal gyrus
	5	52	+32.0	+7.0	-42.0	L	inferior temporal gyrus
	6	37	+37.0	+19.0	+39.0	L	precentral gyrus
	7	24	+38.0	+67.0	-42.0	L	pyramis
	8	23	+48.0	-36.0	+25.0	L	inferior frontal gyrus
	9	20	-49.0	-12.0	-33.0	R	medial temporal gyrus
KOS	10	609	+52.0	+12.0	+29.0	L	Pre- postcentral gyrus
	11	398	-50.0	+12.0	+33.0	R	Pre- postcentral gyrus
	12	81	+36.0	-11	+2.0	L	insula, inferior frontal gyrus
	13	79	-36.0	-11.0	+5.0	R	insula, inferior frontal gyrus
	14	29	+30.0	-80.0	+15.0	L	middle prefrontal gyrus
	15	59	-33.0	-60.0	+17.0	R	middle prefrontal gyrus
	16	47	0.0	-18.0	+21.0	B	Anterior cingulate
	17	38	0.0	+75.0	+22.0	B	Cuneus
	18	26	-7.0	+88.0	-14.0	R	Lingual gyrus
	19	24	-40.0	+68.0	+50.0	R	superior parietal gyrus
	20	21	0.0	-7.0	+70.0	B	Medial frontal gyrus
Interaction	21	63	-3,0	+74.0	+4.0	R	cuneus
	22	45	+12.0	+85.0	+32.0	L	cuneus
	23	27	-38.0	+62.0	+52.0	R	inferior parietal Lobule
	24	27	-2.0	+68.0	+46.0	R	precuneus
	25	25	+6.0	+61.0	+46.0	L	precuneus
	26	23	0.0	-44.0	-2.0	B	medial frontal gyrus

Supplementary materials

Group ICA result is directly influenced by the input NIC value. Therefore, statistical analysis of the ICA result is also affected by the specified NIC. To study the impact of NIC on the statistical contrasts derived from 3-way ANOVA modelling of the group ICA result, we systematically analyzed the ICA results corresponding to NIC=2-19. Figs. S1-3 depict the 3-way ANOVA results for NIC=11. It is apparent that there are substantial differences between the results shown in Figs. 4-6 and Figs S1-3, although the corresponding NIC values differ only by 1. For comparison, ROIs with significant statistical contrast (FWER p≤0.05) are also detailed in Table S1.

Table S1: List of brain regions with significant statistical contrast (p<0.05, corrected) as identified by voxel-wise 3-way ANOVA modeling of the ICA results with NIC=11. X, Y, and Z represent the peak locations of ROIs in the standard MNI coordinates. The referred voxel size is 4 mm isotropic.

Statistical Contrast	ROI	**Volume (voxel)**	**X (mm)**	**Y (mm)**	**Z (mm)**	**L/R**	**Location label**
Group	1	118	-18.0	+90.0	-21.0	R	fusiform gyrus
	2	96	0.0	-28.0	+25.0	B	anterior cingulate
	4	57	+15.0	+2.0	-20.0	L	parahippocampal gyrus
	5	52	+32.0	+7.0	-42.0	L	inferior temporal gyrus
	6	37	+37.0	+19.0	+39.0	L	precentral gyrus
	7	24	+38.0	+67.0	-42.0	L	pyramis
	8	23	+48.0	-36.0	+25.0	L	inferior frontal gyrus
	9	20	-49.0	-12.0	-33.0	R	medial temporal gyrus
KOS	10	609	+52.0	+12.0	+29.0	L	Pre- postcentral gyrus
	11	398	-50.0	+12.0	+33.0	R	Pre- postcentral gyrus
	12	81	+36.0	-11	+2.0	L	insula, inferior frontal gyrus
	13	79	-36.0	-11.0	+5.0	R	insula, inferior frontal gyrus
	14	29	+30.0	-80.0	+15.0	L	middle prefrontal gyrus
	15	59	-33.0	-60.0	+17.0	R	middle prefrontal gyrus
	16	47	0.0	-18.0	+21.0	B	Anterior cingulate
	17	38	0.0	+75.0	+22.0	B	Cuneus
	18	26	-7.0	+88.0	-14.0	R	Lingual gyrus
	19	24	-40.0	+68.0	+50.0	R	superior parietal gyrus
	20	21	0.0	-7.0	+70.0	B	Medial frontal gyrus
Interaction	21	63	-3,0	+74.0	+4.0	R	cuneus
	22	45	+12.0	+85.0	+32.0	L	cuneus
	23	27	-38.0	+62.0	+52.0	R	inferior parietal Lobule
	24	27	-2.0	+68.0	+46.0	R	precuneus
	25	25	+6.0	+61.0	+46.0	L	precuneus
	26	23	0.0	-44.0	-2.0	B	medial frontal gyrus

17

With increasing NIC, there is an evident tendency of increased number of ROIs and larger brain volume possessing significant statistical significance. It is plausible that the parcellated brain networks become more functionally specific at higher NIC, and the statistical moiling becomes more sensitive. On the other hand, there exist also relatively stable ROIs insensitive to the choice of NIC. How to select the optimal NIC for ICA in the parcellation of resting-state fMRI data is beyond the scope of this study[47-49]. Dimensionality of ICA is currently an unsolved problem in data-driven analysis of resting-state fMRI[47].

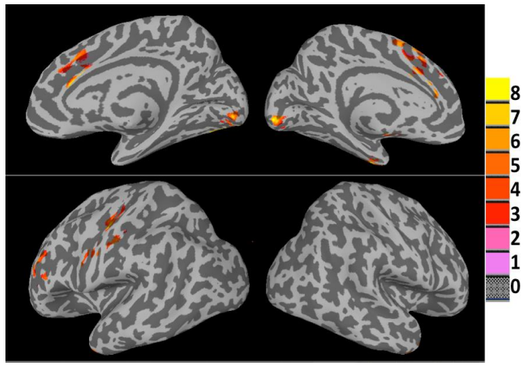

Figure S1: Brain regions with significant group differences (migraine patients versus healthy controls) in functional connectivity at NIC=11. The statistical significance was assessed with the 3-way ANOVA (model type=5) at voxel-wise F-score threshold F≥7.385 (numerator DF=1, denominator DF=36, uncorrected p≤0.01) and a minimum cluster size of 20 contiguous voxels. The color bar indicates the F-score level.

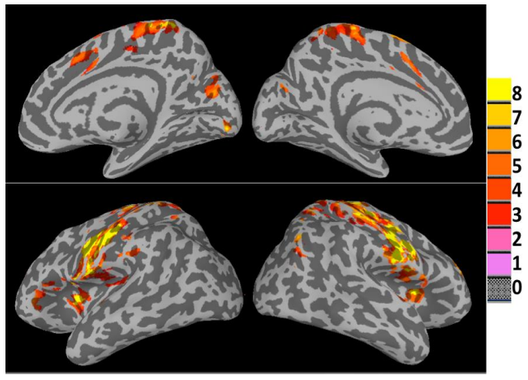

Figure S2: Brain regions with significant KOS treatment effect on functional connectivity at NIC=11. The statistical significance was assessed with the 3-way ANOVA (model type=5) at voxel-wise F-score threshold F≥4.373 (numerator DF=3, denominator DF=36, uncorrected p≤0.01) and a minimum cluster size of 20 contiguous voxels. The color bar indicates the F-score level.

With increasing NIC, there is an evident tendency of increased number of ROIs and larger brain volume possessing significant statistical significance. It is plausible that the parcellated brain networks become more functionally specific at higher NIC, and the statistical moiling becomes more sensitive. On the other hand, there exist also relatively stable ROIs insensitive to the choice of NIC. How to select the optimal NIC for ICA in the parcellation of resting-state fMRI data is beyond the scope of this study[47-49]. Dimensionality of ICA is currently an unsolved problem in data-driven analysis of resting-state fMRI[47].

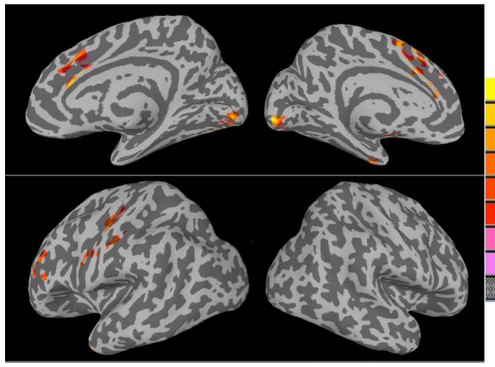

Figure S1: Brain regions with significant group differences (migraine patients versus healthy controls) in functional connectivity at NIC=11. The statistical significance was assessed with the 3-way ANOVA (model type=5) at voxel-wise F-score threshold F≥7.385 (numerator DF=1, denominator DF=36, uncorrected p≤0.01) and a minimum cluster size of 20 contiguous voxels. The color bar indicates the F-score level.

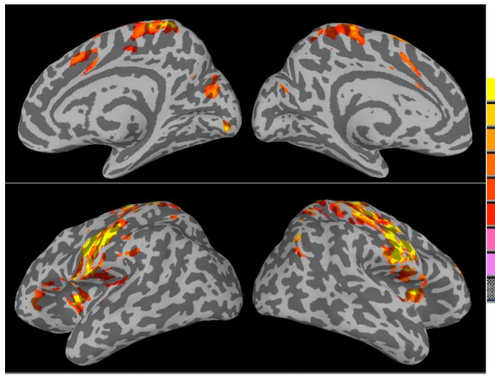

Figure S2: Brain regions with significant KOS treatment effect on functional connectivity at NIC=11. The statistical significance was assessed with the 3-way ANOVA (model type=5) at voxel-wise F-score threshold F≥4.373 (numerator DF=3, denominator DF=36, uncorrected p≤0.01) and a minimum cluster size of 20 contiguous voxels. The color bar indicates the F-score level.

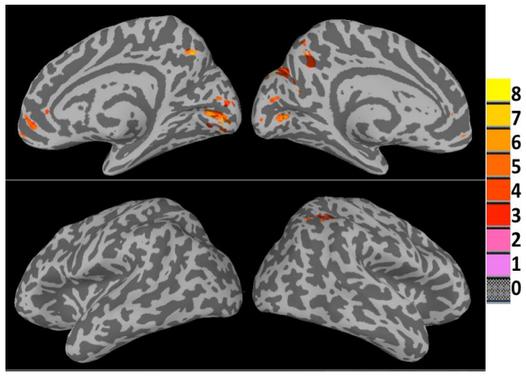

Figure S3: Brain regions with significant interaction between the two main fixed factors. That is the brain regions where the KOS treatment resulted in significantly difference in functional connectivity (at NIC=11) between migraine patients and normal controls. The statistical significance was assessed with the 3-way ANOVA (model type=5) at voxel-wise F-score threshold F≥4.373 (numerator DF=3, denominator DF=36, p≤0.01 uncorrected) and a minimum cluster size of 20 contiguous voxels. The color bar indicates the F-score level.

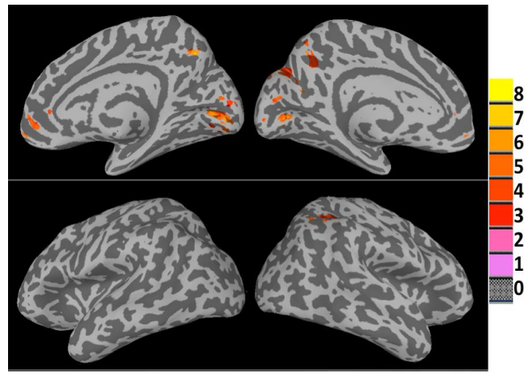

Figure S3: Brain regions with significant interaction between the two main fixed factors. That is the brain regions where the KOS treatment resulted in significantly difference in functional connectivity (at NIC=11) between migraine patients and normal controls. The statistical significance was assessed with the 3-way ANOVA (model type=5) at voxel-wise F-score threshold F≥4.373 (numerator DF=3, denominator DF=36, p≤0.01 uncorrected) and a minimum cluster size of 20 contiguous voxels. The color bar indicates the F-score level.